Design, safety and applications of radio-frequency antennas for ultra-high field MRI of the body

Bart Romke Steensma

538843-L-bw-Steensma
Processed on: 17-12-2019

Colophon

© Bart R. Steensma 2020

Cover design: Bart Steensma

Printed by: Ipskamp Printing

ISBN: 978-94-028-1865-9

All rights reserved. No parts of this publication may be reproduced or transmitted in any form or by any means, without written prior permission of the author.

This work is part of the research programme 'From coil to antenna' with project number 3507, which is (partly) financed by the Netherlands Organisation for Scientific Research (NWO).

Financial support for the printing of this thesis was provided by WaveTronica B.V.

Design, safety and applications of radio-frequency antennas for ultra-high field MRI of the body

Ontwikkeling, veiligheid en toepassingen van radiofrequentie antennes voor ultrahoog veld MRI van het lichaam

met een samenvatting in het Nederlands

Proefschrift

ter verkrijging van de graad van doctor aan de
Universiteit Utrecht
op gezag van de
rector magnificus, prof.dr. H.R.B.M. Kummeling,
ingevolge het besluit van het college voor promoties
in het openbaar te verdedigen op

donderdag 16 januari 2020 des middags te 4.15 uur

door

Bart Romke Steensma

geboren op 10 februari 1991
te Amsterdam

Promotor:	Prof. dr. D.W.J. Klomp
Copromotoren:	Dr. A.J.E. Raaijmakers Dr. C.A.T. van den Berg

This work is part of the research programme 'From coil to antenna' with project number 3507, which is (partly) financed by the Netherlands Organisation for Scientific Research (NWO).

Financial support for the printing of this thesis was provided by WaveTronica B.V.

Table of Contents

Chapter 1 **7**
Introduction

Chapter 2 **20**
Technical Background

Chapter 3 **28**
Design of a forward view antenna for prostate imaging at 7T

Chapter 4 **47**
Comparing signal-to-noise ratio for prostate imaging at 7T and 3T

Chapter 5 **66**
An 8-channel Tx/Rx dipole array combined with 16 Rx loops for high-resolution functional cardiac imaging at 7 T

Chapter 6 **88**
SAR and Temperature Distributions in a Database of Realistic Human Models for 7T Cardiac Imaging

Chapter 7 **112**
Local SAR assessment for multi-transmit systems: a study on the peak local SAR value as a function of magnetic field strength

Chapter 8 **134**
Geometry optimization of dipole antenna array for 10.5T body imaging

Chapter 9 **153**
Performance of a local 32-channel Tx/Rx-array for prostate imaging at 7T

Chapter 10 **172**
Summary and discussion

Appendix I **188**
Nederlandse samenvatting

Appendix II **192**
Tier system for safety validation of custom-built RF coils

Appendix III **198**
List of publications

Appendix IV **201**
Dankwoord

Appendix V **205**
Curriculum vitae

Chapter 1

Introduction

1.1. General introduction

Magnetic resonance imaging (MRI) is a medical imaging modality based on the phenomenon of nuclear magnetic resonance (NMR) [1]-[4]. Nowadays, MRI is used in every modern hospital because of its ability to resolve water-rich tissues with good contrast without the use of ionizing radiation. In a 2001 survey, the development of imaging methods such as CT and MRI was marked as the most important development in medicine in the last 25 years [5]. Since the 80's, more than 40.000 MRI systems have been installed worldwide and in 2015, 39 million MRI scans were done in the USA [6].

In an MRI system, three magnetic fields are used to generate and acquire the image. A static background (B_0) field is used to enable precession of nuclear spins at the Larmor frequency:

$$f_0 = \frac{\gamma}{2\pi} B_0 \quad [1]$$

The Larmor frequency for clinical MRI systems is 64 or 128 MHz for 1.5 Tesla (T) and 3T respectively. To generate and receive a signal from the precessing spins, an additional magnetic field called the radio-frequency (B_1) field is used. The B_1 field is generated by one or multiple "RF-coils" which are tuned to resonate at the Larmor frequency. Finally, gradient magnetic fields are used to make the B_0 field spatially dependent, which enables spatial encoding which is necessary to generate an image from the NMR signal. Since the invention of MRI there has been a strong drive to increase the field strength of the main magnetic field strength (B_0) [6]-[11]. By increasing the B_0-field strength, intrinsically available signal-to-noise ratio (SNR) increases [12]-[20]. When the image resolution of an MRI image increases or when MRI images are acquired at a faster rate using under-sampling methods, the SNR of the image also decreases resulting in an image that is distorted by noise. When going to a higher B_0-field strength, MR images can be acquired at an increased resolution or with an accelerated acquisition but still with acceptable SNR. Additionally, at higher field strengths tissue relaxation based contrast mechanisms are enhanced and spectral line separation increases which is beneficial for MR spectroscopy. In functional MRI experiments, MRI images are acquired in which the contrast depends on changing regional blood concentrations of oxy- and deoxy-hemoglobin (Blood Oxygen Level Dependent contrast/BOLD contrast). The sensitivity of the BOLD signal increases with field strength which enables more precise functional MRI brain research, which is another important driver for increasing the B_0 field strength.

538843-L-bw-Steensma
Processed on: 17-12-2019
PDF page: 8

Current clinical MRI systems have a field strength of 1.5T or 3T, while exploratory research is done at ultra-high field (UHF, 7.0T and beyond) MRI systems. For research purposes, the first full-body 10.5T and brain-only 11.7T human MRI scanners have become operational in the last two years. In 2017, one vendor obtained FDA approval for brain and extremity MRI at 7T which is a prerequisite for clinical scanning. 7T has been successfully applied to study the function and anatomy of the human brain with unprecedented detail [6], [21], [22]. For example, the higher BOLD-sensitivity at 7T was used to visualize orientation columns in the human brain with fMRI [21], while the available SNR could be used to image the brain with a 250 mm^3 resolution [6].

However, when imaging objects larger than the brain, image quality does not necessarily improve compared to 1.5T or 3T because of non-uniformity in the images at UHF that can be related to radiofrequency effects. The wavelength of the RF excitation field in tissue is determined by the Larmor frequency, the speed of light in vacuum c and the relative permittivity ε_r in the material of interest. Table 1 shows the wavelength in muscle tissue as a function of B_0 field strength.

$$\lambda = \frac{c}{f_0\sqrt{\varepsilon_r}} \quad [2]$$

With increasing field strength, the Larmor frequency f_0 increases which results consequently in a shorter wavelength of the B_1 field in tissue. At 7T, the wavelength of B_1 field becomes comparable to the dimensions of the head and significantly smaller than the body. The decreased wavelength leads to standing wave effects which causes severe signal inhomogeneity in the image (even complete signal voids) which obviously compromises diagnostic application.

B_0 [T]	f_0 [MHz]	Relative permittivity muscle tissue [a.u.]	Wavelength in muscle tissue [cm]
1.5	64	72.2	55
3.0	128	63.5	29
7.0	298	58.2	13
10.5	447	56.8	8.9
14	596	56.0	6.7

Table 1: field strength dependency of relative permittivity and wavelength in muscle tissue from Gabriel et al [23]

Next to signal inhomogeneity, UHF also needs to address larger levels of local energy dissipation. The electromagnetic interaction of the B_1 field with tissue leads to power dissipation in the tissue, which is quantified as specific absorption rate

538843-L-bw-Steensma
Processed on: 17-12-2019
PDF page: 9

(SAR). Both the increased frequency and the higher conductivity of tissue at UHF lead to more rapid power dissipation in the sample compared to 1.5T or 3T. This leads to low field intensity in tissue situated far away from the surface of the sample.

Additionally, power dissipation results in tissue heating, which is an unwanted side effect of all MRI scans. When the field strength is increased from 3T to 7T, more power is dissipated locally which can cause strong local tissue heating effects because of increased local SAR [15], [24]. The increase in local SAR needs to be addressed by extensive simulation efforts to predict SAR exposure and, subsequently, by appropriate scanning limitations such as sufficiently long repetition times.

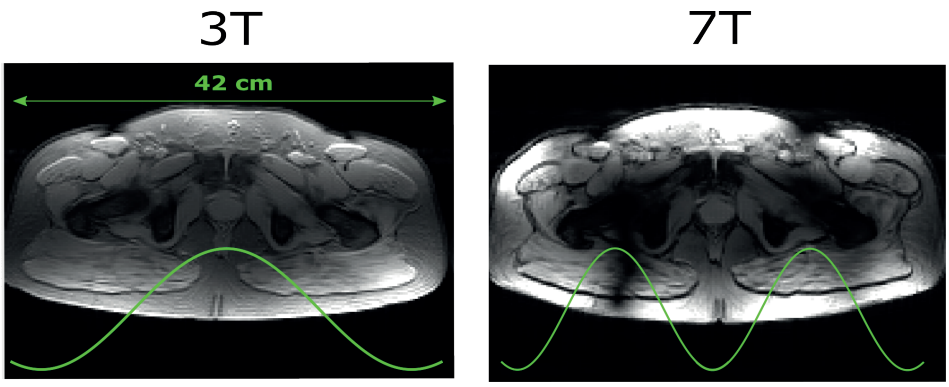

Figure 1: MR image of the pelvis at 3T and 7T, showing non-uniform contrast at 7T. The green line indicates the wavelength of the RF excitation field in the body for both field strengths.

The first body imaging experiments at 7T [24] were done with a birdcage-coil [25], [26], which is commonly used for RF transmission in 1.5T and 3T MRI systems. These initial results showed non-uniform images and an overall low SNR. Because of the short wavelength of the RF excitation field at 7T, interference artifacts were present throughout the image and a low efficiency was achieved because of increased conductive losses in the sample compared to 1.5T or 3T MRI. As presented in this same study, researchers realized that for 7T body imaging, a different approach was necessary. Instead of a volume-resonator such as the birdcage coil, arrays of multiple (8 or 16) local transmit/receive coils were introduced [24]. By using multiple transmit elements, the interference patterns in the RF excitation field could be manipulated to achieve good image quality in the imaging region. By using local instead of volume coils, the efficiency of the coil could be increased. Initial local transmit/receive coils were designed using either micro-strip or loop elements [24], [27].

538843-L-bw-Steensma
Processed on: 17-12-2019
PDF page: 10

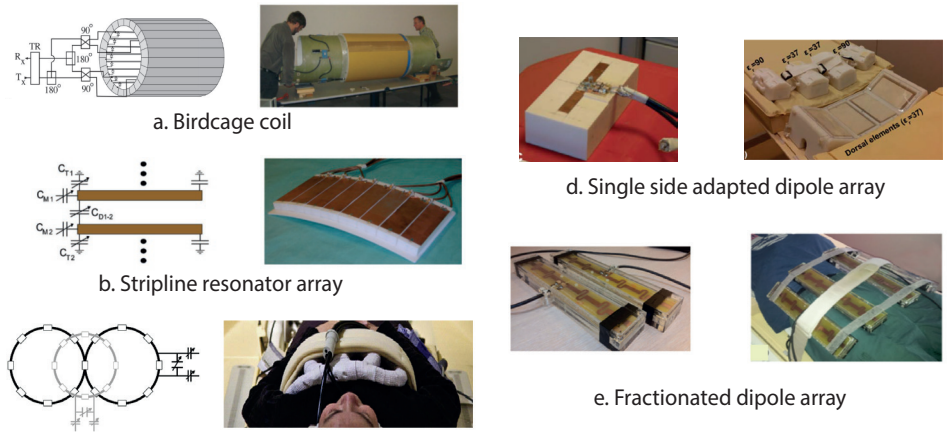

Figure 2: different coil array designs for body imaging at 7T. The birdcage coil (a) and stripline resonator array (b) were developed in Minneapolis by Vaughan et al [24]. An example of a loop-coil, combined with a butterfly coil (c) was developed in Leiden by Versluis et al [27] for cardiac imaging. The single side adapted dipole array [28] (d) and the fractionated dipole array [29] (e) were both developed in Utrecht by Raaijmakers et al.

The type of coil element that is used for signal transmission and reception has a strong influence on the image quality for UHF MRI. Adopting lower field RF design resonant loop coils or strip-line elements were initially often used as Tx/Rx elements for local coil arrays [18], [30]-[32]. However, at UHF those types of elements are not necessarily optimal [33]-[35]. At increased field strength, the transmit profile of a loop coil becomes non-symmetric which leads to dark banding artifacts on the surface of an imaging volume [33]. Furthermore, loop and strip-lines are example of resonant near field probes, storing RF magnetic energy in the strong reactive magnetic field in its near field. Relatively early in 7T body imaging research, it was observed that these probes do not provide the best signal penetration. When considering RF transmit field at UHF, it is important to notice the different characteristic regions that exist close to a transmitting element (figure 3).

538843-L-bw-Steensma
Processed on: 17-12-2019
PDF page: 11

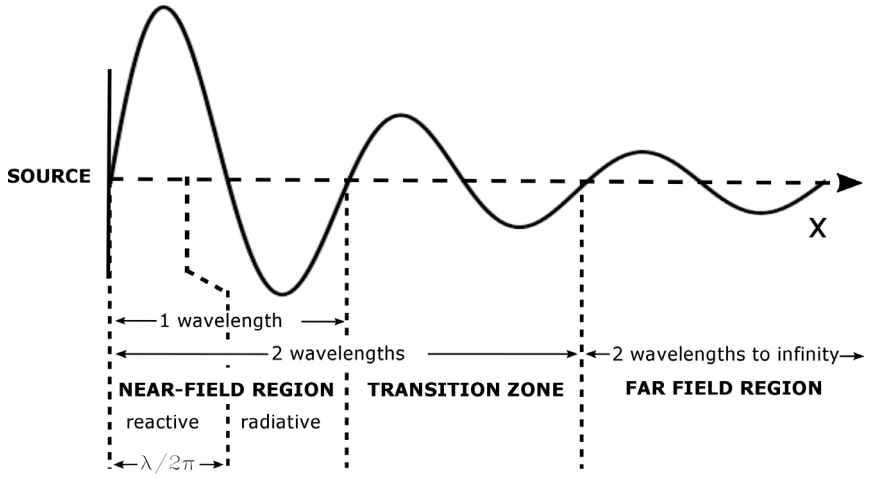

Figure 3: different radiation regions as a function of distance from the source. At 7T, the wavelength in muscle tissue is 13 cm, implying that tissue in the center of the body is located in the transition zone.

In the case of 7T body imaging, the imaging target is no longer located in the reactive near-field regime, but in the transition zone where the fields have already decayed significantly. For imaging at 1.5T or 3T, it is sufficient to have a coil as this reactive near field is large enough to contain all imaging sites in the body. At UHF however, it is more beneficial to have a coil that has a high efficiency in the transition zone, while a strong but rapidly decaying near-field will lead to image non-uniformity at the surface of the sample. A more suitable coil element is a radiative dipole antenna, which radiates energy towards the imaging target instead of storing energy in the reactive near-field .

In 2011, the single-side adapted dipole antenna (SSAD) was introduced for 7T prostate imaging [28], [36]. The dipole design was based on antenna arrays originating from RF hyperthermia treatment [37], [38]. The single-side adapted dipole antenna consists of a ceramic substrate with a short dipole antenna (11 cm) mounted on top. The ceramic substrate has a permittivity which is relatively close to the permittivity of the human body (e_r=37) in order to minimize reflections at the substrate-tissue interface [39]. Later research indicated that the use of this ceramic substrate was not necessary, and that long dipole antennas (30 cm) with an added inductance would give better results. A redesign of dipole antenna based on an optimization of length and inductance led to the design of the fractionated dipole antenna [29]. This antenna design showed marked improvements in image quality and lower SAR compared to the SSAD. Furthermore, the heavy ceramic substrate was removed which was more subject friendly and improved the overall usability of the array. The fractionate dipole is

538843-L-bw-Steensma
Processed on: 17-12-2019
PDF page: 12

now used for body imaging at multiple 7T sites around the world and a modified design has been used for the first body imaging experiments at 10.5T [20], [34].

1.2. Thesis aim and outline

This thesis project aims to improve RF coil arrays by investigating the use of alternative dipole antenna geometries and by the use of an increased number of transmit and receive channels to obtain more control over the RF field in the human body. The RF safety and performance of dipole antenna arrays is investigated for different human models, antenna arrays and B_0 field strengths. Finally, the dipole antenna arrays are used in cardiac and prostate imaging applications.

Chapter 2 provides a technical background to enable understanding of terminology used throughout this thesis. A general introduction is given on RF coils and antennas, multi-transmit RF excitation and RF safety.

Throughout the development of the single side adapted dipole array and the fractionated dipole array, prostate imaging has been the primary focus. Prostate cancer is the most frequently diagnosed type of cancer among men in Europe and the United States [40], as a result of the increasing age of the population and the use of prostate-specific antigen blood tests. In the Netherlands, 10.000 men are diagnosed on a yearly basis, while per year 2.500 men die of prostate cancer (Integraal Kanker Centrum Nederland). Prostate cancer often has an unaggressive nature, which leads to overdiagnosis and overtreatment in many men [41], [42]. A more specific diagnostic tool is needed to distinguish the potentially dangerous tumors from the harmless slowly growing lesions. One of the potential candidates for such a tool is 7T imaging, where the high signal-to-noise ratio and the improved possibilities for MR spectroscopy can be utilized to aid in more specific diagnosis. For this reason, the prostate is one of the first organs of interest outside the brain. It has therefore been the imaging target of interest for the development of the SSAD and the fractionated dipole antenna and it is also the primary focus for most studies in this project.

Prostate imaging at 7T is typically done using an array of transmit/receive antennas, which are aligned in a belt-like fashion around the pelvis. However, because of the deeply situated position of the prostate, much of the available signal intensity at the antenna is attenuated considerably at the depth of the prostate. A shorter distance from antenna to the prostate would be highly desirable. One way to reduce the distance between the antenna and the imaging target is by inserting the antenna in the rectum using an “endo-rectal coil”. Previous work demonstrated the benefits of using an endo-rectal coil as an addition to a local

538843-L-bw-Steensma
Processed on: 17-12-2019
PDF page: 13

array [30], [43]. As a less invasive alternative, we investigated the use of a local waveguide antenna, "the forward view antenna", which is placed against the perineum of the subject. By targeting the perineum, the coil is positioned closer to the prostate than the dipole antennas which are arranged around the pelvis in a belt-like fashion. In chapter 3, the performance of the forward view antenna is investigated for prostate imaging at 7T.

Another way to improve imaging performance of a dipole array is by adding loop coils for improved signal reception. Wiggins et al. demonstrated in 2013 that a loop-coil can be positioned on the same axis as a dipole antenna, without adding any inter-element coupling [44]. By combining loops and dipoles in receive mode, the SNR of an array could be improved compared to a situation with only loops or only dipoles. Therefore, the fractionated dipole antenna array was modified by adding 16 receive only loops. By adding the receive loops, SNR can be improved strongly [45] without having to place a coil in the rectum or perineum region, thereby simplifying the experimental setup. With this improved antenna array design, signal-to-noise ratio and parallel imaging performance is compared for prostate imaging at 3T and 7T. To make the comparison as fair as possible, all sequence related parameters that affect SNR but are not a result of the coils' EM-field distribution in the body, were carefully corrected for. T2 weighted prostate images are acquired in a prostate cancer patient at 3T and 7T to demonstrate 7T imaging performance in a clinically relevant setting. Results of this study are shown in chapter 4.

Next to prostate imaging, cardiac imaging is an application that can benefit from the increased SNR and different contrast mechanisms at 7T compared to lower field strengths. The improved SNR could be used to decrease examination times, which are typically quite long for cardiac MRI exams. To enable the use of the previously designed dipole/loop-array for cardiac imaging, a modification is made to the geometry of the antenna array. The two central anterior elements were constructed with an angle at the center of the element to allow the elements fit closely to the curvature of the torso. SNR contributions of the receive-only loops and the dipole antennas were evaluated for cardiac imaging. Two experienced readers were asked to rate the image quality of cardiac CINE images in 8 volunteers. Using the available SNR, cardiac CINE images were acquired at increased resolution compared to standard clinical exams. The results of this study are demonstrated in chapter 5.

For all local coil arrays used in MRI, limits are specified for both global and local SAR levels by the IEC. For 7T body imaging, local SAR is often the limiting factor that restricts shortening of the repetition time. Since local SAR levels

538843-L-bw-Steensma
Processed on: 17-12-2019
PDF page: 14

are strongly dependent on the subject and the RF shim setting, conservative methods are applied to estimate SAR levels during an MRI exam on a multi-transmit system. The downside of this approach is that using conservative SAR estimations leads to limitations on the allowed average power or repetition time, leading to either decreased image quality of longer examination times. To enable calculation of realistic, but less conservative SAR levels, a simulation study can to be done on multiple dielectric models, to evaluate local SAR for many different shim settings. In previous work by Meliado et al [46], a simulation study was done on 25 custom built human dielectric models which were generated based on automatic segmentation of Dixon scans of the pelvis. These models were used to study inter-subject variability of local SAR for 7T prostate imaging and to calculate realistic SAR limits. In chapter 6, the same methodology is used to generate 14 dielectric models of the torso to study inter-subject variation of local SAR for 7T cardiac imaging. In addition, temperature simulations were done to estimate potential temperature rise during short cardiac MRI examinations which are acquired during a breath-hold and to study inter-subject variation of temperature rise.

It is expected from basic electromagnetics that with increasing B_0-field strength, SNR increases approximately linearly while local SAR increases quadratically. However, some studies indicate that for ultra-high field strengths, the increase in SNR is more than linear, while SAR does not necessarily increase quadratically. However, most of these studies were done on phantoms or on human head models, but not for the body. In chapter 7, SNR and local SAR levels were evaluated for antenna arrays at different field strengths. After providing a general introduction on RF safety assessment for local multi-transmit arrays, a simulation study is done to investigate peak local SAR, transmit efficiency and SNR for a human model of the pelvis at 3T, 7T, 10.5T and 14T.

When increasing the B_0 field strength beyond 7T, local peak SAR values further increase as demonstrated in chapter 7. The geometry of a dipole antenna can have a strong effect on peak local SAR [33], [47]. Within an ongoing collaboration with the Center of Magnetic Resonance Research in Minnesota, where the first full body human 10.5T MRI system was installed, the effect of dipole antenna geometry on local peak SAR was evaluated for body imaging at 10.5T in chapter 8. A new coil array design named “the snake antenna array” was introduced. After validating simulation results by measurements and obtaining approval by the FDA to scan human subjects with the snake antenna array, in vivo images were acquired at 10.5T.

While in chapter 8, the geometry of the coil element was used to lower effective

538843-L-bw-Steensma
Processed on: 17-12-2019
PDF page: 15

SAR levels, it is also possible to decrease effective SAR levels by increasing the number of transmit channels. The effect of using this method was investigated for prostate imaging at 7T. First, a simulation study was done to investigate the ultimate possible coil performance for prostate imaging at 7T. Realistic coil arrays including up to 32 channels were simulated and their performance was benchmarked against the ultimate performance. Finally, the integration of a 32 channel transmit amplifier as an addition to the Philips Achieva system, and the construction of a 32 channel local coil array is demonstrated. Results of this study are demonstrated in chapter 9.

Finally, chapter 10 provides a summary of the results obtained within this thesis and a general discussion on the results and future perspectives .

References

[1] E. M. Purcell, H. C. Torrey, and R. V. Pound, "Resonance absorption by nuclear magnetic moments in a solid", Physical Review. vol. 69, no. 37, 1946.

[2] R. Damadian, "Tumor detection by nuclear magnetic resonance", Science, vol. 19. no. 171, pp1151-3, 1971.

[3] P. C. Lauterbur, "Image formation by induced local interactions: Examples employing nuclear magnetic resonance," Nature, vol. 242, pp 190-191, 1973.

[4] P. Mansfield and P. K. Grannell, "Nmr 'diffraction' in solids?," Journal of Physics C: Solid State Physics., vol. 6, no. 22, 1973.

[5] V. R. Fuchs and H. C. Sox, "Physicians' views of the relative importance of thirty medical innovations," Health Aff., 2001.

[6] M. E. Ladd et al., "Pros and cons of ultra-high-field MRI/MRS for human application," Prog. Nucl. Magn. Reson. Spectrosc., vol. 109, pp. 1–50, 2018.

[7] E. Moser, "Ultra-high-field magnetic resonance: Why and when?," World J. Radiol., 2010.

[8] K. Ugurbil, "Magnetic resonance imaging at ultrahigh fields," IEEE Trans. Biomed. Eng., 2014.

[9] T. F. Budinger et al., "Toward 20 T magnetic resonance for human brain studies: opportunities for discovery and neuroscience rationale," Magnetic Resonance Materials in Physics, Biology and Medicine. 2016.

[10] O. Kraff, A. Fischer, A. M. Nagel, C. Mönninghoff, and M. E. Ladd, "MRI at 7 Tesla and above: Demonstrated and potential capabilities," J. Magn. Reson. Imaging, vol. 41, no. 1, pp. 13–33, 2015.

[11] B. K. Rutt and D. H. Lee, "The impact of field strength on image quality in MRI," J. Magn. Reson. Imaging, 1996.

[12] D. I. Hoult and P. C. Lauterbur, "The sensitivity of the zeugmatographic experiment involving human samples," J. Magn. Reson., 1979.

538843-L-bw-Steensma
Processed on: 17-12-2019
PDF page: 16

[13] W. A. Edelstein, G. H. Glover, C. J. Hardy, and R. W. Redington, "The intrinsic signal-to-noise ratio in NMR imaging," Magn. Reson. Med., vol. 3, no. 4, pp. 604–618, 1986.

[14] O. Ocali and E. Atalar, "Ultimate intrinsic signal-to-noise ratio in MRI," Magn. Reson. Med., vol. 39, no. 3, pp. 462–473, 1998.

[15] C. M. Collins and M. B. Smith, "Signal-to-noise ratio and absorbed power as functions of main magnetic field strength, and definition of '90°' RF pulse for the head in the birdcage coil," Magn. Reson. Med., 2001.

[16] J. T. Vaughan et al., "7T vs. 4T: RF power, homogeneity, and signal-to-noise comparison in head images," Magn. Reson. Med., vol. 46, no. 1, pp. 24–30, 2001.

[17] F. Wiesinger, P. Boesiger, and K. P. Pruessmann, "Electrodynamics and ultimate SNR in parallel MR imaging," Magn. Reson. Med., vol. 52, no. 2, pp. 376–390, 2004.

[18] A. B. Rosenkrantz et al., "T2-weighted prostate MRI at 7 Tesla using a simplified external transmit-receive coil array: Correlation with radical prostatectomy findings in two prostate cancer patients," J. Magn. Reson. Imaging, vol. 41, no. 1, pp. 226–232, 2015.

[19] R. Pohmann, O. Speck, and K. Scheffler, "Signal-to-noise ratio and MR tissue parameters in human brain imaging at 3, 7, and 9.4 tesla using current receive coil arrays," Magn. Reson. Med., 2016.

[20] M. A. Ertürk et al., "Toward imaging the body at 10.5 tesla," Magn. Reson. Med., vol. 00, pp. 1–10, 2016.

[21] E. Yacoub, N. Harel, and K. Ugurbil, "High-field fMRI unveils orientation columns in humans," Proc. Natl. Acad. Sci., 2008.

[22] J. J. M. Zwanenburg, J. Hendrikse, T. Takahara, F. Visser, and P. R. Luijten, "MR angiography of the cerebral perforating arteries with magnetization prepared anatomical reference at 7T: Comparison with time-of-flight," J. Magn. Reson. Imaging, 2008.

[23] S. Gabriel, R. W. Lau, and C. Gabriel, "The dielectric properties of biological tissues: II. Measurements in the frequency range 10 Hz to 20 GHz," Phys. Med. Biol., 1996.

[24] J. T. Vaughan et al., "Whole-body imaging at 7T: Preliminary results," Magn. Reson. Med., vol. 61, no. 1, pp. 244–248, 2009.

[25] C. E. Hayes, "The development of the birdcage resonator: A historical perspective," NMR in Biomedicine. 2009.

[26] C. E. Hayes, W. A. Edelstein, J. F. Schenck, O. M. Mueller, and M. Eash, "An efficient, highly homogeneous radiofrequency coil for whole-body NMR imaging at 1.5 T," J. Magn. Reson., 1985.

[27] M. J. Versluis, N. Tsekos, N. B. Smith, and A. G. Webb, "Simple RF design for human functional and morphological cardiac imaging at 7 tesla," J. Magn. Reson., 2009.

[28] A. J. E. Raaijmakers et al., "Design of a radiative surface coil array element at 7 T: The single-side adapted dipole antenna," Magn. Reson. Med., vol. 66, no. 5, pp. 1488–1497, 2011.

[29] A. J. E. Raaijmakers et al., "The fractionated dipole antenna: A new antenna for body imaging at 7 Tesla," Magn. Reson. Med., vol. 75, no. 3, pp. 1366–1374, 2016.

[30] G. J. Metzger et al., "Performance of external and internal coil configurations for prostate investigations at 7 T," Magn. Reson. Med., vol. 64, no. 6, pp. 1625–1639, 2010.

[31] G. Adriany et al., "Transmit and receive transmission line arrays for 7 tesla parallel imaging," Magn. Reson. Med., vol. 53, no. 2, pp. 434–445, 2005.

538843-L-bw-Steensma
Processed on: 17-12-2019
PDF page: 17

[32] A. Graessl et al., "Modular 32-channel transceiver coil array for cardiac MRI at 7.0T," Magn. Reson. Med., vol. 72, no. 1, pp. 276–290, 2014.

[33] A. J. E. Raaijmakers, P. R. Luijten, and C. A. T. van den Berg, "Dipole antennas for ultrahigh-field body imaging: a comparison with loop coils," NMR Biomed., vol. 29, no. 9, pp. 1122–1130, 2016.

[34] M. A. Ertürk, A. J. E. Raaijmakers, G. Adriany, K. Ugurbil, and G. J. Metzger, "A 16-channel combined loop-dipole transceiver array for 7 Tesla body MRI," Magn. Reson. Med., vol. 00, pp. 1–11, 2016.

[35] S. H. G. Rietsch, S. Orzada, A. K. Bitz, M. Gratz, M. E. Ladd, and H. H. Quick, "Parallel transmit capability of various RF transmit elements and arrays at 7T MRI," Magn. Reson. Med., vol. 00, pp. 1–11, 2017.

[36] Ö. Ipek, a J. E. Raaijmakers, D. W. J. Klomp, J. J. W. Lagendijk, P. R. Luijten, and C. a T. van den Berg, "Characterization of transceive surface element designs for 7 tesla magnetic resonance imaging of the prostate: radiative antenna and microstrip," Phys. Med. Biol., vol. 57, no. 2, pp. 343–355, 2011.

[37] M. Seebass, R. Beck, J. Gellermann, J. Nadobny, and P. Wust, "Electromagnetic phased arrays for regional hyperthermia: Optimal frequency and antenna arrangement," Int. J. Hyperth., 2001.

[38] H. Kroeze, M. Van Vulpen, A. A. C. De Leeuw, J. B. Van De Kamer, and J. J. W. Lagendijk, "Improvement of absorbing structures used in regional hyperthermia," Int. J. Hyperth., 2003.

[39] A. J. E. Raaijmakers et al., "Design of a radiative surface coil array element at 7 T: The single-side adapted dipole antenna," Magn. Reson. Med., vol. 66, no. 5, pp. 1488–1497, 2011.

[40] R. L. Siegel, K. D. Miller, and A. Jemal, "Cancer Statistics , 2017," vol. 67, no. 1, pp. 7–30, 2017.

[41] M. R. Cooperberg, P. R. Carroll, and L. Klotz, "Active surveillance for prostate cancer: Progress and promise," J. Clin. Oncol., vol. 29, no. 27, pp. 3669–3676, 2011.

[42] G. L. Lu-Yao et al., "Outcomes of localized prostate cancer following conservative management," Jama, vol. 302, no. 11, pp. 1202–1209, 2009.

[43] B. Van den Bergen et al., "Uniform prostate imaging and spectroscopy at 7 T: Comparison between a microstrip array and an endorectal coil," NMR Biomed., vol. 24, no. 4, pp. 358–365, 2011.

[44] G. C. Wiggins et al., "Mixing loops and electric dipole antennas for increased sensitivity at 7 Tesla," in In: Proceedings of the 21th scientific meeting, International Society for Magnetic Resonance in Medicine, Salt Lake City, 2013, vol. 21, p. 2737.

[45] I. J. Voogt et al., "Combined 8-channel transceiver fractionated dipole antenna array with a 16-channel loop coil receive array for body imaging at 7 Tesla," Proc. 23th Sci. Meet. Int. Soc. Magn. Reson. Med. Vancouver, vol. 200, no. 2007, p. 631, 2015.

[46] E. F. Meliadò, C. A. T. van den Berg, P. R. Luijten, and A. J. E. Raaijmakers, "Intersubject specific absorption rate variability analysis through construction of 23 realistic body models for prostate imaging at 7T," Magn. Reson. Med., no. April 2018, pp. 2106–2119, 2018.

[47] B. R. Steensma, A. V. Obando, D. W. J. Klomp, C. A. T. van den Berg, and A. J. E. Raaijmakers, "Body imaging at 7 tesla with much lower SAR levels: an introduction of the Snake Antenna Array," in Proc. Intl. Soc. Mag. Reson. Singapore, 2016.

538843-L-bw-Steensma
Processed on: 17-12-2019
PDF page: 18

538843-L-bw-Steensma
Processed on: 17-12-2019

Chapter 2

Technical Background

2.1. RF coils for MRI

To be able to acquire a signal with MRI, nuclear magnetic spins precessing at the Larmor frequency have to be excited using an external magnetic field (referred to as the B_1-field) that oscillates at the Larmor frequency $f_{0:}$

$$f_0 = \frac{\gamma}{2\pi} B_0 \quad [1]$$

The magnitude of the B_1-field and the pulse length τ determine the flip angle FA that can be achieved:

$$FA = \int_0^{\tau} \frac{\gamma}{2\pi} B_1 dt \quad [2]$$

Only the component of the B_1-field that is static with respect to the precessing spins is able to tip the magnetic moment of the spins. The result is that only the right rotating part of the B_1-field, which is referred to as the B_1^+-field, is able to excite spins.

$$B_1^+ = \frac{B_{1,x} + jB_{1,y}}{2} \quad [3]$$

After the spins are excited by the RF coil, a very small RF-signal will be emitted back to and received by the RF-coil. According to the principle of reciprocity [1], [2], the signal propagating back from the spins towards the RF coil (the receive field) is right-rotating. The sensitivity of the RF coil to the receive signal can be found by considering the receive field and swapping the source and the detector (antenna becomes source and spin becomes detector). When swapping the source and the detector, it can be seen that the sensitivity of the RF coil to the receive signal is the left-rotating part of the B_1 field that would be transmitted by the RF coil. This field is referred to as the B_1^--field:

$$B_1^- = \frac{B_{1,x} - jB_{1,y}}{2} \quad [4]$$

Figure 1 shows the B_1 field of a 15cm diameter loop coil on a rectangular phantom with tissue mimicking properties S=0.4 S/m, ε_r=34. The transmit and receive fields are mirror images on this phantom.

538843-L-bw-Steensma
Processed on: 17-12-2019

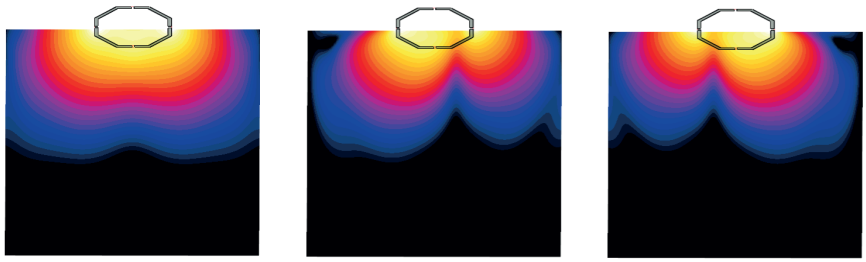

Figure 1: the B_1-field of a loop coil at 298 MHz, the right-hand rotating transmit field (B1+) and the left-hand rotating receive (B1-) field are mirror images in a symmetric phantom. Electrical properties of the phantom: S=0.4 S/m, ε_r=34.

In practice, an RF coil is implemented as a structure of conducting wire that is able to transmit and receive RF signals at the Larmor frequency. The historical term 'coil' refers to solenoid or loop structures that are often used, but an 'RF-coil' can have many different geometries. The coil geometry depends especially on the Larmor frequency at which the MRI system operates. Shortly after the introduction of superconducting MRI magnets, researchers at General Electric developed the 'birdcage-coil' [3], [4], which is a resonant RF coil that is able to generate a uniform B_1-field over a large volume. In all commonly available 1.5T and 3T MRI systems, this birdcage coil is used as a transmit-only (Tx) coil. For signal detection, modern MRI system, utilize multiple local receive (Rx) coils [5]. These receive coils have a complete different appearance and location than the transmit birdcage coil. High numbers of receive coils (up to 128) are placed closely to the body for optimal sensitivity, where the combined information of all coils can be used to accelerate the acquisition (parallel MRI) [5]–[10].

2.2. Multi-transmit

In multi-transmit, multiple transmit channels are powered by separate RF amplifiers. The input voltage and phase of these transmit channels can be modified to manipulate the interferences of the individual B_1^+ field of the various channels, resulting in an overall more optimal B_1^+ transmit field. This is typically achieve by modifying the phase of the individual B_1^+transmit fields such that constructive interference is achieved leading to high efficiency and local homogeneity [11]–[14]. Standard available birdcage coils have 2 transmit channels, which provide a moderate control over the RF transmit field. More advanced systems include numbers of transmit channels ranging from 8 to 64 [15]. These systems are mainly used in 7T MRI, especially for body imaging. The first successful experimental demonstration of 7T body imaging using a

538843-L-bw-Steensma
Processed on: 17-12-2019
PDF page: 22

multi-transmit system was published in 2008 by Metzger et al [11]. The method of 'RF shimming' was introduced, where constructive phase interference of the individual channel B_1^+ field was obtained by changing the individual phase of the transmitters.

$$B^+_{1,combined} = \sum_{i=1}^{Ntx} a_i B^+_{1,i} \qquad [5]$$

Figure 2 shows a schematic representation of RF phase shimming with multiple amplifiers, leading to improved image quality in the prostate.

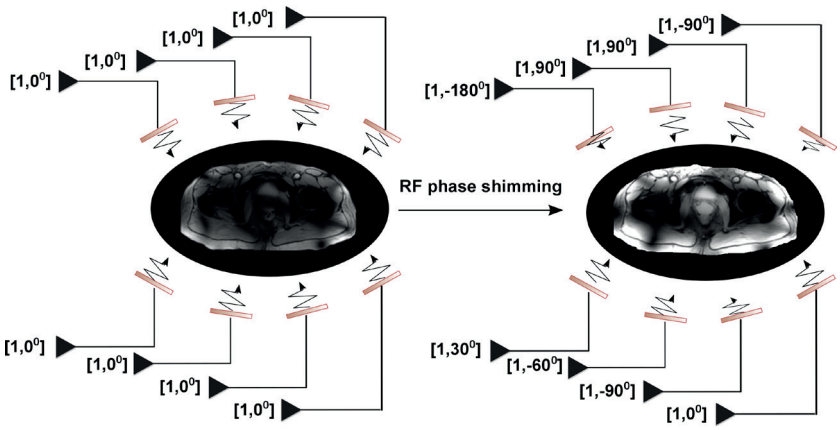

Figure 2: schematic example of a multi-transmit setup and the effect of phase-only RF shimming on the image quality of a 7T prostate MRI scan. By modifying the transmit phase of the individual amplifiers, constructive phase interference of the RF fields is obtained in the prostate region, which leads to a strong signal in the prostate. Phase settings were obtained from Meliado et al [16].

More advanced RF-shimming method do not only change the phase and amplitude of the RF-pulse, but also modify the shape of the RF pulse and the interplay with the gradient trajectory (these methods are often referred to as pTx or transmit SENSE) [13], [14].

Multi-transmit RF coils are normally connected to the MRI system using coaxial cables with a characteristic impedance of 50 Ω. The impedance of single port of a loaded and matched RF coil is normally close to 50 Ω but not necessarily equal. When the coil is used in transmit mode, some power is reflected at the coil connection. Additionally, power can be coupled to other ports of the multi-transmit system through inter-element coupling. As a result, when forward power is applied at the ports of a multi-transmit system, power will scatter towards other ports. Given a vector of forward power waves , the vector with reflected power waves can be calculated using the scattering matrix S [17]:

538843-L-bw-Steensma
Processed on: 17-12-2019
PDF page: 23

$$b = Sa \quad [6]$$

The scattering matrix has dimensions [nports*nports] and depends on the coil geometry, coil position and on sample in the coil. Scattering can be measured on the bench using a vector network analyzer or in the MRI system by using directional couplers. When designing an RF coil array, it is desirable to have a low reflection at the coil connection, and as less inter-element coupling as possible. To achieve low reflection, lumped elements are used to build tune and matching circuits. Multiple techniques can be used to achieve low inter-element coupling, such as loop overlapping [5], using coil with orthogonal field patterns [18] or self-decoupling methods [19]. High reflection and high inter-element coupling will reduce the efficiency of the coil array. Scattering parameters are used throughout this document as a quick quantitative assessment of coil efficiency.

2.3. RF safety

During RF transmission in an MRI exam, power is dissipated in the body through conduction currents, which can result in local and global tissue heating. To ensure safety of the subject during an MRI exam, the international electro technical committee (IEC) has set limits to temperature and temperature elevation during an MRI examination.

	Maximal body core temperature in °C	Maximal local tissue temperature in °C	Maximal body core temperature elevation in °C
Normal Operating Mode	39	39	0.5
1st Level Controlled Mode	40	40	1
2nd Level Controlled Mode	> 40	> 40	> 1

Table 1: Limits for maximum body core temperature, maximum local tissue temperature, and maximum body core temperature elevation (IEC 60601-2-33:2015).

Since MR thermometry measurements in the MRI scanner are not sensitive enough to measure temperature change within the safety guidelines, EM simulations are used to assess the safety of RF coils in an MRI system. Commercial software packages are available to simulate RF coils for MRI to a high degree of detail, even including a range of human models with realistic electric and thermal properties [20], [21]. Because of the inability to fully simulate individual thermoregulatory responses in the human body which is necessary for accurate temperature simulations, EM simulations are used to calculate specific absorption rate (SAR) instead to estimate the risk of local tissue heating. SAR is defined as the power absorption per unit mass:

538843-L-bw-Steensma
Processed on: 17-12-2019
PDF page: 24

$$SAR(r) = \frac{dP(r)}{dm} = \frac{\sigma}{2\rho} |E(r)|^2 \quad [7]$$

SAR can be calculated on a global level (input power divided by total mass) and locally, in which local power deposition is averaged over a mass of 10g. In addition to the temperature limits, the IEC has set the following limits for global and local SAR [22]:

Operating mode	Normal	1st Level Controlled	2nd Level Controlled
Global SAR (W/kg)	**Volume Transmit Coils**		
Whole Body	2	4	> 4
Partial Body	2 - 10	4 - 10	> 4 - 10
Head	3.2	3.2	> 3.2
Local SAR (W/kg)	**Local Transmit Coils**		
Head	10	20	> 20
Trunk	10	20	> 20
Limbs	20	40	> 40

Table 2: Limits for global and local SAR. SAR is averaged over a time of 6 min (IEC 60601-2-33:2015). The partial body SAR limit is calculated by linearly interpolating between the maximum and minimum as a function of the ratio of the exposed patient mass (mass receiving 95% of the RF power) to the total mass (Figure AA.8 of IEC60601-2-33). Local SAR is averaged over cubes with a mass of 10 g.

Calculations of local SAR distributions are specifically computationally challenging for multi-transmit coils, where the SAR depends strongly on how the different transmit channels are combined. To rapidly calculate local SAR for any given a complex transmit vector v which contains the transmit phase and amplitude of every channel, the Q-matrix formalism [23] is defined as:

$$SAR = \frac{\sigma}{2\rho} |E|^2 = \frac{\sigma}{2\rho} \left\{ v^H E_x^H E_x v + v^H E_y^H E_y v + v^H E_z^H E_z v \right\} =$$

$$\frac{\sigma}{2\rho} v^H \left\{ E_x^H E_x + E_y^H E_y + E_z^H E_z \right\} v = v^H Q v \quad [8]$$

The Q-matrix enables quick calculation of SAR for any transmit vector v. The Q-matrix has dimensions [N_{ports}*N_{ports}]. For local SAR calculations, a Q-matrix needs to be constructed for every voxel while for global SAR calculations a Q-matrix is averaged over the whole sample volume. Since simulation models often contain millions of voxels, calculations with the Q-matrix are highly memory intensive. For local SAR calculations, there are often several voxels

538843-L-bw-Steensma
Processed on: 17-12-2019
PDF page: 25

in the models that have a risk of achieving a high SAR, but also voxels that will never achieve a high SAR. For calculation of peak local SAR values, it is sufficient to monitor only the voxels which are at risk of achieving a high SAR. To find these voxels, a compression technique called 'virtual observation points [24], [25]' is used throughout this work to compress the number of voxels in a local Q-matrix, while still being able to calculate peak local SAR values without underestimation.

References

[1] D. I. Hoult and P. C. Lauterbur, "The sensitivity of the zeugmatographic experiment involving human samples," *J. Magn. Reson.*, 1979.

[2] D. I. Hoult, "The principle of reciprocity in signal strength calculations - A mathematical guide," *Concepts Magn. Reson.*, 2000.

[3] C. E. Hayes, "The development of the birdcage resonator: A historical perspective," *NMR in Biomedicine*. 2009.

[4] C. E. Hayes, W. A. Edelstein, J. F. Schenck, O. M. Mueller, and M. Eash, "An efficient, highly homogeneous radiofrequency coil for whole-body NMR imaging at 1.5 T," *J. Magn. Reson.*, 1985.

[5] P. B. Roemer, W. A. Edelstein, C. E. Hayes, S. P. Souza, and O. M. Mueller, "The NMR phased array," *Magn. Reson. Med.*, vol. 16, no. 2, pp. 192–225, Nov. 1990.

[6] A. D. Hendriks, P. R. Luijten, D. W. J. Klomp, and N. Petridou, "Potential acceleration performance of a 256-channel whole-brain receive array at 7 T," *Magn. Reson. Med.*, vol. 81, no. 3, pp. 1659–1670, 2019.

[7] M. Schmitt *et al.*, "A 128-channel receive-only cardiac coil for highly accelerated cardiac MRI at 3 tesla," *Magn. Reson. Med.*, 2008.

[8] B. Keil *et al.*, "A 64-channel 3T array coil for accelerated brain MRI," *Magn. Reson. Med.*, 2013.

[9] K. Uğurbil, L. Delabarre, G. Adriany, P. F. Van De Moortele, C. Olman, and A. Grant, "Brain imaging with improved acceleration and SNR at 7 Tesla obtained with 64-channel receive array," no. December 2018, pp. 1–15, 2019.

[10] B. Keil and L. L. Wald, "Massively parallel MRI detector arrays," *J. Magn. Reson.*, vol. 229, pp. 75–89, 2013.

[11] G. J. Metzger *et al.*, "Local B1+ shimming for prostate imaging with transceiver arrays at 7T based on subject-dependent transmit phase measurements," *Magn. Reson. Med.*, vol. 59, no. 2, pp. 396–409, 2008.

[12] U. Katscher, "Basic and Tailored RF Shimming in a Multi-transmit Whole Body MR System," *PIERS Online*, vol. 4, no. 1, pp. 781–784, 2008.

[13] F. Padormo, A. Beqiri, J. V. Hajnal, and S. J. Malik, "Parallel transmission for ultrahigh-field imaging," *NMR Biomed.*, vol. 29, no. 9, pp. 1145–1161, 2016.

538843-L-bw-Steensma
Processed on: 17-12-2019
PDF page: 26

[14] U. Katscher and P. Boernert, "Parallel RF transmission in MRI," *NMR Biomed.*, vol. 19, no. 3, pp. 393–400, 2006.

[15] K. Feng, N. A. Hollingsworth, M. P. McDougall, and S. M. Wright, "A 64-channel transmitter for investigating parallel transmit MRI," *IEEE Trans. Biomed. Eng.*, 2012.

[16] E. F. Meliadò, C. A. T. van den Berg, P. R. Luijten, and A. J. E. Raaijmakers, "Intersubject specific absorption rate variability analysis through construction of 23 realistic body models for prostate imaging at 7T," *Magn. Reson. Med.*, no. April 2018, pp. 2106–2119, 2018.

[17] D. M. Pozar, *Microwave Engineering*. Wiley, 2004.

[18] M. A. Ertürk, A. J. E. Raaijmakers, G. Adriany, K. Ugurbil, and G. J. Metzger, "A 16-channel combined loop-dipole transceiver array for 7 Tesla body MRI," *Magn. Reson. Med.*, vol. 00, pp. 1–11, 2016.

[19] X. Yan, J. C. Gore, and W. A. Grissom, "Self-decoupled radiofrequency coils for magnetic resonance imaging," *Nat. Commun.*, 2018.

[20] S. Gabriel, R. W. Lau, and C. Gabriel, "The dielectric properties of biological tissues: II. Measurements in the frequency range 10 Hz to 20 GHz," *Phys. Med. Biol.*, 1996.

[21] A. C. and W. K. and E. G. H. and K. H. and M. Z. and E. N. and W. R. and R. J. and W. B. and J. C. and B. K. and P. S. and H.-P. H. and J. Kuster, "The Virtual Family—development of surface-based anatomical models of two adults and two children for dosimetric simulations," *Phys. Med. Biol.*, vol. 55, no. 2, p. N23, 2010.

[22] IEC, "Medical electrical equipment. Part 2-33: particular requirements for the safety of magnetic resonance equipment for medical diagnosis.," *IEC 60601-2-33*, 2015.

[23] J. L. Volakis, K. Caputa, M. Okoniewski, and M. A. Stuchly, "An algorithm for computations of the power deposition in human tissue," *IEEE Antennas Propag. Mag.*, 1999.

[24] G. Eichfelder and M. Gebhardt, "Local specific absorption rate control for parallel transmission by virtual observation points," *Magn. Reson. Med.*, vol. 66, no. 5, pp. 1468–1476, 2011.

[25] J. Lee, M. Gebhardt, L. L. Wald, and E. Adalsteinsson, "Local SAR in parallel transmission pulse design," *Magn. Reson. Med.*, vol. 67, no. 6, pp. 1566–1578, 2012.

538843-L-bw-Steensma
Processed on: 17-12-2019
PDF page: 27

Chapter 3

Design of a forward view antenna for prostate imaging at 7T

Bart R. Steensma
Ingmar J. Voogt
Peter R. Luijten
Cornelis A.T. van den Berg
Dennis W.J. Klomp
Alexander J.E. Raaijmakers

Appeared in:
NMR in Biomedicine Volume 31, Issue 9, e3993, September 2018

Abstract

Purpose

To design a forward view antenna for prostate imaging at 7T, which is placed between the legs of the subject in addition to a dipole array.

Materials and Methods

The forward view antenna is realized by placing a cross-dipole antenna at the end of a small rectangular waveguide. Quadrature drive of the cross-dipole can excite a circularly polarized wave propagating along the axial direction to and from the prostate region. Functioning of the forward view antenna is validated by comparing measurements and simulations. Antenna performance is evaluated by numerical simulations and measurements at 7T.

Results

Simulations of B_1^+ on a phantom are in good correspondence with measurements. Simulations on a human model indicate that signal-to-noise ratio, SAR efficiency and SAR (specific absorption rate) increase when adding the forward view antenna to a previously published dipole array. Signal-to-noise ratio increases up to 18% when adding the forward view antenna as a receive antenna to an 8-channel dipole array in vivo.

Conclusions

A design for a forward view antenna is presented and evaluated. SNR improvements up to 18% are demonstrated when adding the forward view antenna to a dipole array.

538843-L-bw-Steensma
Processed on: 17-12-2019
PDF page: 29

Introduction

Diagnostic methods for prostate cancer can be improved by development of techniques such as high-resolution MRI, MRS (MR spectroscopy) and diffusion weighted MRI [1]–[10] . These techniques can benefit from the gain in signal-to-noise-ratio (SNR) that is provided by ultra-high field MRI (UHF-MRI, $B_0 \geq 7$T). Multiple studies at 7T have until now showed promising results for T2w imaging [11], [12] and ^{1}H and ^{31}P MRS [6], [13], [14] on patients. However, UHF-MRI is hindered by Radio-Frequency- (RF-) related limitations such as interferences, rapid signal attenuation and high energy deposition [15]–[18]. These problems can be overcome by using local transmit arrays with multiple transceive elements and RF phase shimming [15], [19], [28], [20]–[27].

In receive, optimal imaging performance is obtained by using an endorectal coil [1], [5], [25], [28]. The position inside the rectum provides a close vicinity to the prostate resulting in very high SNR values. However, an endorectal coil suffers from an obvious and severe drawback in terms of patient comfort. As an alternative, reception can be performed with an external receive array which, for UHF MRI, may (partially) be a transceive array. Commonly used transceive surface array elements for MR prostate imaging are positioned around the pelvis in a belt-like fashion. These elements are emitting and detecting radiofrequency signals that propagate predominantly in the transverse plane to and from the prostate. As a result, the distance from the elements to the prostate is relatively large and the resulting SNR is much lower than with an endorectal coil. However, the prostate is located relatively close to the perineum (the region between the anus and the scrotum). Targeting the prostate from this region could provide a potential gain in SNR without invasive procedures. However, this approach is fundamentally different from the traditional approach in terms of signal polarization. The signal that is emitted or detected by this single antenna needs to have a circular polarization along the direction of propagation.

This work outlines the design of an external transmit receive element which is placed between the legs of a subject against the perineum. This element is able to transmit and receive a circularly polarized field in the longitudinal direction. It is therefore called the 'Forward View Antenna'. The forward view antenna combines a cross dipole antenna with a small rectangular waveguide [29]. Waveguides have been used in MRI before in travelling wave imaging, where the bore of the MRI scanner is used as a waveguide [30]–[32]. Dielectric waveguides have also been used as transmit elements for imaging the ankle and carotid arteries in the neck [33], [34]. Closely resembling the use of a dielectric waveguide is the use of a cavity resonator enclosed by a layer of conductive material for use

538843-L-bw-Steensma
Processed on: 17-12-2019
PDF page: 30

in NMR systems, which was described in a patent [35].

In this study, a metallic water-filled waveguide is used that guides a circularly polarized propagating wave along the longitudinal direction into the tissue, towards the prostate.

The purpose of this study is to demonstrate the design and optimization of this antenna. Electromagnetic simulations are used to assess RF safety and the potential gain of using the forward view antenna. The forward view antenna is evaluated as a receive-only element in addition to an 8-channel fractionated dipole array in an in vivo setup on 3 volunteers [21].

Materials and methods

Forward View Antenna construction

The forward view antenna consists of a small rectangular copper-shielded waveguide which is filled with deionized water and open at both ends. The orthogonal TE_{01}- and TE_{10}-modes (transverse-electromagnetic modes) are excited in this waveguide [36] . Since these modes are orthogonal, their field patterns are equal but the field lines are pointing along orthogonal directions (in the YZ- and the XZ-plane). The magnetic and electric field patterns for the TE_{01}-mode is shown in Figure 1.

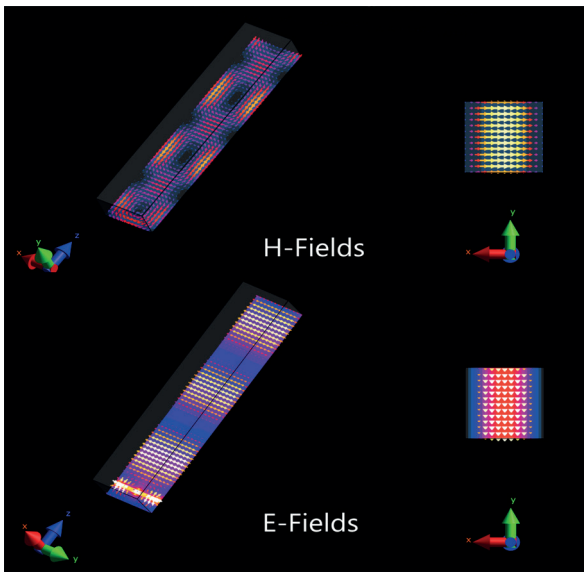

Figure 1: TE_{01}-modes in a rectangular shielded waveguide. Both magnetic (top) and electrical (bottom) field components are shown. The TE_{10}-mode has an identical field pattern but is orthogonal to the TE_{01}-mode.

538843-L-bw-Steensma
Processed on: 17-12-2019

The modes are excited by a small cross dipole antenna at the distal end of the waveguide. By feeding both separate dipole antennas with a 90^0 phase shift, a circularly polarized field is created by the antenna that propagates in the waveguide. This field can only propagate when the operating frequency (298.2 MHz at 7T) is above the cutoff frequency for the TE_{01}- and TE_{10}-modes in this specific waveguide structure. The cutoff frequency of the lowest order TE-modes of a rectangular conductive waveguide is given by the following equation [37].

$$f_{cutoff,1,0} = \frac{c}{2a\sqrt{\varepsilon_r}} \quad [1]$$

In equation 1, c is the speed of light, is the relative permittivity of the material inside the waveguide and a gives the inner width of the rectangular waveguide. Equation 1 shows that by increasing the permittivity of the medium in the waveguide, the minimum dimensions of the waveguide can be decreased. The waveguide was filled with deionized water, which leads to a minimum waveguide width of 57 mm for a cutoff frequency of 298.2 MHz and a relative permittivity of 78. The waveguide dimensions were therefore chosen to be 60*60*100 mm (slightly above cutoff). A schematic image of the forward view antenna is shown in Figure 2

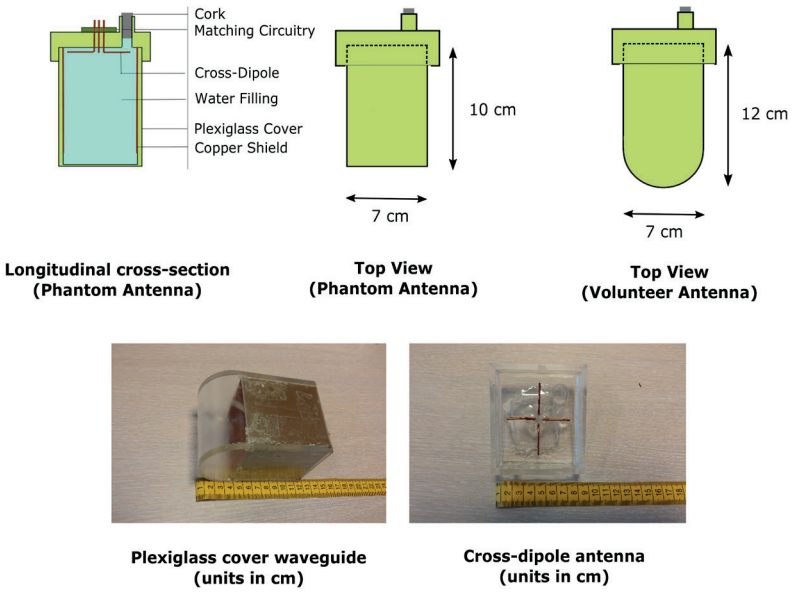

Figure 2: schematic image of the forward view antenna. Different waveguide models have been used for the phantom experiments and the experiments on volunteers. Measurement units are in cm.

538843-L-bw-Steensma
Processed on: 17-12-2019
PDF page: 32

The waveguide was constructed from a small plexiglass box while four Printed Circuit Board (PCB) patches were used as the conductive walls. The PCB patches were soldered together and were covered in a layer of varnish to prevent oxidation of the copper. The plexiglass cover is in between the body and the waveguide shield (plexiglass of 5 mm thickness, 10 mm thickness at the position of the dipole antennas). The cross-dipole antenna was constructed from copper wire, the total length of a single antenna was 5 cm. Both dipoles were placed inside the waveguide and were connected to small copper patches outside of the waveguide, where the matching circuitry was placed. The tuning and matching network consisted of a parallel capacitor (8.2 pF) and a series capacitor (8.2 pF) for both channels. The maximum reflection coefficient for the forward view antenna was -12 dB. Coupling between the two orthogonal channels of the forward view antenna as well as maximum coupling between the forward view antenna and fractionated dipole antennae was low (-26 and -23 dB). The geometrical design of the forward view antenna that was used for in vivo measurements deviated slightly from the initial rectangular design. The rectangular waveguide was extended with a half-round end in order to maintain full contact with the tissue at the perineum. Both waveguide designs are presented in Figure 2. Figure 3 shows a schematic overview of the forward view antenna and its function as an addition to the fractionated dipole array.

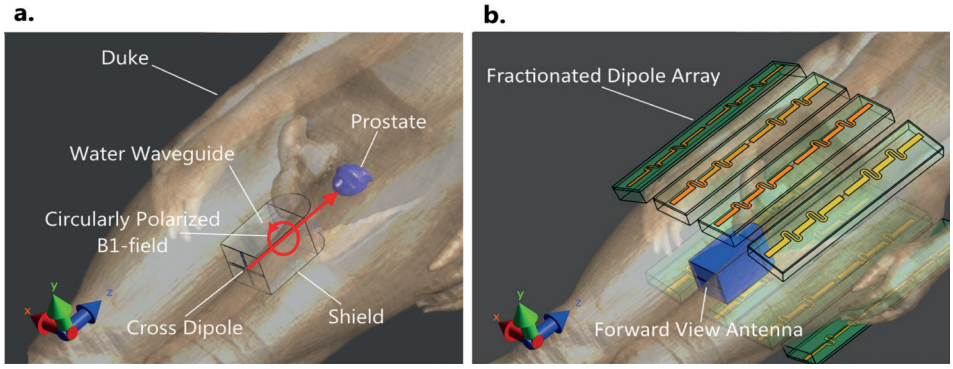

Figure 3: schematic overview of the forward view antenna and the fractionated dipole antennas on the Duke model. Figure 3a. represents the basic working principle of the forward view antenna. Red lines indicate the propagation direction and polarization of the transmit field. Figure 3b. represents an imaging setup where the forward view antenna is used in addition to the fractionated dipole array.

Phantom simulations and scans

Initial simulations were carried out to optimize the length of the waveguide in terms of signal strength in a phantom, 6 cm away from the waveguide end. This distance was chosen because it equals the distance from the perineum to the

538843-L-bw-Steensma
Processed on: 17-12-2019
PDF page: 33

prostate in the human model Duke (34 years old, Body-mass index 22.4, height 1.77m, weight 70.2 kg) [38].The forward view antenna and a phantom with pelvic-like electrical properties (250*250*200 mm^3, σ= 0.4 S/m, ε = 34) were modelled in an electromagnetic simulation environment (Sim4Life, Zurich MedTech, Zurich, Switzerland) [39]. The length of the waveguide was varied, while the signal efficiency ($B_1^+/\sqrt{W}$) in the phantom was evaluated. MR experiments (MR system: Achieva 7T, Philips Healthcare, Best, The Netherlands) were carried out on a phantom for a consistency check. A phantom was constructed from a small container filled with saline solution (380*240*150 mm^3, 4 g/L, ε=78, σ=0.4 S/m). The forward view antenna was used as a transceive element, where both ports of the forward view antenna were driven through a quadrature hybrid box (Philips Healthcare, Best). B_1^+-maps were acquired using the actual flip angle method [40] for a quantitative assessment of the efficiency and confirmation that the simulation model matches the experimental results. Two B_1^+-maps were made at different input powers, because the B_1^+-values inside and outside the waveguide could not be mapped within the dynamic range of a single measurement. This experimental setup was modelled in an electromagnetic simulation environment (Sim4Life, Zurich MedTech, Zurich, Switzerland), using the same electrical properties, and including the plexiglass structural parts, to verify the antenna concept.

Human Model Simulations

Electromagnetic simulations were carried out on human model Duke of the virtual family [38] to evaluate the performance of the forward view antenna in addition to the fractionated dipole array setup [21]. The following setups were evaluated:

- Eight fractionated dipole antenna.
- The two channel forward view antenna
- Eight fractionated dipole antennas in combination with the forward view antenna

The same simulation setup was used for the three setups, in which the unused elements where still present but not active. Tissue in the area of the legs that overlapped with the forward view antenna was cut away, in order to fit the forward view antenna between the legs of Duke.

Resulting field distributions were exported to Matlab. the electric fields were used to calculate 10g-averaged quality-matrices (Q-matrices) and virtual

538843-L-bw-Steensma
Processed on: 17-12-2019
PDF page: 34

observation points [41]. Based on the B_1^+ distributions per channel and the virtual observation points, the average B_1^+ in the prostate normalized by the square root of maximum SAR_{10g} (SAR efficiency) was optimized using the Matlab routine fmincon (Mathworks, Natick, Massachusetts, USA). The sum of absolute values of the Q-matrix was calculated to obtain the maximum possible peak SAR_{10g} value given unity input power for all channels, and any phase setting [42]. This value represents the maximum possible SAR value that can be obtained with phase-only B_1^+-shimming. Receive performance was evaluated by combining the resulting B_1^--fields, normalized by input current, with Roemer's sensitivity weighted corrected sum-of-squares method [43] into relative SNR maps. A separate simulation was done to compare the field distributions of the fractionated dipole array with and without the passive forward view antenna present, results are shown as supplementary material.

Volunteer scans

The forward view antenna was tested on three volunteers in receive only mode. These scans were conducted with the approval of our Institutional Review Board. Three healthy male volunteers (22, 26 and 36 years old, BMI 24.4, 20.9 and 26) were scanned using the forward view antenna and eight fractionated dipole antennas [21]. Three different combinations of receive elements were reconstructed in post-processing: receiving with the fractionated dipole antennas only, receiving with the forward view antenna only and receiving with all elements combined. In all cases, only the fractionated dipole array was used for transmission. Low flip angle gradient echo scans (Surveys) were acquired to obtain general insight into the performance of the different receive setups. To evaluate SNR in the prostate, the method of Kellman et al. [44], [45] was used for reconstruction of SNR scaled images. Raw data was exported for every separate receive channel, the different combinations of receive elements were all derived from the same dataset. Receive combination was done using the sensitivity weighted sum-of-squares method [43]. The following imaging parameters were used: 3D FFE sequence, FOV 100x369x8 mm, voxel size 1.56x2.65x2 mm^3, 3 slices, flip angle 1^0, TE 10 ms, TR 50 ms. SNR was evaluated as the average signal the prostate, considering only the middle slice of the SNR scaled images. In one example volunteer, a high resolution T2w image was acquired, and reconstructed with different combinations of receive setups (forward view antenna, fractionated dipole array, both) and SNR scaling. The following imaging parameters were used for the T2w acquisition: 2D SE sequence, FOV 250x421x3 mm, voxel size 0.7x0.7x3mm^3, flip angle 90^0, flip angle refocusing pulse 180^0, TE 90 ms, TR 5000 ms, multishot turbo-spin-echo (TSE), with TSE factor 17.

538843-L-bw-Steensma
Processed on: 17-12-2019
PDF page: 35

Results

Phantom scans and simulations

Results of the optimization of length versus transmit efficiency have been added as supplementary material. It is shown that the length of the waveguide has no influence on the transmit efficiency in the phantom, which is to be expected from a lossless waveguide. The results of simulations and measurements on a phantom are shown in Figure 4. 4a and 4b show the measured and simulated B_1^+-maps for an input power of 56 W. Figure 4c. shows a line plot through the measured and simulated data, as indicated by the black lines in the figures. Figure 4d-f. shows the same data, but for an input power of 2000 W. The measured field pattern in the waveguide corresponds very well to the simulated pattern, which indicates that the waveguide works as expected. However, close to the interface between the element and the phantom, measured B_1^+ appears lower than expected from simulations. A slight mismatch in modeling the interface between the phantom, which consists of plexiglass and a thin layer air, may have caused a deviation between simulations and measurements in this region of rapidly changing B_1^+.

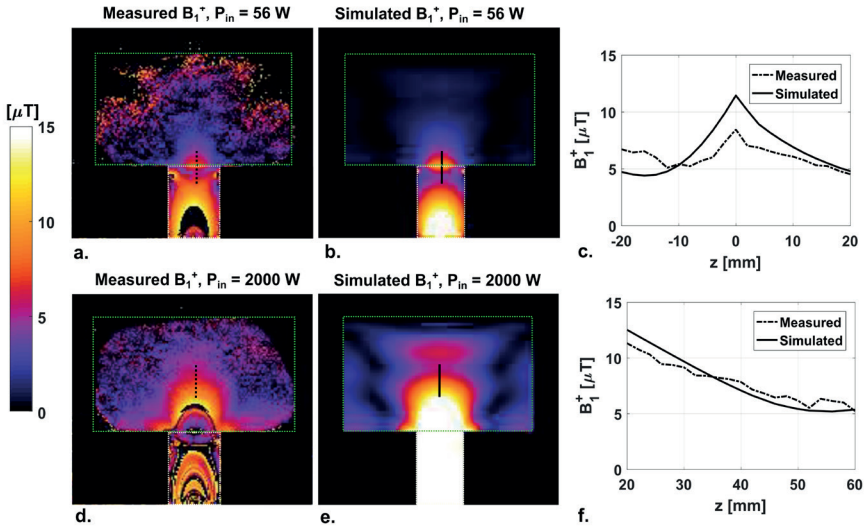

Figure 4: 4a-b. Measured (a.) and simulated (b.) transmit field of the forward view antenna, using an input power of 56 W. 4c. Simulated and measured transmit field along the black lines indicated in figures 4a-b. 4d-f. shows the same results, but for an input power of 2000 W and for a different positioning of the black lines. The outlines of the waveguide and the phantom are indicated by the white and green lines in all figures. The transmit field was mapped using the AFI sequence, using the following scan parameters: FOV 320x320x30 mm^3, voxel size 2x2x10 mm^3, TE 2 ms, TR 50/250 ms, flip angle 65^0.

538843-L-bw-Steensma
Processed on: 17-12-2019
PDF page: 36

Human model simulations

Figure 5 shows maximum intensity projections of the worst case SAR_{10g} distributions, considering phase only shimming and equal input power for all transmit channels. The forward view antenna has an increased worst case local peak SAR (7.1 W/kg) as compared to the fractionated dipole array (5.1 W/kg). The worst case local peak SAR for the fractionated dipole array in this simulation, where the forward view antenna is also present, is exactly the same as the worst case local peak SAR reported for the fractionated dipole array without passive forward view antenna present[21]. Worst case peak SAR is highest when both the forward view antenna and the fractionated dipole array are used (10.4 W/kg). When the forward view antenna is used, the highest peak SAR values occur close to the proximal end of the waveguide, two SAR peaks can be seen at both sides of the waveguide. Constructive interference between the transmit fields of the fractionated dipole array and the forward view antenna causes a further increase in these SAR values when the combined setup is used.

Figure 6 shows B_1^+-distributions normalized to peak SAR_{10g} (SAR efficiency) for an optimized drive phase and amplitude of each transmit channel. When using the forward view antenna alone, a SAR efficiency of 0.23 was reached. With the fractionated dipole array, the SAR efficiency is 0.52 . With the combined setup, SAR efficiency increases to 0.68 . This implies that using the forward view antenna and the fractionated dipole array can improve the SAR efficiency by 30.8%, compared to using only the fractionated dipole array.

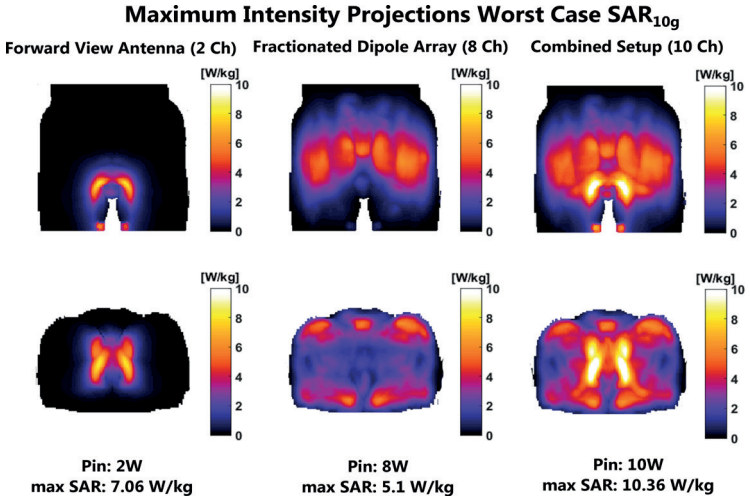

Figure 5: worst cage peak SAR_{10g} distributions for different combinations of the dipole antenna array and the forward view antenna on the human model Duke for 1 W input power.

538843-L-bw-Steensma
Processed on: 17-12-2019
PDF page: 37

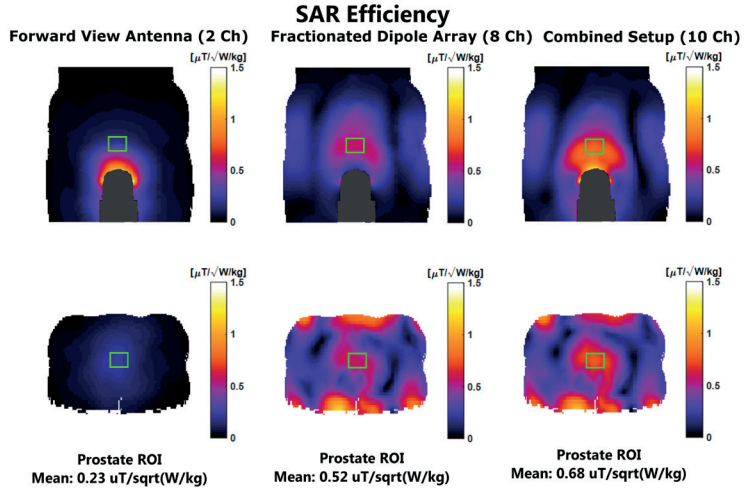

Figure 6: B_1^+ field distributions in the model Duke normalized to maximum local peak SAR_{10g} (SAR efficiency). Phase and amplitude-shimming was done for every setup to generate SAR efficiency in the prostate region.

Figure 7 shows the simulated SNR-maps for different receive setups. With the forward view antenna alone, an SNR of 29 is reached in the prostate, while the fractionated dipole antenna alone achieves an SNR of 33. Combining the fractionated dipole array and the forward view antenna leads to an SNR of 44, which is 33% higher than for the fractionated dipole array alone.

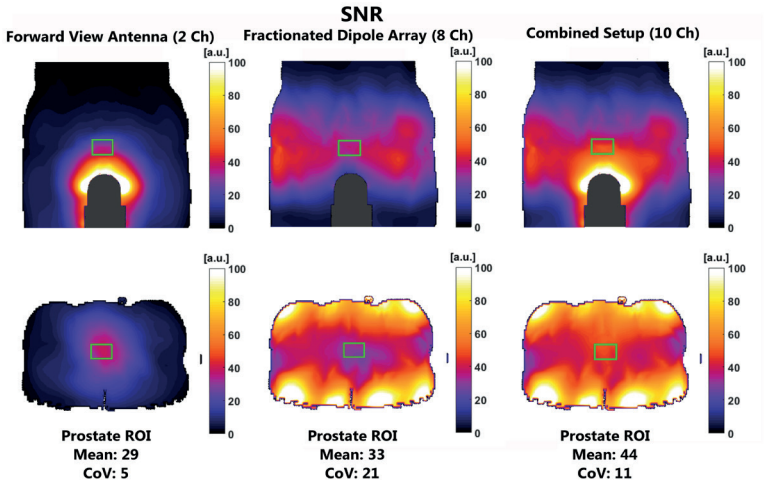

Figure 7: SNR field distributions in the model Duke using the indicated antenna setups. SNR was obtained by combining sensitivity (B_1^-) maps with the sum of squares method. Results show the forward view antenna potentially provides a 33% increase in SNR in comparison to the array of fractionated dipoles alone.

538843-L-bw-Steensma
Processed on: 17-12-2019
PDF page: 38

Volunteer scans

Low flip angle images for three different setups are shown in Figure 8. When only the fractionated dipole antennas are used, the signal intensity close to the perineum is low close to the perineum. The two channels of the forward view antenna receive a signal that is highly intense close to the waveguide, but decays strongly when moving away from the waveguide. The signal intensity in the prostate region shows a strong gradient. Both observations also apply to the simulated receive fields in the prostate (Figure 7). The image of the combined setup looks comparable to the image that was obtained with the fractionated dipole antennas only, although the signal void close to the perineum is no longer present.

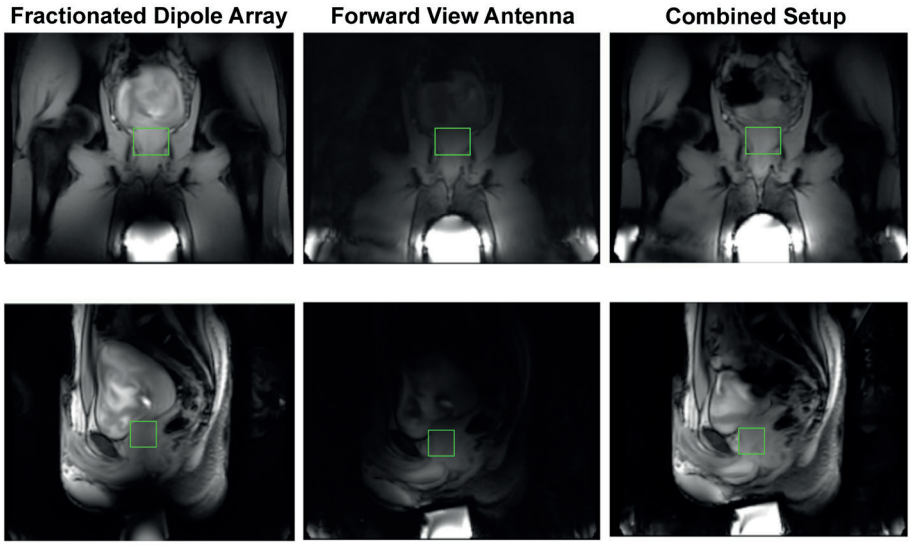

Figure 8: Survey scans acquired with different antenna combinations for receiving. The fractionated dipole array is used for transmission in all cases. The prostate is delineated by the green box. Imaging parameters: M2D FFE sequence, FOV 250x355x30 mm^3, voxel size 2x2x10 mm^3, 3 slices, flip angle 15^0, TFE factor 64, TE 4.93 ms, TR 11 ms.

Figure 9 shows the average SNR in the prostate for three volunteers. It is demonstrated in all volunteers that adding the forward view antenna as a receive element improves SNR compared to a situation where only the fractionated dipole array is used. In volunteer 1, SNR increases from 9 to 10.7 (+19%), in volunteer 2 SNR increases from 8.1 to 9.5 (+17%) and in volunteer 3 SNR increases from 8.7 to 9.1 (+5%). The average increase in SNR over all volunteers and slices is 13.6%. The distance from the tip of the forward view antenna to the tissue was measured in survey images for all volunteers. This distance was 7.4, 7.9 and 12.55 cm for

538843-L-bw-Steensma
Processed on: 17-12-2019
PDF page: 39

volunteer 1 to 3. Despite the round end of the forward view antenna, a small air gap is still present between the perineum and the forward view antenna for all volunteers.

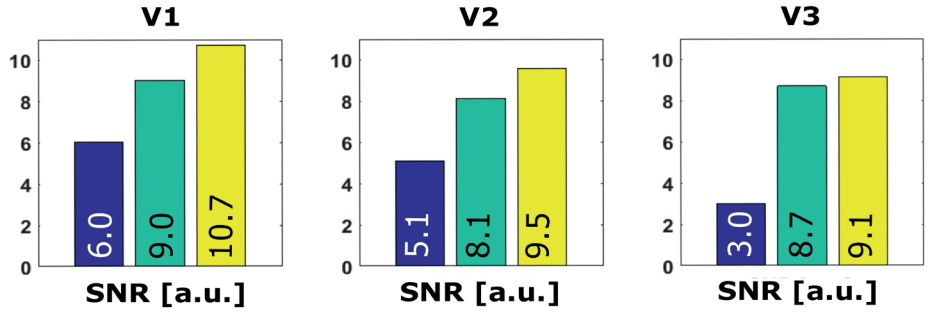

Figure 9: SNR values obtained in a rectangular ROI inside the prostate for 3 volunteers. SNR increases up to 18% when a forward view antenna is used in combination with the fractionated dipole array, as compared to the fractionated dipole array only.

Figure 10 shows a T2w image, reconstructed with different receive setups, and the average SNR values in an indicated ROI in the prostate. As expected, the highest SNR is obtained when both the forward view antenna and the fractionated dipole array are used in receive mode.

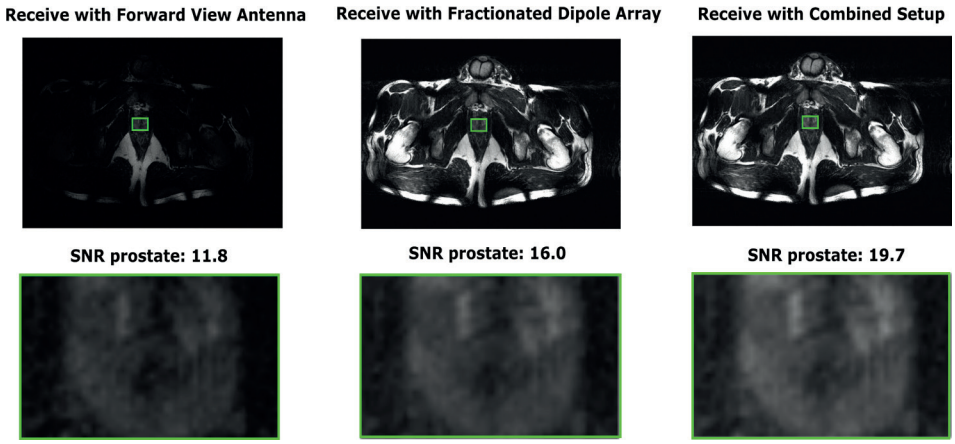

Figure 10: T2w images for an example volunteer (V1), with SNR scaled reconstruction. The same transmit setup (8 fractionated dipole antennas) was used in all cases, but different receive setups. The green ROI indicates a region in the prostate where SNR was evaluated. The following scan parameters were used: FOV 240x421x3 mm^3, voxel size 0.7x0.7x3 mm^3, TE 90 ms, TR 5000 ms, flip angle 90^0.

538843-L-bw-Steensma
Processed on: 17-12-2019
PDF page: 40

Discussion

Simulations on a phantom show that the B_1-field inside the forward view antenna has a circular polarization when using the right phase offset for both channels, the B_1^+-field in the waveguide is highly intense while the B_1^--field is very low. Comparison of simulation and experimental results on a phantom shows that the simulated field patterns correspond to the experimental data. The correspondence in field patterns shows that the forward view antenna behaves as it is supposed to, i.e. generates a circularly polarized wave in the longitudinal direction.

Simulations on a human model show that adding the forward view antenna to the fractionated dipole array can lead to an increase of SAR efficiency of 30.8%. However, the worst-case SAR level for this combined setup (10.4 W/kg), and for the forward view antenna (7.1 W/kg) is much higher than for the fractionated dipole array (5.1 W/kg). Simulated SNR maps show that using the combination of a fractionated dipole array and the two channel forward view antenna will yield the highest SNR in the prostate in receive mode.

Although it is possible to increase SAR efficiency when adding the forward view antenna, the worst-case SAR also increases strongly. Since worst case SAR is the current metric that is used at our site to set safe upper limits on average power, the forward view antenna was not used as a transmit element on volunteers in this work. The use of the forward view antenna antenna in transmit mode on volunteers would require an update of the safety evaluation methods that are used at our site, including the use of multiple human models and MR thermometry for validation. This is ongoing work, and is considered to be out of the scope of this paper[46]. For the volunteer experiments, the forward view antenna was evaluated for receive purposes only. SNR measurements in a volunteer demonstrate that combining the forward view antenna and the fractionated dipole array in receive mode leads to the best SNR. Adding the forward view antenna to the fractionated dipole array in receive can lead to an SNR increase of 19% in the prostate, but this is not the case for all volunteers. In the case of volunteer 3, SNR increases only 5% when adding the forward view to the fractionated dipole array. In this volunteer, the distance from the antenna to the tissue is relatively large (12.6 cm). This observation leads to the conclusion that anatomic differences and rigorous placement of the forward view antenna is essential for its performance. In spite of the adapted shape of the waveguide end, the tissue and the waveguide are not fully connected which results in more reflection at the waveguide-subject interface.

The high signal intensity in the forward view antenna increases the dynamic

538843-L-bw-Steensma
Processed on: 17-12-2019

range in the image. This can cause problems in the ADC scaling of the image, and it can also harm the visibility of neighboring anatomic structures. This issue could be resolved by replacing the deionized water in the forward view antenna by deuterium to remove the signal from the waveguide [33].

Although this paper describes the use for prostate imaging, several other targets could be imaged as well. For example, anatomical targets in the same area such as the rectum can benefit from the additional SNR provided by the forward view antenna. The brain could be a potential target for the forward view antenna, as the antenna could be used to realize improved coverage of the cranial side of the brain.

Endorectal coils provide another possibility to improve SNR and SAR efficiency for prostate imaging when adding them to an external transceiver array [1], [5], [25], [28]. Reported SNR improvements when adding an endorectal coil to an external transceiver array range from 40% to 367%, which is an order of magnitude larger than SNR improvement caused by adding the forward view antenna. However, the use of an endorectal coil can cause inhomogeneity in the signal, which is clearly visible in Figure 7d in the work of Ertürk et al [25]. Additionally, an endorectal coil causes patient discomfor t [47].

The limitations of the work described in this paper mainly relate to the ergonomic design and the placement of the forward view antenna. Using a non-shielded waveguide, which has no cut-off frequency, or a waveguide comprised of a high-permittivity material would make it possible to design a smaller waveguide which is beneficial for ergonomics. These options are not explored in this work, and could make it easier and more subject-friendly to use the forward view antenna. The results presented in this work show that SNR performance of the forward view antenna differs per subject. Although a mechanical placeholder was made to fixate the forward view antenna, more attention can go into integrating the forward view antenna in the scanner bed. This would ensure full contact between the forward view antenna and the body, thus leading to maximum efficiency. The clinical T2w image shown in figure 10 is acquired using a vendor available T2w sequence. Using the same scan parameters as in the work of Maas et al could further improve the image quality[11], but would require the use of modified RF pulses and a modified sequence, which is considered out of the scope of this work.

In conclusion, a forward view antenna was designed for prostate imaging at 7T. The waveguide length of the antenna design was optimized in simulations. The forward view antenna functions as predicted in simulations on a phantom. By

538843-L-bw-Steensma
Processed on: 17-12-2019
PDF page: 42

adding the forward view antenna to an array of fractionated dipole antennas, signal-to-noise ratio was improved as compared to the fractionated dipole array only.

References

[1] B. Van den Bergen et al., "Uniform prostate imaging and spectroscopy at 7 T: Comparison between a microstrip array and an endorectal coil," NMR Biomed., vol. 24, no. 4, pp. 358–365, 2011.

[2] D. W. J. Klomp, T. W. J. Scheenen, C. S. Arteaga, J. van Asten, V. O. Boer, and P. R. Luijten, "Detection of fully refocused polyamine spins in prostate cancer at 7 T," NMR Biomed., vol. 24, no. 3, pp. 299–306, 2011.

[3] C. S. Arteaga de Castro, M. P. Luttje, M. Van Vulpen, P. R. Luijten, U. A. Van der Heide, and D. W. J. Klomp, "Composite slice-selective adiabatic excitation for prostate MRSI," NMR Biomed., vol. 26, no. 4, pp. 436–442, 2013.

[4] C. S. Arteaga de Castro et al., "Temporal B0 field variation effects on MRSI of the human prostate at 7T and feasibility of correction using an internal field probe," NMR Biomed., vol. 27, no. 11, pp. 1353–1360, 2014.

[5] C. S. Arteaga De Castro, B. Van Den Bergen, P. R. Luijten, U. A. Van Der Heide, M. Van Vulpen, and D. W. J. Klomp, "Improving SNR and B 1 transmit field for an endorectal coil in 7 T MRI and MRS of prostate cancer," Magn. Reson. Med., vol. 68, no. 1, pp. 311–318, 2012.

[6] M. P. Luttje et al., "(31) P MR spectroscopic imaging combined with (1) H MR spectroscopic imaging in the human prostate using a double tuned endorectal coil at 7T.," Magn. Reson. Med., vol. 72, no. 6, pp. 1516–21, 2014.

[7] M. A. Haider et al., "Combined T2-Weighted and Diffusion-Weighted MRI for Localization of Prostate Cancer," http://dx.doi.org/10.2214/AJR.07.2211, 2012.

[8] C. Sato et al., "Differentiation of noncancerous tissue and cancer lesions by apparent diffusion coefficient values in transition and peripheral zones of the prostate.," J. Magn. Reson. Imaging, vol. 21, no. 3, pp. 258–62, Mar. 2005.

[9] K. Hosseinzadeh and S. D. Schwarz, "Endorectal diffusion-weighted imaging in prostate cancer to differentiate malignant and benign peripheral zone tissue.," J. Magn. Reson. Imaging, vol. 20, no. 4, pp. 654–61, Oct. 2004.

[10] B. Issa, "In vivo measurement of the apparent diffusion coefficient in normal and malignant prostatic tissues using echo-planar imaging.," J. Magn. Reson. Imaging, vol. 16, no. 2, pp. 196–200, Aug. 2002.

[11] M. C. Maas et al., "Feasibility of T2 -weighted turbo spin echo imaging of the human prostate at 7 tesla.," Magn. Reson. Med., vol. 71, pp. 1711–9, 2014.

[12] E. K. Vos et al., "Image quality and cancer visibility of T2-weighted Magnetic Resonance Imaging of the prostate at 7 Tesla," Eur. Radiol., vol. 24, no. 8, pp. 1950–1958, 2014.

[13] M. W. Lagemaat et al., "Phosphorus magnetic resonance spectroscopic imaging at 7 T in patients with prostate cancer," Invest. Radiol., vol. 49, no. 5, pp. 363–372, 2014.

[14] M. W. Lagemaat et al., "1H MR spectroscopic imaging of the prostate at 7T using spectral-spatial pulses," Magn. Reson. Med., vol. 75, no. 3, pp. 933–945, 2016.

538843-L-bw-Steensma
Processed on: 17-12-2019
PDF page: 43

[15] J. T. Vaughan et al., "Whole-body imaging at 7T: Preliminary results," Magn. Reson. Med., vol. 61, no. 1, pp. 244–248, 2009.

[16] J. T. Vaughan et al., "7T vs. 4T: RF power, homogeneity, and signal-to-noise comparison in head images," Magn. Reson. Med., vol. 46, no. 1, pp. 24–30, 2001.

[17] C. M. Collins et al., "Temperature and SAR calculations for a human head within volume and surface coils at 64 and 300 MHz," J. Magn. Reson. Imaging, vol. 19, no. 5, pp. 650–656, 2004.

[18] L. Alon, C. M. Deniz, G. Carluccio, R. Brown, D. K. Sodickson, and C. M. Collins, "Effects of anatomical differences on electromagnetic fields, SAR, and temperature change," Concepts Magn. Reson. Part B Magn. Reson. Eng., vol. 46, no. 1, pp. 8–18, Feb. 2016.

[19] S. Orzada et al., "A flexible 8-channel transmit/receive body coil for 7 T human imaging," in Proceedings of the 17th Annual Meeting of ISMRM, Honolulu, Hawaii, USA, 2009, p. 2999.

[20] A. J. E. Raaijmakers et al., "Design of a radiative surface coil array element at 7 T: The single-side adapted dipole antenna," Magn. Reson. Med., vol. 66, no. 5, pp. 1488–1497, 2011.

[21] A. J. E. Raaijmakers et al., "The fractionated dipole antenna: A new antenna for body imaging at 7 Tesla," Magn. Reson. Med., vol. 75, no. 3, pp. 1366–1374, 2016.

[22] G. C. Wiggins et al., "Mixing loops and electric dipole antennas for increased sensitivity at 7 Tesla," in In: Proceedings of the 21th scientific meeting, International Society for Magnetic Resonance in Medicine, Salt Lake City, 2013, vol. 21, p. 2737.

[23] A. Graessl, W. Renz, F. Hezel, and others, "Modular 32-channel transceiver coil array for cardiac MRI at 7.0 T [Epub ahead of print]," Magn Reson Med.

[24] M. A. Ertürk, A. J. E. Raaijmakers, G. Adriany, K. Ugurbil, and G. J. Metzger, "A 16-channel combined loop-dipole transceiver array for 7 Tesla body MRI," Magn. Reson. Med., vol. 00, pp. 1–11, 2016.

[25] M. A. Ertürk, J. Tian, P. F. Van De Moortele, G. Adriany, and G. J. Metzger, "Development and evaluation of a multichannel endorectal RF coil for prostate MRI at 7T in combination with an external surface array," J. Magn. Reson. Imaging, vol. 43, no. 6, pp. 1279–1287, 2016.

[26] G. J. Metzger, C. Snyder, C. Akgun, T. Vaughan, K. Ugurbil, and P. F. Van De Moortele, "Local B1+ shimming for prostate imaging with transceiver arrays at 7T based on subject-dependent transmit phase measurements," Magn. Reson. Med., vol. 59, no. 2, pp. 396–409, 2008.

[27] A. B. Rosenkrantz et al., "T2-weighted prostate MRI at 7 Tesla using a simplified external transmit-receive coil array: Correlation with radical prostatectomy findings in two prostate cancer patients," J. Magn. Reson. Imaging, vol. 41, no. 1, pp. 226–232, 2015.

[28] G. J. Metzger et al., "Performance of external and internal coil configurations for prostate investigations at 7 T," Magn. Reson. Med., vol. 64, no. 6, pp. 1625–1639, 2010.

[29] P. Steensma, B.R., Raaijmakers, A.J.E., Voogt, I., Haghnejad, S.A., Klomp, D.W.J., van den Berg, C.A.T., Luijten, "Design of a forward view antenna for prostate imaging at 7 tesla," in Proc Int Soc Magn Reson Med, 2016.

[30] D. O. Brunner, N. De Zanche, J. Fröhlich, J. Paska, and K. P. Pruessmann, "Travelling-wave nuclear magnetic resonance," Nature, vol. 457, no. 7232, pp. 994–998, 2009.

[31] A. Andreychenko, J. J. Bluemink, A. J. E. Raaijmakers, J. J. W. Lagendijk, P. R. Luijten, and C. A. T. den Berg, "Improved RF performance of travelling wave MR with a high permittivity

538843-L-bw-Steensma
Processed on: 17-12-2019
PDF page: 44

dielectric lining of the bore," Magn. Reson. Med., vol. 70, no. 3, pp. 885–894, 2013.

[32] A. Andreychenko, H. Kroeze, D. W. J. Klomp, J. J. W. Lagendijk, P. R. Luijten, and C. A. T. den Berg, "Coaxial waveguide for travelling wave MRI at ultrahigh fields," Magn. Reson. Med., vol. 70, no. 3, pp. 875–884, 2013.

[33] W. Koning et al., "High-resolution MRI of the carotid arteries using a leaky waveguide transmitter and a high-density receive array at 7 T," Magn. Reson. Med., vol. 69, no. 4, pp. 1186–1193, 2013.

[34] J. J. Bluemink et al., "Dielectric waveguides for ultrahigh field magnetic resonance imaging," Magn. Reson. Med., p. n/a--n/a, 2015.

[35] John Thomas Vaughan, "Cavity Resonator for NMR systems," 1995.

[36] Constantine A . Balanis, Antenna Theory, Analysis and Design. 2005.

[37] D. M. Pozar, Microwave Engineering. Wiley, 2004.

[38] A. C. and W. K. and E. G. H. and K. H. and M. Z. and E. N. and W. R. and R. J. and W. B. and J. C. and B. K. and P. S. and H.-P. H. and J. Kuster, "The Virtual Family—development of surface-based anatomical models of two adults and two children for dosimetric simulations," Phys. Med. Biol., vol. 55, no. 2, p. N23, 2010.

[39] B. Van Den Bergen, C. A. T. Van Den Berg, D. W. J. Klomp, and J. J. W. Lagendijk, "SAR and power implications of different RF shimming strategies in the pelvis for 7T MRI," J. Magn. Reson. Imaging, vol. 30, no. 1, pp. 194–202, 2009.

[40] V. L. Yarnykh, "Actual flip-angle imaging in the pulsed steady state: A method for rapid three-dimensional mapping of the transmitted radiofrequency field," Magn. Reson. Med., vol. 57, no. 1, pp. 192–200, 2007.

[41] G. Eichfelder and M. Gebhardt, "Local specific absorption rate control for parallel transmission by virtual observation points," Magn. Reson. Med., vol. 66, no. 5, pp. 1468–1476, 2011.

[42] F. Meliado, E., A. J. E. Raaijmakers, P. R. Luijten, and C. A. T. van den Berg, "Fast method to get an upper bound of the maximum SAR10g for body coil arrays," Proc. 9th Sci. Meet. Int. Soc. Magn. Reson. Med. Benelux Chapter, Tilbg., p. p-070, 2017.

[43] P. B. Roemer, W. A. Edelstein, C. E. Hayes, S. P. Souza, and O. M. Mueller, "The NMR phased array," Magn. Reson. Med., vol. 16, no. 2, pp. 192–225, Nov. 1990.

[44] P. Kellman and E. R. McVeigh, "Image reconstruction in SNR units: A general method for SNR measurement," Magn. Reson. Med., vol. 54, no. 6, pp. 1439–1447, 2005.

[45] P. Kellman, "Erratum to Kellman P, McVeigh ER. Image reconstruction in SNR units: a general method for SNR measurement.," Magn. Reson. Med., vol. 58, pp. 211–212, 2007.

[46] F. Meliado, E., A. J. E. Raaijmakers, M. Restivo, M. Maspero, P. R. Luijten, and C. A. T. van den Berg, "Database Construction for Local SAR Prediction: Preliminary Assessment of the Intra and Inter Subject SAR Variability in Pelvic Region," in In: Proceedings of the 24th scientific meeting, International Society for Magnetic Resonance in Medicine, Singapore, 3660, 2016.

[47] S. H. Lee et al., "Is endorectal coil necessary for the staging of clinically localized prostate cancer? Comparison of non-endorectal versus endorectal MR imaging," World J. Urol., vol. 28, no. 6, pp. 667–672, 2010.

538843-L-bw-Steensma
Processed on: 17-12-2019
PDF page: 45

Supplementary material

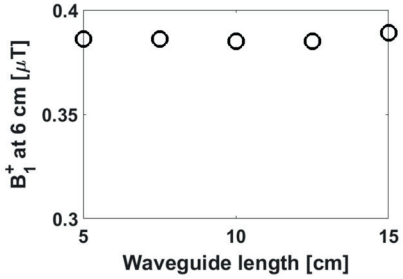

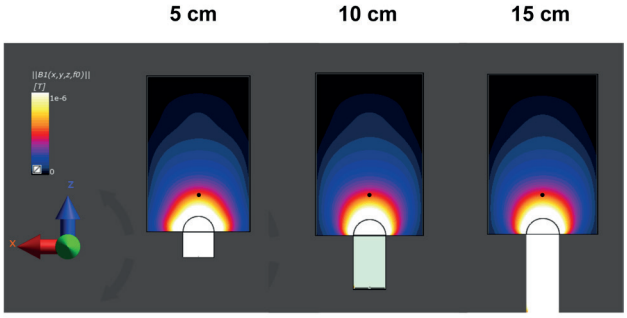

Transmit efficieny inside the phantom, 6 cm away from the tip of the rounded waveguide, for different lengths of the waveguide (not including the 3 cm tip). Field distributions are shown for three example lengths (5, 10 and 15 cm).

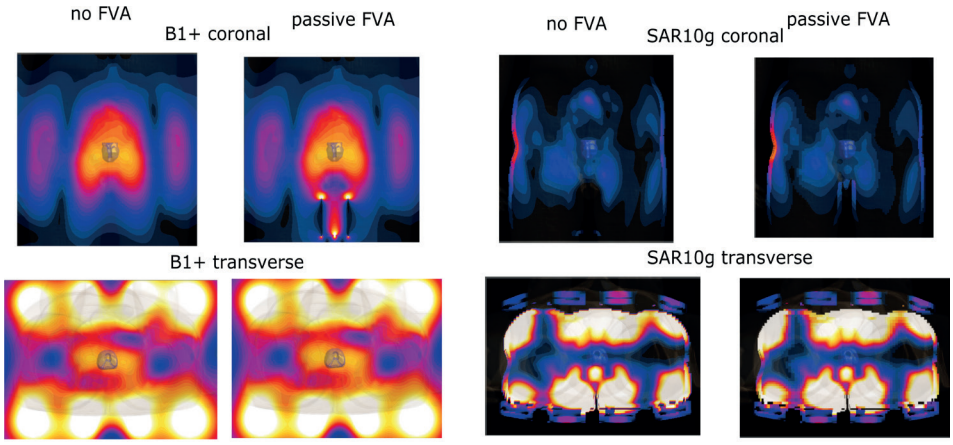

B1+ fields and SAR distributions for a setup of 8 fractionated dipole antennas, with and without the forward view antenna present as a passive element. All slices cut through the center of the prostate, which is marked in blue in the center of the images.

538843-L-bw-Steensma
Processed on: 17-12-2019

Chapter 4

Comparing signal-to-noise ratio for prostate imaging at 7T and 3T

Bart R. Steensma
Mariska Luttje
Ingmar J. Voogt
Peter R. Luijten
Cornelis A.T. van den Berg
Dennis W.J. Klomp
Alexander J.E. Raaijmakers

Appeared in:
Journal of Magnetic Resonance Imaging 2019; 49(5), 1446-1455

Abstract

Background

In MR imaging, the signal-to-noise ratio (SNR) theoretically increases with B_0-field strength. However, because of attenuation of the radiofrequency (RF) fields at 7T, it is not certain if this SNR gain can be realized for prostate imaging.

Purpose

To investigate the signal-to-noise ratio gain in prostate imaging at 7T as compared to 3T.

Field strength/sequence

All subjects were scanned at 3T and at 7T using optimal coil setups for both field strengths. For all volunteers, proton density weighted images were acquired for SNR analysis and actual flip angle imaging (AFI) B_1^+-maps were acquired for correction of measured SNR values. In the patient, a T2w image was acquired at 3T and at 7T.

Assessment

SNR was calculated in the prostate region for all volunteers. SNR was normalized for flip angle, receiver bandwidth and voxel volume. SNR was also calculated for different sensitivity encoding (SENSE) acceleration factors.

Results

On average, a 2.2-fold increase in SNR was measured in the prostate at 7T in comparison to 3T for four volunteers. At 7T, it is possible to achieve a 4-fold SENSE acceleration in the LR direction with similar SNR to a non-accelerated 3T image. The enhanced SNR at 7T facilitated T2w MRI as demonstrated in one patient within the prostate up to 0.35x0.35x2mm^3.

Conclusion

An overall gain in SNR of 2.2-fold was observed between 7T and 3T for prostate imaging. At 7T, it is possible to achieve 4-fold acceleration compared to 3T without compromising SNR. The additional available SNR enables higher resolution T2w imaging of the prostate at 7T.

538843-L-bw-Steensma
Processed on: 17-12-2019
PDF page: 48

Introduction

Prostate cancer is one of the most common forms of cancer in men, affecting 1 out of 6 men during their lifetime[1]. Prostate cancer is often indolent and could be followed up by a watchful-waiting program when non-invasive imaging/ characterization methods are available. Therefore, it is necessary to improve non-invasive tumor characterization methods for selective treatment of only those tumors which are potentially harmful and which have extracapsular extension [2].

Multiple studies have shown that multi-parametric prostate MRI at 1.5 and 3T is helpful in detecting, localizing and staging prostate cancer, however so far, good correlation with disease aggressiveness is insufficient to prevent potentially unnecessary treatment [3]–[7]. More insight into tumor metabolism and aggressiveness could be obtained by using MR spectroscopy (MRS) [8]–[10] and higher resolution imaging for capsular extension [11], but for better results a higher signal-to-noise ratio (SNR) is needed. The SNR for prostate MR imaging increases by going from 1.5 to 3T [12], and further increase is expected to when going to 7T systems. A recent study [13] compared 7T abdominal imaging to 1.5T and 3T, but focused mainly on image quality and did not show results for prostate imaging.

Patient studies at 7T involving prostate cancer showed until now satisfactory results for T2w (T2weighted) imaging compared to 3T [14] and the first results of ^{1}H and ^{31}P MRS [15]–[18] at 7T were published. Imaging at 7T is technically challenging owing to radiofrequency (RF) inhomogeneity, increased tissue heating and reduced RF field penetration. These challenges could potentially diminish the advantages of 7T. Though numerous studies have documented the use of custom-built external arrays dedicated to prostate imaging at 7T to obtain good T2w imaging [19]–[23], until now the superior imaging performance of 7T over 3T has not been demonstrated in terms of SNR. This, combined with the increased RF field attenuation at 7T casts doubts on whether or not imaging of deeply located structures within the body such as the prostate will actually be beneficial at 7T.

SNR comparisons over field strengths are challenging as they depend on a wide range of parameters. Relaxation time constants are different, causing sequence parameters like echo time and repetition time optimized for one field strength to be different for the other field strength. Moreover, the RF coil arrays that can be used will be different, and even if the identical coil geometry is used, the electromagnetic interaction with the body is completely different, causing an

538843-L-bw-Steensma
Processed on: 17-12-2019
PDF page: 49

optimized array for one field to be suboptimal for the other. Next, the uniformity of excitation will be different between field strengths, causing inhomogeneous flip angles, tissue contrast and SNR. Finally, specific absorption rate (SAR) may prohibit the use of optimized sequence parameters that can result in suboptimal scan efficiencies and thus SNR penalties.

One of the ways to minimize the number of parameters in comparing SNR over field strengths is to assess the SNR for a proton density weighted acquisition at a high flip angle [24]–[26]. An image acquisition with a 90° flip angle, very short echo time and large repetition time can negate the effect of relaxation parameters and RF transmit uniformity differences between field strengths. The long TR acquisition will not be limited by SAR constraints, so can be applied uncompromised at all field strengths. Based on the individual multichannel images, coil sensitivity data and noise pre-scan data, SNR scaled images can be reconstructed [27], [28]. These SNR scaled images can be corrected with a flip angle map, the receiver bandwidth and the voxel size to provide a measure for the SNR that actually can be obtained at each system, independent of scan parameters and tissue relaxation times. This is referred to as system SNR. Further corrections with quality factor ratio and pre-amplifier noise figure are needed to assess what is called intrinsic SNR [24] which is the SNR at a system corrected for potential system imperfections. Because of difficulties in determining the Q-factor ratios for commercial arrays, the intrinsic SNR can only be determined by estimates of this ratio with accompanying uncertainties. This is discussed in more detail in the discussion section. Also, because the choice of going from one field strength to the other is determined by the system SNR, this study will focus predominantly on a system SNR comparison.

A higher SNR is not the only gain at 7T, also parallel imaging performance is expected to improve when moving from 3T to 7T because of the more distinct sensitivity profiles of individual coil elements at 7T [29]. Based on the multichannel images and sensitivity data, g-factor maps and SNR scaled images can be compared at different sensitivity encoding (SENSE) acceleration factors, to compare parallel imaging performance at 3T and 7T.

The purpose of this work was to to investigate the signal-to-noise ratio gain in prostate imaging at 7T as compared to 3T. It is demonstrated in 4 volunteers and a phantom that SNR improves more than twofold in the prostate. SNR performance is also compared for different acceleration factors in the left-right (LR) direction. To demonstrate utilization of the enhanced SNR at 7T, T2w images were acquired in one patient with prostate cancer.

538843-L-bw-Steensma
Processed on: 17-12-2019
PDF page: 50

Materials and methods

This study was approved by the Institutional Review Board and informed consent from all subjects was obtained.

Coil configuration and setup

For this study an 8-element transceiver array consisting of fractionated dipole antennas [22] was combined with a detunable 16-element receive only loop coil array [30], [31], Figure 1. 8 building blocks consisting of 1 transceive dipole and 2 receive loops where distributed over the pelvis as indicated in figure 1, with 4 columns of receive elements distributed in the LR-direction. Under each antenna two oval shaped receive loops (long axis: 16cm, short axis 10cm) were positioned with mutual overlap. The antenna length is 30 cm with two meanders distributed evenly in each leg. The receive coil dimensions are based on the dipole size as well as the circumference of an average European adult, for which a certain optimal loop size exists [32]. The antenna was placed at a distance of 2cm from the body. To reduce coupling of the receive loops to the antenna, while ensuring sufficient coupling to the human body a body-loop distance of 6mm was found for the optimal $Q_{unloaded}/Q_{loaded}$ ratio (140/11). Detuning networks block the current inside the loops at three locations during transmit. A lattice balun was used to suppress common mode currents. Preamp decoupling was implemented to reduce inter-element coupling. Simultaneously, the preamp decoupling network in each receive loop (where the cable is connected) acts as a high impedance for induced currents in the loop, which in addition to detuning contributes to suppressing induced currents in the loop during transmit. More details on the tuning and matching circuitry and the RF safety profile of this coil array are provided in [31]. Each antenna/two loop structure is one of eight separate elements that are placed around the pelvis.

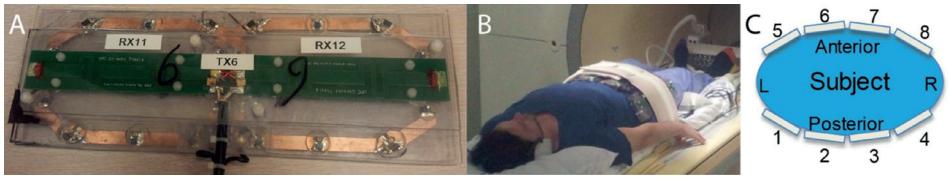

Figure 1: Experimental setup: (A) Under each antenna two oval shaped receive loops were positioned. To ensure spacing from the antenna towards the patient a 20 mm polycarbonate placeholder was designed in which the loops were at 6 mm distance from the patient. (B,C) The 8-element array with receive loops was positioned in a belt-like fashion around the pelvis.

To ensure RF safety a conservative worst-case SAR scenario was assumed [33] resulting in average power limits of 4 W per channel to abide the 20 W/kg

538843-L-bw-Steensma
Processed on: 17-12-2019
PDF page: 51

SAR limit of the IEC guidelines for any phase setting. The described array was interfaced using an 8-channel Transmit/Receive switch and receive interface box (MR Coils BV, Zaltbommel, the Netherlands) to an Achieva 7T MR system (Philips Healthcare, Best, The Netherlands). 3T results were acquired on a Philips Ingenia 3T system (Philips Healthcare, Best, The Netherlands), using the commercially available Anterior and Posterior Body Array with up to 32 elements (Philips Healthcare, Best, the Netherlands), with 4 columns of receive loops in distributed the LR-direction.

MRI Acquisition volunteers and phantom

Four healthy volunteers (Age 29, 44, 38 and 33, BMI 25.5, 25.5, 23.6 and 27.1kg/m^2) were included in this study. The MRI protocol for healthy volunteers included the following exams at 3T and 7T: A survey for localization purposes, a dynamic series of spoiled gradient echoes with alternating active transmit channels (shim series) to calibrate B1 levels in the prostate [34], AFI B1 map [35], T2w imaging for anatomical images and a proton density weighted gradient echo acquisition for SNR comparison. Noise levels were determined using a noise pre-scan, which was acquired without RF or gradients. The proton density weighted gradient echo sequence (SNR scan) was obtained using TR/TE = 10000/5 ms, flip angle = 90^0, FOV = 320x440x44 mm^3, voxel size = 5x10x10 mm^3, receive bandwidth = 1011 Hz, nominal B_1^+ 12 μT, pulse width = 3.866 ms, acquisition time = 1305 s. The echo time (TE) was kept short to exclude T2 effects, while for T1 exclusion the repetition time (TR) was kept long. A flip angle of 90^0 was used to be relatively insensitive to transmit non-uniformities. The actual flip angle method [35] was used for B_1^+-mapping, using the following scan parameters: 3D FFE sequence, TR/TE = 50/2.6 ms. TR extension = 200 ms, flip angle = 65^0, FOV = 250x422x50 mm^3, resolution = 3.9x3.8x10 mm^3. Receive bandwidth = 257 Hz (7T) and 110 Hz (3T), nominal B_1^+ = 11.8 μT (7T) and 13.46 μT (3T), pulse width = 2.99 ms (7T), 2.48 ms (3T), acquisition time 105 s. All experiments were repeated on a phantom with electric properties and dimensions comparable to the human pelvis (ethylene glycol, 50 g NaCl/L, ε_r=34, σ=0.4 S/m, width = 390 mm, height = 190 mm, length = 370 mm) [36].

MRI acquisition patient

One patient (62 years, Prostate Specific Antigen: 9.7 ng/ml) with biopsy-proven prostate cancer (Gleason score: 3+4 in 9/10 biopsies) was included in this study. A clinical prostate MRI exam was performed at 3T using a 32 element torso/cardiac coil (Philips Ingenia, Best, the Netherlands). The T2w acquisition was acquired using the following parameters: TR/TE= 5900/100 ms, TSE factor=29,

538843-L-bw-Steensma
Processed on: 17-12-2019

SENSE factor RL=1.5, FOV =200x200x90mm^3, voxel size= 0.78x0.78x3 mm^3 and reconstruction voxel size = 0.5x0.5x3mm^3.

At 7T the protocol consisted of a survey for localization purposes, B1 shim series to optimize B1 levels in the prostate [34], AFI B1 map [35] and one single slice T2w sequence (TR/TE=2500/90ms) with the same voxel dimensions as the clinical sequence at 3T. In addition, this sequence has been repeated with higher resolutions (voxel size: 0.5x0.5x4mm^3, 0.5x0.5x2mm^3, 0.35x0.35x4mm^3 and 0.35x0.35x2mm^3) to explore the possibilities that the extra SNR provides.

SNR analysis

Complex image data, coil sensitivity data and noise data was acquired for every channel and exported using ReconFrame (Gyrotools LLC, Switserland). The method of Kellman et al. [25], [27], [28] was used to obtain SNR scaled images, using the following steps. A noise-covariance matrix R with dimension (N_{ch} x N_{ch}) was calculated from the pre-scan noise data. R was corrected for the bandwidth of the digital receiver using a bandwidth correction factor of B_c = 0.73, which was calculated based on measuring the noise equivalent bandwidth in the noise data for both setups as described in Kellman et al. [27]. The noise covariance data R was then scaled as $R_{corrected} = R/B_c$. The lower triangular cholensky product L of the noise covariance matrix ($L^{-1}L = R$) was calculated for noise pre-whitening. A noise-pre-whitening step was applied to the sensitivity data b and the image data p (both vectors of length N_{ch}) for every voxel

$$\tilde{p} = pL, \tilde{b} = bL \quad [1]$$

The noise pre-whitening step ensures that standard deviation of the noise is uniform for every channel in the reconstructed image. Sensitivity weighted reconstruction with SNR scaling was done following the approach of Roemer et al [25]:

$$SNR_{pixel} = \sqrt{2}\,|\tilde{b}^T \tilde{p}\,| / \sqrt{\tilde{b}^T \tilde{b}} \quad [2]$$

The reconstructed image provides a quantitative map in which the value in every voxel represents the local SNR. This SNR is indicated as pixel SNR. For each SNR image a rectangular region of interest (ROI, 10x10 voxels) was delineated within the prostate, after which the measured SNR could be determined as the mean signal level in the ROI. The SNR images consisted of 3 slices, of which only the middle slice was considered, to avoid intra-voxel dephasing due to slice profile imperfections. The pixel SNR still is potentially biased by differences in scan

538843-L-bw-Steensma
Processed on: 17-12-2019
PDF page: 53

parameters and transmit efficiency. Therefore the pixel SNR is corrected based on receive bandwidth (BW_R), voxel volume (V), average flip angle in the prostate (θ_p) according to the following formula [24] to result in the system SNR:

$$SNR_{system} = SNR_{pixel} \frac{\sqrt{BW_R}}{V \sin(\theta_P)} \quad [3]$$

Further corrections are possible to remove system imperfections from the equation. The result is the co-called intrinsic SNR:

$$SNR_{\text{int}} = SNR_{system} \frac{10^{\frac{NF}{20}}}{[1 - \frac{Q_{loaded}}{Q_{unloaded}}]^{1/2}} \quad [4]$$

The pre-amplifier noise figures were measured using a Hewlett-Packard 8970A Noise Figure Meter (Hewlet-Packard, Palo Alto, California, USA). The Q-factors of the loops at 7T were measured using a sniffer coil [37]. The Q-factor of the dipole antennas was measured using the recently published method of Chen et al [38]. The Q-factors of the commercial loop array at 3T could not be measured.

Parallel Imaging Performance

The coil sensitivity data and image data was also used for assessment of parallel imaging performance. Image data was undersampled in k-space, after which a geometry-factor (g-factor) map was calculated using SENSE reconstruction [39]. SNR for the accelerated images was calculated as

$$SNR_{accelerated} = \frac{SNR_{unaccelerated}}{g\sqrt{R}} \quad [5]$$

For this work, undersampling was applied only in the left-right direction. This corresponds to the phase-encoding direction that is normally used in 2D T2w-acquitisions at this site, to avoid folding-artifacts of the iliac arteries in the prostate region.

Results

Coil array characterization

The pre-amplifier noise figure was 0.56 dB at 3T and 0.78 dB at 7T. The unloaded to loaded Q-ratio at 7T was 13 for the loops and 11 for the dipole antennas. Noise correlation between coil array elements can potentially decrease the SNR in MR imaging. The noise correlation matrix of an array is therefore one of the indicators

538843-L-bw-Steensma
Processed on: 17-12-2019
PDF page: 54

of an array's imaging performance. The noise correlation matrix was obtained for each volunteer at both 3T and 7T. A typical example of a matrix is shown in Figure 2. Noticeable is that the coupling between elements, particularly within the posterior part of the coil array at 3T is higher compared to any coupling between elements at 7T.

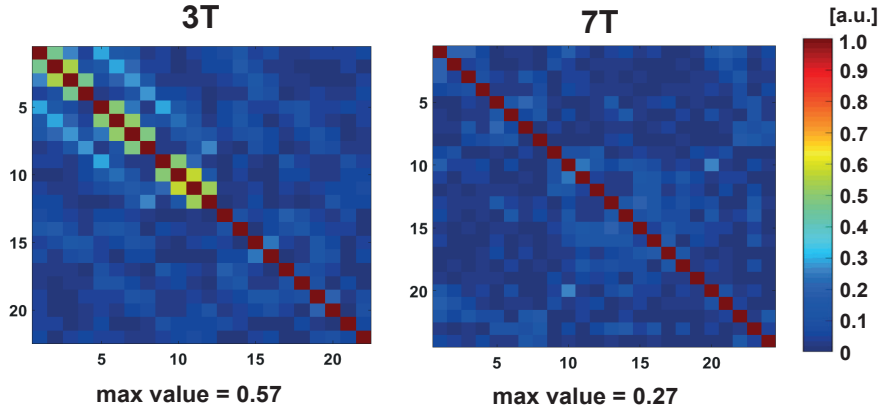

Figure 2: Noise correlation between coil elements at 7T and 3T. At 3T, the first 11 rows and colums represent the posterior array, which is integrated in the bed while the second 11 rows and columns correspond to the anterior array that is placed on the subject's pelvis. At 7T, colums and rows 1-16 represent the receive only loops while columns and rows 17-24 correspond to the fractionated dipole antennas.

Flip angle maps

Figure 3 shows the relative flip angle distributions in the phantom and in four volunteers.

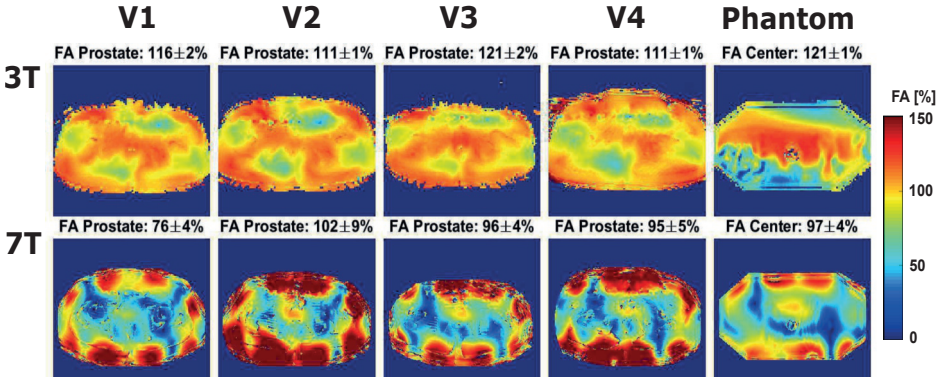

Figure 3: Flip angle maps in the phantom and four volunteers at 3T and 7T. B1 inhomogeneities are clearly present throughout the image at 7T. Signal voids are also present at 3T, but less severe. The flip angle seems lower at the edges of the phantom at 3T due to the limited dynamic range of the AFI-method.

It is clearly visible that at 7T, the penetration depth of the RF transmit fields is decreased and B1 inhomogeneities are present throughout the pelvis. At 3T, three distinct regions of lower B1 are present in all volunteers, showing that B1 inhomogeneities are also present at 3T, however clearly less severe than at 7T. At

538843-L-bw-Steensma
Processed on: 17-12-2019
PDF page: 55

7T, the flip angle distribution is less uniform than at 3T (coefficient of variation 44.4% at 7T and 16.6% at 3T), this difference is caused by the shorter wavelength and interference effects at 7T.Above each figure, the average and standard deviation of the flip angle in the ROI is shown. The average relative flip angle in the prostate is 93.2% at 7T and 116% at 3T. The large flip angle at 3T is because the RF power calibration tries to optimize the flip angle over the whole field of view which also contains many regions where the flip angle is lower than 100% (figure 3). Standard deviation of the flip angle in the prostate is 5.2% at 7T and 1.4% at 3T. At 7T, an average peak input power of 8*622.7 W and a 2.989 ms Gaussian pulse were used. At 3T, an average peak input power of 5008 W (channel 1) and 9891 W (channel 2) and a Gaussian pulse of 2.483 ms were used.

Signal to noise ratio

Pixel SNR maps are shown in figure 4. For all scans, SNR in the prostate increases when going from 3T to 7T. The signal-to-noise ratio at 7T is especially very high close to the coil, which is less visible at 3T.

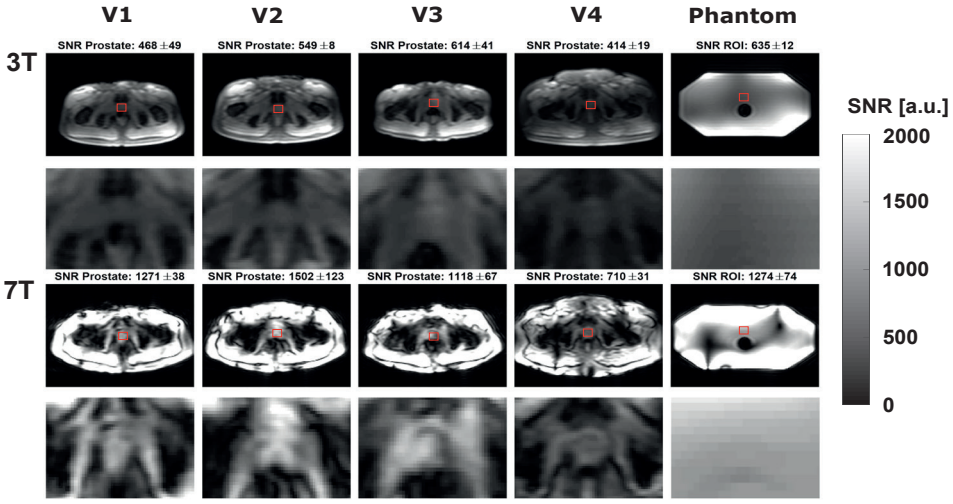

Figure 4: SNR scaled images on a phantom and four volunteers for 3T and 7T.The SNR values in this figure are pixel SNR values, and are not yet corrected for scan parameters.

The average flip angles in the prostate, the readout bandwidth (1011 Hz) and the voxel volume were used to normalize SNR values in the prostate to system SNR values. These values are shown in figure 5. Average signal-to-noise ratio in the prostate increases from (3.4±0.6, max 4.1, min 2.7)*10^4 √Hz/ml at 3T to (7.5±2.2, max 9.5, min 4.5)*10^4 √Hz/ml at 7T, which corresponds to a 2.2-fold increase. The SNR in the phantom is 4.3*10^4 √Hz/ml at 3T and 8.1*10^4 √Hz/ml at 7T.

538843-L-bw-Steensma
Processed on: 17-12-2019
PDF page: 56

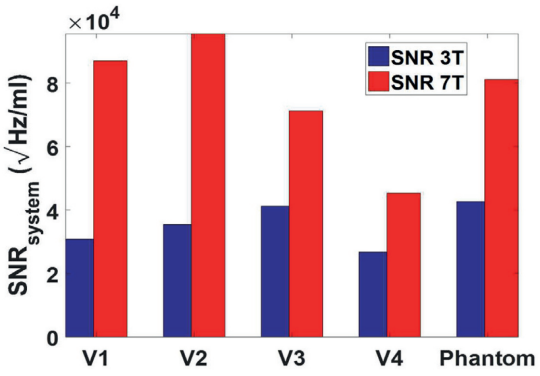

SNR [10^4 $Hz^{1/2}ml^{-1}$]	V1	V2	V3	V4	Phantom
3T	3.1	3.5	4.1	2.7	4.3
7T	8.7	9.6	7.1	4.5	8.1

Figure 5: system SNR values were obtained by normalizing the average pixel SNR values in the prostate to readout bandwidth, voxel size and flip angle. At 3T, an average SNR value of 3.4e4±0.6e4 √Hz/ml is measured. At 7T, this value increases to 7.5e4±2.2e4 √Hz/ml, which corresponds to a 2.2-fold increase.

Parallel imaging performance

Figure 6 shows g-factor maps (two top rows) and SNR scaled images (two bottom rows) for 3T and 7T. At 3T, g-factors above 2 start appearing in the image at acceleration factor R=3, while at 7T acceleration factors up to R=5 can be applied before g-factors above 2 appear. As a result of this, SNR values degrade more strongly for high acceleration factors (starting from R=3) at 3T as compared to 7T.

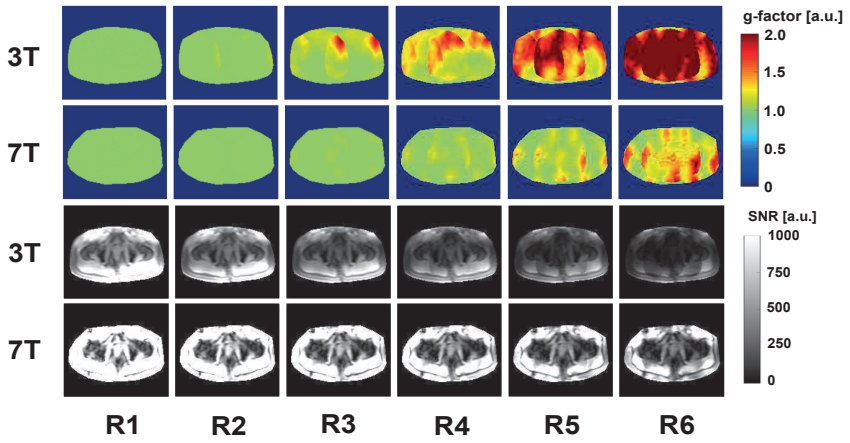

Figure 6: g-factor maps (two top rows) and pixel SNR values (two bottom rows) for 3T and 7T using different LR-acceleration factors in an exemplary volunteer (V1). The pixel SNR maps are not yet corrected to system SNR values.

538843-L-bw-Steensma
Processed on: 17-12-2019

Figure 7 shows the normalized SNR values in the prostate, for different acceleration factors and averaged over all volunteers. Because of the improved parallel imaging performance and the improved SNR at 7T, an acceleration factor of R=4 can be applied at 7T with SNR comparable to an unaccelerated 3T prostate image.

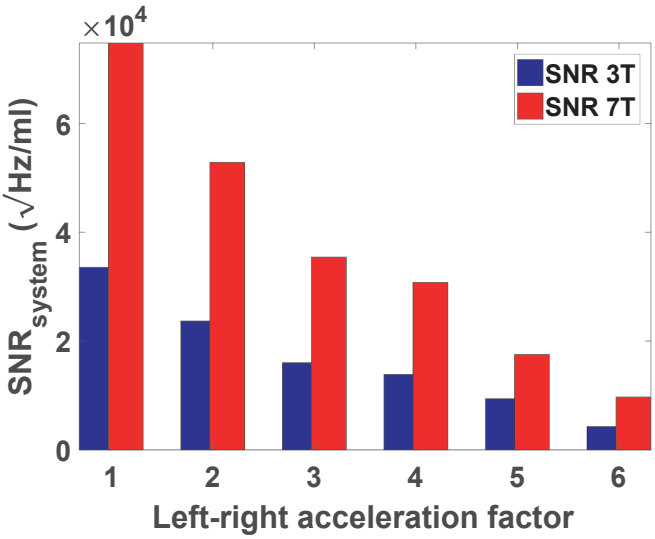

SNR [10^4 $Hz^{1/2}ml^{-1}$]	R=1	R=2	R=3	R=4	R=5	R=6
3T	3.4	2.4	1.6	1.4	0.9	0.4
7T	7.5	5.3	3.5	3.1	1.8	1.0

Figure 7: system SNR values in the prostate for 3T and 7T for different LR-acceleration factors, averaged over all 4 volunteers.

538843-L-bw-Steensma
Processed on: 17-12-2019
PDF page: 58

T2w imaging

In one prostate cancer patient (62 years, PSA: 9.7 ng/ml, Gleason score: 3+4) T2w images are acquired at 7T after the clinical 3T MR examination. When comparing the clinical 3T examination to the 7T scan with the same resolution (Figure 8) it can be noticed that the 7T image is less noisy.

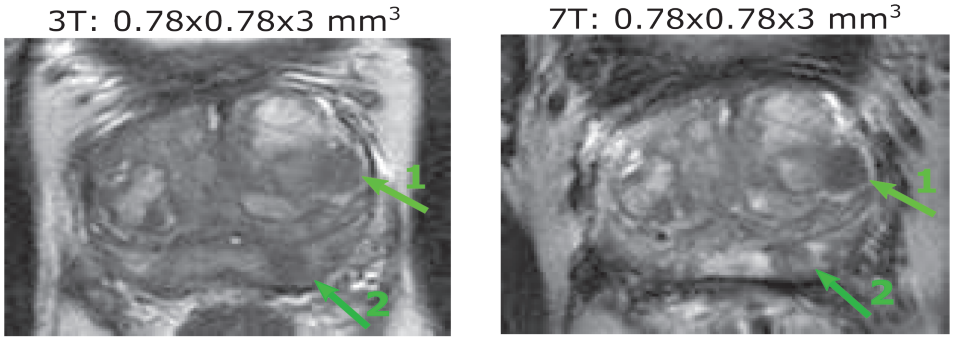

Figure 8: In this patient (62 years, PSA: 9.7 ng/ml) with biopsy-proven prostate cancer (Gleason score: 3+4 in 9/10 biopsies) two tumor areas are visible mid-prostate. Noticeable is the good T2w contrast between healthy and tumor areas at 7T.

Even when going to higher resolution T2w images, the noise levels stay low at 7T and the clear anatomical details remain, Figure 9.

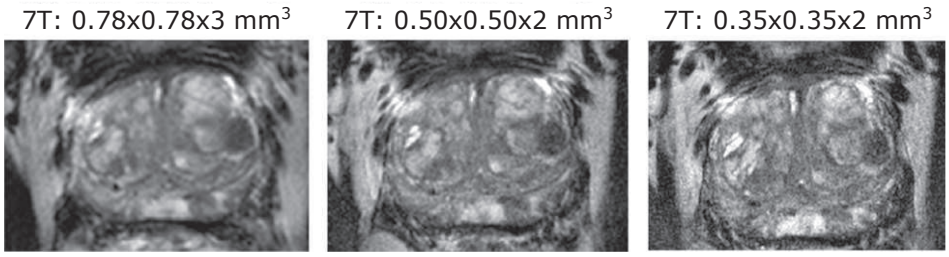

Figure 9: T2w images acquired at 7T with increased resolution. Anatomical details and contrast between healthy and tumor areas remain visible even at the resolution of 0.35x0.35x2mm3 while the SNR clearly decreases.

538843-L-bw-Steensma
Processed on: 17-12-2019
PDF page: 59

Discussion

In this work, we have demonstrated a 2.2-fold increase in SNR for prostate MRI at 7T in comparison to 3T. The gain in SNR ranges from 1.7-fold to 2.8-fold. No direct relationship between BMI and SNR can be observed except that the subject with the highest BMI shows the lowest SNR at both field strengths and also the lowest SNR gain at 7T. This is potentially related to the decreased penetration depth of the RF fields at 7T. The SNR-values reported in this work are comparable to the SNR values reported by Erturk et al. with a 16-channel loop-dipole array [40] (7.2e4±1.0e4 √Hz/ml in Erturk et al vs. 7.5e4±2.4e4 √Hz/ml in this work). Parallel imaging performance was also evaluated for 7T and 3T. At 7T, higher acceleration factors can be applied (R=5) as compared to 3T (R=3) before g-factors in the imaging region exceed the value of 2. The enhanced parallel imaging performance with increasing field strength corresponds to predictions based on an analytical model [29]. The high SNR and low g-factor at 7T enable 4-fold acceleration with comparable SNR to a 3T unaccelerated image. (SNR at 7T 3.1e4 √Hz/ml at R=4, SNR at 3T: 3.4e4 √Hz/ml at R=1). This effectively means that the g-factor with R=4 is almost entirely equal to 1 so the loss in SNR from acceleration is determined by the square root of the acceleration factor. This loss for R=4 is equal to 2 which is then compensated by the SNR gain at 7T. The improved parallel imaging performance at 7T can be used to accelerate clinical protocols as compared to 3T, making it possible to acquire 4-fold more slices in the same amount of time and with similar SNR. However, this is only possible if SAR limitations are not exceeded, which can be a problem for clinical protocols at 7T. The T2w images in this study were acquired with only one slice to avoid any SAR violations. Currently, tools are being created to reduce the uncertainties in SAR levels between subjects and provide more accurate SAR assessments without the severe overestimations as used in this study [41], [42]. Also additional measures have been published to further reduce SAR levels [20], [43]. The work of Maas et al. [20] specifically showed that clinical T2w protocols are feasible within the SAR limitations of 7T.

Comparing the clinical T2w images at 3T and 7T shows that the same anatomical information is present at both field strengths, arguably with an improved contrast at 7T. Using the SNR gain at 7T we have acquired T2w images of a prostate cancer patient with improved spatial resolution up to 0.35x0.35x2 mm^3.A higher resolution can be beneficial for detecting or ruling out extracapsular tumor extension. Furthermore, the gain in SNR may open up the possibility to detect the multifocal nature of prostate cancer better without the use of endorectal coils [3],

538843-L-bw-Steensma
Processed on: 17-12-2019
PDF page: 60

[44]–[46]. Not only T2w imaging benefits from the higher SNR: MR spectroscopy, dynamic contrast enhanced sequences and diffusion weighted imaging are only a few of the prostate cancer characterization methods that can also profit from a higher SNR, while some of these simultaneously profit from an enhanced contrast mechanism at higher field strengths which comes on top of the SNR gain. This study has focused on the comparison of system SNR values. To account for differences in system losses, the loaded to unloaded Q-factor ratio of the coils and the pre-amplifier noise figure can be used as a correction factor to obtain intrinsic SNR values [24]. However, for the commercial array it was not possible to measure the loaded-to-unloaded Q-factor ratio. A worst case assumption based on literature values for very small loop coils in an array setup [37] would result in a correction factor of 0.79 for the 3T array. The high loaded-to-unloaded Q-factor ratio of the 7T array would result in a correction factor of 0.96 [31]. According to this worst case assumption, and including a correction factor for the pre-amplifier noise figure (0.93 at 3T and 0.91 at 7T), intrinsic SNR gain at 7T would be 1.9-fold instead of 2.2-fold.

Intrinsic SNR values are determined by the B_0 field strength but also by the receive sensitivities of the coil arrays. Different coil setups were used at 3T and 7T, which may be considered a source of bias even after correcting for loaded to unloaded Q-factor ratio. However, a 3T vs 7T comparison with identical coils would favor one of the field strengths as optimal coil design depends on the field strength. In this study, the 7T coil array is an in-house developed array that has resulted from a gradual evolution of body imaging arrays at 7T (21,22,30). The 3T coil array is a widely used, state of the art commercial coil and it is also the coil array that is used for prostate cancer patients at our department. It is therefore considered an appropriate reference. Nevertheless, it is not impossible that for both field strengths the SNR may be improved by adapted coil array designs. Although still too computationally expensive, future work on investigating the ultimate signal-to-noise-ratio in realistic human body models (48–50) could indicate how much SNR could potentially be gained at both field strengths by the introduction of new coil array designs for prostate imaging (51,52).

A main limitation of this work is the limited number of subjects included in the study. Including more subjects can potentially provide more information about the relation between SNR, and SNR gain as a function of BMI and torso size. Another limitation lies in the clinical data that is included in this work. Data is presented for only one patient, which makes it impossible to do a systematic comparison of image quality in a clinical setting. However, the main aim of this work is to show the SNR gain that is obtained from an electromagnetics point of

538843-L-bw-Steensma
Processed on: 17-12-2019
PDF page: 61

view, and to show that even though penetration depth of the RF fields decreases when going to 7T, substantial SNR gains can still be obtained. Therefore, a systematic clinical comparison is considered out of the scope of this work. In conclusion, this study shows a comparison of SNR for prostate imaging at 7T and 3T. Compared to a clinically used prostate imaging setup at 3T, 7T imaging resulted in an overall gain in SNR of 2.2-fold. LR-acceleration factor R=4 can be applied at 7T to acquire an image with comparable SNR to an unaccelerated 3T image. Furthermore high resolution imaging was obtained at 7T in one prostate cancer patient, to show the potential of going up to ultrahigh field prostate imaging with ultrahigh resolutions.

References

[1] R. L. Siegel, K. D. Miller, and A. Jemal, "Cancer Statistics , 2017," vol. 67, no. 1, pp. 7–30, 2017.

[2] G. Draisma *et al.*, "Lead times and overdetection due to prostate-specific antigen screening: estimates from the European Randomized Study of Screening for Prostate Cancer.," *J. Natl. Cancer Inst.*, vol. 95, no. 12, pp. 868–878, 2003.

[3] A. Shukla-Dave and H. Hricak, "Role of MRI in prostate cancer detection," *NMR Biomed.*, vol. 27, no. 1, pp. 16–24, 2014.

[4] R. Nagarajan *et al.*, "MR spectroscopic imaging and diffusion-weighted imaging of prostate cancer with Gleason scores.," *J. Magn. Reson. Imaging*, vol. 36, no. 3, pp. 697–703, 2012.

[5] C. Tempany and F. Franco, "Prostate MRI: Update and current roles," *Appl. Radiol.*, vol. 41, no. 3, pp. 17–22, 2012.

[6] T. W. J. Scheenen, A. B. Rosenkrantz, M. A. Haider, and J. J. Fütterer, "Multiparametric magnetic resonance imaging in prostate cancer management: Current status and future perspectives," *Invest. Radiol.*, vol. 50, no. 9, pp. 594–600, 2015.

[7] B. Turkbey, A. M. Brown, S. Sankineni, B. J. Wood, P. A. Pinto, and P. L. Choyke, "Multiparametric Prostate Magnetic Resonance Imaging in the Evaluation of Prostate Cancer," *CA Cancer J Clin*, vol. 66, pp. 326–336, 2016.

[8] T. Kobus *et al.*, "In vivo assessment of prostate cancer aggressiveness using magnetic resonance spectroscopic imaging at 3 T with an endorectal coil," *Eur. Urol.*, vol. 60, no. 5, pp. 1074–1080, 2011.

[9] J. Kurth, E. Defeo, and L. L. Cheng, "Magnetic resonance spectroscopy: a promising tool for the diagnostics of human prostate cancer?," *Urol Oncol*, vol. 29, no. 5, pp. 562–571, 2011.

[10] E. K. Vos *et al.*, "Multiparametric Magnetic Resonance Imaging for Discriminating Low-Grade from High-Grade Prostate Cancer," *Invest. Radiol.*, vol. 50, no. 8, pp. 490–497, 2015.

[11] J. J. Fütterer, "High-Resolution Diffusion-weighted Imaging Increases Prostate Cancer Visibility?," *EBioMedicine*, vol. 7. p. 12, 2016.

[12] D. M. Cornfeld and J. C. Weinreb, "MR Imaging of the Prostate: 1.5T versus 3T," *Magnetic Resonance Imaging Clinics of North America*, vol. 15, no. 3. pp. 433–448, 2007.

[13] A. Laader *et al.*, "1.5 versus 3 versus 7 Tesla in abdominal MRI: A comparative study," *PLoS One*, vol. 12, no. 11, p. e0187528, 2017.

538843-L-bw-Steensma
Processed on: 17-12-2019
PDF page: 62

[14] E. K. Vos *et al.*, "Image quality and cancer visibility of T2-weighted Magnetic Resonance Imaging of the prostate at 7 Tesla," *Eur. Radiol.*, vol. 24, no. 8, pp. 1950–1958, 2014.

[15] M. W. Lagemaat *et al.*, "Phosphorus magnetic resonance spectroscopic imaging at 7 T in patients with prostate cancer," *Invest. Radiol.*, vol. 49, no. 5, pp. 363–372, 2014.

[16] M. W. Lagemaat *et al.*, "1H MR spectroscopic imaging of the prostate at 7T using spectral-spatial pulses," *Magn. Reson. Med.*, vol. 75, no. 3, pp. 933–945, 2016.

[17] M. P. Luttje *et al.*, "(31) P MR spectroscopic imaging combined with (1) H MR spectroscopic imaging in the human prostate using a double tuned endorectal coil at 7T.," *Magn. Reson. Med.*, vol. 72, no. 6, pp. 1516–21, 2014.

[18] C. S. Arteaga de Castro, M. P. Luttje, M. Van Vulpen, P. R. Luijten, U. A. Van der Heide, and D. W. J. Klomp, "Composite slice-selective adiabatic excitation for prostate MRSI," *NMR Biomed.*, vol. 26, no. 4, pp. 436–442, 2013.

[19] G. J. Metzger *et al.*, "Performance of external and internal coil configurations for prostate investigations at 7 T," *Magn. Reson. Med.*, vol. 64, no. 6, pp. 1625–1639, 2010.

[20] M. C. Maas *et al.*, "Feasibility of T2 -weighted turbo spin echo imaging of the human prostate at 7 tesla.," *Magn. Reson. Med.*, vol. 71, pp. 1711–9, 2014.

[21] A. J. E. Raaijmakers *et al.*, "Design of a radiative surface coil array element at 7 T: The single-side adapted dipole antenna," *Magn. Reson. Med.*, vol. 66, no. 5, pp. 1488–1497, 2011.

[22] A. J. E. Raaijmakers *et al.*, "The fractionated dipole antenna: A new antenna for body imaging at 7 Tesla," *Magn. Reson. Med.*, vol. 75, no. 3, pp. 1366–1374, 2016.

[23] A. B. Rosenkrantz *et al.*, "T2-weighted prostate MRI at 7 Tesla using a simplified external transmit-receive coil array: Correlation with radical prostatectomy findings in two prostate cancer patients," *J. Magn. Reson. Imaging*, vol. 41, no. 1, pp. 226–232, 2015.

[24] W. A. Edelstein, G. H. Glover, C. J. Hardy, and R. W. Redington, "The intrinsic signal-to-noise ratio in NMR imaging," *Magn. Reson. Med.*, vol. 3, no. 4, pp. 604–618, 1986.

[25] P. B. Roemer, W. A. Edelstein, C. E. Hayes, S. P. Souza, and O. M. Mueller, "The NMR phased array," *Magn. Reson. Med.*, vol. 16, no. 2, pp. 192–225, Nov. 1990.

[26] J. T. Vaughan *et al.*, "7T vs. 4T: RF power, homogeneity, and signal-to-noise comparison in head images," *Magn. Reson. Med.*, vol. 46, no. 1, pp. 24–30, 2001.

[27] P. Kellman and E. R. McVeigh, "Image reconstruction in SNR units: A general method for SNR measurement," *Magn. Reson. Med.*, vol. 54, no. 6, pp. 1439–1447, 2005.

[28] P. Kellman, "Erratum to Kellman P, McVeigh ER. Image reconstruction in SNR units: a general method for SNR measurement.," *Magn. Reson. Med.*, vol. 58, pp. 211–212, 2007.

[29] F. Wiesinger, P. Boesiger, and K. P. Pruessmann, "Electrodynamics and ultimate SNR in parallel MR imaging," *Magn. Reson. Med.*, vol. 52, no. 2, pp. 376–390, 2004.

[30] I. J. Voogt *et al.*, "Combined 8-channel transceiver fractionated dipole antenna array with a 16-channel loop coil receive array for body imaging at 7 Tesla," *Proc. 23th Sci. Meet. Int. Soc. Magn. Reson. Med. Vancouver*, vol. 200, no. 2007, p. 631, 2015.

[31] B. R. Steensma *et al.*, "An 8 - channel Tx / Rx dipole array combined with 16 Rx loops for high - resolution functional cardiac imaging at 7 T," *Magn. Reson. Mater. Physics, Biol. Med.*, no. 0123456789, 2017.

538843-L-bw-Steensma
Processed on: 17-12-2019
PDF page: 63

[32] A. J. E. Raaijmakers, P. R. Luijten, and C. A. T. van den Berg, "Dipole antennas for ultra-high-field body imaging: a comparison with loop coils," *NMR Biomed.*, vol. 29, no. 9, pp. 1122–1130, 2016.

[33] Ö. Ipek, A. J. Raaijmakers, J. J. Lagendijk, P. R. Luijten, and C. A. T. Van Den Berg, "Intersubject local SAR variation for 7T prostate MR imaging with an eight-channel single-side adapted dipole antenna array," *Magn. Reson. Med.*, vol. 71, no. 4, pp. 1559–1567, 2014.

[34] G. J. Metzger, C. Snyder, C. Akgun, T. Vaughan, K. Ugurbil, and P. F. Van De Moortele, "Local B1+ shimming for prostate imaging with transceiver arrays at 7T based on subject-dependent transmit phase measurements," *Magn. Reson. Med.*, vol. 59, no. 2, pp. 396–409, 2008.

[35] V. L. Yarnykh, "Actual flip-angle imaging in the pulsed steady state: A method for rapid three-dimensional mapping of the transmitted radiofrequency field," *Magn. Reson. Med.*, vol. 57, no. 1, pp. 192–200, 2007.

[36] B. Van Den Bergen, C. A. T. Van Den Berg, D. W. J. Klomp, and J. J. W. Lagendijk, "SAR and power implications of different RF shimming strategies in the pelvis for 7T MRI," *J. Magn. Reson. Imaging*, vol. 30, no. 1, pp. 194–202, 2009.

[37] A. Kumar, W. A. Edelstein, and P. A. Bottomley, "Noise figure limits for circular loop MR coils," *Magn. Reson. Med.*, vol. 61, no. 5, pp. 1201–1209, 2009.

[38] G. Chen, C. M. Collins, D. K. Sodickson, and G. C. Wiggins, "A method to assess the loss of a dipole antenna for ultra-high-field MRI," *Magn. Reson. Med.*, vol. 00, 2017.

[39] K. P. Pruessmann, M. Weiger, M. B. Scheidegger, and P. Boesiger, "SENSE: Sensitivity encoding for fast MRI," *Magn. Reson. Med.*, vol. 42, no. 5, pp. 952–962, 1999.

[40] M. A. Ertürk, A. J. E. Raaijmakers, G. Adriany, K. Ugurbil, and G. J. Metzger, "A 16-channel combined loop-dipole transceiver array for 7 Tesla body MRI," *Magn. Reson. Med.*, vol. 00, pp. 1–11, 2016.

[41] F. Meliado, E., A. J. E. Raaijmakers, M. Restivo, M. Maspero, P. R. Luijten, and C. A. T. van den Berg, "Database Construction for Local SAR Prediction: Preliminary Assessment of the Intra and Inter Subject SAR Variability in Pelvic Region," in *In: Proceedings of the 24th scientific meeting, International Society for Magnetic Resonance in Medicine, Singapore, 3660*, 2016.

[42] F. Meliado, E., A. J. E. Raaijmakers, P. R. Luijten, and C. A. T. van den Berg, "Fast method to get an upper bound of the maximum SAR10g for body coil arrays," *Proc. 9th Sci. Meet. Int. Soc. Magn. Reson. Med. Benelux Chapter, Tilbg.*, p. p-070, 2017.

[43] A. Sbrizzi, H. Hoogduin, J. J. Lagendijk, P. Luijten, G. L. G. Sleijpen, and C. A. T. Van Den Berg, "Fast design of local N-gram-specific absorption rate-optimized radiofrequency pulses for parallel transmit systems," *Magn. Reson. Med.*, vol. 67, no. 3, pp. 824–834, 2012.

[44] J. J. Fütterer *et al.*, "Initial experience of 3 tesla endorectal coil magnetic resonance imaging and 1H-spectroscopic imaging of the prostate," *Invest. Radiol.*, vol. 39, no. 11, pp. 671–680, 2004.

[45] J. Sosna, I. Pedrosa, W. C. Dewolf, H. Mahallati, R. E. Lenkinski, and N. M. Rofsky, "MR imaging of the prostate at 3 tesla: Comparison of an external phased-array coil to imaging with an endorectal coil at 1.5 tesla," *Acad. Radiol.*, vol. 11, no. 8, pp. 857–862, 2004.

[46] Y. Mazaheri, A. Shukla-Dave, A. Muellner, and H. Hricak, "MRI of the prostate: Clinical relevance and emerging applications," *J. Magn. Reson. Imaging*, vol. 33, no. 2, pp. 258–274, 2011.

538843-L-bw-Steensma
Processed on: 17-12-2019
PDF page: 64

538843-L-bw-Steensma
Processed on: 17-12-2019

Chapter 5

An 8-channel Tx/Rx dipole array combined with 16 Rx loops for high-resolution functional cardiac imaging at 7 T.

Bart R. Steensma
Ingmar J. Voogt
Tim Leiner
Peter R. Luijten
Jesse Habets
Cornelis A.T. van den Berg
Dennis W.J. Klomp
Alexander J.E. Raaijmakers

Appeared in:
Magnetic Resonance Materials in Physics, Biology and Medicine, 31, Issue 1, pp7-18, February 2018

Abstract

Object

To demonstrate imaging performance for cardiac MR imaging at 7 T using a coil array of 8 transmit/receive-dipole antennas and 16 receive-loops.

Materials and Methods

An 8 channel dipole array was extended by adding 16 receive only loops. Average power constraints were determined by electromagnetic simulations. Cine imaging was performed on 8 healthy subjects. Geometical factor (g-factor) maps were calculated to assess acceleration performance. Signal-to-Noise Ratio (SNR) scaled images were reconstructed for different combinations of receive channels, to demonstrate the SNR benefits of combining loops and dipoles.

Results

The overall image quality of the cardiac functional images was rated a 2.6 on a 4-point scale by two experienced radiologists. Imaging results at different acceleration factors demonstrate that acceleration factors up to 6 could be obtained while keeping the average g-factor below 1.27. SNR-maps demonstrate that combining loops and dipoles provides a more than 50% enhancement of SNR in the heart, compared to a situation where only loops or dipoles are used.

Conclusion

This work demonstrates the performance of a combined loop/dipole array for cardiac imaging at 7 T. With this array, acceleration factors of 6 are possible without increasing the average g-factor in the heart beyond 1.27. Combining loops and dipoles in receive mode enhances SNR compared to receiving with loops or dipoles only.

538843-L-bw-Steensma
Processed on: 17-12-2019
PDF page: 67

Introduction

Cardiac magnetic resonance imaging (CMRI) at ultrahigh field strengths (UHF, $B_0 \geq 7.0$ T) holds promise for several clinical applications. Coronary artery imaging has been applied at UHF, and is reported to have higher Signal-to-Noise Ratio (SNR) and Contrast-to-Noise Ratio (CNR) compared to 3 T [1], [2]. Applications such as functional imaging and quantitative parameter mapping have also been demonstrated at 7T [3]–[7]. However, UHF-CMRI is challenging due to UHF-inherent phenomena such as transmit field (B_1^+) and background field (B_0) inhomogeneities and increased energy deposition [4], [8]. Recent advances in RF-transmit coil array design have been utilized to enhance transmit efficiency and homogeneity while keeping the specific absorption rate (SAR) within the required limits [9]–[13]. Improved RF shimming and pulse design can be used for further improvements [14]–[16], and advances in RF modelling have led to the adoption of less conservative SAR limits [17], [18].

Developments in transmit array design have demonstrated the beneficial use of dipole antenna arrays for body imaging at 7T [9], [10], [13], [19]. The use of fractionated dipole antennas can lead to lower SAR levels while maintaining transmit efficiency [9]. Conversely, for signal reception, current patterns corresponding to a combination of electric dipoles and magnetic dipoles yield the theoretical ultimate-intrinsic signal-to-noise ratio [20]–[22]. These current patterns correspond to a receive array composed of dipole antennas and loop coils.

Loop coils are commonly used as receive elements in cardiac imaging, often in combination with a body coil at 1.5 and 3T, or in transmit/receive-mode at 7T [12], [23]. More recently, dipole antennas have been used as transmit/receive-elements for cardiac imaging at 7T [2], [10], [13]. We present a body array that consists of 8 fractionated dipole antennas in transmit/receive (Tx-/Rx-) and 16 loop coils in receive (Rx-) mode [10, 11, 24] resulting in an 8 channel Tx-/24 channel Rx-array. This should provide SNR enhancement, while not having to extend the 8 channel transmit chain in our current multi-transmit system. The array is specifically adapted for cardiac imaging by modifying the shape of the elements to the torso to maintain full contact between the antenna elements and the tissue. Electromagnetic simulations have been used to assess safety limitations of this setup for cardiac imaging. Imaging performance is demonstrated for functional cine imaging, and compared to the imaging performance reported for cardiac 7 T imaging in the literature [12], [13].

538843-L-bw-Steensma
Processed on: 17-12-2019
PDF page: 68

Materials and Methods

Transmit/Receive-Setup

A custom-built 8 channel Tx-, 24 channel Rx-setup was fabricated (*Figure 1*). The setup consists of 8 building blocks, composed of 8 fractionated dipole antennas (300 mm length) that were used for both transmit and receive. In each building block, two loop coils (160/100 mm, long/short axis) were positioned between the dipole and the subject along the longitudinal direction with overlap for decoupling. These 16 loop coils were used for receive-only [9], [11]. The dimensions of the loops and the dipoles are based on simulations on ideal loop and dipole size, which were done in references [9], [25].

The loop coils were kept at 6 mm spacing from the body and the dipole was kept at 20 mm distance from the body by a polycarbonate housing of each building block. The two medial anterior elements were bent in the middle and positioned at a fixed angle to maintain full contact with the chest. Each loop coil was detuned at three positions by PIN-diodes. Preamplifier decoupling ensured a high impedance at the cable connection point during reception. A lattice balun was used for impedance matching of both the dipole antennas and the loop coils. More details on geometry and circuitry are presented in figure 1. Reflection and coupling levels (S11 and S12) were determined to ensure good array performance as well as Qunloaded/Qloaded ratios for the loop coil elements.

Electromagnetic Modeling

The 8 channel Tx-/24 channel Rx-setup was modeled using the Sim4Life environment (Zurich Medtech, Zurich, Switzerland). Simulations were carried out on human models Duke and Ella (body-mass-index (BMI) 23.1 and 22 kg/m^2), using a resolution of 1.5x1.5x1.5mm^3 to render the coil geometry and the nearby tissue, resulting in 13.862*10^6 cells for Duke and 13.746*10^6 cells for Ella [26]. Simulations were done on a graphic processor unit (GPU, NVIDIA GeForce GTX TITAN Black, NVIDIA, Santa Clara, USA). [26]. The worst case SAR was calculated as the maximum sum of the modulus of all Quality-matrix (Q-matrix) entries [18]. This value was used to derive average power limits for imaging applications, based on a 10g-averaged SAR limit of 20 W/kg in the trunk for first level controlled mode [27]. To validate the simulations, single-channel B_1^+-maps have been acquired for all transmit channels on a phantom filled with ethylene glycol and saline (ε=34, σ=0.4 S/m, 0.4g/L saline) [9]. The dual refocusing angle acquisition mode (DREAM) B_1^+-mapping method was used to acquire the B_1^+-

538843-L-bw-Steensma
Processed on: 17-12-2019
PDF page: 69

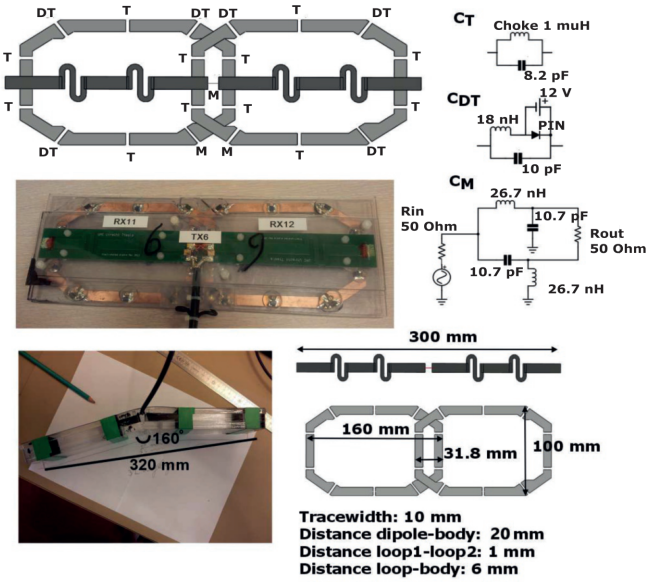

Figure 1: Schematic overview of a single loop-dipole element. 1a. shows a model of the loops and the dipoles, and indicates the position of the tuning, detuning and matching circuitry. A lattice balun was used for matching both the loops and the dipoles. 1b. shows a photograph of a single loop-dipole element. 1c. shows the detuning and matching circuitry. 1d. shows one of the two elements that is adapted to the curvature of the chest, by bending both ends of a single element. 1e. shows the sizes of the loop and dipole elements.

maps [28]. The imaging parameters of this sequence were as following: 2D Acquisition, Echo Time (TE) = 1.57 ms, Repetition Time (TR) = 10 ms, field of view (FOV) = 320*400*30 mm^3, in plane resolution = (5*5) mm^2 slice thickness = 30 mm, flip angle = 10^0, pulse width = 0.17 ms, STE angle = 60^0, pulse width = 1.01 ms, nominal B_1^+ = 16 μT, receive bandwidth = 4882.8 Hz, acquisition time = 11 seconds. A model of the phantom was imported from SolidWorks (SolidWorks, Dassault Systèmes SolidWorks Corp., Massachusetts, USA) into Sim4Life and used for simulations of the B_1^+-fields. An isotropic resolution of 1.5x1.5x1.5 mm^3 was used for the full model, resulting in a total of 22.687*10^6 cells.

Cine Imaging Experiments

A 7 T Philips Achieva multi-transmit system with 8 x 2 kW RF amplifiers (Philips Healthcare, Best, The Netherlands) was used to scan 8 healthy volunteers (7 males, 1 female, age 22-35, average Body Mass Index (BMI)=21.6 ±1.14 kg/m^2, minimum BMI=20.1 kg/m^2,maximum BMI=23.1 kg/m^2). The study was approved by the local medical ethics committee and all subjects signed informed consent prior to inclusion in the study. RF phase-shimming was applied on three slices in the heart,

538843-L-bw-Steensma
Processed on: 17-12-2019
PDF page: 70

in order to obtain maximum average signal in the heart [29], [30]. For the phase shimming, low flip angle gradient echo images were acquired in three slices for every transmit channel, these images were combined to obtain maximum signal intensity averaged over three slices in the heart, the optimum phase settings were calculated with a numerical minimization in Matlab (Mathworks, Natick, USA) [30]. The same phase-settings were used for all three slices, while the amplitudes of the channels where all set equally. This procedure was done once for every volunteer, while the same phase settings were used for all views. Phase-only RF-shimming was used for every acquisition in this work. The following imaging parameters were used for the low flip angle gradient echo images: 2D multislice acquisition (M2D), TE = 1.68 ms, Repetition Time (TR) = 24 ms, field of view (FOV) = 309*522*60 mm^3, in plane resolution = (1.3*1.3) mm^2, slice thickness = 20 mm, flip angle = 3^0, turbo field echo-factor (TFE-factor) = 15, receive bandwidth = 498.7 Hz, pulse width = 0.20 ms, nominal B_1^+ = 4 μT, acquisition time = 102.7 seconds. Subsequently, a 10-slice cine planning sequence in the transverse orientation was acquired during 5 breath-holds (R=2). The obtained images were used for planning of cine cardiac imaging. Pseudo 2 chamber-, pseudo 4 chamber-, short axis and 4 chamber- (p2Ch-, p4Ch-, SAX-, 4Ch- respectively) view images were acquired during breath-hold. The following imaging parameters were used for the cine imaging: TE = 2.7 ms, TR = 4.2 ms, field of view (FOV) = 280*420*8 mm^3, in plane resolution = (1.3*1.3) mm^2, slice thickness = 8 mm, flip angle = 9^0, turbo field echo-factor (TFE-factor) = 10, receive bandwidth = 998.2 Hz , pulse width = 0.61 ms, nominal B_1^+ = 4 μT, acquisition time = 10 heartbeats/10 seconds on average, 30 cardiac phases. Retrospective gating with electrocardiographic (ECG) pads and breathhold triggering were used for motion compensation. For one volunteer, the 4Ch-view acquisition was repeated at increasing resolutions (1.3x1.3x8 mm^3, 1.1x1.1x2.5 mm^3 and 0.75x0.75x1.75 mm^3), using a sensitivity encoding (SENSE) acceleration factor of R2 in the anterior-posterior- (AP-) direction. Acquisition times increased from 10 to 12 and 17 heartbeats, respectively.

Cine Image Analysis

To get a measure of the overall image quality, the cine images of all 8 volunteers were rated on a four-point scale by two experienced readers. Overall image quality, artifacts and noise where taken into account in this rating [23], where higher scores represent better image quality. The rating scale and scoring criteria are shown in detail in *Table 1*. Inter-observer agreement percentages and Cohens kappa were used to calculate inter-observer variability for all ratings [31].

538843-L-bw-Steensma
Processed on: 17-12-2019
PDF page: 71

Score	3	2	1	0
Artifacts	No artifacts	Minor artifacts (not impairing diagnostic quality)	Moderate artifacts (may partially impair diagnostic quality)	Major artifacts, not diagnostic images
Noise	No remarkable noise	Little noise (not impairing diagnostic quality)	Moderate noise (may partially impair diagnostic quality)	High noise level, not diagnostic
Overall image quality	Excellent	Good	Diagnosis may be limited	Poor, not diagnostic.

Table 1: rating scale and scoring criteria for the functional Cine images.

SNR and Acceleration Performance

In order to make a quantitative comparison to other literature, the imaging parameters used in [13], have been reproduced to the best of our ability. The following imaging parameters were used for the SNR analysis: Echo Time (TE) = 3.8 ms, Repetition Time (TR) = 6.0 ms, field of view (FOV) = 280*420*2.5 mm^3, in plane resolution = (1.1*1.1) mm^2 , slice thickness = 2.5 mm, flip angle = 20^0, turbo field echo-factor (TFE-factor) = 9, receive bandwidth = 998.2 Hz , pulse width = 3.6 ms, nominal B_1^+ 1.5 μT, acquisition time = 20 heartbeats/20 seconds on average, 28 cardiac phases, acceleration factor R = 2, applied along the anterior-posterior- (AP-) direction. This was done on three additional volunteers (2 males, 1 female, age 25-36, average BMI = 21.9 ±1.12 kg/m^2, minimum BMI = 20.01 kg/m^2, maximum BMI = 23.03 kg/m^2) in the 4Ch-view and the SAX-view. Phase shimming was done for all acquisitions on three transverse slices in the heart. To assess the SNR performance of the coil array, as well as the separate contributions of the loop and dipole elements, SNR scaled imaged were reconstructed according to the method described by Robson et al. [32]. The mean SNR in the heart, and the CNR between the myocardium and the blood, defined as (SNR_{blood}-SNR_{myo}), was calculated for all three volunteers, according to [13].

To assess the acceleration performance of the array, the cine acquisitions were repeated on the same three volunteers, using sensitivity enconding (SENSE) with acceleration factors ranging from R=2 to R=6. Phase encoding was applied along the left-right (LR-) direction for the 4Ch-view images and along the feet-head (AP-) direction for the SAX-view images. Geometrical factor (g-factor) maps were reconstructed on the scanner using reconstruction software available on the Philips system (delayed reconstruction). The mean g-factor in the heart was calculated for all three volunteers.

538843-L-bw-Steensma
Processed on: 17-12-2019
PDF page: 72

Results

Transmit/Receive-Setup

The elements were tuned and matched to obtain matching and decoupling values of -12 dB on the torso. Bench measurements show a $Q_{unloaded}/Q_{loaded}$-ratio of 140/11 for the loop elements. PIN-diodes were used to detune the loops during RF-transmission. Decoupling between the loops and the dipoles was improved from -12 dB to -18 dB or less after detuning of the receive loop. The geometry and circuitry of a single loop/dipole element is shown in *Figure 1*. *Figure 2* shows a schematic overview of the imaging setup on a volunteer.

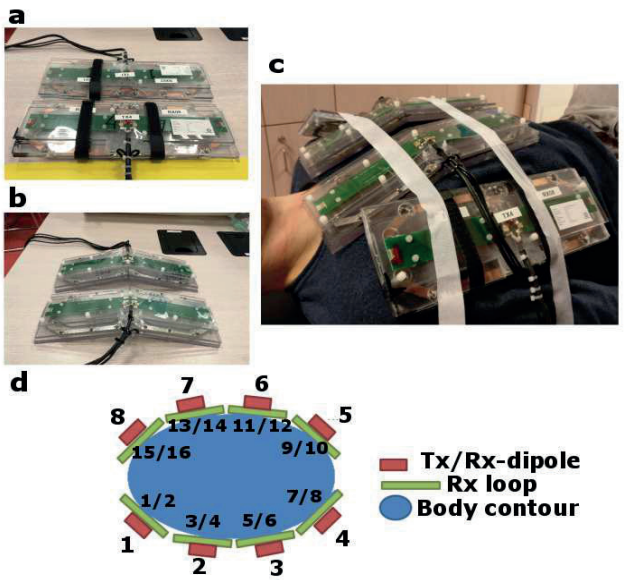

Figure 2: Schematic overview of the imaging setup. 1a. Shows two elements consisting of a Tx-/Rx-antenna and two Rx-loops. 1b. shows the two elements that are adapted to fit on the chest. 1c. shows a schematic drawing of the setup on a torso model 1d. shows the transmit setup on a male volunteer. 1e. shows a noise covariance matrix on an exemplary volunteer.

Electromagnetic Modeling

Figure 3 shows maximum intensity projections of 10g-averaged SAR (SAR_{10g}) and 1g-averaged SAR (SAR_{1g}) distributions for human models Duke and Ella. Phase-only shimming was used to optimize for maximum average B_1^+ in the heart and results are normalized to an average input power of 1.0 W per channel (8.0 W total).

538843-L-bw-Steensma
Processed on: 17-12-2019

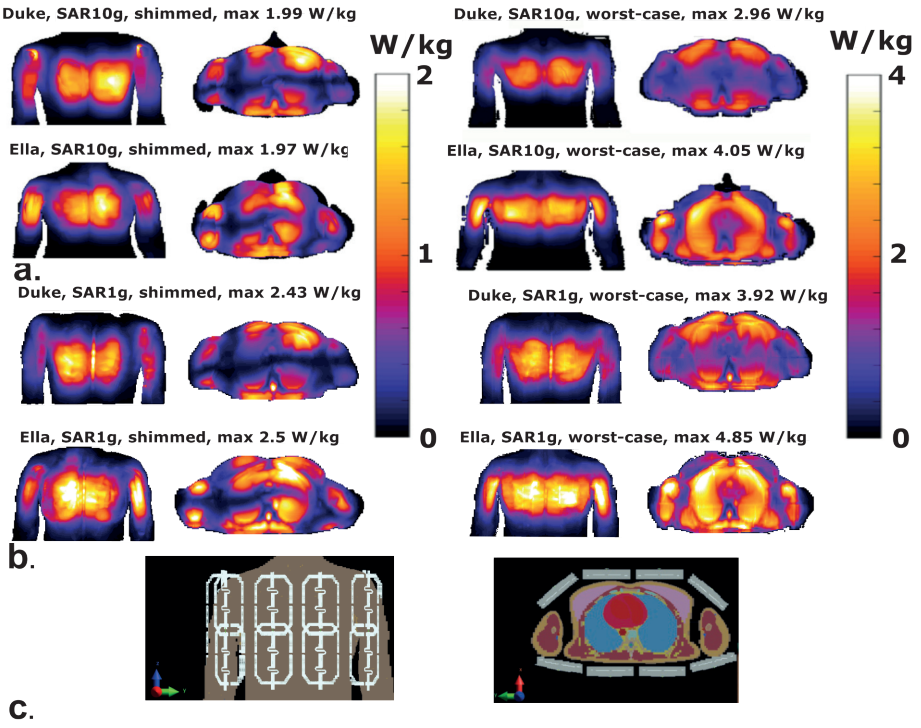

Figure 3: a. Coronal and transverse maximum intensity projections of SAR_{10g} for the Duke and Ella model. Results are normalized to 1 W input power for every input channel, using a total input power of 8 W. Input transmit phases are used to maximize average B_1^+ in the heart for the image on the left. The image on the right displays the worst case SAR. 3b. shows a voxelized model of Duke from a frontal and transverse point of view.

It was demonstrated that SAR_{10g} does not exceed 2.0 W/kg for both models using phase-shimmed transmit phases. The worst-case SAR_{10g} is calculated to be 4.05 W/kg for the Ella model, and 2.96 W/kg for the Duke model, using an input power of 1.0 W per channel (8.0 W total input power). Considering a maximum allowed SAR_{10g} of 20 W/kg in the first level controlled mode, the maximum average power limit is 20 W/4.05 = 4.92 W per channel based on these two models. The transmit phases for which the worst case SAR values are obtained do not correspond to the transmit phases that maximize B_1^+ in the heart, so this value represents a conservative estimate of the required power constraint. However, with only two subjects investigated, inter subject variability may still increase the maximum SAR value. A recent study has investigated these opposing effects for prostate imaging at 7 T [18], [33]. Based on these results, and including a safety margin of 20%, the average power limit in these experiments was set to 4.0 W per channel. The maximum worst-case SAR_{1g} that is calculated in simulations is 4.85 W/kg for a total input power of 1.0 W per channel. If the average power limit of 4.0 W/

538843-L-bw-Steensma
Processed on: 17-12-2019

channel is applied, the local SAR limits are also not exceeded when using this small averaging volume.

Figure 4 shows the simulation and measurement results on a phantom. The overall field patterns and the magnitude of the B_1^+-fields correspond qualitatively, however some differences between simulations and measurements are to be noted. For all the single transmit channels, minor differences between the simulated and measured field patterns can be discerned. In the shimmed combination, the field distribution in the center of the antenna corresponds well, but the measured transmit field at the bottom of the phantom has a lower intensity than the simulated field. The absence of highly intense peaks in the measured B_1^+-fields indicate that the loops are detuned well, and do not influence the transmit fields of the dipole antennas.

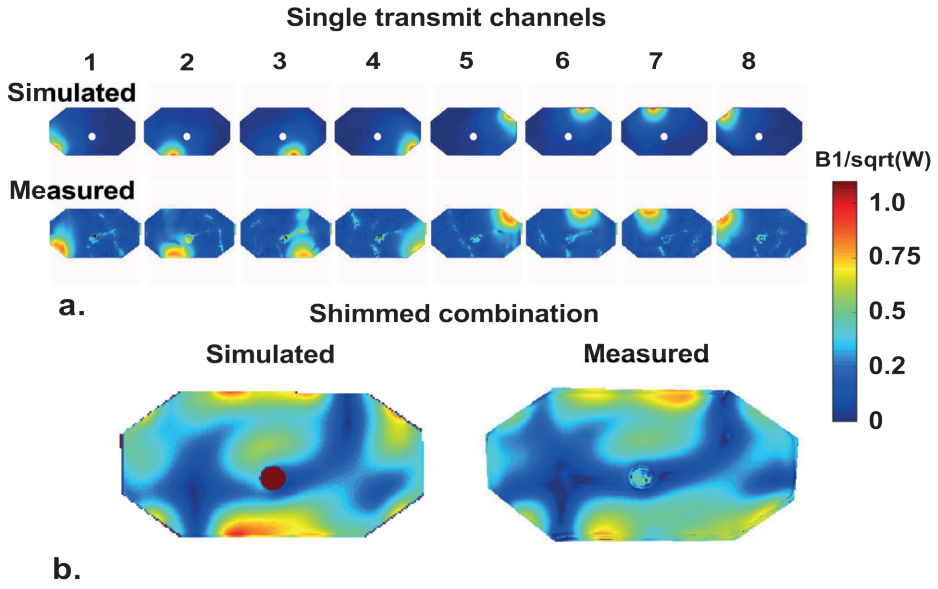

Figure 4: Phantom simulation setup. 4a. shows simulated (top) and measured (bottom) B_1^+-maps on the ethylene-glycol phantom. 4b. shows the same B_1^+-maps, now both combined using the same transmit phases.

Cine Imaging Experiments and Analysis

Figure 5 shows the imaging results of functional imaging for all 8 subjects. Below each image the average rating of overall image quality is reported. The image quality ratings are shown in *Table 2* where 0 corresponds to poor image quality and 3 represents excellent image quality. A document with all the separate ratings is added as supplementary material.

538843-L-bw-Steensma
Processed on: 17-12-2019
PDF page: 75

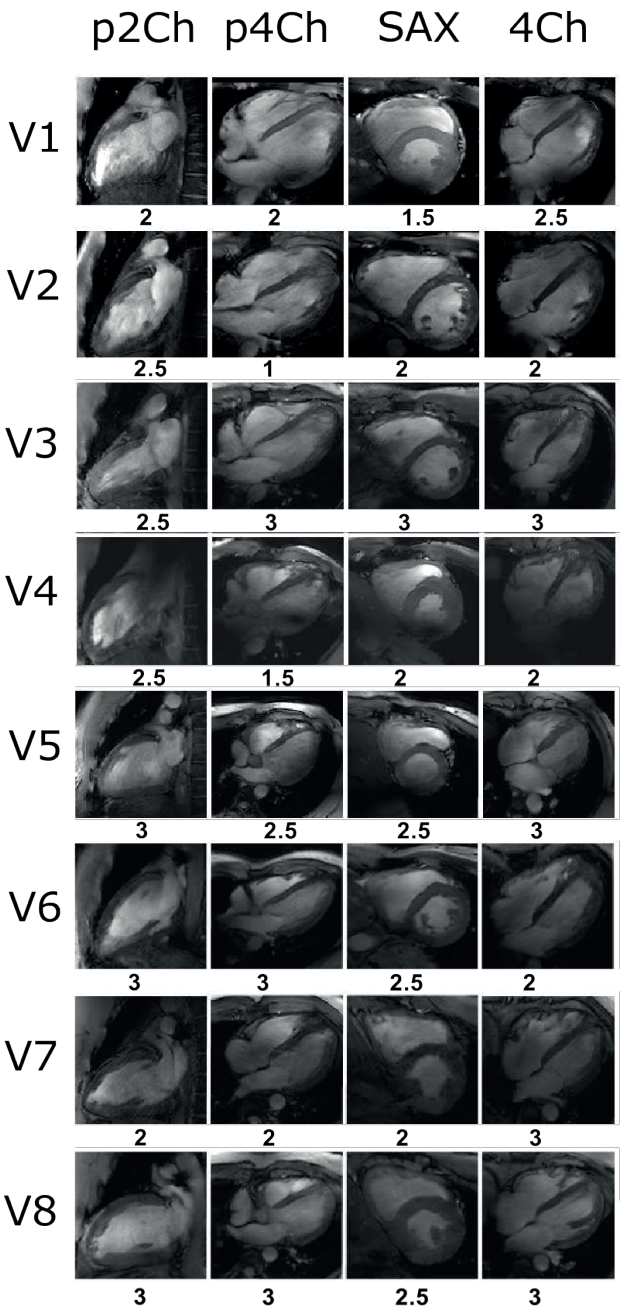

Figure 5: Pseudo two chamber views (p2Ch), pseudo four chamber views (p4Ch), short axis views (SAX) and four chamber views (4Ch) for 8 volunteers. Phase-only shimming was applied to maximize signal in three transverse slices for each individual volunteer. The same transmit phases were used for all acquisitions. All images were acquired with a resolution of 1.3x1.3x8 mm^3, and an average scantime of 10 seconds. The overall image quality rating is displayed underneath each separate image.

538843-L-bw-Steensma
Processed on: 17-12-2019
PDF page: 76

Parameter/view	2 Chamber View	pseudo 4 Chamber View	Short Axis View	4 Chamber View
Artifacts	2.50±0.50 (75%)	2.25±0.90 (50%)	2.50±0.50 (37.5%)	2.6±0.50 (62.5%)
Noise	3.00±0.00 (100%)	3.00±0.00 (100%)	3.00±0.00 (100%)	3.00±0.00 (100%)
Overall image quality	2.60±0.50 (62.5%)	2.25±0.90 (62.5%)	2.50±0.50 (50%)	2.60±0.50 (87.5%)

Table 2: mean and standard deviation of image quality scores over all volunteers, for the different views and rating parameters. Interobserver agreement for the different views and criteria are displayed below the scores. The average interobserver agreement over all samples is 74%. Interagreement variability was also calculated using Cohen's Kappa, which was κ=0.5221 over all observations.

The overall image quality is rated between good and excellent (overall score 2.41). No remarkable noise is present in any of the images (overall score 3). Some of the images show artifacts (overall score 2.28), which can be recognized in *Figure 5* for volunteer 1 and volunteer 4. Inter-observer agreement was calculated for every view and criterion. The overall inter-observer agreement was 74%. Inter-observer variability was calculated using Cohen's kappa, which is κ=0.56 for all observations. This corresponds to a moderate agreement between both raters.

Figure 6 shows the four chamber view results of volunteer 6, using an acceleration factor of R=2 and different resolutions. In general, as spatial resolution increases, SNR is reduced. However, due to the higher spatial resolution, more details can be recognized in the image, especially in the region close to the cardiac walls. The maximal resolution that was reached in this experiment on one volunteer is 0.75x0.75x1.75 mm^3, which corresponds to a cubic resolution of 0.98 mm^3. At this resolution, noise becomes more clearly present in the image, especially at locations far away from the transmit/receive-elements.

538843-L-bw-Steensma
Processed on: 17-12-2019
PDF page: 77

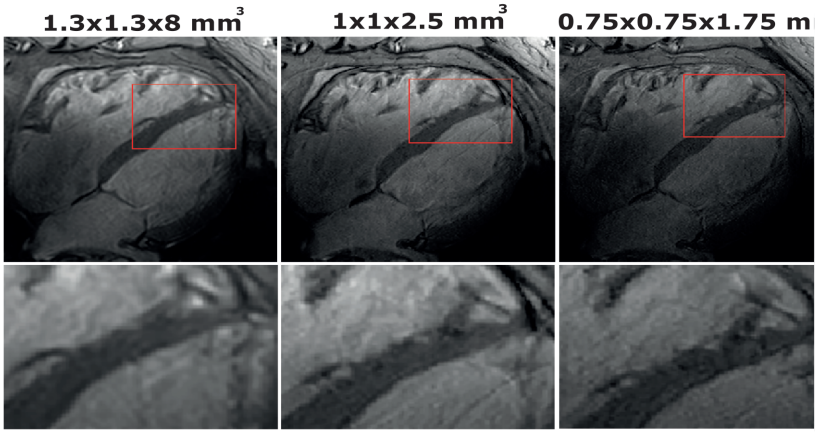

Figure 6: Four chamber views using 2D Cine acquisitions, at different spatial resolutions. All images were acquired with the same imaging parameters as the Cine acquisition shown in figure 4, with AP acceleration factor R2 and at different spatial resolutions. Acquisition time increased from 10 to 12 and 17 seconds. Bottom row shows the same images but zoomed in on the right cardiac chamber. At high resolution, improved depiction of myocardial trabeculae in the right ventricular wall can be seen.

SNR and Acceleration Performance

Figure 7 shows SNR maps of a single volunteer, acquired in the 4Ch-view and SAX-view. The separate contributions of the loop and dipole elements are demonstrated in this image.

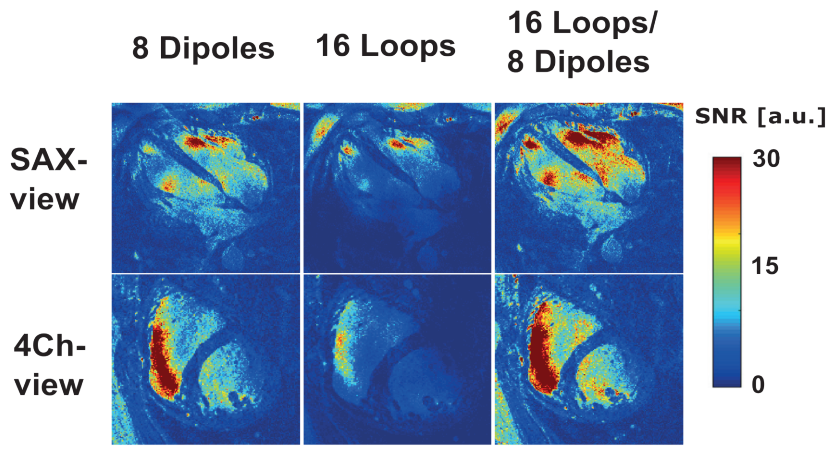

Figure 7: SNR scaled images for a single volunteer in the SAX-view and the 4Ch-view. The separate contributions of the loop and dipole elements are displayed here. Phase shimming was applied on three transverse slices through the heart for all volunteers, the same shim settings were used for all acquisitions. Images were acquired at a resolution of 1.1x1.1x2.5 mm^3, at an average scantime of 20 seconds.

538843-L-bw-Steensma
Processed on: 17-12-2019
PDF page: 78

It can be seen in both views, that combining the loop and dipole elements leads to a remarkable enhancement of the SNR in the heart. Table 3 shows the SNR and CNR values in the heart for the different views, averaged over the three volunteers.

View	Setup	CNR (myocardium/blood)	SNR (whole heart)	Normalized SNR (whole heart) (√Hz/ml)
SAX	16 Loops	3.70±2.70	2.70±1.40	2.84±1.5*1e4
4Ch	16 Loops	2.50±0.450	4.60±0.80	4.80±0.80*1e4
SAX	8 Dipoles	9.07±6.23	7.90±3.60	8.30±3.80*1e4
4Ch	8 Dipoles	7.00±1.01	7.60±2.06	8.00±2.20*1e4
SAX	16 Loops/8 Dipoles	12.70±8.20	10.90±4.70	11.50±5.00*1e4
4Ch	16 Loops/8 Dipoles	10.30±1.20	11.90±1.60	12.50±1.70*1e4

Table 3: summarized results of the mean signal-to-noise ratio (SNR) and the mean blood/myocardium contrast-to-noise ratio ($CNR_{blood/myo}$). The contributions of the loop and dipole elements and the combined array are shown here for two views, averaged over three volunteers. SNR was normalized based on receive bandwidth and voxel volume.

When using all receive elements, the average SNR in the heart is 10.9 and 11.9 for the SAX-view and the 4Ch-view, respectively. The $CNR_{blood/myo}$ for these views is 10.7 and 12.3 . The SNR increases over two-fold when all elements are used, compared to the situation where only loops coils are used for receive. Compared to a situation where only dipoles are used in receive mode, the SNR increases 50% when all elements are used.

Figure 8 shows reconstructed images and g-factor maps for a single volunteer, acquired in the SAX-view and the 4ch-view.

538843-L-bw-Steensma
Processed on: 17-12-2019
PDF page: 79

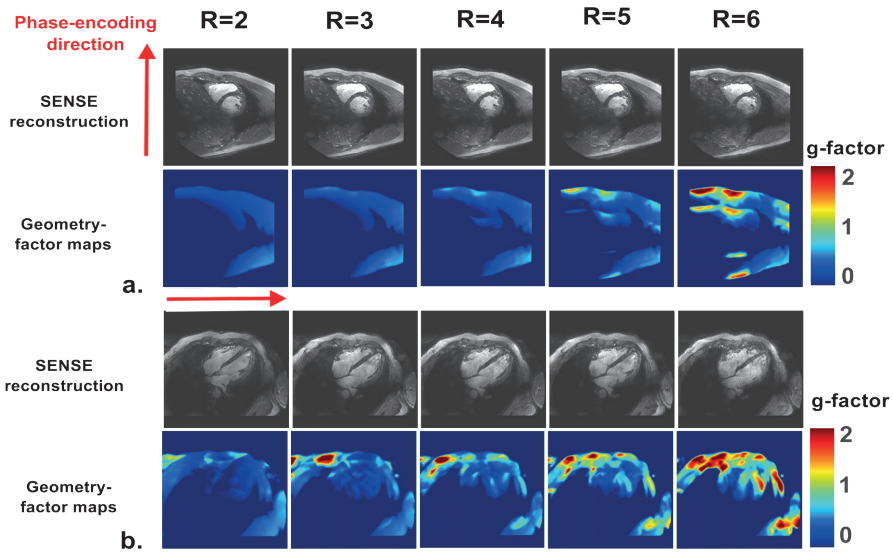

Figure 8: g-factor maps for different SENSE acceleration factors (R=2 to R=6) on a single volunteer in the SAX-view and the 4Ch-view. Increasing the acceleration factors increases the g-factor in the heart. Phase shimming was applied on three transverse slices through the heart for all volunteers, the same shim settings were used for all acquisitions. Images were acquired at a resolution of 1.1x1.1x2.5 mm^3, with scantimes ranging from 20 to 7 seconds.

As the acceleration factor is increased, the g-factor in the heart clearly increases, and noise becomes more present in the reconstructed images. However, even for an acceleration factor of R=6, the anatomy of interest is still clearly visible. The average g-factor in the heart increases from 1.02 to 1.08 in the SAX-view and from 1.04 to 1.27 when moving from an acceleration factor of R=2 to R=6. The maximum g-factor obtained in the SAX-view is 2.00 at R=6, in the 4Ch-view a g-factor of 3.1 is reached at R=6.

		Acceleration Factor				
		R = 2	R = 3	R = 4	R = 5	R = 6
View	Phase-encoding direction	Average/maximum g-factor in the heart				
SAX	A-P	1.02/1.10	1.03/1.25	1.05/1.35	1.05/1.57	1.08/2.00
4Ch	L-R	1.04/1.43	1.06/1.61	1.10/1.65	1.19/2.40	1.27/3.10

Table 4: g-factors in the heart for increasing acceleration factors, averaged and maximum over three volunteers.

538843-L-bw-Steensma
Processed on: 17-12-2019
PDF page: 80

Discussion

This work demonstrates the potential of cardiac imaging at 7 T with a combined loop-dipole array. Several RF transmit setups have been developed for cardiac imaging, but the addition of 16 receive only loops to a dipole array has not been demonstrated before. It is demonstrated here that combining 16 receive loops and 8 transceive dipoles leads to a 50% increase of SNR in the heart compared to a setup which used 8 transceive dipoles. SNR is sufficient to acquire detailed images at a high spatial resolution (1.1x1.1x2.5mm^3). When moving to a resolution of (0.75x0.75x1.75 mm^3) a clear degradation of SNR is visible.

Electromagnetic modeling

The worst-case SAR calculated here corresponds to the phase setting that yields the highest possible SAR value in the entire subject. This phase setting will not correspond to a realistic phase setting that is used for scanning. The safety simulations indicate that there is a large difference between the worst-case SAR and a SAR that corresponds to a realistic shim setting (The SAR corresponding to a realistic shim setting is 33% and 51% lower than the worst case SAR, respectively for Duke and Ella). While it is not likely that the worst case SAR is obtained during a scan, this value was nevertheless used to set the upper limit of the total average power[33]. In other work [13], the total average power limits are derived based on peak SAR calculated in human models for fixed phase settings. These fixed phase settings are also used in the scan. Using this method leads to a total average power limit of 65 W, more than two fold higher than the 8*4 = 32 W that is used in this work. This difference in the average power limit does not necessarily represent a difference in the efficiency of these two setups, but a difference in choices regarding transmit phase optimization and safety assessment.

Much effort is already spent on matching SAR simulations with measurements as closely as possible [17], [18]. Future work into worst-case SAR estimations will very likely focus on deriving realistic drive settings for multiple human models and matching those to scan results, with the use of bi-directional couplers [33]. These methods have the potential to increase the average power limits, leading to faster cardiac exams at 7 T. Work focused on using nonlinear optimization of the transmit phases and amplitudes to reduce maximum local SAR, or the use of SAR constraint RF pulses has not yet been applied in this work, and do also have the potential to improve transmit efficiency [15], [17], [34]–[36].

Electromagnetic simulations were validated by comparing simulated to measured B_1^+-maps. Field measurements or MR thermometry are a possible

538843-L-bw-Steensma
Processed on: 17-12-2019
PDF page: 81

alternative for safety validation, but are not treated within the scope of this paper. A comparison between simulated and measured transmit fields on a phantom correspond qualitatively. However, when comparing the results in detail, differences between the simulations and measurements are clearly visible. The qualitative correspondence between the results indicates that the antennas perform as modeled in the simulation, and it indicates that the loops are detuned properly. The results could be improved upon by exactly matching the simulation and measurement geometry by doing a computed tomography scan of the measurement setup and importing this in Sim4Life. Exactly matching the simulated and measured coupling parameters by using circuit co-simulations would be another way of improving the correspondence between simulations and measurements. This will be necessary for deriving SAR limits that closely match simulations for realistic drive settings, but it is not treated within the scope of this work.

Cine Imaging Experiments and Analysis

High quality functional images were acquired for a total of 8 volunteers. Image quality of the Cine images has been scored by two experienced readers, leading to an average score of 2.4 (between good and excellent) for overall image quality. The rating shows that the diagnostic quality of the Cine images is not at all affected by noise. The image quality scores are impacted by artifacts, which are most generally caused by a non-uniform excitation field. This is clearly present in volunteers 1 (SAX-view) and 4 (p4Ch-view), which is represented by the lower rating of the images. Although optimized RF transmit phase settings are calculated for every volunteer, it is clear that RF shimming methods that are used in this work do no suffice for every situation. The shimming method that is currently used maximizes the average signal in the heart, but does not necessarily provide a uniform signal. Additional RF calibrations can be used to enhance homogeneity of the signal, but this can also increase acquisition time and examination complexity [14], [16]. Future work will explore more advanced techniques to acquire homogeneous excitation fields combined with rapid calibration scans and procedures.

SNR and acceleration performance

For SNR comparison, cine images have been acquired using scan parameters reproduced from literature to the best of our ability [13]. The flip angle of 30^0 could not be reproduced within a reasonable scan-time. This is caused by different choices in setting the average power limits, as mentioned earlier in this discussion. The TR and TE that are reported by Oezerdem et al. (2.17/4.17 ms)

538843-L-bw-Steensma
Processed on: 17-12-2019
PDF page: 82

was also not reproducible with our system and the other sequence parameters. The overall SNR values that we report at R=2 are lower than for the two coil setups mentioned by Oezerdem et al. (11.9 compared to 29 for the 4Ch view, 10.9 compared to 29 for the SAX-view). The $CNR_{blood/myo}$ values that we report are comparable (10.3 compared to 11 for the 4Ch-view, 9.9 compared to 9 for the SAX-view). Because of the differences in acquisition methods, the results of this comparison should be interpreted with caution. An interesting comparison would be to scan both coil setups at the same imaging site, however this will not be treated within the scope of this paper.

The average g-factor that we report at R=6 is lower than the g-factors mentioned in literature (1.08 compared to 1.5 for the SAX-view, 1.27 compared to 1.6 for the 4Ch-view) [13]. As a result of the difference in MRI system vendor, SENSE is used in our work, while generalized autocalibrating partial parallel acquisition (GRAPPA) is used in [13]. Results show that the average g-factor remains low even up to an acceleration factor of 6. Although such accelerations may provide insufficient SNR for many applications, these results show that in terms of encoding power of the array, it is possible.

The SNR maps presented here show that a setup which combines loops and dipoles in receive, increases SNR in the heart by more than 50% compared to a setup where only loops or dipoles are used. This strong increase in SNR in not only caused by the receive sensitivity of the combined setup, but also relates to the improved acceleration that is gained my moving from 16 or 8 to 24 channels. Most setups that are used specifically for cardiac imaging make use of loop coils, while some setups use dipole antennas [9], [12], [13], [37]–[39]. This work shows that these kind of setups can be improved by combining both elements.

Conclusion

High-resolution cardiac cine imaging is demonstrated at 7T using an 8 channel Tx-/24 channel Rx- array which combines loops and dipoles. The overall image quality of cine imaging results is rated a 2.6 on a 4-point scale by two experienced radiologists. Acceleration factors up to R=6 can be used while the average g-factor in the heart does not exceed 1.27. Adding 16 receive only loops to an 8 channel transceiver dipole array increases the SNR in the heart by more than 50% compared to the use of dipoles only.

538843-L-bw-Steensma
Processed on: 17-12-2019
PDF page: 83

Appendix A

Electromagnetic simulations on a phantom were done to assess the signal-to-noise performance of a 8-dipole/16-loop array, compared to a 8-dipole/8 loop array, as is presented in [10]. The phantom had tissue-like properties (ε=34, σ=0.4 S/m), the dimensions of the phantom were 450*300*236 mm^3. Signal-to-noise ratio was calculated from the receive fields, which were normalized to input power and combined in a sum of magnitude sense, as in reference [10]. Figure 1 of the supplementary material shows the results of these simulations.

The black ellipse represents a region with comparable dimensions to the heart of human model Duke. The sagittal and coronal slices clearly indicate that the array with two loops has a larger field of view. When looking at the SNR ratio in the central transverse slice, it can be seen that SNR increases only by a maximum of 10%, and even decreases closer to the coil elements. However, the central coronal and sagittal slices show that when moving away from the central slice, the SNR increases are strong (up to 50%) because of the larger field of view of the antennas. This is beneficial for cardiac imaging, which typically has a relatively large field-of-view.

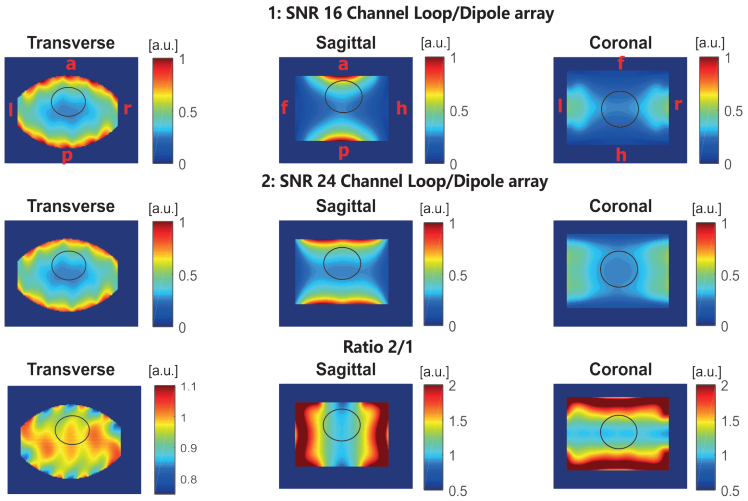

Figure S1: simulated SNR for an 8 dipole/8 loop array and an 8 dipole/16 loop array. The dimensions of the phantom are 450*300*236 mm3. The black ellipse represents a region comparable in size to the heart of virtual family model Duke.

538843-L-bw-Steensma
Processed on: 17-12-2019
PDF page: 84

References

[1] M. J. Versluis, J. J. M. Westenberg, N. B. Smith, M. Stuber, A. De Roos, and A. G. Webb, "Right Coronary MR Angiography at 7 T : A Direct Quantitative and Qualitative Comparison with 3 T in Young Healthy Volunteers," *Radiology*, vol. 257, no. 1, pp. 1527–1315, 2010.

[2] A. J. E. Raaijmakers *et al.*, "Comprehensice coronary artery imaging at 7.0 T: Proof of feasibility," *Proc. 22th Sci. Meet. Int. Soc. Magn. Reson. Med. Milan, 3660*, vol. 7, p. 4923, 2014.

[3] T. Niendorf *et al.*, "W(h)ither human cardiac and body magnetic resonance at ultrahigh fields?technical advances , practical considerations , applications , and clinical opportunities," *NMR Biomed.*, vol. 29, no. 9, pp. 1173–97, 2016.

[4] M. A. Dieringer, F. Hezel, and L. Winter, "Progress and promises of human cardiac magnetic resonance at ultrahigh fields : A physics perspective," *J. Magn. Reson. Imaging*, vol. 229, pp. 208–22, 2013.

[5] F. Von Knobelsdorff-Brenkenhoff *et al.*, "Cardiac chamber quantification using magnetic resonance imaging at 7 Tesla-a pilot study," *Eur. Radiol.*, vol. 20, no. 12, pp. 2844–2852, 2010.

[6] A. Brandts *et al.*, "Quantitative assessment of left ventricular function in humans at 7 T," *Magn. Reson. Med.*, vol. 64, no. 5, pp. 1472–1478, 2010.

[7] F. von Knobelsdorff-Brenkenhoff *et al.*, "Assessment of the right ventricle with cardiovascular magnetic resonance at 7 Tesla," *J. Cardiovasc. Magn. Reson.*, vol. 15, no. 1, p. 1, 2013.

[8] C. J. Snyder *et al.*, "Initial results of cardiac imaging at 7 Tesla," *Magn. Reson. Med.*, vol. 61, no. 3, pp. 517–524, 2009.

[9] A. J. E. Raaijmakers *et al.*, "The fractionated dipole antenna: A new antenna for body imaging at 7 Tesla," *Magn. Reson. Med.*, vol. 75, no. 3, pp. 1366–1374, 2016.

[10] M. A. Ertürk, A. J. E. Raaijmakers, G. Adriany, K. Ugurbil, and G. J. Metzger, "A 16-channel combined loop-dipole transceiver array for 7 Tesla body MRI," *Magn. Reson. Med.*, vol. 00, pp. 1–11, 2016.

[11] I. J. Voogt *et al.*, "Combined 8-channel transceiver fractionated dipole antenna array with a 16-channel loop coil receive array for body imaging at 7 Tesla," *Proc. 23th Sci. Meet. Int. Soc. Magn. Reson. Med. Vancouver*, vol. 200, no. 2007, p. 631, 2015.

[12] A. Graessl *et al.*, "Modular 32-channel transceiver coil array for cardiac MRI at 7.0T," *Magn. Reson. Med.*, vol. 72, no. 1, pp. 276–290, 2014.

[13] C. Oezerdem *et al.*, "16-channel bow tie antenna transceiver array for cardiac MR at 7.0 tesla," *Magn. Reson. Med.*, vol. 75, no. 6, pp. 2553–2565, 2016.

[14] S. Schmitter *et al.*, "Cardiac imaging at 7 tesla: Single- and two-spoke radiofrequency pulse design with 16-channel parallel excitation," *Magn. Reson. Med.*, vol. 70, no. 5, pp. 1210–1219, 2013.

[15] F. Padormo, A. Beqiri, J. V. Hajnal, and S. J. Malik, "Parallel transmission for ultrahigh-field imaging," *NMR Biomed.*, vol. 29, no. 9, pp. 1145–1161, 2016.

[16] B. R. Steensma *et al.*, "DREAM-based B1-shimming for cardiac imaging at 7 T," *Proc. 9th Sci. Meet. Int. Soc. Magn. Reson. Med. Benelux Chapter, Tilbg.*, 2017.

[17] S. Orzada, M. E. Ladd, and A. K. Bitz, "A method to approximate maximum local SAR in multichannel transmit MR systems without transmit phase information," *Magn. Reson. Med.*, vol. 00, 2016.

538843-L-bw-Steensma
Processed on: 17-12-2019
PDF page: 85

[18] F. Meliado, E., A. J. E. Raaijmakers, P. R. Luijten, and C. A. T. van den Berg, "Fast method to get an upper bound of the maximum SAR10g for body coil arrays," *Proc. 9th Sci. Meet. Int. Soc. Magn. Reson. Med. Benelux Chapter, Tilbg.*, p. p-070, 2017.

[19] D. W. Klomp *et al.*, "31P MRSI and 1H MRS at 7 T: initial results in human breast cancer," *NMR Biomed.*, vol. 24, no. 10, pp. 1337–1342, 2011.

[20] G. C. Wiggins *et al.*, "Mixing loops and electric dipole antennas for increased sensitivity at 7 Tesla," in *In: Proceedings of the 21th scientific meeting, International Society for Magnetic Resonance in Medicine, Salt Lake City*, 2013, vol. 21, p. 2737.

[21] G. C. Wiggins, B. Zhang, R. Lattanzi, G. Chen, and D. K. Sodickson, "The Electric Dipole Array : An Attempt to Match the Ideal Current Pattern for Central SNR at 7 Tesla," *Proc. 20th Sci. Meet. Int. Soc. Magn. Reson. Med. Melb.*, vol. 23, no. 2008, p. 541, 2012.

[22] R. Sodickson, Daniel K., Wiggins, Graham C., Chen, Gang, Karthik, Lakshmanan, Lattanzi, "More than meets the eye: The mixed character of electric dipole coils, and implications for high-field performance," *Proc. 24th Sci. Meet. Int. Soc. Magn. Reson. Med. Singapore*, p. 0398, 2016.

[23] B. J. Wintersperger *et al.*, "Cardiac CINE MR imaging with a 32-channel cardiac coil and parallel imaging: Impact of acceleration factors on image quality and volumetric accuracy," *J. Magn. Reson. Imaging*, vol. 23, no. 2, pp. 222–227, 2006.

[24] A. Kumar and P. A. Bottomley, "Optimized quadrature surface coil designs," pp. 41–52, 2008.

[25] A. J. E. Raaijmakers, P. R. Luijten, and C. A. T. van den Berg, "Dipole antennas for ultrahigh-field body imaging: a comparison with loop coils," *NMR Biomed.*, vol. 29, no. 9, pp. 1122–1130, 2016.

[26] A. C. and W. K. and E. G. H. and K. H. and M. Z. and E. N. and W. R. and R. J. and W. B. and J. C. and B. K. and P. S. and H.-P. H. and J. Kuster, "The Virtual Family—development of surface-based anatomical models of two adults and two children for dosimetric simulations," *Phys. Med. Biol.*, vol. 55, no. 2, p. N23, 2010.

[27] IEC, "Medical electrical equipment. Part 2-33: particular requirements for the safety of magnetic resonance equipment for medical diagnosis.," *IEC 60601-2-33*, 2015.

[28] K. Nehrke and P. Boernert, "DREAM-a novel approach for robust, ultrafast, multislice B1 mapping," *Magn. Reson. Med.*, vol. 68, no. 5, pp. 1517–1526, 2012.

[29] G. J. Metzger *et al.*, "Local B1+ shimming for prostate imaging with transceiver arrays at 7T based on subject-dependent transmit phase measurements," *Magn. Reson. Med.*, vol. 59, no. 2, pp. 396–409, 2008.

[30] K. Van De Moortele, PF ;Snyder , C ;Delabarre, L; Adriany, G; Vaughan, T; Ugurbil, "Calibration Tools for RF Shim at Very High Field with Multiple Element RF Coils: From Ultra Fast Local Relative Phase to Absolute Magnitude B1+ Mapping," *Ismrm*, vol. 15, p. 1, 2007.

[31] M. L. McHugh, "Interrater reliability: the kappa statistic," *Biochem. Medica*, vol. 22, no. 3, pp. 276–282, Oct. 2012.

[32] P. M. Robson, A. K. Grant, A. J. Madhuranthakam, R. Lattanzi, D. K. Sodickson, and C. A. McKenzie, "Comprehensive Quantification of Signal-to-Noise Ratio and g-Factor for Image-Based and k-Space-Based Parallel Imaging Reconstructions," *Magn. Reson. Med.*, vol. 60, no. 4, pp. 895–907, Oct. 2008.

[33] F. Meliado, E., A. J. E. Raaijmakers, M. Restivo, M. Maspero, P. R. Luijten, and C. A. T. van den Berg, "Database Construction for Local SAR Prediction: Preliminary Assessment of the Intra

538843-L-bw-Steensma
Processed on: 17-12-2019
PDF page: 86

and Inter Subject SAR Variability in Pelvic Region," in *In: Proceedings of the 24th scientific meeting, International Society for Magnetic Resonance in Medicine, Singapore, 3660*, 2016.

[34] A. Sbrizzi, H. Hoogduin, J. J. Lagendijk, P. Luijten, G. L. G. Sleijpen, and C. A. T. Van Den Berg, "Fast design of local N-gram-specific absorption rate-optimized radiofrequency pulses for parallel transmit systems," *Magn. Reson. Med.*, vol. 67, no. 3, pp. 824–834, 2012.

[35] J. Lee, M. Gebhardt, L. L. Wald, and E. Adalsteinsson, "Local SAR in parallel transmission pulse design," *Magn. Reson. Med.*, vol. 67, no. 6, pp. 1566–1578, 2012.

[36] U. Katscher and P. Boernert, "Parallel RF transmission in MRI," *NMR Biomed.*, vol. 19, no. 3, pp. 393–400, 2006.

[37] L. Winte *et al.*, "Comparison of three multichannel transmit/receive radiofrequency coil configurations for anatomic and functional cardiac MRI at 7.0T: Implications for clinical imaging," *Eur. Radiol.*, vol. 22, no. 10, pp. 2211–2220, 2012.

[38] A. Gräßl *et al.*, "Design, evaluation and application of an eight channel transmit/receive coil array for cardiac MRI at 7.0 T," *Eur. J. Radiol.*, vol. 82, no. 5, pp. 752–759, 2013.

[39] C. Thalhammer *et al.*, "Two-Dimensional sixteen channel transmit/receive coil array for cardiac MRI at 7.0 T: Design, evaluation, and application," *J. Magn. Reson. Imaging*, vol. 36 (4), pp. 847–854, 2012.

538843-L-bw-Steensma
Processed on: 17-12-2019
PDF page: 87

Chapter 6

SAR and Temperature Distributions in a Database of Realistic Human Models for 7T Cardiac Imaging

Bart R. Steensma
Ettorè F. Meliado
Peter R. Luijten
Cornelis A.T. van den Berg
Dennis W.J. Klomp
Alexander J.E. Raaijmakers

Submitted to:
Magnetic Resonance in Medicine

Abstract

Purpose

To investigate inter-subject variability of SAR and temperature rise in a database of human models for a 7T cardiac array, and to investigate temperature rise during a breath-hold acquisition.

Methods

DIXON images were acquired of 14 subjects and segmented in dielectric models with a 7T cardiac array in place. EM simulations were done to calculate SAR distributions. Based on the SAR distributions, temperature simulations were performed for an exposure time of 6 minutes (IEC averaging time) and 20 seconds (upper-limit for breath-hold in cardiac exam). Peak local SAR and temperature rise levels were calculated for different RF shim settings. A statistical analysis of resulting peak local SAR and temperature rise levels was performed to arrive at safe power limits.

Results

For random RF shim vectors, a safe average power limit of 4.2 W/channel was determined (1st level controlled mode). When RF shimming is applied, a safe average power limit of 5.0 W/channel was found. When adhering to the local SAR limits, the absolute local temperature limit of 40 ^{0}C will not be exceeded. For a heating time of 20 seconds, worst-case temperature rise remains within 0.34 ^{0}C when adhering to the SAR limits.

Conclusion

Safe power constraints were found for a 7T cardiac array while considering inter-subject variability. For a heating period of 20 seconds, temperature rise remains very limited when adhering to the local SAR limit. Therefore, the double SAR limit that is allowed for a 10 second scan is also safe for a 20 second scan.

538843-L-bw-Steensma
Processed on: 17-12-2019
PDF page: 89

Introduction

The improved signal-to-noise ratio at 7T allows for cardiac magnetic resonance (CMR) imaging at increased resolution as compared to 1.5T or 3T [1]–[3]. Many sequences that are common for CMR at 1.5T or 3T, such as balanced SSFP or inversion recovery sequences, require a high flip angle and/or a short repetition time [4] which leads to high RF power deposition. Because of higher power requirements at 7T compared to 1.5T or 3T [5], [6] and because local transmit arrays are used instead of a volume body coil enforcing local SAR limitations, power limits are more stringent at 7T. Therefore, next to banding artifacts due to increased B_0-inhomogeneity, it is because of these more stringent power constraints that these standard CMR sequences are not easily applicable at 7T.

7T cardiac imaging is typically done using a local transmit (Tx) array. These arrays typically consist of multiple phase/amplitude controlled transmit channels. The use of a local Tx array requires subject specific calibration of the phases and amplitudes (RF shimming) to acquire an efficient and uniform transmit field in the heart. To ensure that the patient is not exposed to severe local tissue heating, the local SAR is used as a metric for RF power deposited by a local transmit array. The peak local SAR level cannot exceed predefined limits, which are described by the IEC [7]. As also described by the IEC, local SAR is averaged over cubes containing a total mass of 10g. Since local SAR cannot be measured, average power limits are typically derived from electromagnetic simulations (using e.g the finite difference time domain (FDTD) method) on generic human models[8]. These generic human models normally do not match the geometry of the subject in the scanner, therefore an additional safety factor needs to be used which accounts for inter-subject variability. This safety factor ensures that peak local SAR limits are never exceeded when the patient anatomy does not match the anatomy of the simulation model, but often leads to severe overestimation of the actual peak local SAR resulting in overly conservative power constraints and increased examination time.

Inter-subject variability has a strong influence on peak SAR levels for various imaging targets at 7T. Previous studies have investigated inter-subject variability for multi-transmit head imaging [9], [10]. De Greef et al [9] investigated SAR levels for 6 different head models of the virtual family and virtual classroom, these models originated from manual segmentation. Le Garrec and Boulant et al [10] used an in-house generated, surface based head model to generate a database of 33 transformed head models. From this database, it was possible to sample the parameter space of head length, breadth and shift in the Z- and Y-direction following an unscented transform scheme. Peak SAR values were calculated for

538843-L-bw-Steensma
Processed on: 17-12-2019
PDF page: 90

several RF excitation schemes. For body imaging at 7T, inter-subject variability of SAR has been studied for two dipole arrays in a prostate imaging setup [11], [12]. Ïpek et al studied inter-subject variability of peak local SAR for the single-side adapted dipole array on four different dielectric models [12], [13] which were generated from manual segmentation of DIXON scans with the 7T transmit array in place. More recently, Meliado et al. presented a more rigorous approach where an automated pipeline was created to generate a simulation model from a DIXON scan with a mock-up array and landmarks in place. Using this method, 23 custom-built dielectric models were simulated for the fractionated dipole array to derive power limits for RF shimming on the prostate or for pTx pulses [11].

Similar studies for 7T cardiac imaging are currently still missing. Therefore, the first aim of this work is to investigate inter-subject variability for cardiac imaging at 7T in a database of custom-built dielectric models, using an approach similar to the one used by Meliado et al [11]. A probabilistic analysis of 10g averaged peak local SAR levels for different RF shim phases and subjects is applied to arrive at local SAR levels that have a probability of less than 0.1% of being exceeded ($pSAR_{99}$). These local SAR levels are then used to derive average power limits on a per channel basis.

The second aim of this work is to extend the SAR analysis by also incorporating temperature simulations. Similar studies have been done before for brain imaging [14]–[16], but not for 7T body imaging. The temperature simulations were done for heating intervals that are relevant to cardiac imaging. SAR limits are defined related to time averaged power which is normally averaged over a time window of 6 minutes. In the first level controlled mode, 10g averaged peak local is SAR is allowed to be 20 W/kg. When the averaging time is shorter than 10 seconds, SAR is allowed to be two-fold higher (40 W/kg, first level controlled mode). A CMR acquisition is often acquired during breath-hold, which takes no longer than 20 seconds and is followed by a pause to allow for subject recovery and sometimes additional planning. Neither the 10 seconds averaging time or the 6 minutes averaging time corresponds to this scenario. To be able to suggest alternative metrics for determining power limits for the specific scenario of a breath-hold, the actual temperature rise during CMR needs to be investigated. Therefore, thermal simulations have been done using the subject specific SAR-distributions as an input. This was done for a heating interval of 20 seconds (upper-limit acquisition time for a breath-hold), and for the 6 minutes averaging interval that is specified in the IEC guidelines.

538843-L-bw-Steensma
Processed on: 17-12-2019
PDF page: 91

Methods

Model generation

After obtaining IRB approval and written informed consent from each subject, 14 subjects (age: 25-54, BMI: 18-26) were scanned at 1.5T (Philips Ingenia, Philips Healthcare, Best The Netherlands) with a mockup array in place to achieve realistic body deformation. A multi-echo DIXON scan (TR/TE1/TE2 = 5.56/1.64/3.76 ms, resolution 1.7x1.7x2.5mm^3) was acquired to calculate water, fat, in-phase and out-of-phase images which were segmented [17] into 4 tissue types. The 4 tissues were assigned with the following electrical and thermal properties [18]:

Tissue type		Relative Permittivity [a.u.]	Specific Heat Capacity [J/kg/K]	Thermal	Heat	Perfusion Rate [kg/m^3/s]	Mass Density [kg/m^3]
Muscle	0.77	58.22	3421	0.495	0.9061	0.71	1090.4
Fat	0.08	11.75	2348	0.2115	0.5066	0.53	911
Skin	0.64	49.89	3391	0.3722	1.648	2.1	1109
Lung	0.36	24.80	3886	0.3874	6.209	7.44	394

Table 1: electric and thermal tissue parameters of muscle, fat, skin and lung tissue from the ITIS database[18].

The validity of a 3 tissue model (lung, muscle and fatty tissue) versus a full dielectric model was demonstrated before for local SAR [12], [19], [20]. For temperature, it was found necessary to also include skin (leading to a 4 tissue model) in the model. Skin has a high perfusion rate and significantly affects local temperature[21]. As an additional validation step, SAR and thermal simulations were done for this specific cardiac array, showing no difference in peak SAR and temperature rise (figure S1 and S2). Local temperature rise in the heart is slightly overestimated for the 4 tissue model because the full model has higher perfusion values in blood and heart muscle.

EM-simulations

Simulation settings

Finite difference time domain simulations were done in Sim4Life (Zurich MedTech, Zurich, Switzerland) to calculate EM-field distributions in the segmented body model. An 8 channel dipole array was modelled as the transmit coil [3], [22]. The 8 dipole antennas were tuned and matched with 2 series capacitors of 18 pF. All models were voxelized with an adaptive grid using a maximum resolution of 0.7x0.7x0.7 mm^3, resulting in approximately 30 million voxels per model. Similar to the work of Boulant et al. [15], all simulation results were regridded

538843-L-bw-Steensma
Processed on: 17-12-2019
PDF page: 92

to a 4x4x4 mm^3 rectangular grid to make SAR and temperature calculation less computationally demanding. The electric fields for every transmit channel were filtered with a 3x3x3 median filter, to remove spikes due to stair-casing errors in the FDTD simulations [15]. 10g averaged Q-matrices [23], [24] and virtual observation points were extracted for every model to enable rapid calculation of peak SAR levels for arbitrary RF shims [25]. To enable fast calculation of virtual observation points and to minimize the number of virtual observations points, the generalized VOP method as described by Lee et al. [26] was implemented, in combination with the acceleration method demonstrated by Kuehne et al. [27]

Peak SAR analysis

A statistical analysis on the distribution of peak SAR levels was performed by calculating peak SAR values for every subject for 10.000 random RF shims (14 subjects in total, 140.000 random RF shims). By doing so, the full parameter space that determines peak SAR levels in MR experiments could be sampled. Peak SAR was calculated for randomly distributed transmit phases (range between 0 and 2π, according to a uniform distribution). Input power was set as 1W on each channel, but the uncertainty in the readout of directional couplers was included by selecting the input power of each channel from a normal distribution $N(\mu=1,\sigma=0.064)$, which results in a power between 0.78 and 1.21 W in 99.9% of all RF shims. This corresponds to a 10% uncertainty in the voltage measurements of the directional couplers[28]. Results of the SAR calculations are plotted in a histogram of peak SAR values for all volunteers and all random RF shims together (140.000 in total), similar to the histograms shown in the work of Meliado et al[11]. The resulting distribution corresponds to a gamma distribution, for which a shape-parameter k and a scale parameter θ can be fitted. By fitting a distribution to the histogram data, it is possible to make statistical predictions on the SAR levels over the entire population. In this case, we can define a peak local SAR level that has a probability of less than 0.1% of being exceeded for any subject and any RF shims. This SAR level will be referred to as the $pSAR_{99}$ level.

Temperature simulations

Temperature simulation settings

Temperature rise in the human body as a result of exposure to a SAR distribution can be modelled using Pennes' Bioheat equation[29]: Where ϱ is mass density (W/kg), c_p is the specific heat capacity (J/kg/K), k is the thermal conductivity (W/K/m), Wb is the blood perfusion constant (kg/m3/s), c_b is the blood specific heat capacity (J/kg/K), C is the metabolic heat generation (W/m3) and finally ϱSAR is the heat generation from external sources. Pennes

538843-L-bw-Steensma
Processed on: 17-12-2019
PDF page: 93

bioheat equation can be separated into an equilibrium temperature component (T00) which remains constant and a temperature rise component (Trise)[15], [16], [30]. If the equilibrium temperature T00 is known, the final temperature can be calculates as T=T00+Trise. The temperature rise component can be modelled as following:

$$\rho c_p \frac{\delta T}{\delta t} = \nabla \cdot k \nabla T + W_b c_b \left(T_b - T\right) + C + \rho SAR \quad [1]$$

$$\rho c_p \frac{\delta T_{rise}}{\delta t} = \nabla \cdot k \nabla T_{rise} + W_b c_b \left(-T_{rise}\right) + \rho SAR \quad [2]$$

For a multi-channel transmit array, the SAR distribution of all combined channels given an RF shim vector v can be expressed using the Q-matrix formalism:

$$SAR = \frac{\sigma}{2\rho} \boldsymbol{v}^{\boldsymbol{H}} \boldsymbol{Q} \boldsymbol{v} \quad [3]$$

In equation 3, the Q-matrix has size N*N, where N is the number of transmit channels and every entry of the Q-matrix corresponds to a certain combination of transmit channels. Since the solution of equation 2 scales linearly with SAR, the temperature rise can be expressed with a similar formalism:

$$T_{rise} = \boldsymbol{v}^{\boldsymbol{H}} \boldsymbol{T}_{\boldsymbol{rise}} \boldsymbol{v} \quad [4]$$

The entries of Trise correspond to a single solution of the Pennes' bioheat equation that is found for every combination of transmit channels i,j:

$$\boldsymbol{T}_{\boldsymbol{rise}} = \begin{pmatrix} T_{1,1} & \cdots & T_{1,N} \\ \vdots & \ddots & \vdots \\ T_{N,1} & \cdots & T_{N,N} \end{pmatrix} \quad [5]$$

$$\rho c_p \frac{\delta T_{rise,i,j}}{\delta t} = \nabla \cdot k \nabla T_{rise,i,j} + W_b c_b \left(-T_{rise,i,j}\right) + \rho SAR_{i,j} \quad [6]$$

Equation 6 can be solved for every combination of transmit channels (i,j) and a pre-defined heating interval to fill the entries of the Trise matrix. Equation 4 can

538843-L-bw-Steensma
Processed on: 17-12-2019
PDF page: 94

then be used to calculate temperature rise quickly for every RF shim vector v. A Matlab based online available temperature solver[31], [32] was used to solve Pennes Bioheat Equation for every entry of the Q-matrix to obtain a temperature matrix Trise for every model. Pennes Bioheat equation was solved for a total heating time of 20 seconds which corresponds to an upper-limit breath-hold time and 6 minutes which is the conventional averaging time in safety guidelines[7] where temperature equilibrium has been realized. Based on the temperature matrix, temperature VOPs were derived for rapid calculation of temperature rise for different RF shim drives[15], [30]. To derive the temperature VOPs, the same algorithm was used as for derivation of VOPs from the SAR Q-matrices.

Peak ΔT temperature analysis

Since the resulting temperature rise matrix Trise depends strongly on the defined heating interval, temperature simulations were done separately for the two heating intervals (20 seconds and 6 minutes). Additionally, for the 20 seconds case, a worst-case scenario was considered where no perfusion or heat conduction was present. Based on the simulated Trise matrices, temperature VOPs[15], [30] were calculated for the three different heating scenarios. Based on the temperature VOPs, peak ΔT values were calculated for the same 10,000 random RF shims as were used in the SAR analysis for all 14 volunteers. The resulting ΔT values were plotted as histograms for all volunteers and RF shims together, which were used to fit gamma-distributions in order to do a probabilistic analysis of peak ΔT values. For all models, a peak ΔT value was found that has a chance of less than 0.1% of being exceeded for a random RF shims (pΔT99). The final result of this procedure was three ΔT histograms and three fitted pΔT99 values (pΔT99,20s, pΔT99,20s,WC and pΔT99,6 min).

RF shimmed SAR and temperature analysis

Based on the simulated per-channel B1+ distributions, a subject specific RF shim drive was determined for every subject to obtain constructive phase interference in a 10 cm3 cube region of interest centered on the heart. For these specific RF shims, B1+, SAR10g and ΔT distributions were calculated on all volunteers. The similarity between these RF shims was evaluated by polar plots. The distribution of optimal RF shim for the entire patient population is likely not fully covered by the 14 RF shims that resulted from this analysis. Therefore, to mimic the effect of variations in the RF shims over the patient population, 10.000 random perturbations of the RF shim vector were calculated for every subject. Input power was varied randomly according to a normal distribution N(μ=1,σ=0.064), which results in a power between 0.78 and 1.21 W in 99.9% of all RF shims. This

538843-L-bw-Steensma
Processed on: 17-12-2019
PDF page: 95

corresponds to a 10% uncertainty in the voltage measurements of the directional couplers[28]. Phase was varied between -5^0 and +5^0, according to a normal distribution around the optimal shim phase (N, μ=0, σ=0.0266). Results will show that the similarity between the 14 optimal RF shims is large. This suggests that one generic phase setting could be used. The B1+ distributions and local SAR distributions for all models using such a generic RF shim vector is also investigated and compared to the subject-specific RF shims.

Correlation between peak SAR10g and ΔT

As a result of the SAR and temperature analysis in sections 2.2 and 2.3, peak SAR10g and ΔT values are calculated for a total of 140.000 RF shims (using each time the same RF shim to calculate peak SAR10g and ΔT). As a final sanity check, the correlation (Pearson Correlation coefficient, calculated using Matlab) between peak SAR10g and peak ΔT was evaluated by combining all 10,000 x 14 pSAR10g and pΔT values in a scatter plot.

Results

Model generation

Figure 1 shows the segmented body models for all volunteers, including BMI, sex and age.

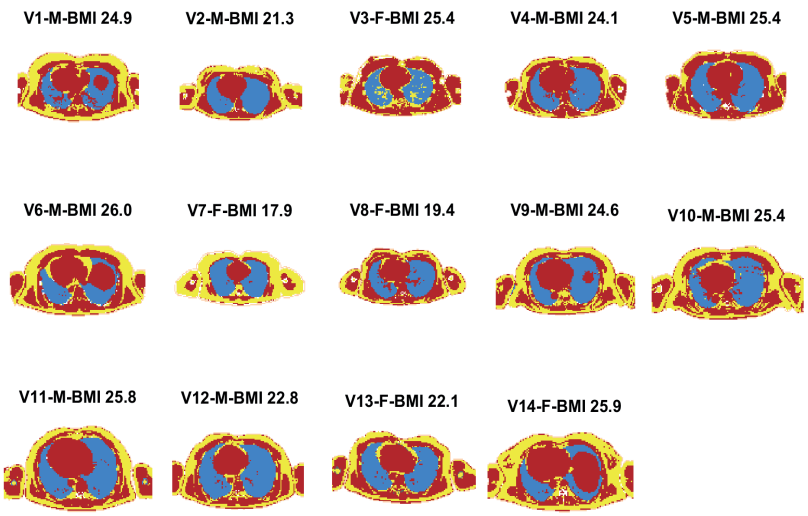

Figure 1: segmented models for every subject. Muscle indicated in red, fat in yellow, lung in blue and skin in light-brown.

538843-L-bw-Steensma
Processed on: 17-12-2019
PDF page: 96

EM-simulations

Figure 2 shows resulting peak SAR10g values for all volunteers for 10,000 random RF shims per model (a), and a histogram (b) of these SAR10g values for all 14 models. A gamma distribution was fitted to the histogram, which was then used to calculate the peak SAR10g value which is not exceeded for 99.9% of all RF shims. The resulting pSAR99 value is 4.8 W/kg. The average SAR value is 2.8 W/kg, which indicates that the pSAR99 value overestimate the average SAR by 71%.

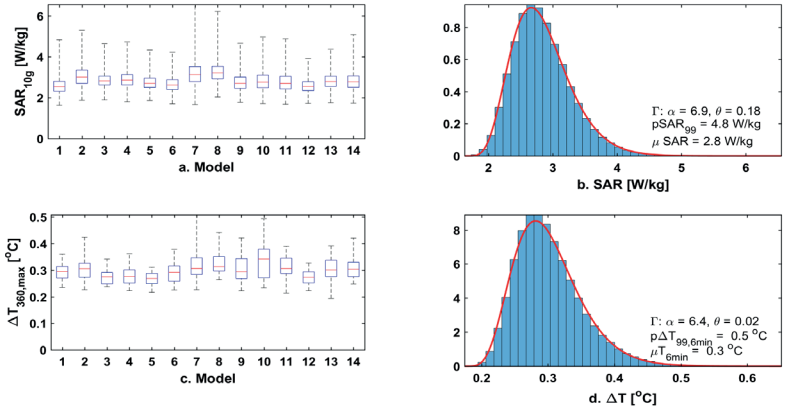

Figure 2: 2a shows peak SAR10g values for 10,000 random RF shims with an average power of 1W per channel , specified for every model. 2b shows a histogram with peak SAR10g values in all volunteers, resulting from 10,000 random RF shims. A gamma distribution was fitted to the SAR histogram (indicated in red). 2c and d show the same results, but for temperature rise.

Temperature simulations

Figure 2c shows the peak temperature rise ΔT6 min, resulting from 10,000 random RF shims. The fitted gamma distribution (2d.) results in a pΔT99,6 min value of 0.5 ^{0}C. Figure 3 shows the same distribution for a 20 seconds heating interval with perfusion and heat diffusion included (a and b, pΔT99,20 = 0.07 ^{0}C) and without perfusion or heat diffusion (c and d, pΔT99,20 = 0.08 ^{0}C)..

538843-L-bw-Steensma
Processed on: 17-12-2019
PDF page: 97

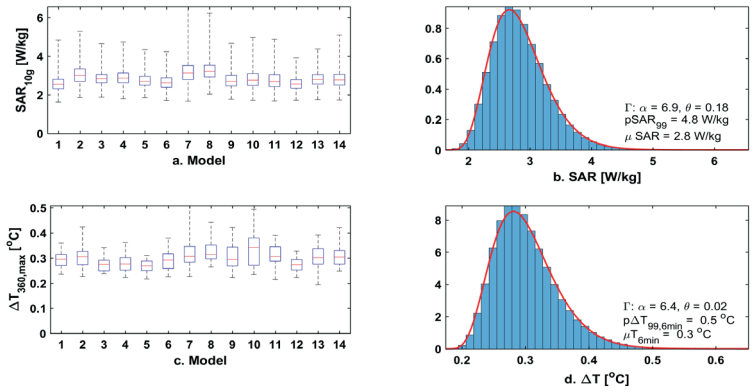

Figure 3: 3a shows peak ΔT values, resulting from a heating interval of 20 seconds for 10,000 random RF shims, specified for every model. 3b shows a histogram with peak ΔT values in all volunteers, resulting from 10,000 random RF shims. A gamma distribution was fitted to the histogram to find a ΔT value that is not exceeded for 99.9% of all RF shims. Figures c and d show the same data, without incorporating perfusion and heat conduction in the model.

RF shimmed SAR and temperature analysis

Figure 4 (top) shows the transmit phase for every channel when RF shimming is applied on the heart ROI, for all volunteers and averaged over all volunteers.

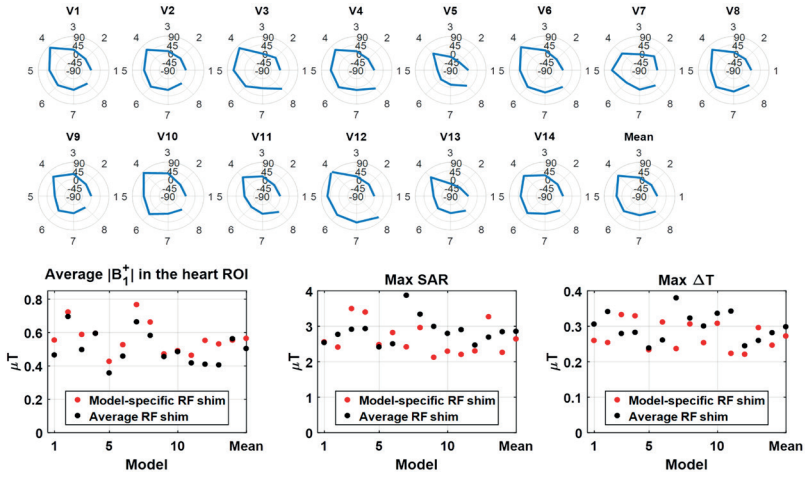

Figure 4: (top) transmit phase (displayed between -90 and 90 degrees) for every transmit channel (1 to 8) to obtain phase coherence in a 10 cm3 cubical region of interest centered the heart. An average input power of 1W was applied to every transmit channel. Data is displayed for every volunteer and averaged over all volunteers. (bottom) B1+, peak SAR and peak ΔT values for the model-specific and average RF shims.

Transmit phases are in general very similar for all volunteers. Figure 4 (bottom)

538843-L-bw-Steensma
Processed on: 17-12-2019
PDF page: 98

shows average B1+ in the ROI, peak SAR and peak ΔT values compared for the subject-specific RF shim drive and the averaged RF shim. Average B1+ decreases from 0.56 μT to 0.50 μT (-11%), peak SAR increases from 2.6 to 2.9 W/kg (+11%) while peak ΔT increases from 0.27 to 0.29 ^{0}C (+7%). Figure 5,6 and 7 show respectively the B1+-fields, the SAR10g distributions and the ΔT distributions when applying subject specific RF shims.

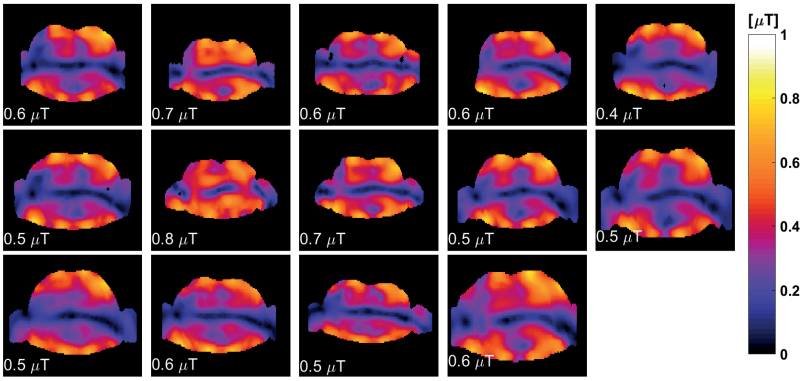

Figure 5: Transverse center slice of the B1+-field for every subject, after application of RF shimming on the white ROI in the heart. An average input power of 1W was applied to every transmit channel. Average B1+ in the ROI is distributed below the field distribution.

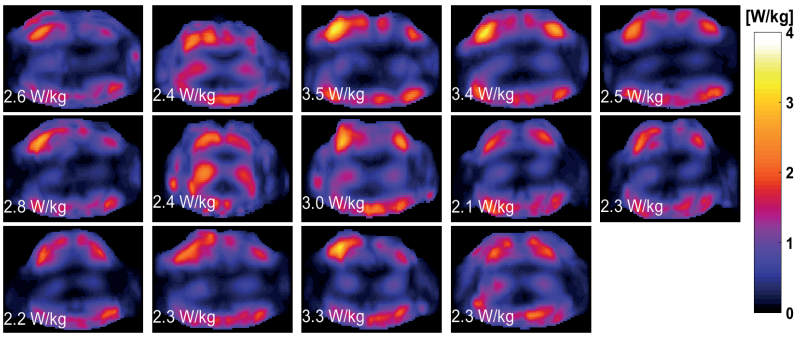

Figure 6: Transverse maximum intensity projection of the SAR10g distribution and the peak SAR10g value for every subject after application of RF shimming. An average input power of 1W was applied to every transmit channel.

538843-L-bw-Steensma
Processed on: 17-12-2019
PDF page: 99

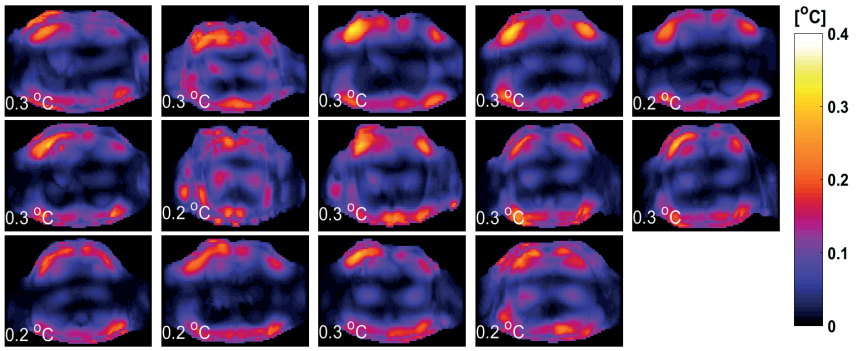

Figure 7: Transverse maximum intensity projection of the peak ΔT value for every subject after application of RF shimming. An average input power of 1W was applied to every transmit channel.

Highest average B1+ in the heart is observed in volunteer 7 (0.8 μT). The highest SAR and peak ΔT values are observed in volunteer 3 (3.5 W/kg and 0.3 ^{0}C). The same distributions, but for the averaged RF shim are added as supplementary material (S2). Figure 8 shows histograms of the peak SAR and ΔT values that were observed for random perturbations on the RF shimmed RF shims. A Gaussian distribution was fitted to both histograms, resulting in a distribution N(μ=2.94 W/kg, σ=0.36 W/kg) for SAR, and N(μ=0.30 ^{0}C. , σ=0.04 ^{0}C.) for ΔT. A pSAR99 of 4.0 W/kg is observed, which overestimates the average SAR of 2.94 W/kg by 36%. A pΔT99 of 0.4 ^{0}C is found, which overestimates the average shimmed ΔT of 0.3 ^{0}C by 33%.

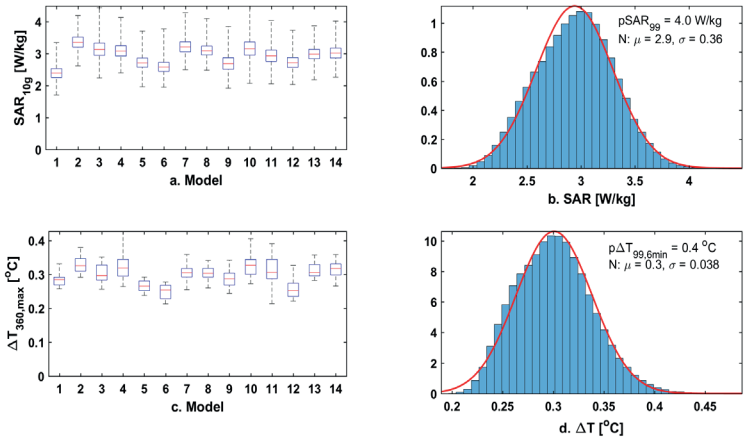

Figure 8: SAR and temperature distributions for a RF shim that is shimmed on the heart. For every volunteer, 10.000 shim vectors were calculated which are random perturbations on the optimal RF shims.

538843-L-bw-Steensma
Processed on: 17-12-2019
PDF page: 100

Correlation between peak SAR10g and ΔT

Figure 9 shows the correlation between peak SAR10g and peak ΔT values for the same RF shims. A strong correlation (Pearson correlation coefficient, r=0.81) is observed between the 10g-averaged SAR values and the ΔT values.

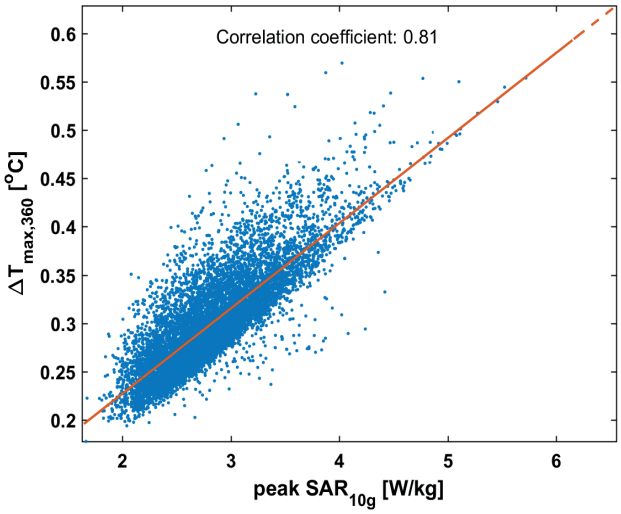

Figure 9: Peak ΔT values for a heating time of 6 minutes plotted versus peak 10g-averaged local SAR values for the same RF shim drives.

Discussion

The inter-subject variability of SAR and temperature distributions was determined for cardiac imaging at 7T for an 8-channel fractionated dipole array. A database of 14 dielectric models with realistic body deformation was generated from DIXON-images and simulated in Sim4life. Virtual observation points were calculated for every model and were used to calculate peak SAR values for 10.000 random RF shim settings per model, taking into account the uncertainty of measuring the average input power with directional couplers. When displaying the peak SAR values for all volunteers and RF shims in a histogram, the result is a distribution of SAR values which corresponds to a gamma distribution. The fitted gamma distribution results in a SAR value that is not exceeded for 99.9% of all random RF shim settings[11] (pSAR99). For this database, a pSAR¬99 of 4.8 W/kg is found (assuming random input phase and an uniform average input power of 1W (σ=0.064 W)). Considering a local SAR limit of 20 W/kg in 1st level controlled mode, an average power of 4.2W per channel is therefore not to be exceeded based on this analysis. If we evaluate a scenario where the phase

538843-L-bw-Steensma
Processed on: 17-12-2019
PDF page: 101

settings are not random but optimized for good B1+ coverage of the heart, the SAR levels are lower. An analysis including likely variation of the optimal shim phase and measurement inaccuracy of the directional couplers has resulted in a pSAR99 level of 4.0 W/kg. Similarly, this SAR level corresponds to an average power limit of 5.0 W per channel. Literature has shown that when calculating SAR limits based on one generic body model such as Duke or Ella, it is advised to take an additional safety factor into account to be robust for inter-subject variation and for variation in power measurements during the exam. For the random RF shims, a comparison of the average pSAR to the pSAR99 value shows an average overestimation of 71%, which would translate into a safety factor of 1.71. If RF shimming is done, the pSAR99 value overestimates the average pSAR by 36%, leading to safety factor of 1.36 In earlier studies, similar safety factors were reported for the prostate (1.7, Ipek et al[12], 1.8 random, Meliado et al.[11], 1.4 RF shimmed, Meliado et al.[11]) and the head (1.5, Le Garrec et al.[10], 1.4, De Greef et al[9]). Since the pSAR99 values resulting from this study include both inter-subject variability and power measurement inaccuracies, these additional safety factors do not need to be included for these uncertainties.

Pennes' Bioheat equation, combined with a post-processing step to rapidly combine multi-channel temperature simulation results were used to quickly calculate peak temperature rise values using 10,000 random RF shims for each of our 14 custom-built models. A probabilistic analysis of peak ΔT values was done for three scenarios (6 minutes, 20 seconds and 20 seconds without heat conduction or perfusion). The six minutes scenario accounts for the time over which power deposition is averaged according to the IEC guidelines. However, cardiac imaging is often performed using breath-hold scans. These breath-holds are always followed by time to recuperate which suggests that larger power limits may be appropriate. The 20 seconds time interval corresponds to an upper-limit for a realistic breath-hold in a cardiac exam. This interval was evaluated to assess the additional power that the patient can be exposed to safely in a typical breath-hold MRI investigation. Results from this second evaluation will result in a severe increase in the suggested power limit. Therefore, an additional more conservative scenario is evaluated where the subject is exposed for 20 seconds without heat conduction or perfusion.

For the 6 minutes heating interval and an average input power of 1W per channel, a $p\Delta T99$ value of 0.5 ^{0}C is found. When adhering to the local SAR limit, an average per channel input power of 4.2 W would be allowed. This implies that when adhering to the local SAR limits defined in first level controlled mode, the $p\Delta T99$ value would be equal to 2.1 ^{0}C. In the case of subject specific RF-shimming, a

538843-L-bw-Steensma
Processed on: 17-12-2019
PDF page: 102

pΔT99 value of 0.4 ^{0}C is found for 1W average power per channel. When adhering to the SAR-based average power limit of 5.0 W per channel, the pΔT99 value would also be 2.1 ^{0}C. As described by the IEC, local tissue temperature may not exceed 40 ^{0}C in the first level controlled mode. Even if the starting equilibrium temperature of the tissue in the VOP with maximum temperature rise is 37^{0}C, a local temperature of 40 ^{0}C will not be achieved when adhering to the SAR limits. It is important to note that all temperature distributions shown here refer to temperature rise (which scales linearly with input power), and not absolute temperature (not linear with input power). Since the equilibrium temperature is generally lower close to the surface of a subject, absolute temperature is likely overestimated by adding the temperature rise to a baseline temperature of 37^{0}C. Additionally, the thermoregulatory response (perfusion increases with temperature rise) is not taken into account in this model, which effectively results in considerable overestimation[33]–[35]. All simulations were done using perfusion values from literature. However, cases were subjects have a decreased perfusion response are not considered within the scope of this work.

For a heating interval of 20 seconds, a pΔT99 value of 0.07^{0}C is found for the full model and 0.08 ^{0}C is found for the case without perfusion or heat conduction present. It is expected that the short duration of the heating interval reduces the influence of heat conduction. Because the temperature rise remains relatively low the influence of perfusion is also relatively small. Therefore, the difference between the two temperature rise values remains low (14% higher temperature for the scenario without heat conduction or perfusion). Again, using a power limit of 4.2 W average power per channel, this translates to a temperature rise of 0.3 ^{0}C and 0.34 ^{0}C. In both cases, local tissue temperature will remain well below the 40 ^{0}C limit that is defined by the IEC. Alternative power limits for a 20s scan could be defined with respect to the resulting temperature rise. If a temperature rise of for example 1 ^{0}C would be allowed, very high average power limits could be allowed (12.5 W/channel for the scenario without heat conduction or perfusion). As a result, the SAR limit of 20 W/kg will be drastically exceeded which is therefore currently not implemented in practice. However, current IEC regulations allow for a SAR limit that is twice as high when the acquisition time does not exceed 10s. Based on the results shown in this work we would advocate that this increased SAR limit can also be advisable for a longer scan-time of 20 seconds. For this specific array and for any RF shim drive, a SAR limit of 40 W/kg would result in an allowable average input power of 8.4 W/channel. This would result in a pΔT99 value of 0.7 ^{0}C for a heating interval of 20 seconds in a worst-case scenario where no perfusion or heat conduction is present, and a pΔT99 value of 0.6 ^{0}C for the full Pennes Bioheat model. In the case that RF-shimming

538843-L-bw-Steensma
Processed on: 17-12-2019
PDF page: 103

is applied, an average input power of 10.0 W/channel could be allowed. The increased power limit is of course only recommended if the subject will spend at least 20 seconds between the scans recuperating from breath holds and no RF is administered during this time.

Conclusion

A database of 14 dielectric models was generated for RF safety assessment of a 7T cardiac array. A statistical approach was followed using 10,000 different RF shims on each model (once for random RF shims and once for a scenario where RF shimming is applied). Resulting peak SAR levels were used to assess the pSAR99 value: a SAR level that is not exceeded in 99.9% of the cases using 8x1 W average input power. The pSAR99 value is 4.8 W/kg and 4.0 W/kg for random RF shims and phase-shimmed RF shims. These values include inter-subject variability and directional coupler inaccuracies. In second level controlled mode, they correspond to per-channel power limits of 4.2 W and 5.0 W. Additionally, resulting SAR distributions were used for temperature simulations on the same models to study temperature rise during a cardiac exam. When adhering to the SAR limits as specified by the IEC in second level controlled mode, the local tissue temperature limit of 40 ^{0}C in first level controlled mode will not be exceeded. When considering a 20-second heating interval, which corresponds to an upper limit for a breath-hold in a cardiac exam, temperature rise remains very small when adhering to the SAR limit (0.34 ^{0}C). Based on these results, we conclude that the increased SAR limit that holds for scans shorter than 10 seconds, can also be applied for a scan of 20 seconds, if followed by an at least equally long recuperation period.

References

[1] C. Oezerdem et al., "16-channel bow tie antenna transceiver array for cardiac MR at 7.0 tesla," Magn. Reson. Med., vol. 75, no. 6, pp. 2553–2565, 2016.

[2] A. Graessl et al., "Modular 32-channel transceiver coil array for cardiac MRI at 7.0T," Magn. Reson. Med., vol. 72, no. 1, pp. 276–290, 2014.

[3] B. R. Steensma et al., "An 8-channel Tx/Rx dipole array combined with 16 Rx loops for high-resolution functional cardiac imaging at 7 T," Magn. Reson. Mater. Physics, Biol. Med., 2017.

[4] C. M. Kramer, J. Barkhausen, S. D. Flamm, R. J. Kim, and E. Nagel, "Standardized cardiovascular magnetic resonance (CMR) protocols 2013 update," J. Cardiovasc. Magn. Reson., vol. 15, no. 91, pp. 1–10, 2013.

[5] C. M. Collins et al., "Temperature and SAR calculations for a human head within volume and surface coils at 64 and 300 MHz," J. Magn. Reson. Imaging, vol. 19, no. 5, pp. 650–656, 2004.

[6] J. T. Vaughan et al., "7T vs. 4T: RF power, homogeneity, and signal-to-noise comparison in

538843-L-bw-Steensma
Processed on: 17-12-2019
PDF page: 104

head images," Magn. Reson. Med., vol. 46, no. 1, pp. 24–30, 2001.

[7] IEC, "Medical electrical equipment. Part 2-33: particular requirements for the safety of magnetic resonance equipment for medical diagnosis.," IEC 60601-2-33, 2015.

[8] A. C. and W. K. and E. G. H. and K. H. and M. Z. and E. N. and W. R. and R. J. and W. B. and J. C. and B. K. and P. S. and H.-P. H. and J. Kuster, "The Virtual Family—development of surface-based anatomical models of two adults and two children for dosimetric simulations," Phys. Med. Biol., vol. 55, no. 2, p. N23, 2010.

[9] M. De Greef, O. Ipek, A. J. E. Raaijmakers, J. Crezee, and C. A. T. Van Den Berg, "Specific absorption rate intersubject variability in 7T parallel transmit MRI of the head," Magn. Reson. Med., vol. 69, no. 5, pp. 1476–1485, 2013.

[10] M. Le Garrec, V. Gras, M. F. Hang, G. Ferrand, M. Luong, and N. Boulant, "Probabilistic analysis of the specific absorption rate intersubject variability safety factor in parallel transmission MRI," Magn. Reson. Med., 2017.

[11] E. F. Meliadò, C. A. T. van den Berg, P. R. Luijten, and A. J. E. Raaijmakers, "Intersubject specific absorption rate variability analysis through construction of 23 realistic body models for prostate imaging at 7T," Magn. Reson. Med., no. April 2018, pp. 2106–2119, 2018.

[12] Ö. Ipek, A. J. Raaijmakers, J. J. Lagendijk, P. R. Luijten, and C. A. T. Van Den Berg, "Intersubject local SAR variation for 7T prostate MR imaging with an eight-channel single-side adapted dipole antenna array," Magn. Reson. Med., vol. 71, no. 4, pp. 1559–1567, 2014.

[13] A. J. E. Raaijmakers et al., "Design of a radiative surface coil array element at 7 T: The single-side adapted dipole antenna," Magn. Reson. Med., vol. 66, no. 5, pp. 1488–1497, 2011.

[14] A. Massire et al., "Thermal simulations in the human head for high field MRI using parallel transmission," J. Magn. Reson. Imaging, 2012.

[15] N. Boulant, X. Wu, G. Adriany, S. Schmitter, K. U◎urbil, and P. F. Van De Moortele, "Direct control of the temperature rise in parallel transmission by means of temperature virtual observation points: Simulations at 10.5 tesla," Magn. Reson. Med., 2016.

[16] C. M. Deniz, G. Carluccio, and C. Collins, "Parallel transmission RF pulse design with strict temperature constraints," NMR Biomed., 2017.

[17] M. Maspero, P. R. Seevinck, G. J. Meijer, J. J. W. Lagendijk, M. A. Viergever, and C. A. T. van den Berg, "SU-E-J-219: A Dixon Based Pseudo-CT Generation Method for MR-Only Radiotherapy Treatment Planning of the Pelvis and Head and Neck," Med. Phys., vol. 42, no. 6Part10, p. 3316, 2015.

[18] S. Gabriel, R. W. Lau, and C. Gabriel, "The dielectric properties of biological tissues: II. Measurements in the frequency range 10 Hz to 20 GHz," Phys. Med. Biol., 1996.

[19] H. Homann, P. Börnert, H. Eggers, K. Nehrke, O. Dössel, and I. Graesslin, "Toward individualized SAR models and in vivo validation," Magn. Reson. Med., 2011.

[20] E. Doran, S. Bawden, W. Bowtell, P. A. Gowland, and P. Glover, "Simplified subject-based models for efficient electromagnetic simulations and evaluation of local SAR for 7 T abdominal MRI," in Proc. Intl. Soc. Mag. Reson. Med. 27 Montreal, 2019, p. 4156.

[21] G. Carluccio, C. Akgun, J. T. Vaughan, and C. M. Collins, "Temperature-based MRI safety assessment with a simplified body model," in Proc. Intl. Soc. Mag. Reson. Med. 27 Montreal, 2019, p. 4161.

[22] A. J. E. Raaijmakers et al., "The fractionated dipole antenna: A new antenna for body

538843-L-bw-Steensma
Processed on: 17-12-2019
PDF page: 105

imaging at 7 Tesla," Magn. Reson. Med., vol. 75, no. 3, pp. 1366–1374, 2016.

[23] G. Carluccio, D. Erricolo, S. Oh, and C. M. Collins, "An approach to rapid calculation of temperature change in tissue using spatial filters to approximate effects of thermal conduction," IEEE Trans. Biomed. Eng., vol. 60, no. 6, pp. 1735–1741, 2013.

[24] S. Oh, G. Carluccio, and C. M. Collins, "Method and tool for improved rapid n-gram average SAR determination," in Proc. Intl. Soc. Mag. Reson. Med. 19, 2011, p. 3868.

[25] G. Eichfelder and M. Gebhardt, "Local specific absorption rate control for parallel transmission by virtual observation points," Magn. Reson. Med., vol. 66, no. 5, pp. 1468–1476, 2011.

[26] J. Lee, M. Gebhardt, L. L. Wald, and E. Adalsteinsson, "Local SAR in parallel transmission pulse design," Magn. Reson. Med., vol. 67, no. 6, pp. 1566–1578, 2012.

[27] A. Kuehne, H. Waiczies, and T. Niendorf, "Massively accelerated VOP compression for population-scale RF safety models," in Proceedings of the 24th Annual Meeting of ISMRM, Singapore, p. 0478.

[28] N. Boulant, V. Gras, A. Amadon, M. Luong, G. Ferrand, and A. Vignaud, "Workflow proposal for defining SAR safety margins in parallel transmission," in Proceedings of the 26th Annual Meeting of ISMRM, Paris, France, 2018, p. 0295.

[29] H. H. Pennes, "Analysis of tissue and arterial blood temperatures in the resting human forearm. 1948.," J. Appl. Physiol., 1998.

[30] S. K. Das, S. T. Clegg, and T. V. Samulski, "Computational techniques for fast hyperthermia temperature optimization," Med. Phys., 1999.

[31] B. Guerin, "Matlab based temperature solver," 2016. [Online]. Available: https://ptx.martinos.org/index.php/Matlab_based_temperature_solver.

[32] B. Guérin et al., "Computation of ultimate SAR amplification factors for radiofrequency hyperthermia in non-uniform body models: impact of frequency and tumour location," International Journal of Hyperthermia, 2017.

[33] M. Murbach et al., "Virtual population-based assessment of the impact of 3 Tesla radiofrequency shimming and thermoregulation on safety and B1+ uniformity," Magn. Reson. Med., 2016.

[34] F. F. J. Simonis, E. T. Petersen, L. W. Bartels, J. J. W. Lagendijk, and C. A. T. Van Den Berg, "Compensating for magnetic field inhomogeneity in multigradient-echo-based MR thermometry," Magn. Reson. Med., vol. 73, no. 3, pp. 1184–1189, 2015.

[35] I. Laakso and A. Hirata, "Dominant factors affecting temperature rise in simulations of human thermoregulation during RF exposure," Phys. Med. Biol., 2011.

538843-L-bw-Steensma
Processed on: 17-12-2019
PDF page: 106

Appendix A: Supporting Information

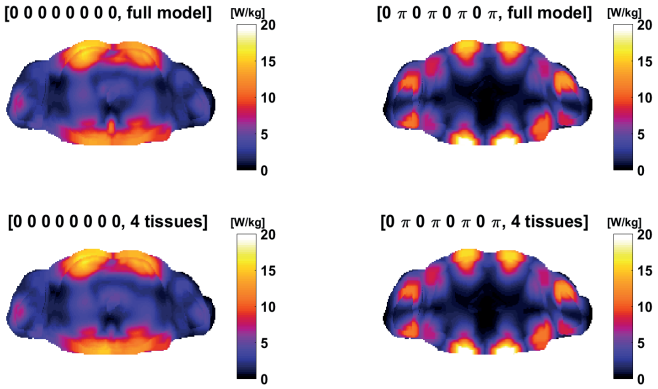

S1: SAR10g in Duke for two distinct RF shims (phases as indicated above the models). No difference in peak SAR is visible for both shim drives.

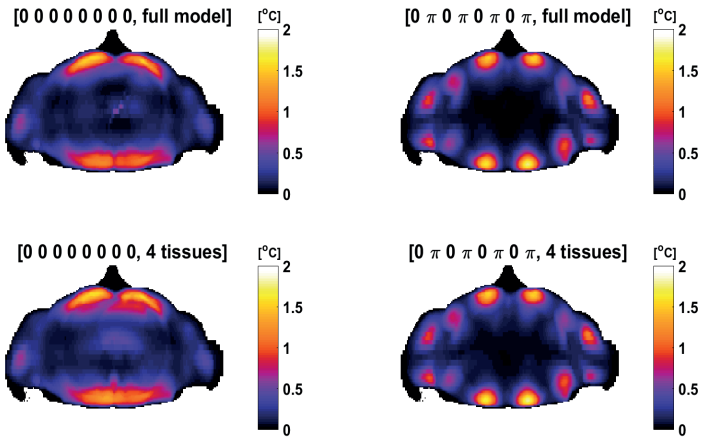

S2: temperature rise in Duke for two distinct RF shims (phases as indicated above the models). No difference in peak temperature rise is visible for both shim drives. Local temperature rise in the heart is slightly overestimated for the 4 tissue model, because the full model has higher perfusion values in blood and heart muscle.

538843-L-bw-Steensma
Processed on: 17-12-2019

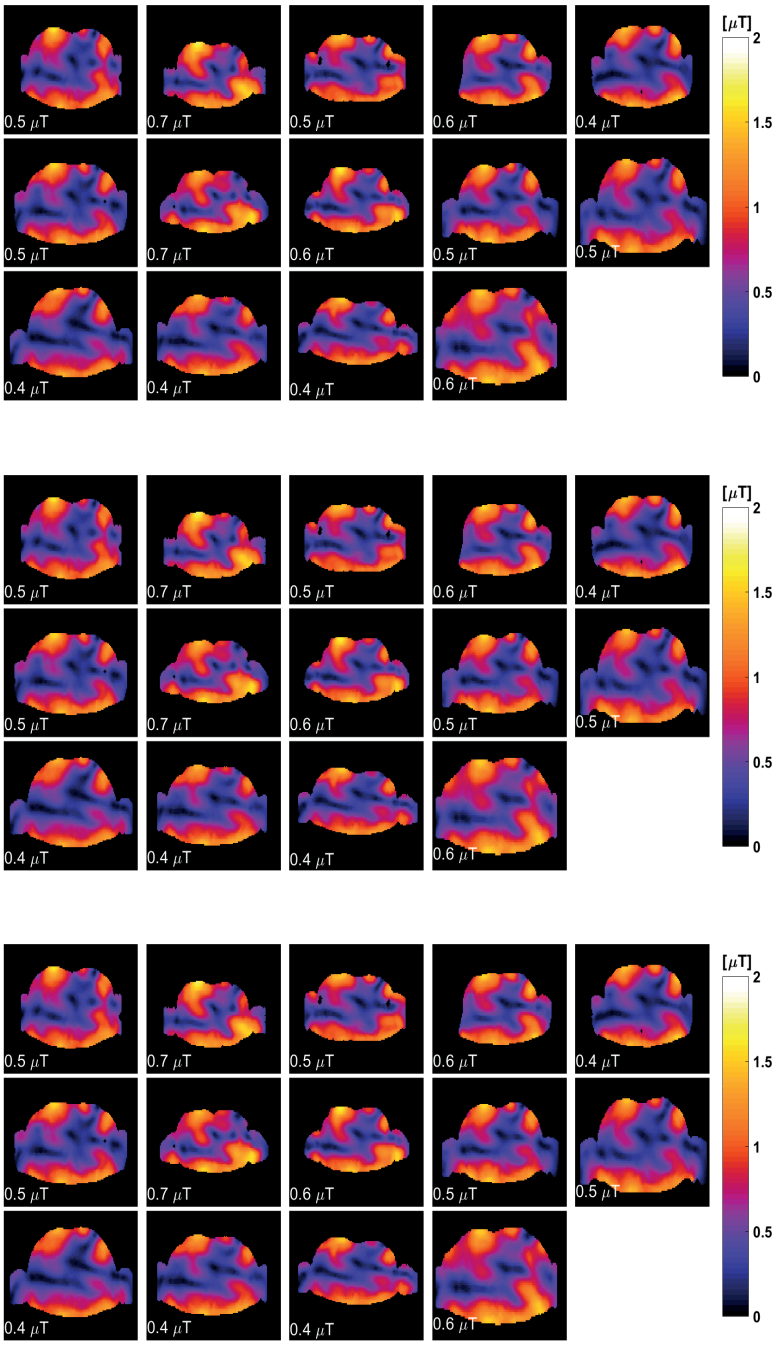

S3: B1+, SAR and DT distributions for the averaged RF shim drive on all volunteers.

6

538843-L-bw-Steensma
Processed on: 17-12-2019

6

538843-L-bw-Steensma
Processed on: 17-12-2019
PDF page: 110

6

538843-L-bw-Steensma
Processed on: 17-12-2019

Chapter 7

Local SAR assessment for multi-transmit systems: a study on the peak local SAR value as a function of magnetic field strength

Alexander J.E. Raaijmakers

Bart R. Steensma

Published in:
eMagRes Volume 8, Issue 1, February 2019

Abstract

With increasing permanent magnetic field strength B_0, the frequency of the radiofrequency field B_1 increases. The concomitantly reduced wavelength results in interference patterns that cause signal inhomogeneities and for ultrahigh field strengths even signal voids. These inhomogeneities are addressed by multi-transmit systems. These systems use multiple transmit elements where the phase and amplitude of each element can be controlled to steer the B_1 field. However, in this way also the electric field that originates from the B_1 field changes. This may pose a safety risk in terms of localized tissue heating. To avoid potential hotspots, the local SAR distribution needs to be determined by simulations. All concepts and methods to process simulation results are presented in this work. In addition, we use the presented methodology to investigate the relationship between the peak local SAR value and magnetic field strength B_0. For this purpose we have simulated the birdcage body coil at 3T and appropriately designed 16 channel dipole-loop transceiver arrays at 3T, 7T, 10.5T and 14T. We demonstrate a linear increase of peak local SAR with B_0 and a quadratic increase of SNR with B_0.

538843-L-bw-Steensma
Processed on: 17-12-2019
PDF page: 113

Introduction

In the classical MRI perspective, the B_1 field is mostly considered perfectly homogeneous so the resulting tip angle after an RF pulse will have the same value everywhere in the excited slab. However, for larger body cross sections and/or larger B_0 values, this perfect homogeneity is not achieved. In fact, for the not so moderate cases the B_1 field may show extreme variations from its peak value to almost zero. This larger B_1 field inhomogeneity with increasing B_0 field strength is caused by wavelength effects. The RF field should be regarded as a (superposition of) propagating electromagnetic waves. These waves have a wavelength that is inversely proportional to their frequency, i.e. the Larmor frequency. If the wavelength is large in comparison to the dimensions of the imaging region, the propagation effects of the RF field are negligible and the RF field is indeed more or less homogeneous. This is the case at 1.5T or lower and for head/extremity imaging at 3T. If the wavelength is comparable to the imaging region, then propagation effects begin to play a role and minor RF field inhomogeneities become apparent [1]. This is the case for body imaging at 3T [2] and head imaging at 7T [3]. If the wavelength is shorter than the dimensions of the imaging region, propagation effects become dominant and the RF field is strongly inhomogeneous. This is the case for body imaging at 7T [4] and also for head imaging at even larger field strengths [5].

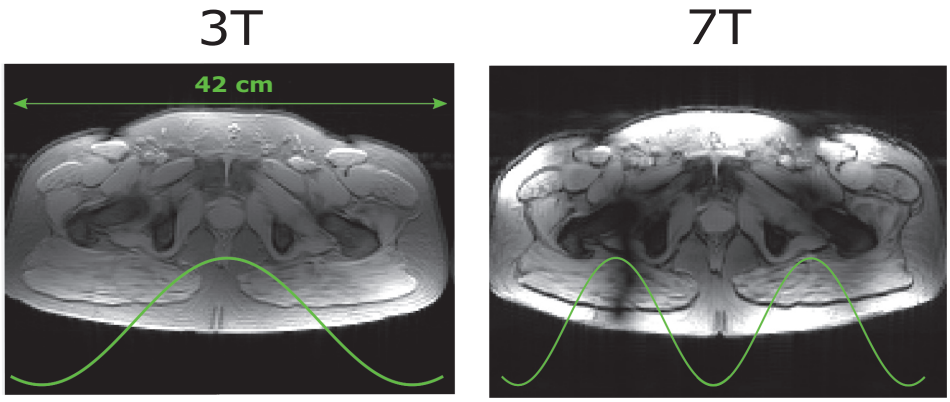

Figure 1: Wavelength in tissue at 3T and 7T and the corresponding signal inhomogeneities for prostate imaging.

These inhomogeneities are caused by a standing wave pattern of the electromagnetic RF waves in the patient. A way to address this issue is to use multiple transmit elements [6]. The resulting B_1^+ field distribution will be the superposition of the B_1^+ field of all these transmit elements. Although this sum distribution will likely also contain inhomogeneities, the pattern of these can be steered by adjusting

538843-L-bw-Steensma
Processed on: 17-12-2019
PDF page: 114

the phases and amplitudes of the individual transmit elements. A system that is capable of this is called a multi-transmit system. By optimizing the phases and amplitudes of the transmit channels, the B1+ homogeneity in the imaging region can be improved [7]–[9].

For 3T imaging, multi-transmit systems are available that have 2 channels [10]. The transmit coil is a birdcage body coil where the two linear modes can be driven independently with optimized phase and amplitude. The same system is used at 7T for head imaging. For body imaging at 7T, the inhomogeneities are too severe to compensate with only two transmit channels. For this purpose, 8- and 16-channel multi-transmit systems have been developed. Transmit coils are mostly surface arrays where the elements are placed directly on the body [11]–[17].

The SAR exposure in MRI systems is regulated by guidelines published by the IEC [18] and the FDA[19]. According to these guidelines, multi-transmit systems need to adhere to limitations on global SAR, regional SAR, and local SAR. Global SAR and regional SAR can easily be measured but the assessment of local SAR is more challenging. The introduction of considerable degrees of freedom in the RF field distribution of multi-transmit systems enables tailoring the B_1^+ field component of this distribution to optimize coverage of the imaging region. However, this also influences the local SAR distribution. The local SAR distribution depends heavily on the actual phase and amplitude settings of the coil array. And therefore also the peak local SAR value (which is the value that needs to be constrained by the guidelines) depends heavily on amplitude and phase settings.

This work will present an overview on local SAR considerations for multi-transmit systems. The presented methodology to assess local SAR for multi-transmit systems will be used to assess the local SAR distribution for prostate imaging at 3T, 7T, 10.5T and 14T. A secondary objective of this work is to investigate the dependency of the peak local SAR value on magnetic field strength. In many standard MRI text books and courses, it is claimed that SAR increases quadratically with magnetic field strength (e.g. Haake et al. section 27.4.5 [20]). This claim is evaluated here for prostate imaging as was also recently done for head imaging [21]. Since simulations on local SAR simultaneously provide distributions of B_1^+ and B_1^-, also transmit efficiency and intrinsic SNR is reported for each field strength.

538843-L-bw-Steensma
Processed on: 17-12-2019
PDF page: 115

Methods

SAR assessment for multi-transmit systems

Both global SAR and regional SAR can be determined by measuring the sum of the average powers that are emitted from the coil array to the body. If considerable coupling and/or reflection takes place between/from the coil array elements, the net power towards the coil array can be calculated from the sum of forward powers minus the sum of reflected powers [22], [23] (equation 1).

$$SAR_{global} = \frac{\sum_n |a_n|^2 - |b_n|^2}{m_{patient}} \quad [1a]$$

$$SAR_{regional} = \frac{\sum_n |a_n|^2 - |b_n|^2}{m_{exposed}} \quad [1b]$$

Here forward and reflected powers are expressed in terms of the forward and reflected wave amplitudes a_n and b_n of channel n. A detailed explanation of the concept of forward and reflected wave amplitudes is provided in many RF text books, for example by Pozar [24]. $m_{patient}$ is the mass of the patient and $m_{exposed}$ is the mass of the region in the patient that is exposed to RF fields. Because forward and reflected wave amplitudes a and b can be measured using directional couplers, global and regional SAR can be easily measured to ensure adherence to the guidelines. However, these constraints do not prevent the occurrence of local temperature hotspots. Therefore, also local SAR needs to be constrained. Local SAR is defined as the deposited power per unit mass. If an infinitesimal amount of power dP is deposited in an infinitesimal amount of tissue with mass dm, then the local SAR at position is defined as:

$$SAR(\vec{x}) = \frac{dP(\vec{x})}{dm(\vec{x})} \quad [2]$$

This is equivalent to the amount of power *dP* deposited in an infinitesimal volume *dV* divided by the mass *dm* of that infinitesimal volume *dV*. The power *dP* deposited in an infinitesimal volume *dV* at position is given by:

$$dP(\vec{x}) = \frac{1}{2}\left(\vec{J}(\vec{x})\right)^* \cdot \vec{E}(\vec{x})\, dV \quad [3]$$

538843-L-bw-Steensma
Processed on: 17-12-2019
PDF page: 116

In this equation and are the complex amplitudes of the current density and electric field in phasor notation. Assuming reciprocal media the current density is in the same direction as the electric field:

$$\vec{J}(\vec{x}) = \sigma(\vec{x})\vec{E}(\vec{x}) \quad [4]$$

Therefore [3] simplifies to:

$$dP(\vec{x}) = \frac{1}{2}\left(\sigma(\vec{x})\vec{E}(\vec{x})\right)^* \cdot \vec{E}(\vec{x})\,dV = \frac{1}{2}\sigma(\vec{x})\left|\vec{E}(\vec{x})\right|^2 dV \quad [5]$$

And considering that

$$dm(\vec{x}) = \rho(\vec{x})\,dV \quad [6]$$

Equation [2] simplifies to

$$SAR(\vec{x}) = \frac{dP(\vec{x})}{dm(\vec{x})} = \frac{\frac{1}{2}\sigma(\vec{x})\left|\vec{E}(\vec{x})\right|^2 dV}{\rho(\vec{x})\,dV} = \frac{\sigma(\vec{x})}{2\rho(\vec{x})}\left|\vec{E}(\vec{x})\right|^2 \quad [7]$$

If all quantities are implicitly assumed to be depending on x, the expression becomes:

$$SAR = \frac{\sigma}{2\rho}\left|\vec{E}\right|^2 \quad [8]$$

Since the guidelines impose restrictions on 10g averaged local SAR, expression [8] is subsequently averaged accordingly:

$$SAR = \int_{Vavg} \frac{\sigma}{2\rho}\left|\vec{E}\right|^2 dV \quad [9]$$

Where, Vavg is the cubical volume of the averaging mass, for example, 10 g.

In a multi-transmit system, the electric field is the superposition of the electric fields of all the individual transmit elements. In this superposition, the electric field of each transmit element is related to the current in that transmit element. This can be expressed by a vector multiplication.

538843-L-bw-Steensma
Processed on: 17-12-2019
PDF page: 117

$$E_x = E_x^{'(1)} I^{(1)} + E_x^{'(2)} I^{(2)} + \ldots + E_x^{'(N)} I^{(N)} = \begin{pmatrix} E_x^{'(1)} & E_x^{'(2)} & \ldots & E_x^{'(N)} \end{pmatrix} \begin{pmatrix} I^{(1)} \\ I^{(2)} \\ \vdots \\ I^{(N)} \end{pmatrix} = \boldsymbol{E}_x^{'T} \boldsymbol{I} \quad [10]$$

Here is the electric field in the x-direction per unit current generated by transmit element n. Again, the dependence of on positional coordinate is implicitly understood. $\boldsymbol{I}$ is the current in transmit element n.

Similarly:

$$E_x = \boldsymbol{E}_x^{'T} \boldsymbol{I}, \quad E_y = \boldsymbol{E}_y^{'T} \boldsymbol{I}, \quad E_z = \boldsymbol{E}_x^{'T} \boldsymbol{I} \quad [11]$$

Now the SAR can be calculated by:

$$SAR = \frac{\sigma}{2\rho} \left\{ \left| \vec{E} \right|^2 \right\} = \frac{\sigma}{2\rho} \left\{ \left| E_x \right|^2 + \left| E_y \right|^2 + \left| E_z \right|^2 \right\} \quad [12a]$$

$$= \frac{\sigma}{2\rho} \left\{ \boldsymbol{I}^T \boldsymbol{E}_x' \boldsymbol{E}_x^{'T} \boldsymbol{I} + \boldsymbol{I}^T \boldsymbol{E}_y' \boldsymbol{E}_y^{'T} \boldsymbol{I} + \boldsymbol{I}^T \boldsymbol{E}_z' \boldsymbol{E}_z^{'T} \boldsymbol{I} \right\} \quad [12b]$$

$$= \boldsymbol{I}^T \left\{ \frac{\sigma}{2\rho} \left(\boldsymbol{E}_x' \boldsymbol{E}_x^{'T} + \boldsymbol{E}_y' \boldsymbol{E}_y^{'T} + \boldsymbol{E}_z' \boldsymbol{E}_z^{'T} \right) \right\} \boldsymbol{I} \quad [12c]$$

The expression [12c] can now be written as:

$$SAR = \boldsymbol{I}^T \boldsymbol{Q} \boldsymbol{I} \quad [13]$$

Where Q is the so-called Q-matrix[25]. It is a spatially dependent matrix that directly relates the currents on the coil array elements to the local SAR at position x. Its definition follows from [12c]:

$$\boldsymbol{Q} = \frac{\sigma}{2\rho} \left(\boldsymbol{E}_x' \boldsymbol{E}_x^{'T} + \boldsymbol{E}_y' \boldsymbol{E}_y^{'T} + \boldsymbol{E}_z' \boldsymbol{E}_z^{'T} \right) \quad [14]$$

Since the relevant guidelines have defined their constraints in terms of 10g-averaged SAR, the following expressions are used to determine this quantity:

538843-L-bw-Steensma
Processed on: 17-12-2019
PDF page: 118

$$SAR_{10g} = \boldsymbol{I}^T \boldsymbol{Q}_{10g} \boldsymbol{I} \quad [15]$$

with:

$$\boldsymbol{Q}_{10g} = \frac{1}{Vavg} \int_{Vavg} \frac{\sigma}{2\rho} \left(\boldsymbol{E}'_x \boldsymbol{E}'^{T}_x + \boldsymbol{E}'_y \boldsymbol{E}'^{T}_y + \boldsymbol{E}'_z \boldsymbol{E}'^{T}_z \right) dV$$

Where again Vavg is the cubical volume of the averaging mass, in this case 10g. Since only 10g-averaged SAR levels are of interest, the 10g-averaged Q-matrix is quite often also just denoted by Instead of . Also note that sometimes simulated E-fields are expressed in terms of their rms-values. In that case, the factor ½ in equation [5] and all subsequent equations should be omitted.

Practical Example

To illustrate these abstract quantities, an example is presented. Consider an 8-channel multi-transmit coil array for prostate imaging at 7T[17]. It consists of eight transmit elements around the pelvis. Per unit current, each coil array element will generate an electric field distribution. These are indicated in figure 2. The E-field vectors , and as used in equations [10]-[16] are created by taking at the same location the values from each of these 8 images.

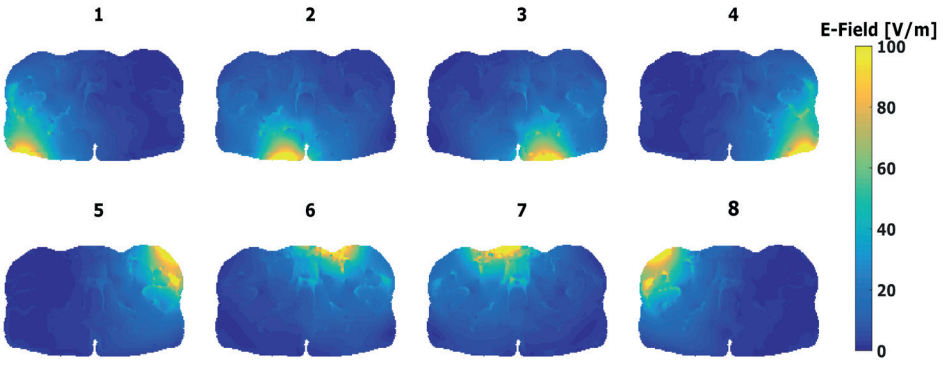

Figure 2: E-field distributions in the human model Duke using a 8-channel transmit/receive coil array for prostate imaging at 7T.

Using the Q-factors of such an array, the local 10g-averaged SAR distribution can be determined by performing the quadratic vector-matrix multiplication for every voxel in the simulated model. In this way, the local SAR distribution can be calculated for a given drive vector (phase/amplitude combination) of the

538843-L-bw-Steensma
Processed on: 17-12-2019
PDF page: 119

transmit array. An example is provided by figure 3.

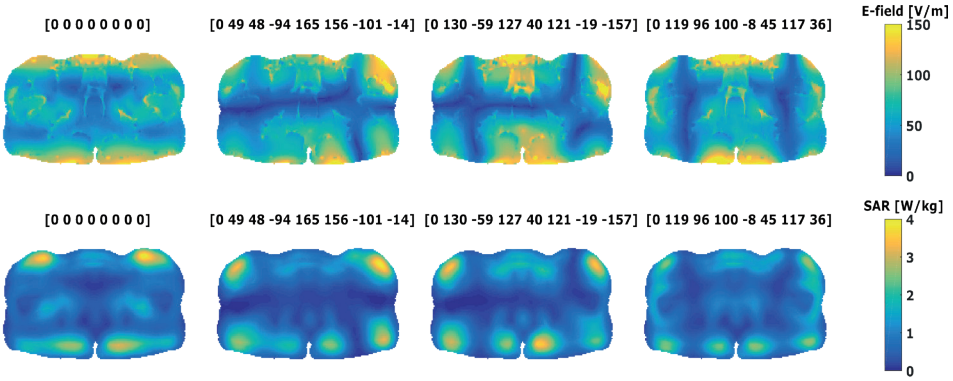

7

Figure 3: Total E-field distributions (top row) and local 10g-averaged SAR distributions (bottom row) in the human model Duke using the 8-channel transmit/receive coil array for prostate imaging at 7T. Presented are distributions for a couple of possible drive vectors. Amplitudes are all equal; phase settings are indicated.

The E-fields as presented in figure 2 are normalized to unit current. However, this is not always the most convenient normalization to work with. Depending on the MRI system vendor and/or the simulation software package, E-field distributions may be preferably expressed per unit voltage or per unit forward power to the coil array element. These can be calculated from the E-field distributions per unit current (and vice versa) using the following equations:

$$E_{x,y,z}\Big|_{I=1A} = Z_{input}\, E_{x,y,z}\Big|_{V=1V} = \sqrt{Z_{input}}\, E_{x,y,z}\Big|_{a=1\sqrt{W}} \qquad [17]$$

Here Z_{input} is the input impedance of the coil array element. Note that only the normalization changes; the spatial distribution of the E-field will stay exactly the same. If an alternative normalization is chosen, the Q-matrix can be constructed with fields normalized to voltage or forward power and also the input drive vectors are then expressed in terms of voltage or forward power.

Domain reduction

The Q-matrices of each voxel in the simulated model can be stacked into a single array with dimension [n_{voxels}*n_{ports}*n_{ports}]. A voxelized model of a coil and human body typically consists of several tens of millions voxels, so the Q-matrix can get very large in size. Storing Q-matrices for multiple human body models or optimizing field distributions with information based on the Q-matrix is too demanding, particularly on a normal PC. Eichenfelder and Gehbardt[26] have proposed the use of Virtual Observation Points (VOPs),

538843-L-bw-Steensma
Processed on: 17-12-2019
PDF page: 120

which is a method that can be used for significant domain reduction of the Q-matrix. The domain reduction comes with a small SAR overestimation where the amount of overestimation is a tradeoff with the amount of domain reduction. The VOP method relies on clustering similar voxel Q-matrices, for voxel locations *v*, into a single Q-matrix(VOP) such that for each voxel in v, the SAR is equal to the SAR in one particular voxel *p* plus an additional allowed overestimation factor. The aim is to have as little VOPs as possible, while peak SAR is still estimated reliably. If a cluster is defined around a certain voxel p with Q-matrix Q_p, then all matrices Q_v which are to be included in the cluster need to satisfy a similarity constraint, which is set by allowing a finite overshoot ε.

$$x^H Q_p x + \varepsilon x^2 \geq x^H Q_v x \quad [18]$$

The matrix Q_v is only included in the cluster if Q_p-Q_v is ε-positive semidefinite (psd). This means that for every x, . This guarantees that for a certain normalized excitation vector x, the following holds: In practice, the matrix Q_p is selected by finding the Q-matrix with the largest primary eigenvalue. The voxels that are to be included in the cluster are then selected by comparing the absolute value of the smallest eigenvalue λ_{min} of the difference matrix Q_p-Q_v against ε. If λ_{min} is smaller than ε, the criterion can be guaranteed with a minimal overestimation, by representing the VOP SAR as . In principle, defines the maximum allowed overestimation, and in cases where the absolute smallest values of λ_{min} are smaller than , SAR in the VOP can also be represented by . If all voxel Q-matrices that satisfy this criterion are included in the cluster, the Q-matrix with the largest eigenvalue in the cluster is selected as the Q-matrix Qp for that VOP. Now the clustering procedure can be repeated to generate a new cluster until all voxels are clustered. Using the method of VOPs can significantly reduce the dimensionality of the Q-matrix array from millions of voxels to hundreds or thousands of VOPs. In general, the number of VOPs can be decreased by choosing a larger overestimation factor , which in turn provides less accurate (but never underestimated) SAR values.

Inter-subject variability

The above presented methodology is used to assess the peak local SAR for a certain numerical model of a patient. This model will not be the same as the subject inside the scanner. As a result, the peak local SAR may be underestimated which is a potential safety risk for the patient.

This can be addressed by application of a scaling factor to reach the maximum peak SAR level that can be found in the entire patient population. For head

538843-L-bw-Steensma
Processed on: 17-12-2019
PDF page: 121

imaging, this scaling factor was found to be 1.4 [27], [28]. For prostate imaging, the inter-subject variability is much larger resulting in a scaling factor of 2 [29].

An alternative methodology has been presented by Homann et al[30] where a Dixon scan is used to generate a subject-specific model of the patient inside the scanner. However, this would require a real-time EM-simulation in between a Dixon scan and subsequent scans. This is currently still out of reach or would require a very considerable investment in GPU facilities.

A very recent publication has presented an extensive analysis on inter-subject variability for prostate imaging at 7T using 23 models [31]. This approach enables the definition of power limits based on statistics over many models and many potential phase settings. As a result, these power limits are applicable for any subject in the patient population.

Field Comparison Study

This chapter will present the dependence of local SAR distributions on the magnetic field strength B_0. For this purpose, a 8-channel multi-transmit array for prostate imaging is simulated for 3T, 7T, 10.5T and 14T using the model Duke of the virtual family [32]. For comparison, also the birdcage body coil is simulated with the model Duke at 3T. The RF field distributions for the corresponding Larmor frequencies are analyzed by comparing the B_1^+ and local SAR distributions with prostate-shimmed phase settings. In addition, the gamma distributions that correspond to the histogram of peak local SAR values with random phase settings is plotted for each field strength.

The design for the multi-transmit array at each investigated field strength is a 16 channel local transceive array consisting of 8 dipole antennas and 8 loop coil elements. All simulations have been performed using the FDTD simulation package Sim4Life (ZMT, Zurich, Switzerland). The simulation geometries with the design on human model Duke are presented in figure 4. The design for 3T consists of 8 meandering dipole antennas (30 cm length, 2 meanders per cm [33]) and 8 square loop coils with rounded corners (width 8 cm, length 16 cm). For 7T, the design for the dipole antennas is equivalent to the fractionated dipole antennas as presented by Raaijmakers et al [17]. (30 cm length, 2 30 mm wide meanders per leg) in combination with 8 square loop coils with rounded corners (width 8 cm, length 16 cm) which constitutes the same setup as presented by Erturk et al. [34] At 10.5T a similar setup was used that was also presented by Erturk et al. [35] Here all the elements are scaled down to correspond to the reduced wavelength at 450 MHz. The total dipole length is 21 cm, the loops are 5.2 cm wide and 10 cm long. For 14T the same approach has been used where

538843-L-bw-Steensma
Processed on: 17-12-2019
PDF page: 122

the antennas are reduced in size even further (dipole length 12.6 cm, loops 4.5 cm wide and 6.5 cm long).

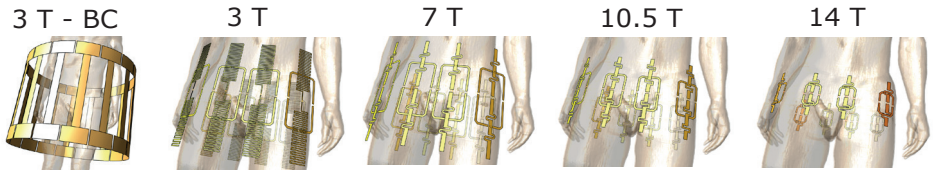

Figure 4: Simulation geometries of the investigated transmit arrays for each field strength on human model Duke.

For each setup, the field response of each individual element was simulated separately after which Q-matrices were generated and VOP compression was performed. The phase settings that provide maximum B_1^+ in the prostate were determined and the corresponding B_1^+ and local SAR distributions were determined. Results are analyzed in terms of peak local SAR per unit power and peak local SAR per unit B_1^+. In addition, the relative SNR values are evaluated for each field strength and array setup.

The SNR for each setup is calculated from the receive sensitivity (B_1^- per unit current), the noise covariance matrix R and the additional quadratic increase of the signal with B0-field strength:

$$SNR \sim \left(B_0\right)^2 \sqrt{\boldsymbol{b}^T \boldsymbol{R}^{-1} \boldsymbol{b}} \qquad [19]$$

Where b is the vector with sensitivities for each receive array element. The expression under the square root is effectively equal to and will therefore be referred to as the B_1^- per unit power. If no different magnetic field strengths are involved and the study aims e.g. at comparing two different coil array designs at the same field strength, the B_1^- per unit power suffices to evaluate the SNR comparison.

Results

Figure 5 shows the B_1^+ distributions with uniform amplitude and prostate-shimmed phase settings for all investigated field strengths. The B_1^+ magnitude that is achieved in the prostate with 16 x 150W input power is 26.1, 19.1, 20.0 and 17.4 μT for the local transmit arrays at 3T, 7T, 10.5T and 14T respectively. With the birdcage coil, 19.5 μT is obtained with 2 x 1200 W. The images clearly show the decreasing wavelength which results in a smaller focus area around the

538843-L-bw-Steensma
Processed on: 17-12-2019
PDF page: 123

prostate for higher field strengths.

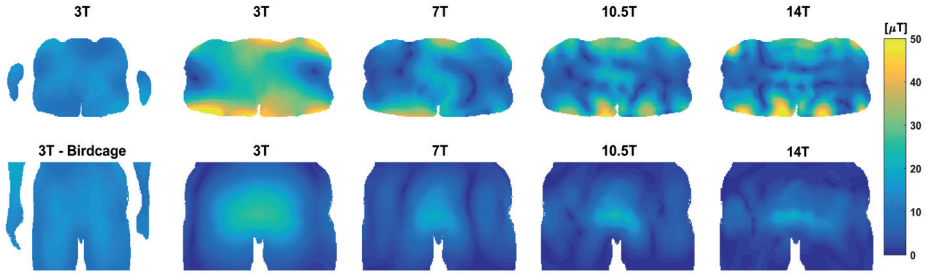

Figure 5: Simulated B1+ field distributions with uniform amplitude and prostate-shimmed phase settings for the 3T birdcage body coil and dipole-loop arrays at 3T, 7T, 10.5T and 14T. Top row: transverse plane through prostate. Bottom row: Coronal plane through prostate. Distributions are presented for 16 x 150W input power.

Figure 6 shows the maximum intensity projection (axial and coronal) of the local SAR distributions that correspond to these prostate-shimmed phase settings. The peak local SAR level that is achieved with 16 x 1 W average input power is 3.6, 3.6, 4.5 and 6.5 for the local transmit arrays W/kg. With the birdcage, 1.3 W/kg is obtained with 2 x 8 W average input power.

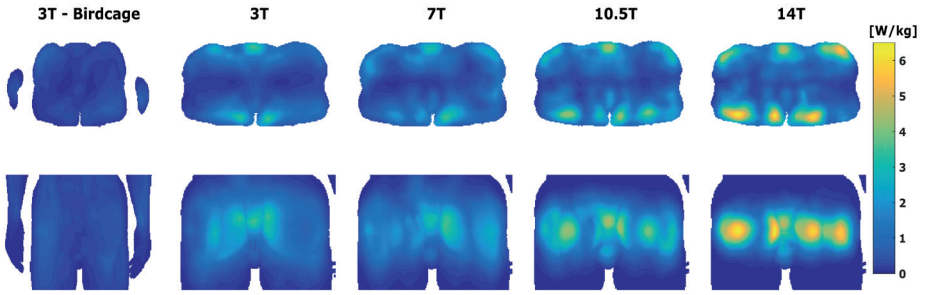

Figure 6: Simulated local SAR10g distributions for uniform amplitude and prostate-shimmed phase settings for the 3T birdcage body coil and dipole-loop arrays at 3T, 7T, 10.5T and 14T. Maximum intensity projection is shown in axial (top row) and coronal (bottom row) orientation. Distributions are presented for 16 x 4 W average input power.

The simulated field distributions also provide us with the relative intrinsic SNR distributions. These are presented in figure 7 along with the B_1^- per unit power.

538843-L-bw-Steensma
Processed on: 17-12-2019
PDF page: 124

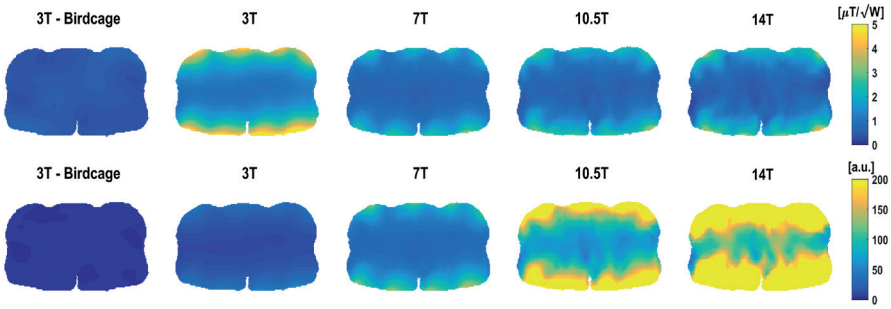

Figure 7: Simulated B_1^- per unit power (top row) and intrinsic SNR distributions (bottom row) for the birdcage body coil at 3T and the investigated transmit/receive arrays at 3T, 7T, 10.5T and 14T.

The local SAR distributions as presented in figure 6 only provide us the local SAR distributions for prostate shimmed phase settings. Different phase settings will provide different local SAR distributions, different peak SAR10g values and consequently different power constraints. If, for a particular field strength setup, the peak SAR10g levels for a large number of random phase settings (with uniform amplitude) is plotted in a histogram, the result will be a gamma distribution with a particular mean and shape parameter k. Such histograms, with the corresponding fitted gamma distribution, are presented in figure 8. From these distributions, a local SAR_{10g} threshold can be identified that is not violated in 99% of the phase settings [31]. In this study we will define it as $pSAR_{99\%}$. The SAR_{10g} could in principle reach higher levels with the highest level being defined as the worst-case SAR value [29], [31]. However, the likelihood of achieving such levels is less than 1% and is therefore not considered relevant for any realistic phase setting or RF pulse sequence.

538843-L-bw-Steensma
Processed on: 17-12-2019
PDF page: 125

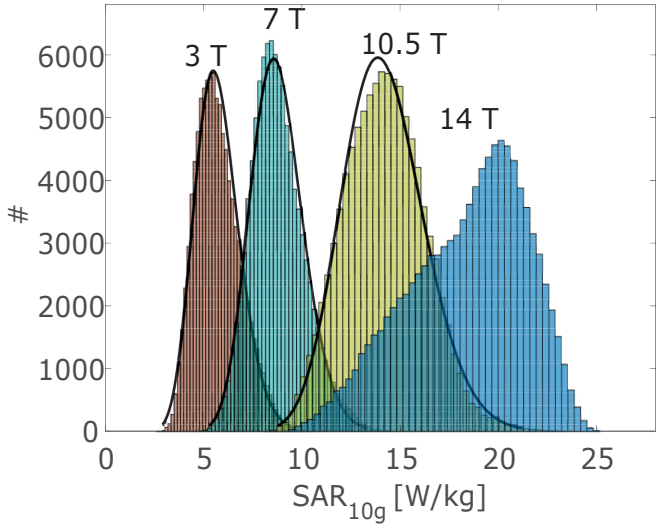

Figure 8: Histograms of peak local SAR for the investigated arrays at 3T, 7T, 10.5T and 14T. Data consists of peak local SAR values for 100,000 random phase settings.

The results presented above provide a clear picture of the spatial distributions of B_1^+, local SAR_{10g} and SNR. However, for B_1^+ and SNR only the value in the prostate is important while for the local SAR_{10g} only the peak value is of interest. Figure 9 is presenting a series of graphs to indicate how these quantities depend on the magnetic field strength. Figure 10a shows the B_1^+ efficiency in the prostate as a function of field strength. In the same diagram, also the SAR efficiency as a function of field strength is plotted against the right axis. Note that SAR efficiency is defined as the B_1^+ per unit peak local SAR_{10g} . Figure 9b shows the peak local SAR per unit power as a function of field strength. In the same graph, also the peak local SAR per unit B_1^+ is plotted against the right axis. This is effectively the reciprocal of the SAR efficiency squared. Finally, figure 9c shows the simulated B_1^- per unit power and the intrinsic SNR as a function of field strength.

538843-L-bw-Steensma
Processed on: 17-12-2019
PDF page: 126

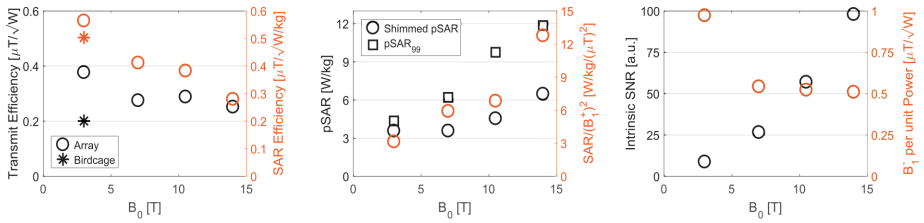

Figure 9: a) B_1^+ efficiency and SAR efficiency in the prostate for the investigated arrays as a function of field strength. The performance of the birdcage body coil at 3T is also indicated for comparison. b) pSAR10g with prostate shimmed phase settings per unit power (left axis) and per unit B_1^+ squared (right axis). In addition, $pSAR_{99\%}$ is plotted for the investigated arrays as a function of field strength (left axis). c) Simulated B_1^- per unit power (right axis) and intrinsic SNR in the prostate (left axis) for the investigated arrays as a function of field strength.

Discussion

This work has provided a detailed overview of the concepts and methods that are involved in local SAR assessment for multi-transmit systems. Maximum allowed exposure levels have been defined for global SAR, regional SAR and the peak local SAR value. To avoid violation of these guidelines, the input powers to the transmit array elements need to be constrained. The challenge is that the peak SAR level (highest local SAR within the body) cannot be measured. In addition, it depends on the phase and amplitude settings of the array. This is dealt with by calculating the peak local SAR level through Q-matrices and domain reduction (virtual observation points). In this way, the peak local SAR can be calculated online without significant computational effort. However, the obtained peak local SAR value has been calculated for one particular model. At best a couple of models have been evaluated. The subject in the scanner may show different SAR behavior. Therefore, a safety factor is needed to ensure that the peak SAR that has been calculated is indeed the peak SAR for the entire patient population. Much better but more demanding is to perform simulations on a larger set of models. These may be used to assess safe power constraints for the entire patient population[31]. An alternative procedure for subject-specific SAR assessment based on B_1^+ maps and deep learning has recently been presented and shows promising results but it is not yet used in practice to assess safe power constraints for multi-transmit imaging (ref). In addition to the inter-subject variability, also other sources of error may be included in the correction factor, e.g. to account for uncertainties in the directional coupler readout[28].

The presented methodology has been used to investigate the B_1^+ efficiency, local SAR levels and SNR for the 2-channel birdcage body coil at 3T and 8-channel local transmit arrays at 3T, 7T, 10.5T and 14T.

538843-L-bw-Steensma
Processed on: 17-12-2019
PDF page: 127

The resulting B_1^+ levels in the prostate as a function of field strength in figure 9a show a remarkable pattern. The 3T body coil is not very efficient as expected while the local transmit array at 3T is outperforming all other cases. At 7T, the transmit efficiency has dropped considerably in comparison to 3T. This may be caused by the loss of near-field advantage. A more detailed explanation of this perspective is presented further down below. After this, the B_1^+ efficiency does not change much.

The resulting SAR efficiencies (B_1^+ in prostate per square root local SAR) that are plotted in the same figure show a slightly better SAR efficiency for the local transmit array in comparison to the body coil at 3T. This is quite remarkable: the array with elements directly on the body has a more beneficial B_1^+/peak local SAR ratio than the birdcage body coil. This is achieved by the extremely high efficiency of the local array in comparison to the birdcage coil. For all subsequent field strengths a gradual reduction in SAR efficiency is shown.

Figure 9b shows the increase in the peak local SAR value when field strength is increased. Peak SAR levels show a clear increasing trend both normalized to power and normalized to B_1^+. But both trends seem to be approached best by a linear relationship; not quadratic. This, in combination with the work presented by Winter et al [21], shows that the assumption that SAR increases quadratically with field strength has no foundation in this range of field strengths. In addition, the $SAR_{99\%}$ is plotted, which is the SAR level that may be violated with a 1% probability if random phase settings are used. Also this value is increasing with a similar linear trend.

The peak local SAR value for a multi-transmit array depends on the phase settings in a rather unpredictable fashion. However, by calculating the peak local SAR for 100,000 random phase settings and plotting the pSAR values in a histogram, some patterns can be observed. Figure 8 is showing these histograms for the investigated field strengths. At 3T, 7T and 10.5T, the histograms show a gamma distribution as observed by Meliado et al [31]. However, at a field strength of 14T, the behavior has changed: the distribution has a large tail towards the lower SAR values instead of the other way around with the gamma distribution. An explanation still requires further investigation.

Figure 9c shows the simulated intrinsic SNR for each field strength together with the B_1^- per unit power. The SNR is by definition the signal in an MRI experiment divided by the noise. Based on the increased magnetization combined with the stronger induction voltage in the receive coil due to the higher frequency, the signal in an MRI experiment increases quadratically with field strength. The noise,

538843-L-bw-Steensma
Processed on: 17-12-2019
PDF page: 128

on the other hand, is thought to increase linearly with field strength (Haacke [36], par 15.8). Combined this would provide a linear increase in field strength if the sensitivity of the coil array remained constant. However, also the sensitivity of the receive array will depend on the operating frequency. And in addition, the noise depends on both the field strength and the coil array design while it does not linearly increase anymore for higher field strengths. The combination of this makes the B_1^- per unit power decrease from 3T to 7T while it is stable for subsequent field strengths. As a result, the SNR as a function of field strength increases quadratically. This corroborates well with findings by others [21], [37].

The expected quadratic increase of SAR with field strength originates from the following line of thoughts: E-fields that are associated with B_1-fields are generated by induction. The amplitude of the E-fields is therefore proportional to the time-derivative of B_1 as expressed by equation [20a].

$$\left|\vec{E}\right| \sim \frac{dB_1}{dt} \qquad [20a]$$

$$\left|\vec{E}\right| \sim \omega B_1 \qquad [20b]$$

$$SAR \sim \omega^2 \sim B_0^2 \qquad [20c]$$

For time-harmonic signals, this translates into a proportionality with the frequency of the signals [20b]. Since SAR is the square of the E-field amplitude, SAR is expected to increase quadratically with field strength [20c].

However, from antenna theory it is known that antennas have a near-field and a far-field. In the far-field, the electric and magnetic field constitute a propagating wave. Propagating electromagnetic waves have a ratio of electric and magnetic field amplitudes (wave impedance) that is determined by the permeability μ and the permittivity ε of the medium in which the wave propagates.

$$Z_{wave} = \frac{E}{H} = \sqrt{\frac{\mu}{\varepsilon}} \qquad [21]$$

In this regime, the electric field cannot be increasing linearly with the Larmor frequency because a particular amplitude of the B_1 field in μT would correspond to a particular electric field amplitude in V/m regardless of the frequency (except for much more lenient frequency-dependence of the tissue properties). This does of course not apply to the near-field region. However, as previous studies have emphasized, dipole antennas as transmit elements in MRI should take care to avoid near-field exposure inside the tissue [11], [17]. Therefore some minimum

538843-L-bw-Steensma
Processed on: 17-12-2019
PDF page: 129

distance is recommended. As a result, the potentially quadratically increasing E-fields in the near-field play only a minor role in the resulting relationship of peak local SAR values with magnetic field strength. This may explain the linear rather than quadratic increase in local SAR values (figure 9b).

The near-field region is characterized by strong magnetic or electric fields that are related to the resonance of the coil. It is therefore in fact favorable to use the near-field of RF coils in MRI. However, the size of the near-field region around an antenna is related to the wavelength. This means that for higher field strengths (smaller wavelengths), the near-field may not extend until the imaging target. It is particularly in this regime where dipole antennas are beneficial for use as transmit array elements in MRI [38]. However, until this regime is entered much larger efficiencies can be reached. This may explain the larger transmit efficiency and receive sensitivity at 3T in comparison to 7T and higher field strengths (figure 9).

Conclusion

A detailed explanation on local SAR assessment for multi-transmit arrays has been presented. With these methods, the peak local SAR, B_1^+ fields and SNR have been evaluated for prostate imaging at 3T, 7T, 10.5T and 14T using loop-dipole transceive arrays. At 3T, also a 2-channel birdcage body coil was included in the comparison. Results show that for these arrays the peak local SAR depends linearly on field strength. The simulated SNR for the investigated setups increases quadratically with field strength.

References

[1] M. A. Bernstein, J. Huston, and H. A. Ward, "Imaging artifacts at 3.0T," *J. Magn. Reson. Imaging*, vol. 24, no. 4, pp. 735–746, 2006.

[2] E. M. Merkle and B. M. Dale, "Abdominal MRI at 3.0 T: The Basics Revisited," *Am. J. Roentgenol.*, vol. 186, no. 6, pp. 1524–1532, 2006.

[3] J. T. Vaughan *et al.*, "7T vs. 4T: RF power, homogeneity, and signal-to-noise comparison in head images," *Magn. Reson. Med.*, vol. 46, no. 1, pp. 24–30, 2001.

[4] J. T. Vaughan *et al.*, "Whole-body imaging at 7T: Preliminary results," *Magn. Reson. Med.*, vol. 61, no. 1, pp. 244–248, 2009.

[5] T. Vaughan *et al.*, "9.4T human MRI: Preliminary results," *Magn. Reson. Med.*, vol. 56, no. 6, pp. 1274–1282, 2006.

[6] Y. Zhu, "Parallel Excitation with an Array of Transmit Coils," *Magn. Reson. Med.*, 2004.

[7] B. K. Li, F. Liu, and S. Crozier, "Focused, eight-element transceive phased array coil for

538843-L-bw-Steensma
Processed on: 17-12-2019
PDF page: 130

parallel magnetic resonance imaging of the chest - Theoretical considerations," *Magn. Reson. Med.*, vol. 53, no. 6, pp. 1251–1257, 2005.

[8] W. Mao, M. B. Smith, and C. M. Collins, "Exploring the limits of RF shimming for high-field MRI of the human head," *Magn. Reson. Med.*, 2006.

[9] G. Adriany *et al.*, "Transmit and receive transmission line arrays for 7 tesla parallel imaging," *Magn. Reson. Med.*, vol. 53, no. 2, pp. 434–445, 2005.

[10] W. a Willinek *et al.*, "Dual-source parallel radiofrequency excitation body MR imaging compared with standard MR imaging at 3.0 T: initial clinical experience.," *Radiology*, 2010.

[11] A. J. E. Raaijmakers *et al.*, "Design of a radiative surface coil array element at 7 T: The single-side adapted dipole antenna," *Magn. Reson. Med.*, vol. 66, no. 5, pp. 1488–1497, 2011.

[12] G. J. Metzger *et al.*, "Local B1+ shimming for prostate imaging with transceiver arrays at 7T based on subject-dependent transmit phase measurements," *Magn. Reson. Med.*, vol. 59, no. 2, pp. 396–409, 2008.

[13] S. Orzada *et al.*, "A flexible 8-channel transmit/receive body coil for 7 T human imaging," in *Proceedings of the 17th Annual Meeting of ISMRM, Honolulu, Hawaii, USA*, 2009, p. 2999.

[14] C. Thalhammer *et al.*, "Two-Dimensional sixteen channel transmit/receive coil array for cardiac MRI at 7.0 T: Design, evaluation, and application," *J. Magn. Reson. Imaging*, vol. 36 (4), pp. 847–854, 2012.

[15] L. Winter *et al.*, "Design and Evaluation of a Hybrid Radiofrequency Applicator for Magnetic Resonance Imaging and RF Induced Hyperthermia: Electromagnetic Field Simulations up to 14.0 Tesla and Proof-of-Concept at 7.0 Tesla," *PLoS One*, 2013.

[16] A. B. Rosenkrantz *et al.*, "T2-weighted prostate MRI at 7 Tesla using a simplified external transmit-receive coil array: Correlation with radical prostatectomy findings in two prostate cancer patients," *J. Magn. Reson. Imaging*, vol. 41, no. 1, pp. 226–232, 2015.

[17] A. J. E. Raaijmakers *et al.*, "The fractionated dipole antenna: A new antenna for body imaging at 7 Tesla," *Magn. Reson. Med.*, vol. 75, no. 3, pp. 1366–1374, 2016.

[18] IEC, "Medical electrical equipment. Part 2-33: particular requirements for the safety of magnetic resonance equipment for medical diagnosis.," *IEC 60601-2-33*, 2010.

[19] FDA, "Guidance for Industry. Guidance for the Submission Of Premarket Notifications for Magnetic Resonance Diagnostic Devices," *Fda*, pp. 1–30, 2016.

[20] E. M. Haacke, R. W. Brown, M. R. Thompson, and R. Venkatesan, *Magnetic Resonance Imaging: Physical Principles and Sequence Design*. 1999.

[21] L. Winter and T. Niendorf, "Electrodynamics and radiofrequency antenna concepts for human magnetic resonance at 23.5 T (1 GHz) and beyond," *Magn. Reson. Mater. Physics, Biol. Med.*, vol. 29, no. 3, pp. 641–656, 2016.

[22] Y. Zhu, L. Alon, C. M. Deniz, R. Brown, and D. K. Sodickson, "System and SAR characterization in parallel RF transmission," *Magn. Reson. Med.*, vol. 67, no. 5, pp. 1367–1378, 2012.

[23] F. Padormo, A. Beqiri, S. J. Malik, and J. V. Hajnal, "RF system calibration for global Q matrix determination," *Magn. Reson. Imaging*, vol. 34, no. 5, pp. 690–693, 2016.

[24] D. M Pozar, *Microwave Engineering, 3rd Edition*. 2005.

[25] F. Bardati, A. Borrani, A. Gerardino, and G. A. Lovisolo, "SAR Optimization in a Phased

538843-L-bw-Steensma
Processed on: 17-12-2019
PDF page: 131

Array Radiofrequency Hyperthermia System," *IEEE Trans. Biomed. Eng.*, 1995.

[26] G. Eichfelder and M. Gebhardt, "Local specific absorption rate control for parallel transmission by virtual observation points," *Magn. Reson. Med.*, vol. 66, no. 5, pp. 1468–1476, 2011.

[27] M. De Greef, O. Ipek, A. J. E. Raaijmakers, J. Crezee, and C. A. T. Van Den Berg, "Specific absorption rate intersubject variability in 7T parallel transmit MRI of the head," *Magn. Reson. Med.*, vol. 69, no. 5, pp. 1476–1485, 2013.

[28] M. Le Garrec, V. Gras, M.-F. Hang, G. Ferrand, M. Luong, and N. Boulant, "Probabilistic analysis of the specific absorption rate intersubject variability safety factor in parallel transmission MRI.," *Magn. Reson. Med.*, 2016.

[29] Ö. Ipek, A. J. Raaijmakers, J. J. Lagendijk, P. R. Luijten, and C. A. T. Van Den Berg, "Intersubject local SAR variation for 7T prostate MR imaging with an eight-channel single-side adapted dipole antenna array," *Magn. Reson. Med.*, vol. 71, no. 4, pp. 1559–1567, 2014.

[30] H. Homann, P. B??rnert, H. Eggers, K. Nehrke, O. D??ssel, and I. Graesslin, "Toward individualized SAR models and in vivo validation," *Magn. Reson. Med.*, 2011.

[31] F. Meliado, E., A. J. E. Raaijmakers, M. Restivo, M. Maspero, P. R. Luijten, and C. A. T. van den Berg, "Database Construction for Local SAR Prediction: Preliminary Assessment of the Intra and Inter Subject SAR Variability in Pelvic Region," in *In: Proceedings of the 24th scientific meeting, International Society for Magnetic Resonance in Medicine, Singapore, 3660*, 2016.

[32] A. C. and W. K. and E. G. H. and K. H. and M. Z. and E. N. and W. R. and R. J. and W. B. and J. C. and B. K. and P. S. and H.-P. H. and J. Kuster, "The Virtual Family—development of surface-based anatomical models of two adults and two children for dosimetric simulations," *Phys. Med. Biol.*, vol. 55, no. 2, p. N23, 2010.

[33] A. A. Haghnejad, M. Gosselink, I. Voogt, D. W. J. Klomp, P. R. Luijten, and A. J. E. Raaijmakers, "Fixed-phase prostate imaging with a 8-channel transmit/receive dipole antenna array on a conventional 3T system," *Proc. 26th Annu. Meet. ISMRM, Paris, Fr.*, p. #1704, 2018.

[34] M. A. Ertürk, A. J. E. Raaijmakers, G. Adriany, K. Ugurbil, and G. J. Metzger, "A 16-channel combined loop-dipole transceiver array for 7 Tesla body MRI," *Magn. Reson. Med.*, vol. 00, pp. 1–11, 2016.

[35] M. A. Ertürk *et al.*, "Toward imaging the body at 10.5 tesla," *Magn. Reson. Med.*, vol. 00, pp. 1–10, 2016.

[36] R. W. Brown, Y.-C. N. Cheng, E. M. Haacke, M. R. Thompson, and R. Venkatesan, *Magnetic Resonance Imaging: Physical Principles and Sequence Design*. 2014.

[37] O. Ocali and E. Atalar, "Ultimate intrinsic signal-to-noise ratio in MRI," *Magn. Reson. Med.*, vol. 39, no. 3, pp. 462–473, 1998.

[38] A J. E. Raaijmakers and C. A. T. Van Den Berg, "Antennas as Surface Array Elements for Body Imaging at Ultrahigh Field Strengths," *Encycl. Magn. Reson.*, 2012.

538843-L-bw-Steensma
Processed on: 17-12-2019
PDF page: 132

7

538843-L-bw-Steensma
Processed on: 17-12-2019

Chapter 8

Geometry optimization of a dipole antenna array for 10.5T body imaging

Bart R. Steensma
Pierre-Francois van de Moortele
Arcan M. Ertürk
Andrea Grant
Gregor Adriany
Peter R. Luijten
Dennis W.J. Klomp
Cornelis A.T. van den Berg
Gregory J. Metzger
Alexander J.E. Raaijmakers

In preparation

Abstract

Purpose

To improve imaging performance for body MRI with a local transmit array at 10.5T, the geometry of a sinusoidal dipole antenna is optimized to achieve lower peak SAR levels and a more uniform transmit profile.

Methods

EM simulations on a phantom were used to evaluate the SAR and B_1^+-performance of different dipole antenna geometries. The best performing antenna (the snake antenna) was simulated on human models in a 12 channel array configuration for safety assessment and for comparison to a previous antenna design. This 12 channel array was constructed, after which EM simulations were validated by B_1^+-maps and temperature measurements. After obtaining approval by the FDA to scan with the snake antenna array, in vivo imaging was done on two volunteers.

Results

Simulation results on a phantom indicate a lower SAR and a higher transmit efficiency for the snake antenna compared to the fractionated dipole array. These results are also found on a human model for the heart and the prostate, but not for the kidneys. When comparing the trade-off between uniformity and peak SAR, the snake antenna performs better for all imaging targets. Simulations and measurements are in good correspondence.

Conclusion

By changing the geometry of a dipole antenna, peak SAR levels could be lowered while achieving a more uniform transmit field as shown in simulations on a phantom and a human model. A 12 channel array of snake antennas was built and was used for in vivo imaging of 2 volunteers.

538843-L-bw-Steensma
Processed on: 17-12-2019
PDF page: 135

Introduction

The development of ultra-high field MRI (UHF, $B_0 \geq 7T$) has been driven by the promise of strongly increasing signal-to-noise ratio (SNR) with increasing B_0-field strength [1]–[6]. Increased chemical shift separation and enhanced susceptibility contrast are additional benefits of UHF MRI. While the benefits have been primarily presented in the human head, applications below the head in the human torso have been demonstrated. Applications in body at UHF have paralleled key developments in the radiofrequency (RF) hardware [7]–[15]. Since the first preliminary results of body imaging at 7T [7], the preferred RF transmit coil design has moved from a traditional whole-body birdcage resonator used commonly at 3T to local transmit coil arrays driven by multiple RF amplifiers as part of a parallel transmit system where multiple amplifiers are used to drive up to 64 separate transmit elements which can be excited with individually controlled waveforms[16–20]. A wide variety of different RF coil designs have been developed and tested for MRI. Resonant structures that are commonly used as transmit/receive elements include loop coils, strip-lines and dipole antennas. The use of the dipole antenna is becoming increasingly popular at UHF owing to the high penetration depth and the relatively uniform transmit field of these elements [8], [9], [12], [21]–[23].

In 2014, the first whole-body 10.5 T human scanner was installed at the Center for Magnetic Resonance Research (CMRR) in Minneapolis, Minnesota. The first RF coil designed and approved for human studies on this system happened to be for body imaging and consisted of a local transmit array based on fractionated dipole antennas has been presented by Ertürk et al [24]. With this body array at 10.5T, an increase in signal-to-noise ratio of more than two-fold was experimentally demonstrated in the center of a body-sized phantom compared to 7.0 T. However, simulations on a human body model indicated that 10g averaged peak local specific absorption rate (SAR_{10g}) for a given B_1^+-excitation homogeneity and number of pulses was always higher at 10.5 T than at 7.0 T. Given that peak local SAR is already a limiting factor at 7.0 T, devising strategies to address the increasing peak local SAR at 10.5 T becomes a critical issue to solve.

The geometry of a dipole antenna strongly influences the magnetic and electric fields that it emits [9], [22]. The peak SAR_{10g}, the B_1^+ per unit power (transmit efficiency) and the B_1^+ per unit peak SAR_{10g} (SAR efficiency) all depend on dipole antenna geometry. Previously, a sinusoidal geometry, henceforth referred to as the snake antenna, has shown good overall characteristics in 7T body imaging [25]. In this work, we present the optimization of the snake antenna's geometry to obtain maximum SAR efficiency for body imaging at 10.5 T. Results from the

538843-L-bw-Steensma
Processed on: 17-12-2019
PDF page: 136

RF array validation process and in vivo imaging at 10.5T are also demonstrated in human volunteers as part of a Food and Drug Administration (FDA) Investigational Device Exemption (IDE) safety study [26].

Methods

1. Antenna geometry optimization

Finite difference time-domain simulations (Sim4Life, Zurich Medtech, Zurich, Switzerland) were used to model two sinusoidally shaped dipole antennas on a phantom with tissue-like properties (σ = 0.37 S/m ε_r= 34). The geometry of the dipole antennas was varied by changing the number of periods, the width and the modulation.

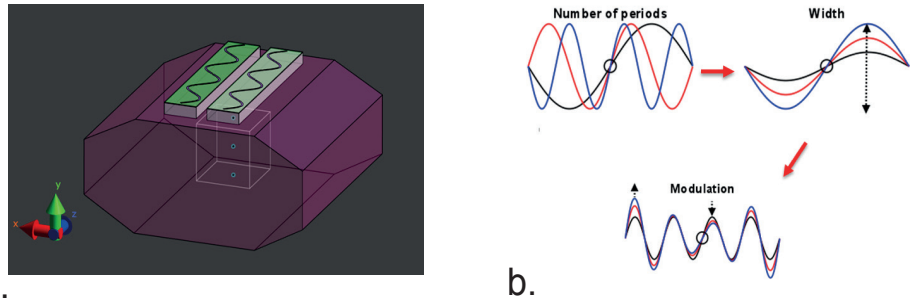

a. b.

Figure 1: optimization setup containing two dipole antennas (center-to-center distance 6 cm), on a phantom with tissue mimicking dielectric properties (ε_r=0.34, σ=0.4 S/m). The number of periods, the width and the modulation of the snake dipole were varied. B_1^+ was calculated in the 10*10*10 cm^3 cubical ROI, centered at 10 cm depth.

The length of the dipole antennas was kept equal to the length of the fractionated dipole antenna for 10.5T in all casesPhase shimming was applied on a cubic region of interest (ROI, 10 cm^3) located at a depth of 10 cm in the phantom. The different antenna geometries were evaluated by calculating the 10g-averaged peak SAR and by assessing B_1^+ in the ROI. The optimum antenna was selected based on the highest $B_1^+/\sqrt{SAR_{10g}}$ in the ROI.

2. Antenna array simulations

To determine safe limits of operation according to the IEC guidelines, EM-simulations were done in Sim4Life to assess peak local SAR levels for the snake antenna array. A 12-channel snake antenna array was simulated on the human models Duke and Ella[27] for four different imaging targets (prostate (Duke), uterus (Ella), Heart and kidneys). Electric and magnetic fields were exported to Matlab (Mathworks, Natick, USA) and re-sampled to a 5 mm isotropic resolution

538843-L-bw-Steensma
Processed on: 17-12-2019
PDF page: 137

to keep SAR calculations tractable. A post-processing script was used to calculate 10g averaged Q-matrices[28] and to calculate generalized virtual observation points[29], [30], (overestimation percentage 1%). Peak SAR values were calculated for all imaging targets. The worst-case SAR value out of all imaging targets was used to derive safe average power limits.

To compare the performance of the snake antenna array with a previous design[24] in a full array setup, two 12-channel setups were compared on the Duke model: a setup consisting of fractionated dipole antennas and a setup consisting of the snake antennas. Based on the simulated B_1^+ fields and the virtual observation points, an optimal shim drive was calculated to maximize transmit efficiency (B_1^+ per square root of P_{in}) and SAR efficiency (B_1^+ per square root of peak local SAR) separately using a constrained minimization procedure (fmincon, Matlab, Mathworks, Natick, USA), with a maximum input power of 1W per channel. The optimization was performed for regions of interest in the prostate, heart and kidneys. Additionally, to investigate coil performance in terms of uniformity and peak local SAR for different shim settings, L-curves were calculated for the fractionated dipole array and the snake antenna array on all imaging targets for Duke. A multi shift conjugate gradient (MSCG) algorithm was used to minimize the following least squares optimization problem:

$$\arg\min_x \left(\left\| Ax - m \right\|^2 + \lambda \left\| x \right\|^2 + \eta \sum_j \alpha_j \left\| S_j x \right\|^2 \right)$$

A is a matrix containing B_1^+ distributions for every channel, m is a vector containing the target B_1^+ (1 μT over the shimming ROI), x is a vector of complex coil weights and S_j is a sparse matrix containing the virtual observation points for peak local SAR calculation. The minimization was done for different values of the regularization η, and could be done simultaneously for different values of λ. After finding an optimal value for η, L-curves are plotted for the different values of λ.

3. Implementation of snake antenna array

An array of 12 snake antennas was built to conduct imaging studies. The dipole conductors were etched on a single-sided FR4 printed circuit board (EuroCircuits Gmbh, Kettenhausen, Germany). The dipoles were placed on 10-mm thick thermoplastic polyetherimide (ULTEM 1000 resin, Sabic Global, Pittsfield, MA) blocks. ULTEM block of 5 mm thickness were placed on top of the PCB to cover the conductors. The dipole antennas were tuned to resonance by two series capacitors (1 pF), matching was achieved by a lattice balun. All channels were

538843-L-bw-Steensma
Processed on: 17-12-2019
PDF page: 138

matched to -12 dB reflection or less. For a center-to-center distance of 6cm, inter-element coupling was lower than -13 dB.

4. Experimental safety assessment

All imaging experiments were done on a Siemens Magnetom whole-body 10.5T system (Siemens Healthcare, Erlangen, Gemany). For validation of the simulations, B_1^+-maps (actual flip angle method, TR 20/120 ms[12]) and Magnetic Resonance Thermometry maps (MRT, Proton-Resonance Frequency-shift method[13], TR 7.5 ms, input voltage 120 V, duty cycle 6.67%, total heating time 4*4:00 minutes) were acquired experimentally on the Siemens Magnetom 10.5T system. The experiments were performed with body size phantom filled with a Hydroxyethyl Cellulose (HEC) solution containing 2.97 g NaCl/L and 14 g HEC/L. These measurements were first done for a single channel of both the snake and fractionated dipole antennas and then for the complete 12 channel arrays both of which were subsequently compared to simulations.

5. In vivo imaging

Subjects provided written signed consent to participate in an FDA and IRB approved IDE safety study primarily investigating effects of static field exposure (REF). The two subjects imaged with the snake antenna array included a 43 year old female (89 kg, 180 cm, abdomen imaging) and a 41 year old male (86 kg, 178 cm, prostate imaging). For the pelvis imaging experiments, anatomical scout images and B1-maps are shown (AFI-method, TR/TE = 70/3 ms, resolution 2.73*2.73*8 mm^3, FA 50^0) .These images are shown as well for the abdominal study, where additionally a high-resolution anatomical image of the kidneys is shown (Fat-saturated 2D GRE, TR/TE 200/3.69 ms 0.83*0.83*5 mm^3, FA 18^0). All images were acquired during a breath-hold.

Results

1. Antenna geometry optimization

Increasing the meander width or the number of meanders, which corresponds to an increase in total conductor length, generally decreases transmit efficiency, but also decreases SAR. The effects of modulating these parameters and their impact on transmit efficiency, SARmax and SAR efficiency are shown in Figure 2.

538843-L-bw-Steensma
Processed on: 17-12-2019
PDF page: 139

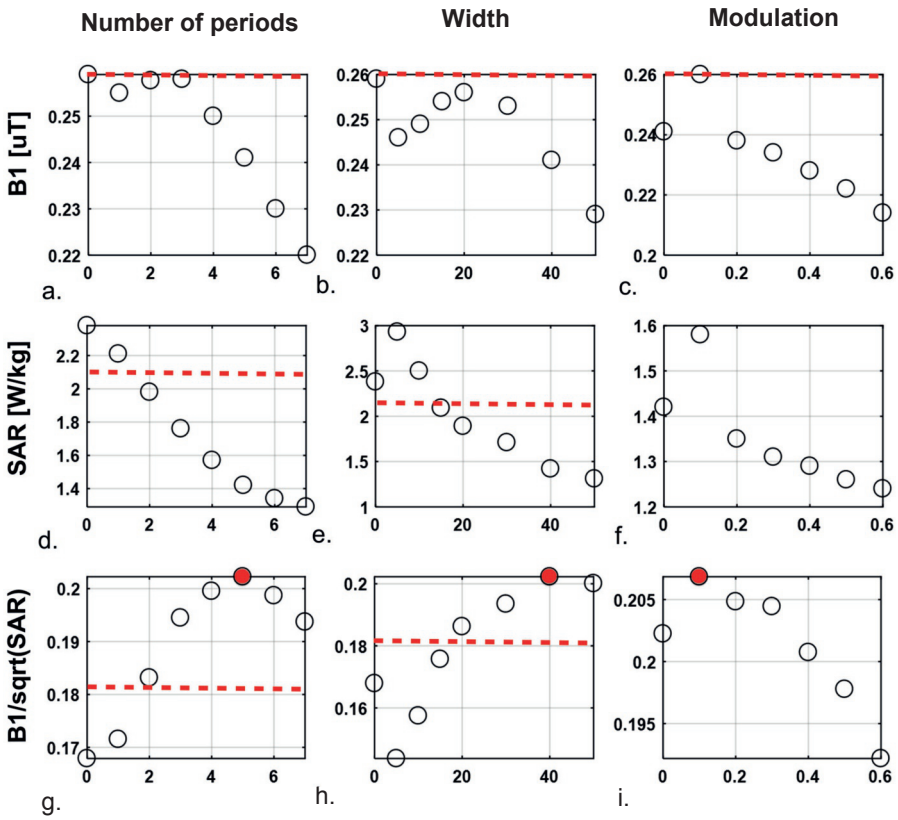

Figure 2: Resulting average B_1^+ in the ROI, peak SAR_{10g} in the phantom and SAR efficiency in the ROI. The effect of number of periods, width and modulation was optimized sequentially. Red dashed line indicates performance for the fractionated dipole array.

When considering SAR efficiency, an optimum can be observed for a number of 5 periods and a meander width of 40 mm. SAR efficiency improves 21% from 0.165 μT/√W/kg for a straight dipole to 0.2 μT/√W/kg for the optimal snake antenna design. Modulation of the antenna geometry in general has a less pronounced effect, SAR efficiency ranges between 0.206 and 0.192 μT/√W/kg, where a linear modulation of 0.1 results in the highest SAR efficiency. Figure 3 shows the current distribution together with the resulting SAR distributions for a single channel on a straight dipole as compared to the snake antenna. Modifying the conductor geometry removes the high current in the center of the dipole antenna. Because of the long conductor length, the first order resonant mode is removed. The effect is a significantly lower SAR for the snake antenna compared to a straight dipole.

538843-L-bw-Steensma
Processed on: 17-12-2019
PDF page: 140

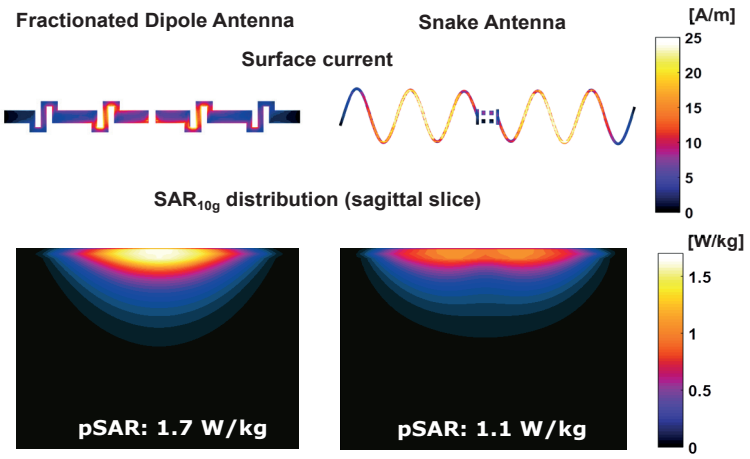

Figure 3: surface current distribution on a fractionated dipole antenna and on the new design of the snake antenna. The low current at the feed-point location of the snake antenna results in a lower peak SAR value.

2. Antenna array simulations - safety

For all shim targets, a worst-case SAR value of 0.5 W/kg is found (Ella, Heart) using 1W input power, uniformly divided over all channels. Based on an allowed peak SAR level of 20 W/kg, a per channel average power of 3.3 W/channel would be allowed.

2. Antenna array simulations – performance

A constrained minimization procedure (fmincon, Matlab, Mathworks, Natick USA) was used to to maximize the average B_1^+ in the shim target, while minimizing the input power or the peak local SAR as calculated from the VOPs. The same procedure was done for the previously designed fractionated dipole array[31]. The calculated field distributions are shown in figure 4.

538843-L-bw-Steensma
Processed on: 17-12-2019
PDF page: 141

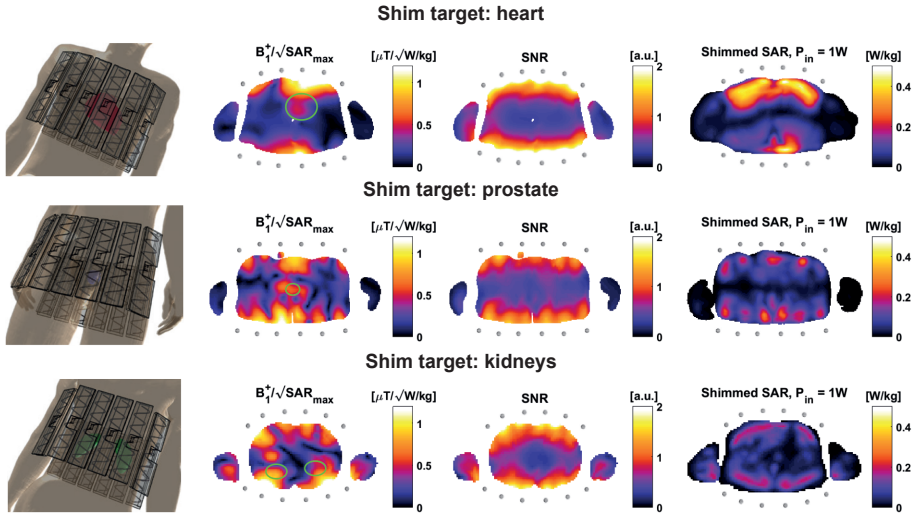

Figure 4: simulated field distributions in Duke for a 12 channel fractionated dipole array. B_1^+ was maximized in the imaging target, while maintaining a low as possible peak SAR_{10g} value.

For the prostate and the heart, the transmit efficiency increases moderately (+7% increase for the snake antenna array compared to the fractionated dipole array) while it decreases for the kidneys (-15%). The SAR efficiency is equal for prostate imaging, while for cardiac imaging the snake antenna array has a higher SAR efficiency (+11%) and for kidney imaging the snake antenna array has a lower efficiency (-15%). SNR decreases for all imaging targets [9], [22](-2.5%-1% and -11% for prostate, heart and kidneys) for the snake antenna array. The optimization values found in all shim targets are shown in table 1.

Shimtarget	Setup	Transmit Efficiency [μT/√W]	SAR efficiency [μT/√(W/kg)]	SNR [μT/√W]
Prostate	**Snake Antenna Array**	0.47 (+7%)	0.49 (+0%)	0.4 (-2.5%)
	Fractionated Dipole Array	0.44	0.49	0.41
Heart	**Snake Antenna Array**	0.44 (+7%)	0.21 (+11%)	0.7 (-2.5%)
	Fractionated Dipole Array	0.41	0.19	0.71
Kidneys	**Snake Antenna Array**	0.29 (-10%)	0.47 (-15%)	0.61 (-11%)
	Fractionated Dipole Array	0.32	0.54	0.68

Table 1: simulated transmit efficiency, SAR efficiency and SNR in three imaging targets: the prostate, the heart and the kidneys for the snake antenna and the fractionated dipole array.

Trade-off curves between RMSE and peak local SAR indicate that for all imaging targets in this comparison, lower RMSE values can be achieved with the snake

538843-L-bw-Steensma
Processed on: 17-12-2019
PDF page: 142

antenna array compared to the fractionated dipole array. For comparable RMSE values, lower peak SAR values are achieved with the snake antennas. Results of RMSE versus peak local SAR are plotted for the prostate, heart and kidneys of Duke in figure 5.

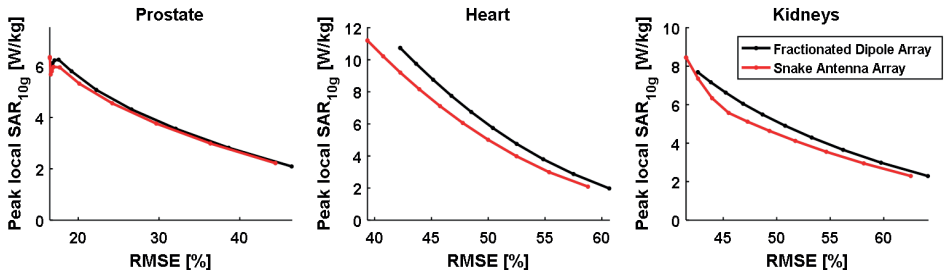

Figure 5: peak local SAR and root mean square excitation error (target B_1^+ 0.5 μT) showing the trade-off between uniformity and peak SAR for both arrays. For both the heart and the kidneys, lower RMSE-values as well as lower peak SAR values can be achieved with the snake antenna array.

3. Experimental safety assessment

Simulated B_1^+-profiles were compared to measurements for a single channel of the snake antenna and the fractionated dipole antenna. Results of this comparison are shown in figure 6.

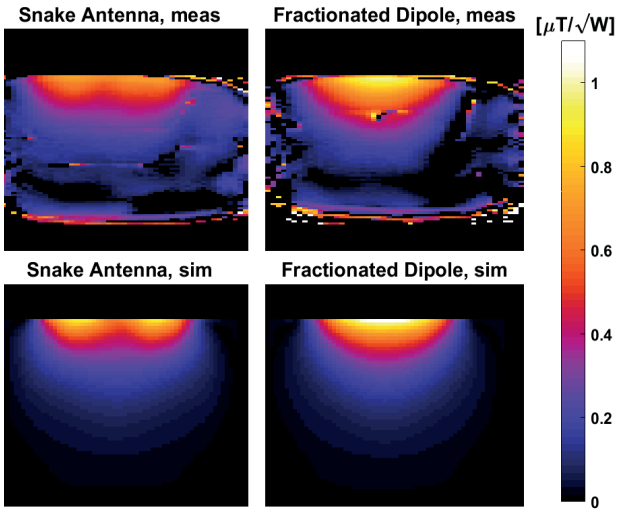

Figure 6: measured (top) and simulated (bottom) transmit efficiency in a sagittal slice through the center of a single snake antenna (left) and a single fractionated dipole antenna (right).

538843-L-bw-Steensma
Processed on: 17-12-2019
PDF page: 143

The snake antenna has a slightly lower transmit efficiency, especially in the center of the antenna. The simulated and measured transmit efficiency show the same patterns and magnitude. The same comparison was done for temperature measurements (MR thermometry) and thermal simulations, which is shown in figure 7.

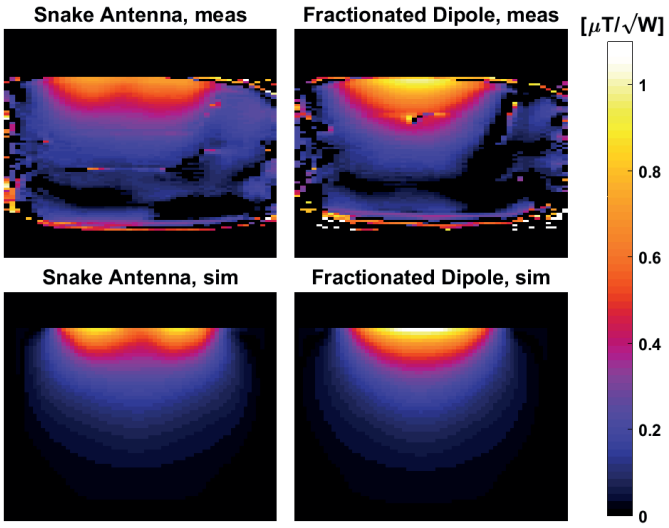

Figure 7: measured (top) and simulated (bottom) temperature rise in a sagittal slice through the center of a single snake antenna (left) and a single fractionated dipole antenna (right). RF heating was applied for a total heating interval of 12 minutes, using a time averaged input power of 20 W. The snake antenna reaches a lower temperature (2.6 ^{0}C versus 3.4 ^{0}C for the fractionated dipole). Simulated and measured temperature rise correspond very well in terms of field pattern and peak temperature (max deviation for the snake antenna, 2.6 ^{0}C measured versus 2.3 ^{0}C simulated).

538843-L-bw-Steensma
Processed on: 17-12-2019
PDF page: 144

4. In vivo imaging results

After validating the simulation results with measurements and obtaining IRB and FDA approval, two volunteers were scanned using the snake antenna array. The results are shown in figure 8.

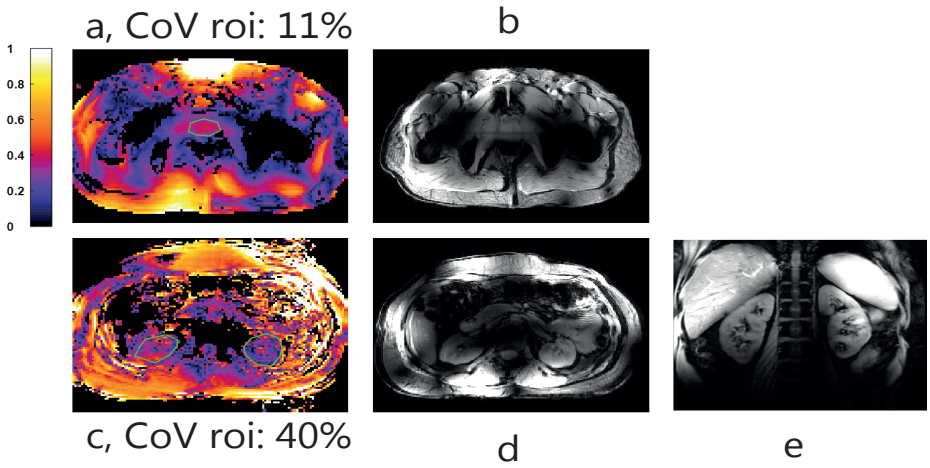

Figure 8: in vivo image of the pelvis (top row) and abdomen (bottom row). B1-maps (a and c) were acquired for both anatomies using the AFI method, as well as scout images (b and). For the kidneys, a fat suppressed coronal image is shown (e).

8a shows a B1-map on the prostate. The coefficient of variation (CoV, standard deviation divided by average of B_1^+) was calculated in the prostate. A CoV of 11% was achieved, indicating that a uniform flip angle can be achieve throughout the prostate. This is reflected in the uniformity of the scout image. For kidney imaging, a lower and less uniform B_1^+ is obtained in the kidneys (CoV 40%). This can be observed in the transverse scout image, where a non-uniform image intensity is visible in the kidneys. However, in the coronal anatomical image, signal intensity remains more uniform throughout the kidneys.

Discussion

This work demonstrates a comprehensive method for optimizing the transmit coil geometry based on a two port simulation on a phantom. The optimization results indicate that dipole antennas with a longer total conductor length (increased number of periods or increased width) have a lower SAR but also a lower transmit efficiency. Similar results were obtained in earlier work for straight dipole antenna with increased length. An optimum is found for an antenna with 5 periods, a conductor width of 40 mm and a modulation of 0.1. When comparing

538843-L-bw-Steensma
Processed on: 17-12-2019
PDF page: 145

the field distribution of a single snake antenna with a fractionated dipole antenna, it is observed that SAR is lower and B_1^+ is more evenly distributed in the z-direction. Close to the surface of the antenna, two peaks appear in the electric and magnetic fields, which indicate that a second order mode exists on the dipole antenna. This second order mode has a low current at the feed-port, resulting in a lower SAR for the snake antenna compared to a fractionated dipole. Transmit efficiency is also lower for the snake antenna, but especially for deeply situated imaging targets this effect is small. Therefore a known desirable characteristic of the dipole antenna (i.e. a more uniform transmit profile with depth[13], [22]) is accentuated with the snake antenna design.

The optimization results in improvements in SAR efficiency of 20% for the snake antenna as compared to a straight dipole. Compared to the fractionated dipole design in which only the inductance of the meander structure is optimized, SAR efficiency improves 10% for the snake antenna. For a full antenna array on human model Duke, the snake antenna improves transmit efficiency with 7% for the heart and the prostate. For the heart, SAR efficiency improves by 10%, while for the prostate the SAR efficiency remains equal. Coil performance is worse when imaging the kidneys, which are located more closely to the surface of the subject. However, the trade-off between uniformity (RMSE) and peak local SAR is better for the snake antenna array, as indicated by the L-curves in figure 5.

Other methods for decreasing SAR of dipole antennas have been reported by different groups, for example using a passive feed-point mechanism to lower SAR of the fractionated dipole antenna[32], increasing the subject-antenna distance[33], increasing the distance between the feed-point and the subject[34] or integrating materials with different dielectric properties in the dipole substrate[35]. Completely different antenna geometries with equivalent current distributions such as a slot antenna[36] or a dual-mode dipole antenna[37] can also be used to lower SAR.. A comparison study of these methods at different field strengths in the same simulation setup, or a combination of the methods could also be explored. The method that is used to find an optimal dipole antenna geometry is this work uses only two channels and a phantom, which deviates from the configuration in which the antennas are used (12 channels on a human subject). The results of this simple optimization procedure are partially confirmed in the full array configuration. The SAR efficiency of the snake antenna array is higher in the prostate and heart compared to the fractionated dipole antenna array, but also shows a higher transmit efficiency which is not seen in the optimization. Recent studies have considered dipole inductance, length[38] and topology[39] in a full array setup on respectively a phantom and a head model. Improvements

538843-L-bw-Steensma
Processed on: 17-12-2019
PDF page: 146

in performance can be expected when optimizing the snake antenna using such a method, but this will be very time intensive. The introduction of faster EM simulation methods[40] could resolve this problem, by enabling the possibility to quickly calculate the efficiency of many more antenna configuration and converge to an optimal design.

Conclusion

The conductor geometry of a sinusoidal dipole antenna was optimized for a two channel setup on a pelvis phantom at 10.5T. SAR efficiency was improved by 20% compared to two straight dipole antennas, and by 11% compared to two fractionated dipole antennas. In a 12 channel array on human model Duke, the snake antenna shows improved transmit efficiency (+7%) for the heart and the prostate and improved SAR efficiency in the heart (+11%) compared to the fractionated dipole array. For imaging of the kidneys, which are located closer to the surface of the body, the fractionated dipole showed a better performance. Simulations were validated by comparison to B_1^+ maps and temperature maps acquired with the PRFS method. A 12 channel array of snake antennas was built and was used for abdominal imaging at 10.5T

References

[1] W. A. Edelstein, G. H. Glover, C. J. Hardy, and R. W. Redington, "The intrinsic signal-to-noise ratio in NMR imaging," *Magn. Reson. Med.*, vol. 3, no. 4, pp. 604–618, 1986.

[2] O. Ocali and E. Atalar, "Ultimate intrinsic signal-to-noise ratio in MRI," *Magn. Reson. Med.*, vol. 39, no. 3, pp. 462–473, 1998.

[3] F. Wiesinger, P. Boesiger, and K. P. Pruessmann, "Electrodynamics and ultimate SNR in parallel MR imaging," *Magn. Reson. Med.*, vol. 52, no. 2, pp. 376–390, 2004.

[4] J. T. Vaughan *et al.*, "7T vs. 4T: RF power, homogeneity, and signal-to-noise comparison in head images," *Magn. Reson. Med.*, vol. 46, no. 1, pp. 24–30, 2001.

[5] M. P. Luttje, I. J. Voogt, M. Van Vulpen, P. R. Luijten, D. W. J. Klomp, and A. J. E. Raaijmakers, "First Proof of More Than Two-Fold Increase in Intrinstic SNR for Prostate Imaging at 7 Tesla in Comparison with 3 Tesla," in *Proc. Intl. Soc. Mag. Reson. Singapore*, 2016.

[6] B. Guérin *et al.*, "The ultimate signal-to-noise ratio in realistic body models," *Magn. Reson. Med.*, vol. 78, no. 5, pp. 1969–1980, 2017.

[7] J. T. Vaughan *et al.*, "Whole-body imaging at 7T: Preliminary results," *Magn. Reson. Med.*, vol. 61, no. 1, pp. 244–248, 2009.

[8] A. J. E. Raaijmakers *et al.*, "Design of a radiative surface coil array element at 7 T: The single-side adapted dipole antenna," *Magn. Reson. Med.*, vol. 66, no. 5, pp. 1488–1497, 2011.

[9] A. J. E. Raaijmakers *et al.*, "The fractionated dipole antenna: A new antenna for body imaging

538843-L-bw-Steensma
Processed on: 17-12-2019
PDF page: 147

at 7 Tesla," *Magn. Reson. Med.*, vol. 75, no. 3, pp. 1366–1374, 2016.

[10] B. R. Steensma *et al.*, "Comparing signal-to-noise ratio for prostate imaging at 7T and 3T," *J. Magn. Reson.*, 2018.

[11] A. B. Rosenkrantz *et al.*, "T2-weighted prostate MRI at 7 Tesla using a simplified external transmit-receive coil array: Correlation with radical prostatectomy findings in two prostate cancer patients," *J. Magn. Reson. Imaging*, vol. 41, no. 1, pp. 226–232, 2015.

[12] C. Oezerdem *et al.*, "16-channel bow tie antenna transceiver array for cardiac MR at 7.0 tesla," *Magn. Reson. Med.*, vol. 75, no. 6, pp. 2553–2565, 2016.

[13] M. A. Ertürk, A. J. E. Raaijmakers, G. Adriany, K. Ugurbil, and G. J. Metzger, "A 16-channel combined loop-dipole transceiver array for 7 Tesla body MRI," *Magn. Reson. Med.*, vol. 00, pp. 1–11, 2016.

[14] S. H. G. Rietsch, S. Orzada, A. K. Bitz, M. Gratz, M. E. Ladd, and H. H. Quick, "Parallel transmit capability of various RF transmit elements and arrays at 7T MRI," *Magn. Reson. Med.*, vol. 00, pp. 1–11, 2017.

[15] C. J. Snyder *et al.*, "Comparison Between Eight- and Sixteen-Channel TEM Transceive Arrays for Body Imaging at 7 Tesla," *Magn. Reson. Med.*, vol. 67, no. 4, pp. 954–964, Apr. 2012.

[16] G. J. Metzger *et al.*, "Local B1+ shimming for prostate imaging with transceiver arrays at 7T based on subject-dependent transmit phase measurements," *Magn. Reson. Med.*, vol. 59, no. 2, pp. 396–409, 2008.

[17] G. Adriany *et al.*, "Transmit and receive transmission line arrays for 7 tesla parallel imaging," *Magn. Reson. Med.*, vol. 53, no. 2, pp. 434–445, 2005.

[18] A. Graessl *et al.*, "Modular 32-channel transceiver coil array for cardiac MRI at 7.0T," *Magn. Reson. Med.*, vol. 72, no. 1, pp. 276–290, 2014.

[19] F. Padormo, A. Beqiri, J. V. Hajnal, and S. J. Malik, "Parallel transmission for ultrahigh-field imaging," *NMR Biomed.*, vol. 29, no. 9, pp. 1145–1161, 2016.

[20] S. Orzada *et al.*, "A flexible 8-channel transmit/receive body coil for 7 T human imaging," in *Proceedings of the 17th Annual Meeting of ISMRM, Honolulu, Hawaii, USA*, 2009, p. 2999.

[21] G. C. Wiggins, B. Zhang, R. Lattanzi, G. Chen, and D. K. Sodickson, "The Electric Dipole Array : An Attempt to Match the Ideal Current Pattern for Central SNR at 7 Tesla," *Proc. 20th Sci. Meet. Int. Soc. Magn. Reson. Med. Melb.*, vol. 23, no. 2008, p. 541, 2012.

[22] A. J. E. Raaijmakers, P. R. Luijten, and C. A. T. van den Berg, "Dipole antennas for ultrahigh-field body imaging: a comparison with loop coils," *NMR Biomed.*, vol. 29, no. 9, pp. 1122–1130, 2016.

[23] M. A. Ertürk, A. J. E. Raaijmakers, G. Adriany, K. Ugurbil, and G. J. Metzger, "Combined Loop-Dipole Transceiver Array for Body Imaging at 7 Tesla," in *Proc. Intl. Soc. Mag. Reson. Singapore*, 2016, pp. 884–894.

[24] M. A. Ertürk *et al.*, "Toward imaging the body at 10.5 tesla," *Magn. Reson. Med.*, vol. 00, pp. 1–10, 2016.

[25] B. R. Steensma, A. V. Obando, D. W. J. Klomp, C. A. T. van den Berg, and A. J. E. Raaijmakers, "Body imaging at 7 tesla with much lower SAR levels: an introduction of the Snake Antenna Array," in *Proc. Intl. Soc. Mag. Reson. Singapore*, 2016.

[26] A. Grant *et al.*, "Safety evaluation of human exposure to a 10.5T whole body magnet: protocol

538843-L-bw-Steensma
Processed on: 17-12-2019
PDF page: 148

design and preliminary results," in *Proc Intl Soc Mag Reson Med Montreal*, 2019, p. 797.

[27] A. C. and W. K. and E. G. H. and K. H. and M. Z. and E. N. and W. R. and R. J. and W. B. and J. C. and B. K. and P. S. and H.-P. H. and J. Kuster, "The Virtual Family—development of surface-based anatomical models of two adults and two children for dosimetric simulations," *Phys. Med. Biol.*, vol. 55, no. 2, p. N23, 2010.

[28] G. Carluccio, D. Erricolo, S. Oh, and C. M. Collins, "An approach to rapid calculation of temperature change in tissue using spatial filters to approximate effects of thermal conduction," *IEEE Trans. Biomed. Eng.*, vol. 60, no. 6, pp. 1735–1741, 2013.

[29] G. Eichfelder and M. Gebhardt, "Local specific absorption rate control for parallel transmission by virtual observation points," *Magn. Reson. Med.*, vol. 66, no. 5, pp. 1468–1476, 2011.

[30] J. Lee, M. Gebhardt, L. L. Wald, and E. Adalsteinsson, "Local SAR in parallel transmission pulse design," *Magn. Reson. Med.*, vol. 67, no. 6, pp. 1566–1578, 2012.

[31] M. A. Ertürk *et al.*, "Towards Imaging the Body at 10.5 Tesla Using a Fractionated Dipole Antenna Array," in *Proc. Intl. Soc. Mag. Reson. Singapore*, 2016.

[32] I. Zivkovic, C. A. Castro, and A. Webb, "Design and characterization of an eight-element passively fed meander-dipole array with improved specific absorption rate efficiency for 7 T body imaging," *NMR Biomed.*, no. March, p. e4106, 2019.

[33] A. A. Hurshkainen *et al.*, "On Optimization of Radiative Dipole Body Array Coils for 7 Tesla MRI," pp. 1–12, 2017.

[34] A. Sadeghi-Tarakameh *et al.*, "Optimizing the Topography of Transmit Coils for SAR Management," *Proc. Intl. Soc. Mag. Reson. Med. 26 Paris*, vol. 0297, 2018.

[35] A. Sadeghi-Tarakameh *et al.*, "A New Coil Element for Highly-Dense Transmit Arrays : An Introduction to Non-Uniform Dielectric Substrate (NODES) Antenna," in *Proc. Intl. Soc. Mag. Reson. Med. 27 Montreal*, 2019, p. 0732.

[36] L. Alon *et al.*, "Transverse slot antenna for high field MRI," *Magn. Reson. Med.*, 2018.

[37] M. P. Luttje *et al.*, "(31) P MR spectroscopic imaging combined with (1) H MR spectroscopic imaging in the human prostate using a double tuned endorectal coil at 7T.," *Magn. Reson. Med.*, vol. 72, no. 6, pp. 1516–21, 2014.

[38] J. Paška, M. A. Cloos, and G. C. Wiggins, "A rigid, stand-off hybrid dipole, and birdcage coil array for 7 T body imaging," *Magnetic Resonance in Medicine*, 2017.

[39] I. R. O. Connell and R. S. Menon, "Shape Optimization of an Electric Dipole Array for 7 Tesla Neuroimaging," *IEEE Trans. Med. Imaging*, vol. PP, no. c, pp. 1–1, 2019.

[40] J. F. Villena *et al.*, "Fast Electromagnetic Analysis of MRI Transmit RF Coils Based on Accelerated Integral Equation Methods," *IEEE Trans. Biomed. Eng.*, 2016.

538843-L-bw-Steensma
Processed on: 17-12-2019
PDF page: 149

Appendix A: supplementary material

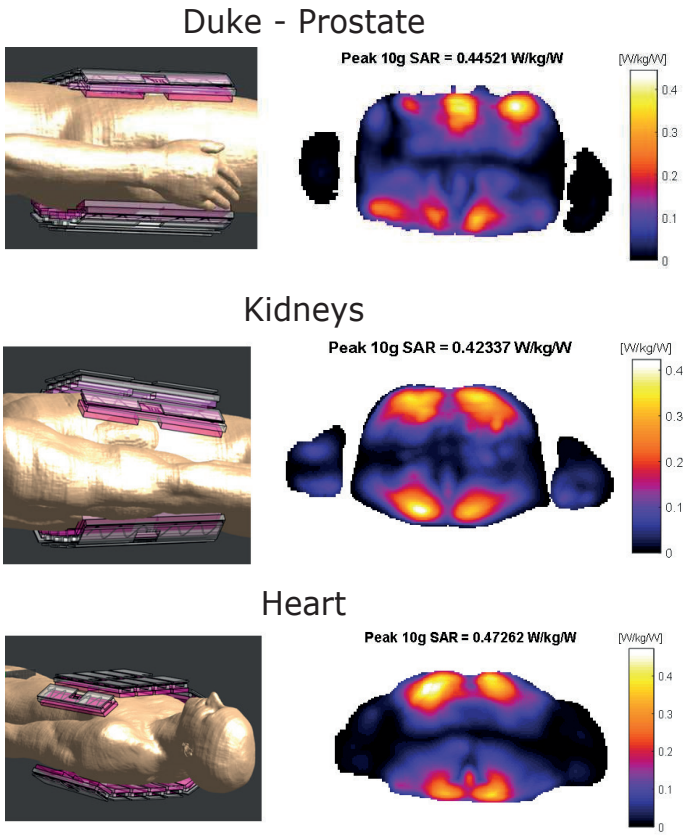

S1: Worst-case SAR distributions on Duke.

538843-L-bw-Steensma
Processed on: 17-12-2019
PDF page: 150

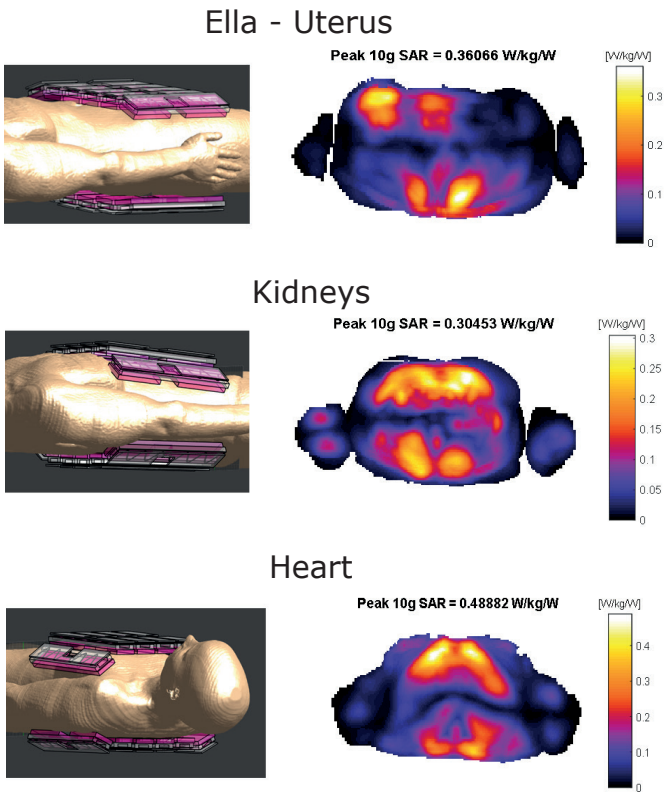

S2: Worst-case SAR distributions in Ella.

538843-L-bw-Steensma
Processed on: 17-12-2019
PDF page: 151

8

538843-L-bw-Steensma
Processed on: 17-12-2019

Chapter 9

Performance of a local 32-channel Tx/Rx-array for prostate imaging at 7T

Bart R. Steensma
Ingmar J. Voogt
Peter R. Luijten
Dennis W.J. Klomp
Cornelis A.T. van den Berg
Alexander J.E. Raaijmakers

In preparation

Abstract

Purpose

To decrease peak local SAR levels for ultra-high field body imaging, massively parallel transmit array configurations using up to 32 transmit receive channels were evaluated.

Methods

Simulations were used to evaluate the best possible coil performance in the pelvis of human model Duke. An EM FDTD solver was used to simulate 6 different coil array configurations with up to 32 transmit channels, which were compared and benchmarked against the ultimate possible coil performance. A 32 channel RF amplifier system was implemented as an add-on to a commercial 7T system. Three coil configurations from the simulation comparison were compared experimentally using the new amplifier system.

Results

Out of all coil arrays, coil array V (8 dipoles+24 loops) performs best, achieving 98% of the ultimate SAR efficiency, 63% of the ultimate transmit efficiency and 59% of the ultimate SNR. L-curves indicate that massively parallel transmit coils that combine loops and dipoles can be used to achieve more uniform flip angles at lower SAR values compared to our current 8 channel dipole array. Worst-case SAR values of 0.39 W/kg, 0.58 W/kg and 0.59 W/kg were found for array I (8 dipoles), IV (8 dipoles+16 loops), and V (8 dipoles+24 loops). Preliminary in vivo data was acquired with array IV.

Conclusion

For the first time, the ultimate possible coil performance is calculated for a human model for prostate imaging. With an array of 8 dipoles and 24 loop coils (array V), the ultimate possible coil performance can be most closely approximated. Massively parallel transmit coils that combine loops and dipoles can be used to achieve more uniform flip angles at lower peak SAR values , showing up to a two-fold improved efficiency compared to our current 8 channel coil array.

538843-L-bw-Steensma
Processed on: 17-12-2019
PDF page: 154

Introduction

Prostate imaging at 7T provides an intrinsic SNR increase of more than two-fold compared to 3T [1], [2]. The increased SNR can be used to acquire images at a higher spatial resolution or with increased acceleration factors. Since at 7T local body arrays are used instead of a volume birdcage coil, local SAR limits need to be considered for subject safety [3]. For sequences that require high flip angles like TSE sequences or adiabatic pulses, local SAR limits typically are the limiting factor for achievable repetition time or maximum flip angle.

At 7T, the type of local coil array that is used has a strong impact on the achievable SNR but also on peak local SAR levels. Dipole antennas have a more uniform transmit and receive field than loop coils and have a slightly better performance in deeply situated imaging targets [4]. For dipole antennas, the length of the conductor, the geometry and the electrical properties of the substrate all have effects on both local SAR and SNR [5]–[8]. Several strategies have been employed to further reduce local SAR levels for dipole antennas: increasing the antenna-subject distance [9], using a strongly meandering dipole [10], moving the feed-point further away from the dipole [11] or using a passive feed mechanism [12]. Combining different coil elements in an array can also be used as a mechanism to increase SNR in receive arrays [13] or to reduce local SAR in transmit mode [14]. Other type of coil elements have been developed such as transverse slot antennas [15], a dual-mode dipole antenna [16], strip-line arrays [17], [18] or multi-channel volume coils [19]. Although some coil arrays clearly outperform some others, no consensus exists over which coil is optimal for prostate imaging at 7T.

The work of Ocali and Atalar [20] introduced the ultimate intrinsic SNR (uiSNR), which is the highest theoretically possible SNR given a certain field strength and sample geometry. In an effort to optimize coil design from a more theoretical point of view, Lattanzi et al [21]. related the uiSNR to ultimate current patterns on a surface around the sample, thus providing more insight in what the optimal receive coil should look like. Lattanzi specifically studied the contribution of loop- and dipole-type elements to the uiSNR [22]. Until recently, all the simulation work on uiSNR was done on uniform phantoms. However, Guerin et al. recently developed a methodology to calculate uiSNR on a realistic model of the head [23]. The methodology of Guerin was shared online, and was be used to calculate a full electromagnetic basis given any sample geometry. The full electromagnetic basis is a set of vectors which converge to approximate any possible field distribution in the sample. Given the full electromagnetic basis, the ultimate possible SNR but also other efficiency metrics such as transmit efficiency and B_1^+ normalized to peak local SAR (SAR efficiency) can be calculated.

538843-L-bw-Steensma
Processed on: 17-12-2019
PDF page: 155

The first aim of this study was to calculate the ultimate theoretically possible coil performance for prostate imaging at 7T, using a realistic model of the pelvis of human model Duke of the virtual family [24]. In addition, a simulation study was done to compare different realistic coil arrays with an increasing number of transmit and receive channels to the ultimate possible coil performance. It is expected that using an increased number of transmit channels can be used to lower local peak SAR levels by distributing the deposited power over a larger area.

The second aim of this study is to demonstrate the integration of a 32 channel amplifier systems as an add-on to our current 7T system. Three coil array designs from the simulation comparison were built for experimental comparison. In vivo prostate images were acquired using a 24 channel coil array and the new amplifier system.

Methods

1. Simulations – ultimate intrinsic coil performance for 7T prostate imaging

To enable calculation of ultimate possible coil performance for 7T prostate imaging, a 'full basis' needs to be calculated: a set of electric and magnetic field 'basis vectors' that can be used to approximate any electromagnetic field in a given sample. Recently, Guerin et al. used a new method to calculate a full basis in a realistic human models. This method is based on Huygens's principle, which states that any electromagnetic (EM) field inside a closed volume can be generated by a current distribution flowing on the surface defining that volume [25].

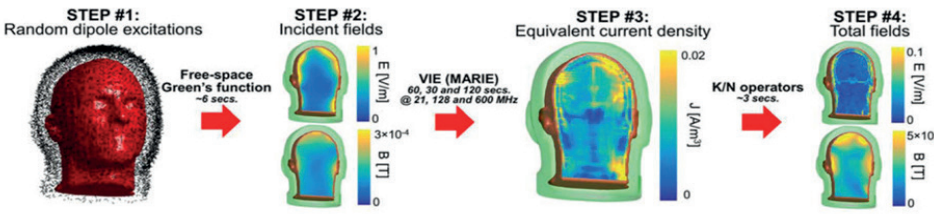

Figure 1: figure adopted from Guerin et al., showing the method for generating a full basis on a dielectric model of the head. A single basis vector consists of the fields generated by a random combination of dipoles positioned in a cloud around the model. The volume integral equation method is used to calculate the total fields in the head model resulting from the dipole excitation.

538843-L-bw-Steensma
Processed on: 17-12-2019
PDF page: 156

EM-fields inside the dielectric model are described by small dipole antennas located at the edges of every surface voxel. Three electric and three magnetic dipoles are located at every edge (dipoles for the +x, +y and +z direction). These dipoles are excited in a random fashion, after which a volume integral equation solver [26] is used to calculate the total EM-field in the model. The total electromagnetic field generated by the randomly exited dipoles together is referred to as a single basis vector. By choosing many basis vectors, or many different random combinations of dipole excitations, a full basis can be generated with a relatively small amount of basis vectors (several thousands of basis vectors can be used to express fields generated by more than a hundred thousand dipoles). This method is used to calculate a full basis of E- and H-fields in a cropped section of the human pelvis (Duke, 5x5x5 mm^3, 30x40x30 cm^3, using 3000 basis vectors.

After the full basis set was generated, we aimed to calculate the ultimate possible coil performance for prostate imaging by calculating three metrics: the uiSNR, but also the ultimate intrinsic transmit efficiency (uiTXE [27]) and SAR efficiency.

To calculate the uiSNR, a root-sum-of-squares combination of the receive fields B_r, vector of size $N_{vectors}$) and the noise covariance Ψ is done (size $N_{vectors}$x$N_{vectors}$):

$$SNR_{ui} = \sqrt{B_r{}^H \Psi^{-1} B_r} \qquad [1]$$

To check that sufficient basis vectors were included, SNR was calculated for an increasing number of basis vectors and convergence was verified.

To find the uiTXE values, the basis vectors need to be combined using optimal complex weighing coefficients (the weighing coefficients are referred to as the shim vector). A shim vector was calculated that maximizes transmit efficiency in an ROI in the prostate [27]. Considering a vector containing the transmit field B_t for every basis vector, a matrix contains the B_1^+ squared for every basis vector, averaged over all N_{voxels} in the ROI. The optimal shim vector for optimization of transmit efficiency are found by finding the eigenvector corresponding to the maximum eigenvalue of the generalized eigenvalue problem:

$$\Gamma w = \lambda \Psi w \qquad [2]$$

After finding the optimal shim vector, the full basis fields are combined and the uiTXE [27] is calculated in an ROI in the prostate as $B_{1\ roi}^+/\sqrt{P_{dep}}$, where P is the power deposited in the sample, which is calculated as:

538843-L-bw-Steensma
Processed on: 17-12-2019
PDF page: 157

$$P_{dep} = x^H Qx, Q = dV \sum_{i=1}^{N_{voxels}} \sigma(r_i) E(r_i) E(r_i)^H \quad [3]$$

Using the same shim vector, we calculate also the SAR efficiency in the prostate, which is defined as $B_1^+{}_{roi}/\sqrt{pSAR_{10g}}$, where $pSAR_{10g}$ is the 10g averaged peak local SAR value. Using this shim vector does not guarantee that the highest possible SAR efficiency is found, but the total power deposition in the sample is minimized which reduces the risk for local SAR.

2. Simulations – comparison of different coil array configurations

EM FDTD simulations were done in Sim4Life (Zurich MedTech, Zurich, Switzerland) to calculate electric and magnetic fields for 6 different coil configurations composed of different combinations of loop coils and dipole antennas. The number of transmit elements was varied between 8 and 32 channels, while the total length of the coil setups never exceeded 35 cm. All transmit elements were tuned to resonance using tuning methods available in Sim4Life. Figure 2 shows an overview of all investigated coil array designs.

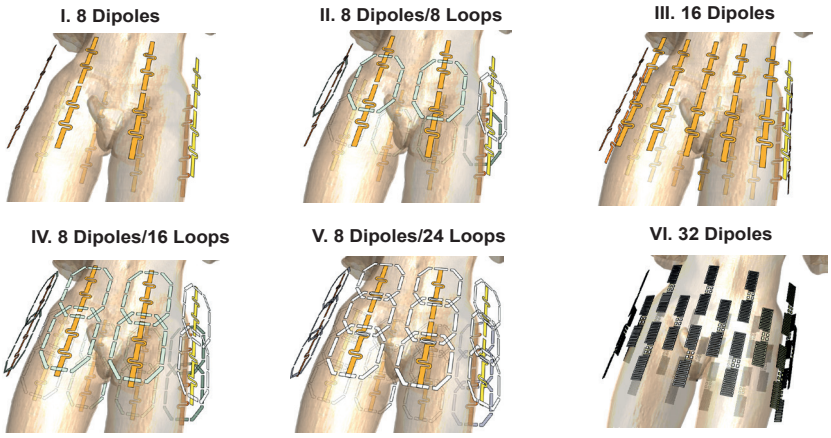

Figure 2: Sim4life visualization of Tx/Rx arrays on human model Duke. Six different combinations of loop and dipole elements with up to 32 Tx channels are considered in this work.

All fields were normalized to input power and electric and magnetic fields were extracted using a python script in the Sim4Life environment. Exported field distributions were regridded to a $5mm^3$ isotropic resolution to keep SAR calculations feasible. Electric fields were used to calculate Q-matrices for SAR calculation. The averaging method of Carluccio et al. was used for 10g averaging

538843-L-bw-Steensma
Processed on: 17-12-2019
PDF page: 158

of the Q-matrix entries. An accelerated [28] method for calculation of general virtual observation points (VOPs) was used to compress the Q-matrices into VOPs for rapid SAR calculation [29], [30].

After processing the simulation results, the same optimization methods as in section 1 were used to calculate intrinsic SNR, intrinsic transmit efficiency and SAR efficiency for the different coil arrays. Optimization results were compared against the ultimate intrinsic SNR, transmit efficiency and SAR efficiency.

To assess the coil performance in terms of uniformity and peak local SAR for different shim settings, an additional optimization routine was done for all Sim4Life coil configurations to generate tradeoff curves (L-curves) between root mean square excitation error (RMSE), peak local SAR and total input power. A cubical 10 cm^3 ROI was chosen in the center of the pelvis. Based on the method of Sbrizzi et al. [31], a multi shift conjugate gradient algorithm was used to minimize the following least squares problem in this ROI:

$$\arg\min_x \left(\left\| B_t x - m \right\|^2 + \lambda \left\| x \right\|^2 + \eta \sum_j \alpha_j \left\| V_j x \right\|^2 \right) \quad [4]$$

Here B_t is a matrix containing the B_1^+ distributions in the ROI for every channel, m is a vector containing the target B_1^+ (1 μT over the whole ROI), x is a vector of complex coil weights and V_j is a sparse matrix containing all the virtual observation points. The values λ and η are regularization terms which are varied in the optimization routine. The multishift conjugate gradient algorithm enables to do the minimization in one run for many different values of λ. This procedure was repeated for different values of η and after finding an optimal value for η, L-curves were plotted for the different values of λ. The available virtual observation points were used to calculate peak local SAR values. Virtual observation points could not be calculated for the full basis set, because the number of vectors in the set (3000, compared to max 32 for the coil arrays) was too large to calculate virtual observation points within a feasible time. Because of the unavailability of virtual observation points, local SAR calculations for a large number of drive vectors was also not possible within an acceptable time. Therefore the L-curve analysis was done only for the realistic coil arrays.

3. Simulations – safety

For array configurations I, IV and V, which are available for scanning, VOPs were used to calculate peak SAR for 10.000 random RF shims with 1W total deposited power and equal input power to all channels. All resulting SAR

538843-L-bw-Steensma
Processed on: 17-12-2019
PDF page: 159

values were plotted in a histogram, on which a gamma distribution was fitted. A peak SAR value was determined that would not be exceeded for 99.9% of all RF shims following the fitted gamma distribution [32]. This $pSAR_{99}$ is considered as the worst-case possible SAR value given maximum average input power to all channels. Based on the $pSAR_{99}$ value, a safe per channel average power limit is determined.

4. Amplifier system

A 32*1 kW amplifier system (Analogic, Peabody, MA, United States) was installed as an add-on to the Philips Achieva 7T system (Philips Healthcare, Best, The Netherlands). Figure 3 shows a schematic overview of the amplifier system.

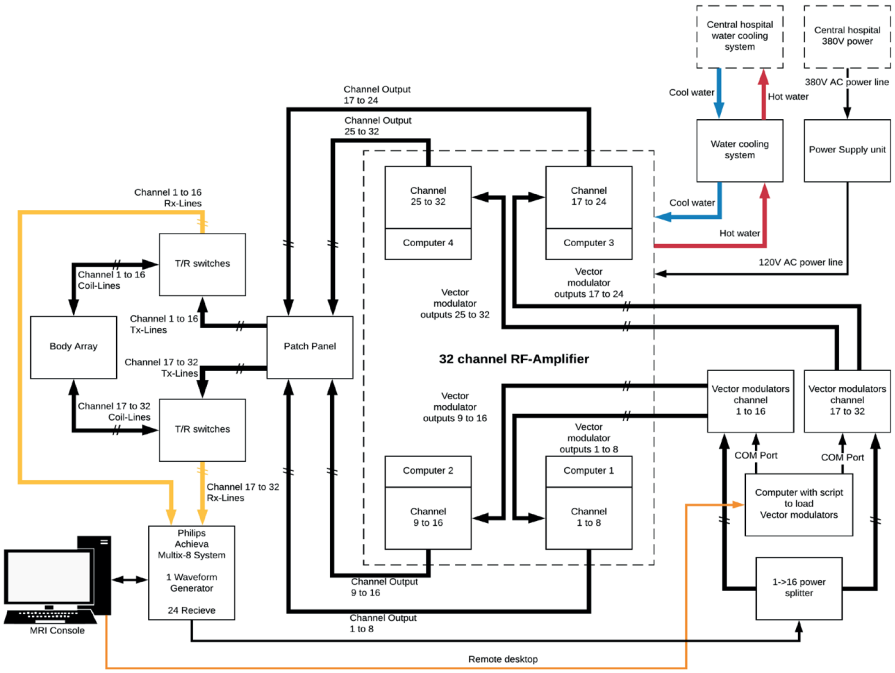

Figure 3: overview of the 32 channel RF amplifier system. 4a. schematic figure detailing the integration of the amplifier as an add-on to the Philips 7T Achieva system. 4b. 32 channel amplifier, connected with low loss coaxial cables to the patch panel (4c.) on the Faraday cage.

Blanking and RF waveforms were obtained from the amplifier and exciter board of the 1st channel on the Philips multi-transmit system. The RF waveform was fed into a 1 to 16 channel power-splitter (Mini-Circuits, Brooklyn, NY, United States), connected to 2 custom-built 16 channel I/O vector modulators that were used to control amplitude and phase of each amplifier output. The vector

538843-L-bw-Steensma
Processed on: 17-12-2019
PDF page: 160

modulators were controlled through a TeraTerm (Tera Term Project, Japan) interface on a host computer which was connected to the vector modulators with a COM-cable. Reaction time of the vector modulator to a trigger event was < 25 μs, with a minimum time of 100 μs between two triggers . The RF amplifiers were connected to the scanner system using 32 low-loss coaxial cables (8m cables, 0.3 dB losses, Sureflex Assembly, Mexico), going into two custom-built transmit/receive-switches (maximum insertion losses 0.53 dB, WaveTronica B.V., Utrecht the Netherlands). Peak power of the 32 amplifiers was monitored using dedicated monitoring software on a PC connected to every subset of 8 amplifiers. Additionally, safety monitoring was done using SAR predictions from the Philips system, which ensures before the sequence that the per channel average power limit is not exceeded. Figure 4 shows an image of the amplifier system.

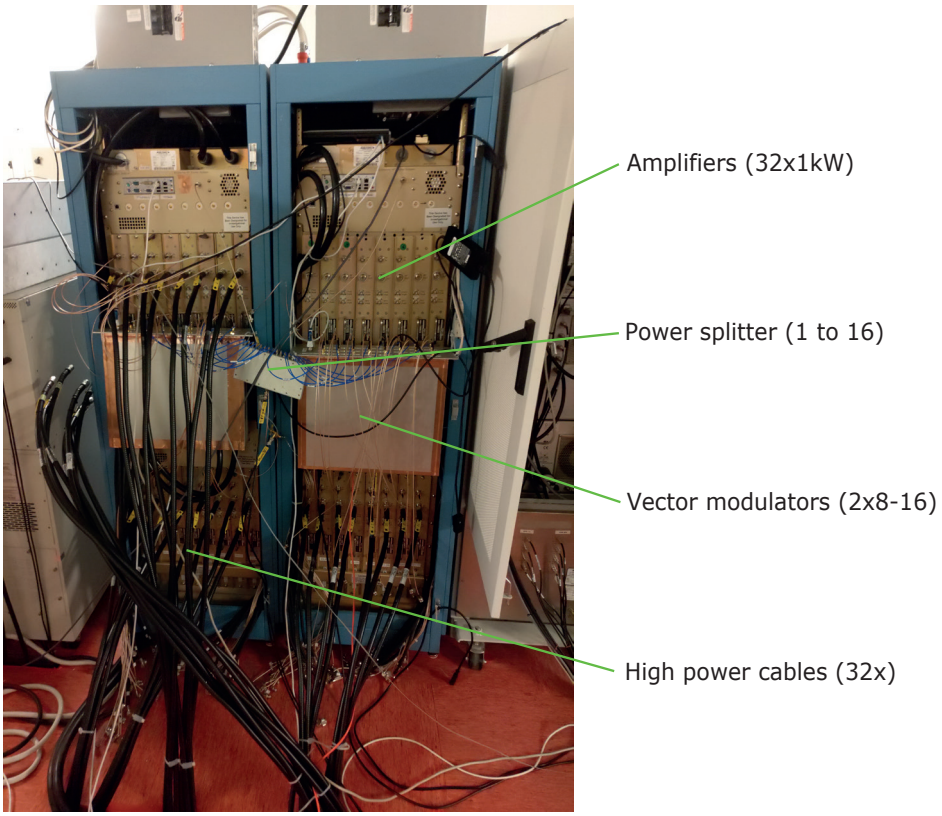

Figure 4: Complete amplifier system with specified subcomponents. 24 out of 32 amplifiers were operational at the moment of writing, 8 cables were not connected to the system for this reason.

538843-L-bw-Steensma
Processed on: 17-12-2019
PDF page: 161

5. Coil array implementation

Two arrays from the simulation comparison where prepared for testing on the 32 channel amplifiers system. Firstly, the coil array with 8 dipoles and 16 loops, which was available from earlier studies [33] was used. The best performing array, which combined 8 dipoles with 24 loops was constructed specifically for this study. Three loop coils (12 cm length, 8 cm width) were printed on an FR4 substrate (Eurocircuits N.V., Mechelen, Belgium), the adjacent loop coils overlapped 1.7 cm in the z-direction. The loops were tuned with eight 10 pF capacitors (American Technical Ceramics Corp, Huntington Station, United States) and matched with a 25 to 50 Ω lattice balun. The loops were placed on a 20 mm thick substrate (10 mm polycarbonate and 10 mm foam) to maintain distance between the subject and the loops coils. On top of the loops coils, a 4 mm thick layer of polycarbonate was placed on which the dipole antenna was positioned. The dipole antenna was tuned by two 18 pF series capacitors and matched using a 25 to 50 Ω lattice balun. For experiments on subjects, the transmit elements were placed in a leather holder which could be fixated around the pelvis of the subject.

7. In vivo imaging

After obtaining local IRB approval and informed consent, a 39-year old subject (m, BMI 25) was scanned using the coil array with 8 loops and 16 dipoles. B_1^+-maps (AFI-method [34]) were acquired with the full array using the and with both the loops and the dipole antennas separately.

Results

1. Simulations – ultimate intrinsic coil performance for 7T prostate imaging

Figure 5 shows the simulation results using the full basis set on the pelvis of dielectric model Duke. For an increasing number of basis vectors, convergence in the different voxels (surface, intermediate and central) increases. Convergence is slowest for the voxels near the surface, similar to results shown by Guerin et al [23]. For the input vector that maximizes transmit efficiency in the prostate, a SAR efficiency of 0.92 μT/√W/kg is found, with a peak local SAR_{10g} of 1.19 W/kg. The ultimate intrinsic SNR is 1.11 μT/√W.

538843-L-bw-Steensma
Processed on: 17-12-2019
PDF page: 162

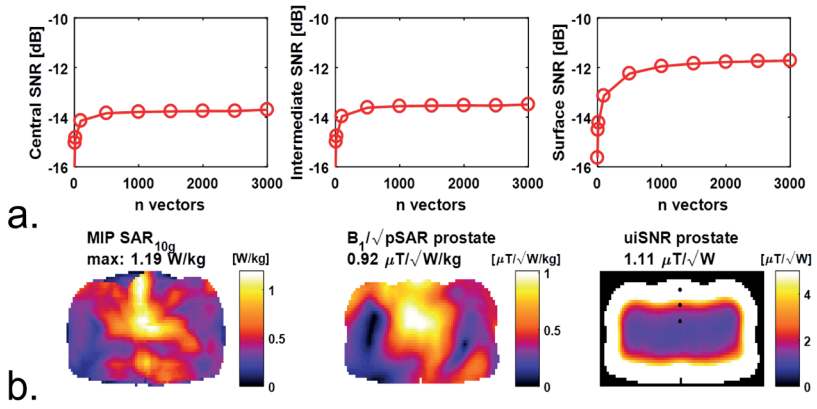

Figure 5: results of full basis calculations for a human model of the pelvis. 1a. shows convergence of SNR as a function of the number of basis vectors, in three different voxels (black dots) Reference value 0 dB = 1T. 1b. shows the optimized SAR, B1/√SAR and the ultimate intrinsic SNR in a slice through the prostate. The peak SAR_{10g}-value in the prostate, and the average B1/SAR and SNR in the prostate are displayed above the distributions.

9

2. Simulations – comparison of different coil array configurations

Simulation results on the prostate indicate that increasing the total number of transmit and receive channels improves imaging performance. Figure 6 shows the SAR efficiency, transmit efficiency and SNR for the different coil arrays as simulated in Sim4life, expressed as a percentage of the ultimate intrinsic SNR.

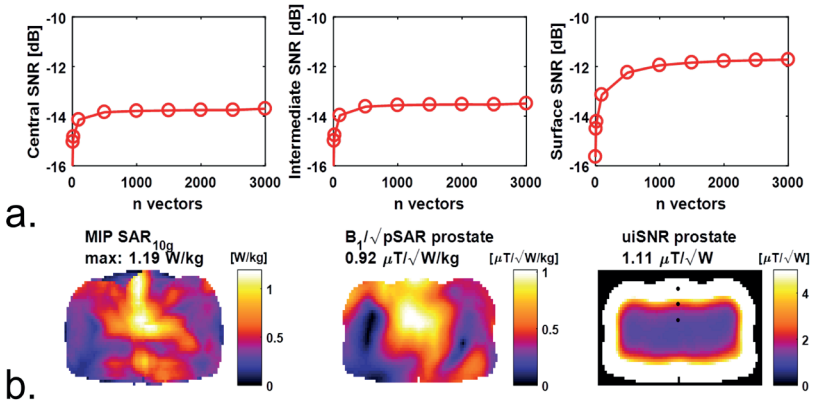

Figure 6: summarized results of Tx/Rx array comparison. SAR efficiency, transmit efficiency and SNR with respect to the ultimate performance, expressed in %.

The array with 8 dipole antennas and 24 loops (array V) performs best on all metrics. The SAR efficiency that is found for this array closely approaches the

538843-L-bw-Steensma
Processed on: 17-12-2019
PDF page: 163

SAR efficiency for the full basis (98%). However, only 62% of the ultimate transmit efficiency and 59% of the ultimate SNR is achieved with the best performing array. Our current array (array I) is outperformed two-fold on all metrics by array V. Array IV performs second best, closely followed by arrays II and III.

Figure 7 shows the tradeoff between peak local SAR and RMSE for the different coil arrays plotted as 'L-curves'. RMSE values were calculated on a relatively large ROI (10 cm^3) in the center of the pelvis. In generable, it is desirable to achieve low RMSE values and low peak SAR values which would result in values as close as possible to the origin of the graph. The lowest RMSE can be achieved with array V (8D+24L), which corresponds to the analysis on the prostate where array V also performs the best. However, array IV also performs very well, showing the lowest peak SAR values for a given RMSE. In general, lower RMSE values can be achieved with arrays that combine loops and dipoles (IV-VI), and with arrays with higher numbers of transmit channels. Results for input power are in general comparable to the results for peak local SAR, except for array III, which has a significantly lower power efficiency compared to the other arrays.

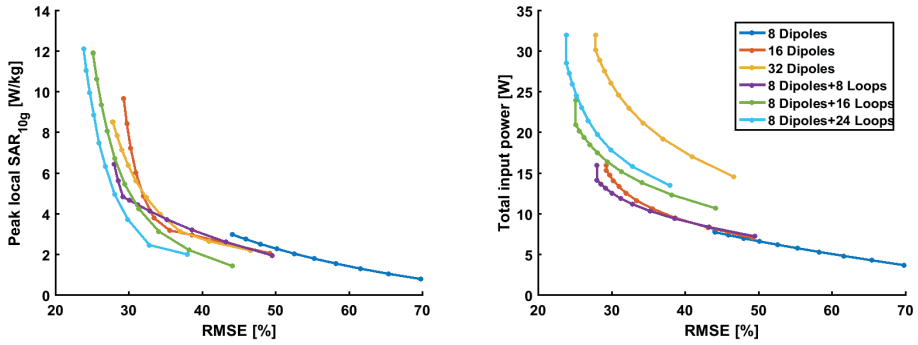

Figure 7: L-curves showing trade-off between root-mean-square excitation error and peak local SAR or total input power.

538843-L-bw-Steensma
Processed on: 17-12-2019
PDF page: 164

3. Simulations – safety

Figure 8 shows a histogram of peak local SAR values for 3 arrays that are available for scanning at our site (array I, IV and V).

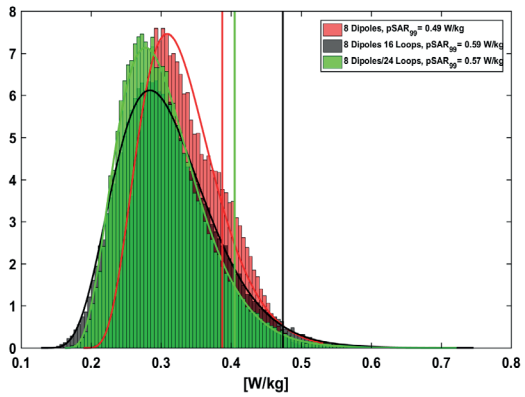

Figure 8: histogram of peak SAR_{10g} values given RF shimming with random input phase for the 8 channel and 32 channel array. The power deposited in the sample was 1W in total, equally distributed over all channels.

The average peak SAR is slightly higher for array I, which has 8 channels. However, $pSAR_{99}$ values are higher for array IV (0.59 W/kg) and V (0.58 W/kg) versus array I (0.39 W/kg). All SAR values are normalized to 1W total deposited power. For safety considerations, an average power limit of 20/(0.59*24)=1.4 W/channel would be allowed in first level controlled mode. An additional conservative safety factor of 2 was applied to account for inter-subject variability[32] and other sources of inaccuracy, leading to a per channel power limit of 0.7 W/channel for array IV which was used for in vivo experiments.

538843-L-bw-Steensma
Processed on: 17-12-2019
PDF page: 165

7. In vivo imaging

In vivo imaging was done using array configuration IV. B_1^+ maps are shown in figure 9. The contributions of the loop and dipole elements were considered separately. Consistent with results for SNR, combining the loops and dipoles improves the achievable B_1^+ to 9 μT, compared to 4 μT for the 8 dipoles and 5 μT for the 16 loops.

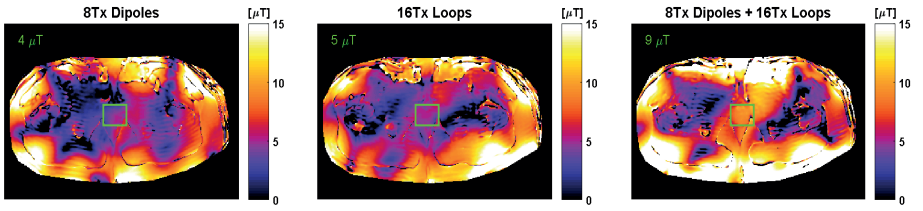

Figure 9: flip angle maps (AFI-method) acquired with 24 out of 32 transmit channels. Array configuration IV was used. Flip angle maps were compared for a situation with 8 dipoles, 16 loops and 8 loops+16 dipoles.

Discussion

The ultimate intrinsic transmit efficiency and SNR was calculated for the first time in a realistic human model of the pelvis.. For simulated coil arrays with a limited number of channels (up to 32 in this study for example), local SAR efficiency in a certain ROI can be maximized by extracting virtual observation points and running a numerical minimization procedure to find the highest possible B_1^+ in the ROI given a peak local SAR level of 1 W/kg. However, since the full basis consists of 3000 basis vectors, extraction of virtual observation points is not feasible. A closed form minimization such as is used to calculate ultimate intrinsic transmit efficiency is not possible for local SAR, it would require solving this minimization problem for all voxels simultaneously. Recently, a method has been suggested to calculate ultimate intrinsic SAR efficiency in an ROI [35], however this method does to our knowledge not guarantee that a global maximum is found for the SAR efficiency. An alternative method would be to calculate the lowest possible SAR for every voxel given a certain excitation profile, to calculate ultimate intrinsic SAR [36]. However, this will lead to excitation profiles where SAR is very low for one voxel but not for all voxels. As an alternative, we evaluated the RF shim that minimizes the power deposited in the sample, for the full basis set and for the realistic coil arrays.

The SAR efficiency that is found for the best performing realistic coil array is very close to the SAR efficiency for the full basis (98%). This could be the result of the RF shim drive that was chosen to calculate SAR efficiency for the full basis, which does not guarantee a global maximum is found. Ultimate intrinsic

538843-L-bw-Steensma
Processed on: 17-12-2019
PDF page: 166

transmit efficiency (62%) and SNR (59%) are lower for the best performing array. A previous study by Lattanzi et al. demonstrated that for the central voxel of a cylindrical phantom, approximately 80% of the ultimate SNR could be obtained using an array of 16 dipole antennas [37]. An array with 8 loops and 8 dipoles performed comparably but had a slightly lower central SNR. In the study by Lattanzi et al., the 16 dipole array performed best. However, array which combine dipoles and a high number of loops (such as array IV and V) were not included in this study. Differences between the sample geometry (a cylinder versus a pelvis model) could explain why the realistic coil arrays do not achieve 80% of the uiSNR.

The benefits of increasing the number of channels becomes even more evident when the trade-off between uniformity and peak local SAR is considered (figure 3). Increasing the number of transmit channels, and using a combination of loops and dipoles is beneficial for array performance in terms of uniformity and peak local SAR. Previous research has demonstrated that the electric fields of loops and dipoles can cancel out while maintaining constructive interference of the B_1^+ [38]. Other work has shown that distributing coil elements in the z-direction is beneficial for array performance [39], which could indicate why the arrays with more loop elements perform increasingly well.

One of the main motivators to increase the parallel transmit capacity of our system was the reduction of peak local SAR. The results in figure 2 and 3 indicate that when a proper RF shim is chosen, $B_1^+/\sqrt{pSAR}$ is two-fold higher with a 32 channel coil array than with our current 8 channel coil for the same B_1^+ value. However, a comparison of peak local SAR values for random RF shim vectors indicates that average peak local SAR values are not much lower for the 32 channel arrays and that worst-case SAR values are actually higher than for our current 8 channel coil. A comparison of the results in figures 2-4 indicates that the improvement in coil performance mainly comes from an improved transmit efficiency and improved control over the RF transmit field. The benefits of 32 channel transmit configurations can only be achieved if power limits are based on the actual predicted SAR level for that drive setting. If power limits are based on a worst-case SAR level, increasing the number of channels will not provide a benefit. Multiple strategies are available to evaluate local peak SAR, the most promising approach to use will be to use a deep-learning algorithm to estimate peak SAR based on B1-maps [40].

Other research sites have been working towards 7T systems with massively parallel transmit capabilities. Researchers from the Center of Magnetic Resonance Research in Minneapolis have simulated a coil array similar to array V, which

538843-L-bw-Steensma
Processed on: 17-12-2019
PDF page: 167

combines 8 dipoles with 24 loops. With this coil, they demonstrated improved performance compared to a 16 channel coil [41]. Researchers from the University of Duisburg-Essen have developed a 32 channel transmit system add-on [42], [43] which was used with a 32 channel remote coil arrays placed behind the covers of the magnet. This coil array was used to do full body imaging at 7T. A remote transmit array provides the benefit of a more clinical workflow. However, peak B_1 that is remoted for remote transmit arrays is lower which is a limiting factor for 7T body imaging.

Currently available massively parallel multi-transmit systems are in an experimental stage and have required large investments both in terms of research effort and resources. However, the performance gains (over two-fold improved efficiency compared to current setup) are so large that it is worthwhile to continue research on this topic. An important issue is the complexity of the workflow introduced by having 32 amplifiers. Solutions were a smaller number of amplifiers is used to drive massively parallel transmit coils (mode compression) could be used to simplify the workflow but this needs more practical demonstration. Finally, more advanced pTx methods [44] such as spokes pulses, SPINS pulses or kT-points have been shown advantageous for massively parallel transmit coils [41]. The availability of these methods will enable the true potential of massively parallel transmit MRI. However, for our current amplifier system dynamic pTx methods are not available as the minimum delay time (100 μs between trigger events) of the vector modulator that is currently used is not sufficiently short. Further improvement in the performance of our current system and coil will be expected when dynamic pTx becomes available.

Conclusion

A full basis was calculated for a realistic model of the human pelvis, which enabled calculation of ultimately achievable coil performance for prostate imaging. 6 different array configurations were simulated in Sim4Life and compared against the ultimate possible coil performance. Array V (8 dipoles+24 loops) was the best performing array for prostate imaging, both in transmit and receive mode. When considering the trade-off between excitation error and peak SAR in a large ROI centered on the pelvis, this array achieved the lowest excitation error, but lower SAR values could be achieved with array IV (8 dipoles+16 loops). Worst-case SAR values were calculated for three arrays configurations (I, IV and V) which are all available for scanning. Average SAR levels are lower for the arrays with 24 and 32 elements in comparison to 8 elements but the worst-case SAR level is lower for the 8 element array. The implementation of a 32 channel RF amplifier as an add-on to a commercial 7T multi-transmit system is demonstrated, as well

538843-L-bw-Steensma
Processed on: 17-12-2019
PDF page: 168

as preliminary in vivo results acquired with array configuration IV.

References

[1] A. B. Rosenkrantz *et al.*, "T2-weighted prostate MRI at 7 Tesla using a simplified external transmit-receive coil array: Correlation with radical prostatectomy findings in two prostate cancer patients," *J. Magn. Reson. Imaging*, vol. 41, no. 1, pp. 226–232, 2015.

[2] H. M. De Feyter *et al.*, "Selective proton-observed, carbon-edited (selPOCE) MRS method for measurement of glutamate and glutamine^{13}C-labeling in the human frontal cortex," *Magn. Reson. Med.*, vol. 80, no. 1, 2018.

[3] IEC, "Medical electrical equipment. Part 2-33: particular requirements for the safety of magnetic resonance equipment for medical diagnosis.," *IEC 60601-2-33*, 2015.

[4] A. J. E. Raaijmakers, P. R. Luijten, and C. A. T. van den Berg, "Dipole antennas for ultrahigh-field body imaging: a comparison with loop coils," *NMR Biomed.*, vol. 29, no. 9, pp. 1122–1130, 2016.

[5] A. J. E. Raaijmakers *et al.*, "Design of a radiative surface coil array element at 7 T: The single-side adapted dipole antenna," *Magn. Reson. Med.*, vol. 66, no. 5, pp. 1488–1497, 2011.

[6] A. J. E. Raaijmakers *et al.*, "The fractionated dipole antenna: A new antenna for body imaging at 7 Tesla," *Magn. Reson. Med.*, vol. 75, no. 3, pp. 1366–1374, 2016.

[7] J. Paška, M. A. Cloos, and G. C. Wiggins, "A rigid, stand-off hybrid dipole, and birdcage coil array for 7 T body imaging," *Magnetic Resonance in Medicine*, 2017.

[8] C. Oezerdem *et al.*, "16-channel bow tie antenna transceiver array for cardiac MR at 7.0 tesla," *Magn. Reson. Med.*, vol. 75, no. 6, pp. 2553–2565, 2016.

[9] A. A. Hurshkainen *et al.*, "On Optimization of Radiative Dipole Body Array Coils for 7 Tesla MRI," pp. 1–12, 2017.

[10] B. R. Steensma, A. V. Obando, D. W. J. Klomp, C. A. T. van den Berg, and A. J. E. Raaijmakers, "Body imaging at 7 tesla with much lower SAR levels: an introduction of the Snake Antenna Array," in *Proc. Intl. Soc. Mag. Reson. Singapore*, 2016.

[11] A. Sadeghi-Tarakameh *et al.*, "Optimizing the Topography of Transmit Coils for SAR Management," *Proc. Intl. Soc. Mag. Reson. Med. 26 Paris*, vol. 0297, 2018.

[12] I. Zivkovic, C. A. Castro, and A. Webb, "Design and characterization of an eight-element passively fed meander-dipole array with improved specific absorption rate efficiency for 7 T body imaging," *NMR Biomed.*, no. March, p. e4106, 2019.

[13] B. R. Steensma *et al.*, "An 8 - channel Tx / Rx dipole array combined with 16 Rx loops for high - resolution functional cardiac imaging at 7 T," *Magn. Reson. Mater. Physics, Biol. Med.*, no. 0123456789, 2017.

[14] M. A. Ertürk, A. J. E. Raaijmakers, G. Adriany, K. Ugurbil, and G. J. Metzger, "A 16-channel combined loop-dipole transceiver array for 7 Tesla body MRI," *Magn. Reson. Med.*, vol. 00, pp. 1–11, 2016.

[15] L. Alon *et al.*, "Transverse slot antenna for high field MRI," *Magn. Reson. Med.*, 2018.

[16] G. Solomakha *et al.*, "The dual-mode dipole: A new array element for 7T body imaging with reduced SAR," *Magn. Reson. Med.*, vol. 81, no. 2, pp. 1459–1469, 2019.

538843-L-bw-Steensma
Processed on: 17-12-2019
PDF page: 169

[17] C. J. Snyder *et al.*, "Comparison Between Eight- and Sixteen-Channel TEM Transceive Arrays for Body Imaging at 7 Tesla," *Magn. Reson. Med.*, vol. 67, no. 4, pp. 954–964, Apr. 2012.

[18] S. H. G. Rietsch, H. H. Quick, and S. Orzada, "Impact of different meander sizes on the RF transmit performance and coupling of microstrip line elements at 7 T," *Med. Phys.*, 2015.

[19] S. H. G. Rietsch, S. Orzada, A. K. Bitz, M. Gratz, M. E. Ladd, and H. H. Quick, "Parallel transmit capability of various RF transmit elements and arrays at 7T MRI," *Magn. Reson. Med.*, vol. 00, pp. 1–11, 2017.

[20] O. Ocali and E. Atalar, "Ultimate intrinsic signal-to-noise ratio in MRI," *Magn. Reson. Med.*, vol. 39, no. 3, pp. 462–473, 1998.

[21] R. Lattanzi and D. K. Sodickson, "Ideal current patterns yielding optimal signal-to-noise ratio and specific absorption rate in magnetic resonance imaging: Computational methods and physical insights," *Magn. Reson. Med.*, vol. 68, no. 1, pp. 286–304, 2012.

[22] R. Lattanzi, G. C. Wiggins, B. Zhang, Q. Duan, R. Brown, and D. K. Sodickson, "Approaching ultimate intrinsic signal-to-noise ratio with loop and dipole antennas," *Magn. Reson. Med.*, vol. 00, pp. 1–15, 2017.

[23] B. Guérin *et al.*, "The ultimate signal-to-noise ratio in realistic body models," *Magn. Reson. Med.*, vol. 78, no. 5, pp. 1969–1980, 2017.

[24] A. C. and W. K. and E. G. H. and K. H. and M. Z. and E. N. and W. R. and R. J. and W. B. and J. C. and B. K. and P. S. and H.-P. H. and J. Kuster, "The Virtual Family—development of surface-based anatomical models of two adults and two children for dosimetric simulations," *Phys. Med. Biol.*, vol. 55, no. 2, p. N23, 2010.

[25] A. Ishimaru, *Wave propagation and scattering in random media*. 1999.

[26] J. F. Villena *et al.*, "Fast Electromagnetic Analysis of MRI Transmit RF Coils Based on Accelerated Integral Equation Methods," *IEEE Trans. Biomed. Eng.*, 2016.

[27] Georgakis, I.P., A. G. Polimeridis, and R. Lattanzi, "Ultimate intrinsic transmit efficiency for RF shimming," in *Proc. Intl. Soc. Mag. Reson. Med. 26 Paris France*, 2018, p. 0139.

[28] A. Kuehne, H. Waiczies, and T. Niendorf, "Massively accelerated VOP compression for population-scale RF safety models," in *Proceedings of the 24th Annual Meeting of ISMRM, Singapore*, p. 0478.

[29] G. Eichfelder and M. Gebhardt, "Local specific absorption rate control for parallel transmission by virtual observation points," *Magn. Reson. Med.*, vol. 66, no. 5, pp. 1468–1476, 2011.

[30] J. Lee, M. Gebhardt, L. L. Wald, and E. Adalsteinsson, "Local SAR in parallel transmission pulse design," *Magn. Reson. Med.*, vol. 67, no. 6, pp. 1566–1578, 2012.

[31] A. Sbrizzi, H. Hoogduin, J. J. Lagendijk, P. Luijten, G. L. G. Sleijpen, and C. A. T. Van Den Berg, "Fast design of local N-gram-specific absorption rate-optimized radiofrequency pulses for parallel transmit systems," *Magn. Reson. Med.*, vol. 67, no. 3, pp. 824–834, 2012.

[32] E. F. Meliadò, C. A. T. van den Berg, P. R. Luijten, and A. J. E. Raaijmakers, "Intersubject specific absorption rate variability analysis through construction of 23 realistic body models for prostate imaging at 7T," *Magn. Reson. Med.*, no. April 2018, pp. 2106–2119, 2018.

[33] B. R. Steensma *et al.*, "An 8-channel Tx/Rx dipole array combined with 16 Rx loops for high-resolution functional cardiac imaging at 7 T," *Magn. Reson. Mater. Physics, Biol. Med.*, 2017.

538843-L-bw-Steensma
Processed on: 17-12-2019
PDF page: 170

[34] V. L. Yarnykh, "Actual flip-angle imaging in the pulsed steady state: A method for rapid three-dimensional mapping of the transmitted radiofrequency field," *Magn. Reson. Med.*, vol. 57, no. 1, pp. 192–200, 2007.

[35] A. Sadeghi-Tarakameh, X. Wu, F. Ulus, Y. Eryaman, and E. Atalar, "Ultimate Intrinsic Specific Absorption Rate Efficiency," in *Proc. Intl. Soc. Mag. Reson. Med. 27 Montreal*, 2019, p. 4166.

[36] R. Lattanzi, D. K. Sodickson, A. K. Grant, and Y. Zhu, "Electrodynamic constraints on homogeneity and radiofrequency power deposition in multiple coil excitations," *Magn. Reson. Med.*, vol. 61, no. 2, pp. 315–334, 2009.

[37] R. Lattanzi, G. C. Wiggins, B. Zhang, Q. Duan, R. Brown, and D. K. Sodickson, "Approaching ultimate intrinsic signal-to-noise ratio with loop and dipole antennas," *Magn. Reson. Med.*, 2018.

[38] B. R. Steensma *et al.*, "Combining loops and dipoles at 7 T and 10.5 T: a simulation study," in *Proc. Intl. Soc. Mag. Reson. Honolulu*, 2017.

[39] J. Paska, J. G. Raya, and M. A. Cloos, "Fast and Intuitive RF-Coil Optimization Pipeline Using a Mesh-Structure," in *Proc. Intl. Soc. Mag. Reson. Med. 27 Montreal*, 2019, p. 0571.

[40] E. F. Meliadò, A. J. E. Raaijmakers, A. Sbrizzi, B. R. Steensma, P. R. Luijten, and C. A. T. van den Berg, "Deep learning method for image-based subject specific local SAR assessment," *Magn. Reson. Med.*, vol. In Press, 2019.

[41] M. A. Ertürk, X. Wu, G. Adriany, R. L. Lagore, K. Ugurbil, and G. J. Metzger, "An improved 32-channel loop-dipole transceiver array design for body imaging at 7.0 Tesla: Simulation study," *Proc. 26th Annu. Meet. ISMRM, Paris, Fr.*, 2018.

[42] S. Orzada *et al.*, "A 32-channel parallel transmit system add-on for 7T MRI," *PLoS One*, 2019.

[43] M. Floser, A. K. Bitz, S. Orzada, K. Solbach, and M. E. Ladd, "Comparison of Local and Remote Transmit Arrays for Body Imaging at 7T under Power and Local SAR Constraint," in *Proc. Intl. Soc. Mag. Reson. Med. 23 Milan Italy*, 2015, p. 0549.

[44] F. Padormo, A. Beqiri, J. V. Hajnal, and S. J. Malik, "Parallel transmission for ultrahigh-field imaging," *NMR Biomed.*, vol. 29, no. 9, pp. 1145–1161, 2016.

538843-L-bw-Steensma
Processed on: 17-12-2019
PDF page: 171

Chapter 10

Summary and discussion

Summary

Magnetic resonance imaging of the body is used in the diagnosis of common diseases such as prostate cancer, ischemic heart disease or spinal cord abnormalities. In an effort to further improve image quality, the first human 7T MRI system was installed in 1999 [1]. After first attempts to apply this technology to imaging targets within the body, it has become widely recognized that the available RF technology needs to be improved to achieve the full potential of 7T for diagnostic purposes [2]. Building upon a wide range of developments on RF antennas in the field of MRI, we aimed to further improve RF antenna performance for 7T body MRI. Improvements in antenna design can only be properly tested when used for the intended imaging application. The two imaging applications in this project both focus on highly prevalent diseases, prostate imaging (diagnosis of prostate cancer) and cardiac imaging (commonly used for diagnosis of ischemic heart disease). The antenna arrays that were developed during the course of this project were all evaluated with either one or both of these applications in mind.

The first effort to improve the dipole array for prostate imaging resulted in a new antenna, 'the forward view antenna' which was placed against the perineum as an alternative for the endo-rectal coil. Chapter 4 demonstrates the design and evaluation of this coil, reporting an SNR improvement of 19% when adding this coil to a dipole transceiver array. An alternative approach for improving SNR is to add receive only loops to a dipole array. Wiggins et al. demonstrated that this improves SNR by 50%[3]. This method was tested in chapter 4 for prostate imaging where 16 receive-only loop coil elements were added to an 8-channel transceiver array of dipole antennas. SNR at 7T was compared to 3T for five voluntary subjects and one patient. Reported improvements ranged between 1.7-fold and 2.8-fold. The array that was tested in chapter 4 for prostate imaging, was modified for cardiac imaging by including two dipole elements that have a bend in the middle for easy positioning on the torso. Experimental results indicated that also for cardiac imaging, SNR improved 50% when using a combination of loops and dipoles compared to a dipole only array. The improved SNR was used to acquire cardiac CINE images at unprecedented spatial resolution. Results of this study were reported in chapter 5.

A basic consideration in coil development and coil performance is the RF safety of coil arrays. The energy that is deposited in the body by the RF excitation field can lead to local tissue heating, which is a more prominent effect at ultra-high field strengths. To study the RF safety of the loop-dipole array in cardiac imaging more closely, 14 custom built simulation models were developed in chapter 6.

538843-L-bw-Steensma
Processed on: 17-12-2019
PDF page: 173

Using these models, the inter-subject variation of local SAR and temperature rise were studied. The simulation results were used to set safe limits of operation for 7T cardiac imaging without introducing unnecessary over-conservative local SAR limitations. Normally, SAR is either averaged over 6 minutes or over 10 seconds. In the latter case (10 seconds), the SAR limits are twice as high as for the 6 minutes averaging time. Temperature simulations in chapter 6 were used to show that the double SAR limits that exist for a 10 second scan, are also safe for a 20 second scan.

Based on on-going efforts to develop MRI beyond 7T, the RF safety and RF performance of antenna arrays as a function of B_0-field strength was studied in chapter 7. It was demonstrated that contrary to prior believes, peak local SAR increases linearly with field strength instead of quadratically. SNR increases quadratically with field strength instead of linearly. This demonstrates that when doing MRI beyond 7T, the benefits in terms of SNR are greater than the downside presented by increased local SAR. To deal with the increased SAR at field strengths beyond 7T, a new low SAR dipole antenna was developed for 10.5T body imaging; the results of this design are shown in chapter 8. With this new dipole design, 'the snake antenna', B_1^+ per unit SAR could be improved by up to 11% compared to the fractionated dipole antenna. FDA approval was obtained to scan human subjects with the snake antenna array at 10.5T. Finally, in chapter 9 an alternative strategy for lowering SAR is used which enables more transmit channels. It is demonstrated that the use of a 32 transceiver channel coil can greatly lower effective SAR levels compared to current 8 channel transmit coil arrays.

Discussion

Coil design

In this thesis, the versatility of dipole antennas for application in ultra-high field body imaging has been investigated. Not only where substantial gains in transmit efficiency obtained, but also more efficient and safe methods of RF excitation were developed for MRI at and beyond 7T. Traditional RF coils such as loop coils or strip-line resonators store energy in the near-field area, whereas in this thesis the radiative character of dipole antennas was optimized to enable maximum transfer of energy into radiation. Alternatively, the use of highly parallel transmit coils was investigated to distribute local power dissipation to achieve high efficiency without having high local SAR.

One important method to improve antenna performance at UHF is to use different antenna geometries. After the introduction of dipole antennas by Raaijmakers

538843-L-bw-Steensma
Processed on: 17-12-2019
PDF page: 174

et al [4]–[6], many groups studied the effect of dipole antenna geometry on coil performance [7]–[14]. Changing the dipole antenna geometry can lead to lower SAR levels, but this is typically achieved at the expense of lower SNR and transmit efficiency. Other groups have investigated the use of dipole antennas with increased space between the antenna and the subject [12], increased space between the dipole feed-point and the subject[14] and passive RF feed mechanism s[13]. All these methods report a trade-off between antenna efficiency and SAR. A more effective approach is to use additional transmit channels, as demonstrated in chapters 3 and 9. By distributing the energy flux over a larger entrance surface, SAR efficiency can be drastically improved as shown here for prostate imaging. In addition, results also show that using more channels benefits homogeneity. This is in line with other research showing that when spokes pulses are used for homogeneous RF excitation, increasing the channel count is beneficial for image uniformity [15], [16].

Currently, to our knowledge, 4 research sites in the world have the possibility of using a 32 channel RF transmit coil at 7T [15], [17]–[19]. The recently developed Siemens Terra clinical system and the Philips 7T multi-transmit systems only facilitate 8 transmit channels. Due to the high costs of a 32 channel RF-transmit system, it is currently unlikely that commercial parties will equip their 7T systems with such large channel counts. However, strong benefits of increasing the number of transmit channels were demonstrated in this work and by other groups. Solutions such as mode-compression [20] which enables the use of 32 channel coils on a 8 or 1 channel system could facilitate the introduction of large channel counts without the need for the same number of expensive amplifiers. Alternatively, on-coil amplifiers may be pursued which would reduce the required power considerably and, thereby, the costs.

With the development of metabolic imaging for the Metascan and MAP scan project [21], the design of multi-tuned RF coils becomes more important. Preliminary research shows the possibility of dual-tuned dipole antennas for phosphorus and proton imaging by use of LC-traps [22]. The use of dipole antennas in multi-tuned receive or transmit arrays could be beneficial for efficiency and could be used to increase the number of channels in a dual-tuned array. However, the benefits compared to other dual-tuning methods have yet to be demonstrated. Another recent publication shows the use of coaxial high-impedance coils for flexible coil arrays where the coils have low inter-element coupling [23]. It is not yet known if or how coaxial cables could be used to design dipole antennas, but the benefits that are shown for loop coils make this an attractive topic of research. Another research topic which has been strongly

538843-L-bw-Steensma
Processed on: 17-12-2019
PDF page: 175

developing in MRI is the use of metamaterials as an addition to RF coils to achieve better coil performance. Metamaterials have been successfully combined with dipole antennas before to achieve reduced coupling or lower effective SAR levels [24], [25]. Future possibilities lie in the design of frequency-selective RF shields with metamaterials, or dual-tuning of antennas using metamaterials.

Safety

According to the guidelines of the IEC, temperature, global SAR and local SAR levels may not exceed pre-defined limits. Standard procedure in RF safety assessment of coils is to simulate the coil on a human model and to calculate peak local SAR to set a maximum allowed average power for the coil which ensures that the SAR limits are not exceeded. A problem with this approach is that there can be a mismatch between the simulation model and the subject in the scanner leading to an underestimation of SAR. Multiple studies have investigated the effects of inter-subject variation on peak local SAR levels, and have calculated safety factors that can be applied to the SAR calculated with a single human model, to ensure that the SAR limits are not exceeded for any human model [26]–[28].

Another problem for peak SAR calculations in multi-transmit setups is that the local SAR depends strongly on the RF shim. Several methods exist to calculate a worst-case possible SAR value, the corresponding maximum power limit will ensure that any RF shim will be safe. However, this SAR value is highly unlikely to be achieved, and the related power limit will be overly conservative. A more rigorous approach to determine the maximum allowed average power is to do a statistical analysis of SAR levels for many different RF shims on multiple different human models, as shown by Meliado et al. for a 7T prostate imaging setup [29]. With this study design, inter-subject variation of SAR can be studied, the effect of different RF shims on the local SAR can be studied and maximum allowed power can be determined that ensures that SAR limits are not exceeded for 99.9% of all RF shims (the $pSAR_{99}$ value).The same approach was chosen in this work to study inter-subject variation of local SAR for 7T cardiac imaging (chapter 6). Additionally, temperature simulations were done to assess temperature rise for short cardiac examinations during a breath-hold (max 20s). By calculating the $pSAR_{99}$ level for different shim scenarios, more realistic SAR limits could be set for 7T cardiac imaging. For acquisitions shorter than 10 seconds, the IEC has set SAR limits that are twice as high as for the standard averaging time of 6 minutes. Because the SAR limits of the IEC are based on limits to absolute temperature and temperature rise, temperature simulations were used to see if the doubled SAR limits would also be safe for scans of 20 seconds. Based on the

538843-L-bw-Steensma
Processed on: 17-12-2019
PDF page: 176

temperature simulations that were done for the short breath-hold examinations, it was demonstrated that temperature rise remains so low that the double SAR limit is also safe for 20 second scans.

An even more promising approach is to do on-line subject-specific local SAR calculation based on MRI data. A first successful in-vivo demonstration was recently published by Meliado et al. who used deep-learning to learn a surrogate-model of the relation between B_1 and local SAR [30]. Based on a B_1-map, local SAR distributions were successfully predicted in vivo. Other methods use fast EM solver s[31] or update-methods [32] with segmented anatomy scans as an input, but have to our knowledge not yet been successfully validated in vivo. In future research, these methods could be used not only for safety assessment, but also to lower effective SAR levels or to deliberately achieve high SAR levels for hyperthermia treatment.

When the SAR of an RF coil is simulated, the simulation results need to be compared to measurements to check the validity of the simulations. In this work, chapter 5 and 8 include a validation of simulation results using two different methods. In chapter 5, only B_1-mapping methods are used to validate the simulations, while in chapter 9 also temperature measurements are used. A thorough validation study must be part of any RF coil safety assessment procedure. Such a procedure should be a prerequisite for scanning human subjects with custom built RF coils. Currently, no standard procedure exists for safety assessment of custom built coils. The International Society of Magnetic Resonance Imaging is currently working on a white paper containing the standard procedures for RF safety assessment of experimental RF hardware in a research setting. Some additional papers are available that contain full descriptions of the possible methodology and the achievable accuracy [33]–[35]. However, these methodologies offer no flexibility in which methods to include and especially on how accurate the simulations should be. Continuing from the work done during this thesis, we have drafted a standardized method for validation of RF coils based on a tier system. This approach is similar to the formalism for RF safety assessment of active implanted medical devices where flexibility is provided by four tier levels [36]. Each subsequent tier level consists of more extensive modeling and validation efforts, while reducing the overestimation of peak SAR levels. The proposed methodology is added in appendix I.

Applications

Prostate cancer is the most frequently diagnosed form of cancer in men in Europe and the US [37]. However, prostate cancer often has an unaggressive nature

538843-L-bw-Steensma
Processed on: 17-12-2019
PDF page: 177

and many men are unnecessarily treated which reduces their quality of life [38]. To enable more specific diagnosis of prostate cancer, 7T MRI is a potentially interesting diagnosis tool. We identified that 7T improves SNR for prostate imaging between 1.7-fold and 2.8-fold compared to 3T. This resulted in visibly improved quality of a T2w image of a prostate cancer patient. These results are in line with results presented by Metzger et al. who reported improved image quality for multi-parametric prostate MRI at 7T compared to 3T and results by Rosenkrantz et al.[39] who reported similar SNR gains when going from 3T to 7T. An important question that remains for 7T prostate imaging is the clinical relevance of the improved image quality and how to integrate new information into a clinical decision process. A currently running study in Utrecht (KWF 10810/2016-2) aims to improve clinical care for prostate cancer patients by using 7T MRI in combination with PET/CT to provide as much information as possible for the development of personal treatment plans. .

A limiting factor for 7T prostate MRI examinations is local SAR, which can limit the number of slices that can be simultaneously acquired (multi-slice efficiency) in for example a T2w –scan. A potential solution was shown by Maas et al. [40], who successfully implemented a clinical 7T prostate exam by using VERSE-pulses. Another solution could be avoid worst-case scenario and perform online local SAR calculations using the deep-learning approach of Meliado et al. [30], to set shim specific and patient specific SAR limits with minimal overestimation of local SAR.

The heart is another imaging application which is extensively studied at 7T [41]. Cardiac MRI is commonly used in the clinic to assess perfusion of a patient with ischemic heart disease. However, cardiac MRI examinations are lengthy and require complex planning procedures. First-pass gadolinium enhanced perfusion CMR is used for the evaluation of perfusion. Gadolinium based contrast agent administration is however not possible in all patients. The possibility to do native perfusion assessment at high resolution with non-contrast enhanced techniques, such as arterial spin labeling [42] or T_1 mapping [43] still has to be evaluated at 7T. Recent advances in cardiac imaging often employ several acceleration strategies involving compressed sensing to reconstruct 3d motion-resolved images of the whole heart [44]. The intrinsically improved acceleration performance at 7T which was demonstrated in this work could be beneficial for these kind of acceleration techniques. As a part of this thesis, the use of 7T MRI for cardiac cine imaging was studied. Figure 1 shows results of cardiac cine imaging (chapter 5) at 7T with increasing spatial resolution.

538843-L-bw-Steensma
Processed on: 17-12-2019
PDF page: 178

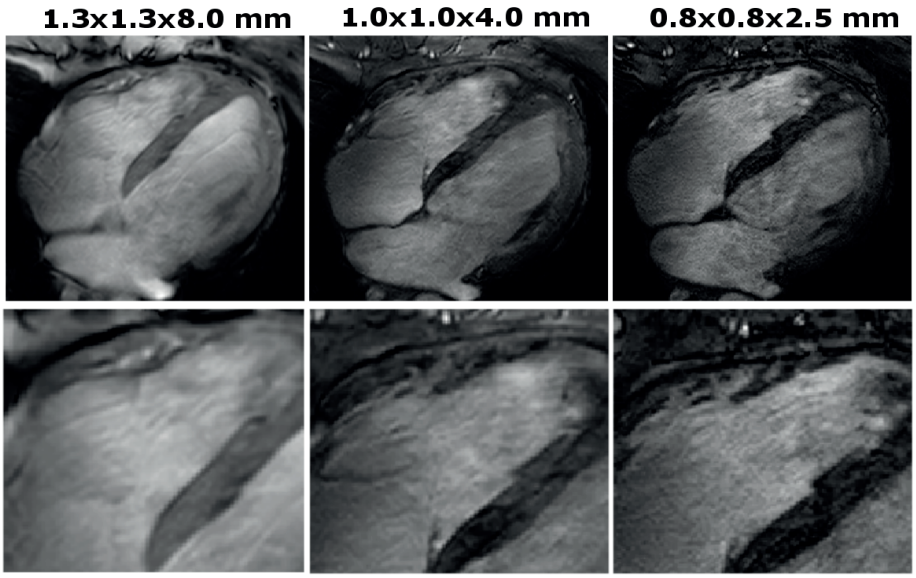

Figure 1: 7T cine images of the heart (4-chamber view) for increasing spatial resolutions.

The details that become visible in and around the myocardium are a topic of ongoing research. An earlier study has investigated the visibility of myocardial crypts at 7T in patients with hypertrophic cardiomyopathy [45]. A study that is currently being completed in our group compared feature tracking of the right ventricle using different sequences and field strengths including 7T cine imaging at high resolution [46].

Even though cardiac imaging at 7T provides a severe challenge due increased RF and susceptibility artifacts the possibilities that exist to scan with higher resolution or with higher acceleration factors are still a strong motivation to go to 7T.

For all body imaging applications except prostate imaging, non-uniformity of the RF transmit field is an unresolved issue. An example is found in chapter 5, where 2 out of 8 volunteers have RF voids appearing in or around the heart. For imaging targets larger than the heart such as the liver, these problems become even more predominant. To mitigate RF non-uniformities, advanced parallel transmit methods (pTx) such as SPINS, spokes or kT-points can be used. A problem of pTx is the overall difficulty of the calibration procedure requiring a high expert level of the user, and the inability to accurately acquire all the necessary calibration data such as single channel B_1-data. This holds for advanced pTx methods, but even standard RF shimming suffers from the same

538843-L-bw-Steensma
Processed on: 17-12-2019
PDF page: 179

problem. A topic for further research could be the development of an automated pTx workflow, where calibration data is derived from an anatomical image, the optimization target is recognized and the RF pulse calculations are accelerated compared to current methods. Some steps in this workflow have already been automated or accelerated using deep-learning [30], [47], [48], but never with the aim of fully automatic the pTx workflow.

MRI beyond 7T

In 2019, around 100 7T MRI systems have been installed worldwide, 9.4T brain imaging is done in multiple research sites [49], the first results of a full body 10.5T MRI system have been shown [50] and 3 brain-only MRI systems at 11.7T are near operation. A couple of research sites around the world including a consortium in the Netherlands are working towards the development of a 14T MRI system.

Two of the main motivators for increasing the field strength beyond 7T is the promise of neuroimaging to study the function of the brain with resolutions of less than 100 μm [51] and to image metabolism dynamically to reveal brain chemistry non-invasively [52]. Fortunately, the challenges facing body imaging at 7T are predicting potentially the same solutions for brain imaging at even higher field strengths. Moreover, body imaging at these field strengths can likely also use the same RF concepts that solved the issue for 7T.

One major obstacle for gaining support for higher field strengths than 7T, is the strongly held belief across a large part of the MRI community how SAR and SNR would develop with higher field strengths. In general, as it is explained in text books [53], SNR is expected to increase only linearly with field strength while SAR is assumed to increase quadratically with field strength. These expectations are based on quasi-static assumptions, i.e. the wave character of the RF fields at higher frequencies is neglected. The results of our studies proves that this assumption does not hold at higher fields. The traditional explanation of SNR and SAR versus field strength is as follows:

The MRI signal as detected by the receive coil increases quadratically with field strength because 1) the available equilibrium magnetization M_0 increases linearly with B_0 and 2) the detected voltage increases linearly with the Larmor frequency and thus B_0 due to the stronger Faraday induction in the coil. As a result:

$$V_{signal} \sim B_0^{\,2} \qquad [1]$$

538843-L-bw-Steensma
Processed on: 17-12-2019
PDF page: 180

However, the receive coils also detectd noise. The noise voltage increases proportionally with the square root of the resistance of the coil.

$$V_{noise} \sim \sqrt{R_{coil}} \quad [2]$$

The resistance of the coil is a sum of the resistance due to copper losses R_{copper}, the resistance due to radiation losses R_{rad} and the resistance due to sample losses R_{sample}. For human MRI beyond 1.5T, sample losses are dominant and $R_{coil} = R_{sample}$. In the reciprocal case where the receive coil is considered as the source and the spin as the detector, the receive signal is expressed as the left-rotating part of the B_1-field that would be transmitted by the coil. The sample resistance is then caused by the power that is deposited in the sample due to eddy currents:

$$R_{sample} = \frac{P_{sample.loss}}{|I_{coil}|^2} = \frac{1}{|I_{coil}|^2}\frac{1}{T}\int_0^T \int_{sample} \sigma |E|^2 \, dV dt = \frac{1}{|I_{coil}|^2} \int_{sample} \frac{1}{2}\sigma |E|^2 \, dV \quad [3]$$

so R_{sample} is proportional to the square of the E-fields. E-fields are not generated directly but are caused by induction. In the quasi-static approximation:

$$E \sim \frac{\partial B}{\partial t} \sim \omega_{Larmor} \sim B_0 \quad [4]$$

Since E-fields increase linearly with B_0 [4], and since R_{sample} increases quadratic with the E-fields [3] and since the detected noise voltage increases with the square root of R_{sample} [2], overall the detected noise voltage increases linearly with B_0 and therefore also SNR increases linearly with B_0:

$$SNR = \frac{V_{signal}}{V_{noise}} \sim \frac{{B_0}^2}{B_0} \quad [5]$$

The local/global SAR level is defined as:

$$SAR_{local/global} = \frac{1}{V_{avg}} \int_{V_{avg}} \frac{\sigma}{2\rho} |E|^2 \, dV \sim {B_0}^2 \quad [6]$$

Since E-fields are assumed to scale linearly with B_0, SAR is assumed to increase quadratically with B_0 [6]. However, studying the ultimate limit of coil array performance as a function of field strength on homogeneous samples using

538843-L-bw-Steensma
Processed on: 17-12-2019
PDF page: 181

an analytical full wave model, Ocali et al. demonstrated already in 1998 that although SNR increases linearly at first, the increase as a function of field strength will become quadratic beyond 7T[54]. As he already anticipated in his introduction, his results demonstrate that the quasi-static approximation breaks down at higher field strengths and the assumptions as presented in the frame are incorrect. However, Ocali's analyses were performed on a homogeneous sample; not on a realistic human model. Chapter 7 has presented expected SNR levels for body imaging at various field strengths using a human model and realistic coil arrays. However, realistic coil arrays bear the disadvantage that they may not be optimal for that field strength. As a result, the trend of SNR and SAR as a function of B_0 may be misleading if the performance at low or high field strengths is biased due to suboptimal coil designs. Therefore, the analyses of chapter 7 has been complemented with a numerical analysis of the ultimate coil performance for these same field strengths. Results were presented at the ISMRM high field workshop 2019 in Dubrovnik [55] and have been included in this thesis (figure 2).

In line with results of chapter 7, SAR efficiency (peak local SAR per unit B_1^+ in the prostate) decreases with field strength, but not very rapidly after 7T, while SNR increased quadratically. Transmit and receive sensitivity decrease strongly when going from 3T to 7T, but actually increase when going beyond 7T. This increase seems remarkable and may not be expected at first. The reason is likely that this study focusses on a very small organ (prostate). With increasing field strength, the wavelength gets shorter which makes it easier to focus the B1 field at a small imaging target. For larger organs, such increase is not expected.

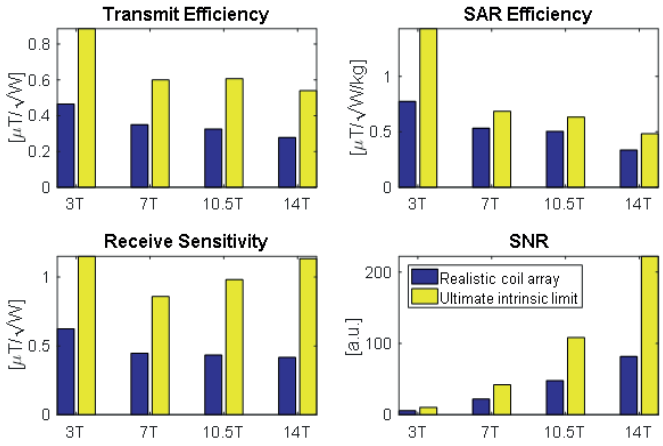

Figure 2: ultimate coil performance and the performance of a 16 channel transceiver coil for prostate imaging at 3T, 7T, 10.5T and 14T.

538843-L-bw-Steensma
Processed on: 17-12-2019
PDF page: 182

Nevertheless, these results indicate that in terms of electromagnetics, the benefits of MRI beyond 7T are expected to be greater than the downsides, even for organs in the middle of the body, like for prostate imaging. These results are corroborated by experimental results at 10.5T, which show improved transmit efficiency for prostate imaging [11] and the potential to do multi-parametric prostate imaging with very good image quality [50].

In fact, it may even be stated that 7T would be an unfortunate choice for a field strength. 7T introduces many challenges with respect to SAR assessment and B_1 inhomogeneity while the quadratic increase with B_0 has not really kicked in yet. However, especially 7T body imaging has set the challenges that prompted many technical development showing the technological roadmaps for higher field strength, even for the brain beyond 7T. Subsequent increments in field strength will require the same technologies as 7T to address these challenges but will profit from a much larger relative increase in SNR.

However, based on the results in figure 2 there appears to be an increasing difference between the ultimate possible coil performance and the 16 channel transceiver array in the simulations shown here. It is very likely that at UHF beyond 7T, more transmit and receive channels are needed to approach the ultimate coil performance. This hypothesis is in line with the results of chapter 9 and simulation studies at 10.5T[56]. Increasing the number of receive channels will require a more complex coil geometry and receive architecture than is commonly applied. However, successful implementations of coils with up to 128 receive channels have been demonstrated in the past [57], [58]. For RF transmit coils with high numbers of transmit channels, SAR management can become increasingly complex and on-line methods of local SAR calculation become more important to calculate SAR for different RF shims.

When targets other than the prostate are chosen, RF homogeneity becomes more difficult to achieve given the shortened wavelength in tissue. To mitigate RF nonuniformity, advanced pTx methods will need to be further developed to enable uniform proton MRI at 10.5T, 11.7T and 14T. Preliminary results shown by the Minnesota group indicate the need for pTx methods in liver imaging at 10.5T[50]. It is highly likely that at 14T, these methods are directly applicable for neuroimaging. An important point for improvement is the complex workflow of pTx methods. For successful application of body imaging at field strengths beyond 7T, this pTx workflow needs to be made more user-friendly. However, a main focus of MRI in the body at field strength beyond 7T lies in the application of metabolic imaging to detect phosphorus, deuterium, sodium, carbon or fluorine. The currently installed Metascan system which enables metabolic imaging at

538843-L-bw-Steensma
Processed on: 17-12-2019
PDF page: 183

7T should provide the groundwork to show what is to be gained for metabolic imaging at and beyond 7T.

References

[1] J. T. Vaughan *et al.*, "7T vs. 4T: RF power, homogeneity, and signal-to-noise comparison in head images," *Magn. Reson. Med.*, vol. 46, no. 1, pp. 24–30, 2001.

[2] J. T. Vaughan *et al.*, "Whole-body imaging at 7T: Preliminary results," *Magn. Reson. Med.*, vol. 61, no. 1, pp. 244–248, 2009.

[3] I. J. Voogt *et al.*, "Combined 8-channel transceiver fractionated dipole antenna array with a 16-channel loop coil receive array for body imaging at 7 Tesla," *Proc. 23th Sci. Meet. Int. Soc. Magn. Reson. Med. Vancouver*, vol. 200, no. 2007, p. 631, 2015.

[4] A. J. E. Raaijmakers, P. R. Luijten, and C. A. T. van den Berg, "Dipole antennas for ultrahigh-field body imaging: a comparison with loop coils," *NMR Biomed.*, vol. 29, no. 9, pp. 1122–1130, 2016.

[5] A. J. E. Raaijmakers *et al.*, "The fractionated dipole antenna: A new antenna for body imaging at 7 Tesla," *Magn. Reson. Med.*, vol. 75, no. 3, pp. 1366–1374, 2016.

[6] B. R. Steensma, A. V. Obando, D. W. J. Klomp, C. A. T. van den Berg, and A. J. E. Raaijmakers, "Body imaging at 7 tesla with much lower SAR levels: an introduction of the Snake Antenna Array," in *Proc. Intl. Soc. Mag. Reson. Singapore*, 2016.

[7] G. C. Wiggins *et al.*, "Mixing loops and electric dipole antennas for increased sensitivity at 7 Tesla," in *In: Proceedings of the 21th scientific meeting, International Society for Magnetic Resonance in Medicine, Salt Lake City*, 2013, vol. 21, p. 2737.

[8] G. C. Wiggins, K. Lakshmanan, and G. Chen, "The Distributed Inductance Electric Dipole Antenna," *Ismrm 2015*, vol. 23, p. 3100, 2015.

[9] J. Paška, M. A. Cloos, and G. C. Wiggins, "A rigid, stand-off hybrid dipole, and birdcage coil array for 7 T body imaging," *Magnetic Resonance in Medicine*, 2017.

[10] M. A. Ertürk, A. J. E. Raaijmakers, G. Adriany, K. Ugurbil, and G. J. Metzger, "A 16-channel combined loop-dipole transceiver array for 7 Tesla body MRI," *Magn. Reson. Med.*, vol. 00, pp. 1–11, 2016.

[11] M. A. Ertürk *et al.*, "Toward imaging the body at 10.5 tesla," *Magn. Reson. Med.*, vol. 00, pp. 1–10, 2016.

[12] A. A. Hurshkainen *et al.*, "On Optimization of Radiative Dipole Body Array Coils for 7 Tesla MRI," pp. 1–12, 2017.

[13] I. Zivkovic, C. A. Castro, and A. Webb, "Design and characterization of an eight-element passively fed meander-dipole array with improved specific absorption rate efficiency for 7 T body imaging," *NMR Biomed.*, no. March, p. e4106, 2019.

[14] A. Sadeghi-Tarakameh *et al.*, "Optimizing the Topography of Transmit Coils for SAR Management," *Proc. Intl. Soc. Mag. Reson. Med. 26 Paris*, vol. 0297, 2018.

[15] M. A. Ertürk, X. Wu, G. Adriany, R. L. Lagore, K. Ugurbil, and G. J. Metzger, "An improved 32-channel loop-dipole transceiver array design for body imaging at 7.0 Tesla: Simulation

538843-L-bw-Steensma
Processed on: 17-12-2019
PDF page: 184

study," *Proc. 26th Annu. Meet. ISMRM, Paris, Fr.*, 2018.

[16] T. M. Fiedler *et al.*, "Comparison of a 32-channel remote body coil for 7 Tesla with local and remote 8- and 16-channel transmit coil arrays," in *Proc. Intl. Soc. Mag. Reson. Med. 25 Honolulu Hawaii*, 2017, p. 4306.

[17] S. Orzada *et al.*, "A 32-channel transmit system add-on for 7 Tesla body imaging," *Proc. 25th Annu. Meet. ISMRM, Honolulu, Hawaii*, p. 1219, 2017.

[18] K. Feng, N. A. Hollingsworth, M. P. McDougall, and S. M. Wright, "A 64-channel transmitter for investigating parallel transmit MRI," *IEEE Trans. Biomed. Eng.*, 2012.

[19] B. R. Steensma *et al.*, "Towards massively parallel multi-transmit for body imaging at 7T," *Proc. 25th Annu. Meet. ISMRM, Honolulu, Hawaii*, p. 1218, 2017.

[20] Z. Cao, X. Yan, and W. A. Grissom, "Array-compressed parallel transmit pulse design," *Magn. Reson. Med.*, 2016.

[21] NWO, "META-scan: A non-invasive metabolic imaging tool to study treatment response," 2015. [Online]. Available: https://www.nwo.nl/en/research-and-results/research-projects/i/18/26418.html.

[22] H. S., C. C.H., J. Felder, and J. N. Shah, "Design and simulation of dual-band dipole antenna for 1H/31P at 9.4T MRI," in *Proc. Intl. Soc. Mag. Reson. Med. 26 Paris*, 2018, p. 4400.

[23] B. Zhang, D. K. Sodickson, and M. A. Cloos, "A high-impedance detector-array glove for magnetic resonance imaging of the hand," *Nat. Biomed. Eng.*, 2018.

[24] A. A. Hurshkainen *et al.*, "Element decoupling of 7 T dipole body arrays by EBG metasurface structures: Experimental verification," *J. Magn. Reson.*, vol. 269, pp. 87–96, 2016.

[25] G. Solomakha *et al.*, "The dual-mode dipole: A new array element for 7T body imaging with reduced SAR," *Magn. Reson. Med.*, vol. 81, no. 2, pp. 1459–1469, 2019.

[26] M. De Greef, O. Ipek, A. J. E. Raaijmakers, J. Crezee, and C. A. T. Van Den Berg, "Specific absorption rate intersubject variability in 7T parallel transmit MRI of the head," *Magn. Reson. Med.*, vol. 69, no. 5, pp. 1476–1485, 2013.

[27] Ö. Ipek, A. J. Raaijmakers, J. J. Lagendijk, P. R. Luijten, and C. A. T. Van Den Berg, "Intersubject local SAR variation for 7T prostate MR imaging with an eight-channel single-side adapted dipole antenna array," *Magn. Reson. Med.*, vol. 71, no. 4, pp. 1559–1567, 2014.

[28] M. Le Garrec, V. Gras, M. F. Hang, G. Ferrand, M. Luong, and N. Boulant, "Probabilistic analysis of the specific absorption rate intersubject variability safety factor in parallel transmission MRI," *Magn. Reson. Med.*, 2017.

[29] E. F. Meliadò, C. A. T. van den Berg, P. R. Luijten, and A. J. E. Raaijmakers, "Intersubject specific absorption rate variability analysis through construction of 23 realistic body models for prostate imaging at 7T," *Magn. Reson. Med.*, no. April 2018, pp. 2106–2119, 2018.

[30] E. F. Meliadò, A. J. E. Raaijmakers, A. Sbrizzi, B. R. Steensma, P. R. Luijten, and C. A. T. van den Berg, "Deep learning method for image-based subject specific local SAR assessment," *Magn. Reson. Med.*, vol. In Press, 2019.

[31] E. Milshteyn *et al.*, "Individualized SAR Calculations Using Computer-Vision-Based MR Segmentation and a Fast Electromagnetic Solver," in *Proc. Intl. Soc. Mag. Reson. Med. 27 Montreal*, 2019, p. 4174.

[32] W. M. Brink, J. van Gemert, R. Remis, and A. G. Webb, "Accelerated SAR Computations

538843-L-bw-Steensma
Processed on: 17-12-2019
PDF page: 185

by Exploiting Sparsity in the Anatomical Domain," in *Proc. Intl. Soc. Mag. Reson. Med. 27 Montreal*, 2019, p. 0735.

[33] N. Boulant, V. Gras, A. Amadon, M. Luong, G. Ferrand, and A. Vignaud, "Workflow proposal for defining SAR safety margins in parallel transmission," in *Proceedings of the 26th Annual Meeting of ISMRM, Paris, France*, 2018, p. 0295.

[34] Y. Zhu, L. Alon, C. M. Deniz, R. Brown, and D. K. Sodickson, "System and SAR characterization in parallel RF transmission," *Magn. Reson. Med.*, 2012.

[35] J. Hoffmann *et al.*, "Safety testing and operational procedures for self-developed radiofrequency coils," *NMR Biomed.*, 2016.

[36] I. 10974:2012(en), "Assessment of the safety of magnetic resonance imaging for patients with an active implantable medical device.," 2012. [Online]. Available: https://www.iso.org/standard/46462.html.

[37] R. L. Siegel, K. D. Miller, and A. Jemal, "Cancer Statistics , 2017," vol. 67, no. 1, pp. 7–30, 2017.

[38] G. Draisma *et al.*, "Lead times and overdetection due to prostate-specific antigen screening: estimates from the European Randomized Study of Screening for Prostate Cancer.," *J. Natl. Cancer Inst.*, vol. 95, no. 12, pp. 868–878, 2003.

[39] A. B. Rosenkrantz *et al.*, "T2-weighted prostate MRI at 7 Tesla using a simplified external transmit-receive coil array: Correlation with radical prostatectomy findings in two prostate cancer patients," *J. Magn. Reson. Imaging*, vol. 41, no. 1, pp. 226–232, 2015.

[40] M. C. Maas *et al.*, "Feasibility of T2 -weighted turbo spin echo imaging of the human prostate at 7 tesla.," *Magn. Reson. Med.*, vol. 71, pp. 1711–9, 2014.

[41] T. Niendorf *et al.*, "W(h)ither human cardiac and body magnetic resonance at ultrahigh fields?technical advances , practical considerations , applications , and clinical opportunities," *NMR Biomed.*, vol. 29, no. 9, pp. 1173–97, 2016.

[42] F. Kober, T. Jao, T. Troalen, and K. S. Nayak, "Myocardial arterial spin labeling," *J. Cardiovasc. Magn. Reson.*, 2016.

[43] R. C.T. *et al.*, "Saturation recovery allows T1 mapping in the human heart at 7T with a commercial MRI scanner," *J. Cardiovasc. Magn. Reson.*, 2015.

[44] L. Feng *et al.*, "5D whole-heart sparse MRI," *Magn. Reson. Med.*, 2018.

[45] M. Prothmann *et al.*, "High spatial resolution cardiovascular magnetic resonance at 7.0 tesla in patients with hypertrophic cardiomyopathy - First experiences: Lesson learned from 7.0 tesla," *PLoS One*, 2016.

[46] M. Bourfiss, B. R. Steensma, A. S. J. . te Riele, T. Leiner, B. K. Velthuis, and A. J. E. Raaijmakers, "Feature tracking cardiac magnetic resonance of the right ventricle: effect of resolution, field strength and imaging sequence," in *EuroCMR*, 2019, p. P160.

[47] J. D. Ianni, Z. Cao, and W. A. Grissom, "Machine learning RF shimming: Prediction by iteratively projected ridge regression," *Magn. Reson. Med.*, 2018.

[48] R. Tomi-Tricot *et al.*, "SmartPulse, a machine learning approach for calibration-free dynamic RF shimming: Preliminary study in a clinical environment," *Magn. Reson. Med.*, 2019.

[49] R. Pohmann, O. Speck, and K. Scheffler, "Signal-to-noise ratio and MR tissue parameters in

538843-L-bw-Steensma
Processed on: 17-12-2019
PDF page: 186

human brain imaging at 3, 7, and 9.4 tesla using current receive coil arrays," *Magn. Reson. Med.*, 2016.

[50] G. J. Metzger *et al.*, "First human imaging studies at 10.5 Tesla: body studies at 450 MHz," in *Proc. Intl. Soc. Mag. Reson. Med. 27 Montreal*, 2019, p. 0696.

[51] T. F. Budinger *et al.*, "Toward 20 T magnetic resonance for human brain studies: opportunities for discovery and neuroscience rationale," *Magnetic Resonance Materials in Physics, Biology and Medicine*. 2016.

[52] A. D. Hendriks, W. J. M. Kemp, P. R. Luijten, N. Petridou, and D. W. J. Klomp, " SNR optimized 31 P functional MRS to detect mitochondrial and extracellular pH change during visual stimulation ," *NMR Biomed.*, 2019.

[53] R. W. Brown, Y.-C. N. Cheng, E. M. Haacke, M. R. Thompson, and R. Venkatesan, *Magnetic Resonance Imaging: Physical Principles and Sequence Design*. 2014.

[54] O. Ocali and E. Atalar, "Ultimate intrinsic signal-to-noise ratio in MRI," *Magn. Reson. Med.*, vol. 39, no. 3, pp. 462–473, 1998.

[55] B. R. Steensma, C. A. T. van den Berg, D. W. J. Klomp, P. R. Luijten, and A. J. E. Raaijmakers, "Comparing Realistic Coil Arrays to the Ultimate Intrinsic Coil Performance: A Simulation Stud," in *Proc. Intl. Soc. Mag. Reson. Med. Workshop on Ultrahigh Field Magnetic Resonance*, 2019.

[56] B. R. Steensma *et al.*, "Combining loops and dipoles at 7 T and 10.5 T: a simulation study," in *Proc. Intl. Soc. Mag. Reson. Honolulu*, 2017.

[57] B. Keil and L. L. Wald, "Massively parallel MRI detector arrays," *J. Magn. Reson.*, vol. 229, pp. 75–89, 2013.

[58] M. Schmitt *et al.*, "A 128-channel receive-only cardiac coil for highly accelerated cardiac MRI at 3 tesla," *Magn. Reson. Med.*, 2008.

538843-L-bw-Steensma
Processed on: 17-12-2019
PDF page: 187

Appendix

Appendix I: Nederlandse samenvatting

Naast toepassingen in het brein wordt MRI gebruikt bij de diagnose van veel voorkomende ziekten zoals prostaatkanker, ischemische hartziekte of ruggenmergafwijkingen. De beeldkwaliteit van MRI scanners wordt sterk beïnvloed door de sterkte van de MRI veld, welke gemeten wordt in Tesla [T]. Normale MRI scanners opereren op een veldsterkte van1.5T of 3T. In potentie gaat de beeldkwaliteit van MRI omhoog als een ogere veldsterkte wordt gebruikt. Om de beeldkwaliteit verder te verbeteren werd het eerste 7T MRI-systeem voor gebruik op mensen geïnstalleerd in 1999 [1]. Na de eerste pogingen om deze technologie toe te passen op imaging targets buiten het brein, werd duidelijk dat de beeldkwaliteit niet beter was dan op 1.5T of 3T systemen. Deze problemen werden veroorzaakt door nonuniformiteiten in de radiofrequente (RF) velden waarmee MRI beelden worden gemaakt. Het werd na deze eerste experimenten duidelijk dat de beschikbare RF-technologie moest worden verbeterd om het volledige potentieel van 7T voor diagnostische doeleinden te bereiken [2]. Voortbouwend op een breed scala aan ontwikkelingen op het gebied van RF-technologie binnen MRI, wilden we de RF antennes die gebruikt worden voor 7T body MRI verder verbeteren. Verbeteringen in het antenne ontwerp kunnen alleen goed worden getest wanneer ze worden gebruikt voor de beoogde beeldvormingstoepassing. De twee toepassingen in dit project zijn beide gericht op veel voorkomende ziekten, beeldvormingvan de prostaat (diagnose van prostaatkanker) en beeldvorming van het hart (vaak gebruikt voor de diagnose van ischemische hartziekte). De RF-antenns die in de loop van dit project zijn ontwikkeld zijn allemaal geëvalueerd met een of beide toepassingen in gedachten.

De eerste poging om het RF antennes voor prostaatbeeldvorming te verbeteren resulteerde in een nieuwe antenne, ‘de forward view antenne’ die tegen het perineum werd geplaatst als alternatief voor een endo-rectale spoel. Hoofdstuk 4 demonstreert e ontwikkeling en de evaluatie van deze spoel en rapporteert een SNR-verbetering van 19% wanneer deze spoel wordt toegevoegd aan een andere onfiguratie van RF antennes, een ‘dipool-array’. Een alternatieve benadering voor het verbeteren van SNR is om een ander soort antennes genaamd ‘loop coils’ toe te voegen aan een dipool array. Wiggins et al. hebben aangetoond dat dit de SNR met 50% verbetert [3]. Deze methode werd getest in hoofdstuk 4 in de prostaat, waarbij 16 loop elementen werden toegevoegd aan een 8-kanaals array van dipoolantennes. SNR op 7T werd vergeleken met 3T in vijf vrijwilligers en één patiënt. De gerapporteerde verbeteringen liepen uiteen van 1.7-voudig tot 2.8-voudig. De array die werd getest in hoofdstuk 4 voor pros-

538843-L-bw-Steensma
Processed on: 17-12-2019
PDF page: 189

taatbeeldvorming, werd aangepast voor cardiale beeldvorming door twee dipoolelementen op te nemen die een buiging in het midden hebben voor gemakkelijke positionering op de romp. Experimentele resultaten gaven aan dat SNR voor eeldvorming van het hart 50% verbeterde bij gebruik van een combinatie vanoop coils en dipolen vergeleken met een alleen dipool-array. De verbeterde SNR werd gebruikt om CINE- MRI afbeeldingen van het hart te maken met een iet eerder gehaalde ruimtelijke resolutie. De resultaten van deze studie werden gerapporteerd in hoofdstuk 5.

Een basisoverweging bij de ontwikkeling van RF antennes is veiligheid. De energie die door het RF-veld in het lichaam wordt gedeponeerd kan leiden tot lokale erhitting van weefsel, it effect is prominenter in MRI scanners met een hoge magneetveld sterkte. Om de RF-veiligheid van het loop-dipoolarray voor beeldvorming van het hart nader te bestuderen, werden in hoofdstuk 6 een totaal aantal van 14 simulatiemodellen ontwikkeld. Met behulp van deze modellen werden variaties van lokale SAR en temperatuurstijging bestudeerd. De simulatieresultaten werden gebruikt om eiligheidslimieiten in te stellen voor T beeldvorming van het hart.

Gebaseerd op de interesse die er is om MRI beelden te maken op veldsterktes hoger dan 7T, werden de RF-veiligheid en RF-prestaties van RF antennes als functie van de veldsterkte bestudeerd in hoofdstuk 7. Er werd aangetoond dat in tegenstelling tot wat eerder werd gedacht, de lokale SAR lineair toeneemt met veldsterkte in plaats van kwadratisch. SNR neemt kwadratisch toe met veldsterkte in plaats van lineair. Dit toont aan dat bij het doen van MRI na 7T de voordelen op het gebied van SNR groter zijn dan e nadelen ten gevolgde van verhoogde lokale SAR. Om de verhoogde SAR bij veldsterkten hoger dan 7T tegen te gaan, werd op een veldsterkte van 10.5T een nieuw soort dipool antenne ontwikkeld met een lage lokale pier SAR. De resultaten van dit ontwerp worden getoond in hoofdstuk 8. Met dit nieuwe dipoolontwerp, ‘de snake antenne’, kon B1 + per eenheid SAR tot 11% worden verbeterd in vergelijking met en een eerder antenne ontwerp. Nadat de snake antenne was goedgekeurd door de FDA voor humane MRI, werden beelden van de pelvis gemaakt op 10.5T. Ten slotte wordt in hoofdstuk 9 een alternatieve strategie gebruikt voor het verlagen van SAR, waarbij gebruik gemaakt wordt van een verhoogd aantal RF antennes. Het wordt aangetoond dat het gebruik van een 32 kanaals RF antenne array de effectieve SAR-niveaus aanzienlijk lager zijn in vergelijking met huidige 8-kanaals RF antenne arrays.

538843-L-bw-Steensma
Processed on: 17-12-2019
PDF page: 190

&

538843-L-bw-Steensma
Processed on: 17-12-2019

Appendix II: Tier system for safety assessment of custom-built RF coils

Synopsis

We propose an RF safety assessment formalism that uses four tier levels to quantify the accuracy of SAR modeling. Each subsequent tier level consists of more modeling and validation efforts while reducing the overestimation of peak SAR levels. The lowest tier level requires no simulations or measurements whereas the highest tier level includes B1+ and thermometry-based validations. The formalism defines a safety factor to account for deviations between the simulation model and the subject adding errors with the sum-of-squares method. A tier 3 validation and error propagation procedure was conducted for a 7T prostate array.

Purpose

To ensure safe use of custom built RF coils in MRI, electromagnetic (EM) simulations are performed to calculate peak local SAR levels. These are used to derive safe average input power limits based on the peak local SAR limits from the IEC [1]. The peak (local) SAR level determined by simulations will deviate from the actual peak SAR level in the patient. Therefore, a safety factor is typically applied to account for these potential deviations. Three potential sources of deviation are identified: inter-subject variability of SAR, inaccuracies in the coil model and inaccuracies in average power monitoring on the scanner [2]. The assessment of these three sources of uncertainty is part of any RF safety assessment procedure [2]–[7]. Presented procedures consist of one approach that aims for the highest accuracy with typically extensive modeling and validation efforts [8]. We propose an alternative RF safety assessment formalism that provides flexibility to trade low overestimation and extensive efforts for larger overestimations and more time-efficient procedures. Similar to the formalism for RF safety assessment of active implanted medical devices flexibility is provided by four tier levels [9]. Each subsequent tier level consists of more extensive modeling and validation efforts, while reducing the overestimation of peak SAR levels.

538843-L-bw-Steensma
Processed on: 17-12-2019
PDF page: 192

Methods

The tier levels are defined in table 1.

Tier Level	Explanation
0	No simulations are performed. All emitted power is assumed to end up in 10g of tissue.
1	Numerical simulations are performed on one or more patient models. No validation is done. Modeling inaccuracies are assumed to be 100%. Measured losses in the coil (e.g. lumped elements and conductive losses) are not considered in the simulation
2	Numerical simulations are performed on one or more patient models. Modeling inaccuracies are determined by comparing B_1^+ measurements **or** MR thermometry on a phantom with simulations. Measured losses in the coil are not considered in the simulation
3	Numerical simulations are performed on one or more patient models. Modeling inaccuracies are determined by B_1^+ measurements **and** MR thermometry. Measured coil losses are included in the simulation model.

Table 1: tier levels, the respective validation methods that need to be included and the methods to deal with inaccuracies that are found in validation.

Tier 0 assumes all power is deposited in 10g of tissue[10]. Tier 1 performs numerical simulations without validation and compensates by a large overestimation of the modelling error. Tier 2 performs simulations and validations based on B_1^+ mapping or MR thermometry. Modeling accuracy is determined by phantom validations. Tier 3 performs validations by B_1^+ mapping and MR thermometry. Now coil losses are no longer neglected resulting in minimal SAR overestimation. To provide an example, the full validation procedure was followed up to tier level 3 for a 7T body array[11]. All simulations were done in Sim4Life (Zurich Med Tech, Zurich, Switzerland). All measurements were done on a polyviniylpyrrolidone [12] (PVP) phantom (ε_r=37, σ=0.4 S/m). After all the inaccuracies have been quantified, they will need to be combined into a total safety factor, which is used, potentially in combination with the coil losses, to arrive at a corrected peak SAR level.

$$SAR_{corr} = SAR_{sim} \times SF \qquad [1]$$

Here SAR_{corr} is the corrected peak SAR level, SAR_{sim} is the peak SAR level that resulted from simulations and SF is the safety factor (SF>1). The safety factor follows from the relative peak SAR uncertainty:

$$SF = 1 + \frac{\Delta SAR_{total}}{SAR_{sim}} \qquad [2]$$

Where ΔSAR_{total} is the total uncertainty on the simulated peak SAR level SAR_{sim}. ΔSAR_{total} follows from the individual sources of uncertainty $\Delta SAR_{int.subj.var}$,

538843-L-bw-Steensma
Processed on: 17-12-2019
PDF page: 193

$\Delta SAR_{model.error}$ and ΔP_{input} [3].

$$\left(\frac{\Delta SAR_{total}}{SAR}\right)^2 = \left(\frac{\Delta P_{input}}{P_{input}}\right)^2 + \left(\frac{\Delta SAR_{\text{int}.subj.\text{var}}}{SAR}\right)^2 + \left(\frac{\Delta SAR_{\text{mod}el.inacc}}{SAR}\right)^2 \quad [3]$$

Because all these sources of error are independent from each other, error propagation will be calculated using the sum of squares method. In addition, we propose a method to determine the modeling error from the validation B_1^+ or temperature/SAR distribution using a statistical approach as explained in step 3 and 4 in figure 1.

Results

For prostate imaging, Meliado et al found an average peak SAR of 2.4 W/kg for 8x1 W input power and an inter-subject variation error of 80%[6]. The power measurement error is 10% based on directional coupler specifications. Figure 1 shows the results of the validation, in which the thermometry shows a modeling inaccuracy of 52%. The total error adds up to 98%, leading to a safety factor of 1.98 (table 2) for random RF shim settings.

Conclusion

A formalism is presented for RF safety assessment of multi-transmit coil arrays, which classifies the level of simulation and validation effort in a tier system. The largest tier level provides minimum overestimation at the expense of considerable modeling and validation efforts and vice versa. Modeling inaccuracy is determined by a statistical approach based on differences between simulated and measured B1+-maps/temperature maps. To address total peak local SAR uncertainty, predicted peak local SAR levels are multiplied by a safety factor which is obtained by adding individual sources of uncertainty in a sum-of-squares way. For the investigated dipole antenna array the resulting per channel power limit is 4.2 W

538843-L-bw-Steensma
Processed on: 17-12-2019
PDF page: 194

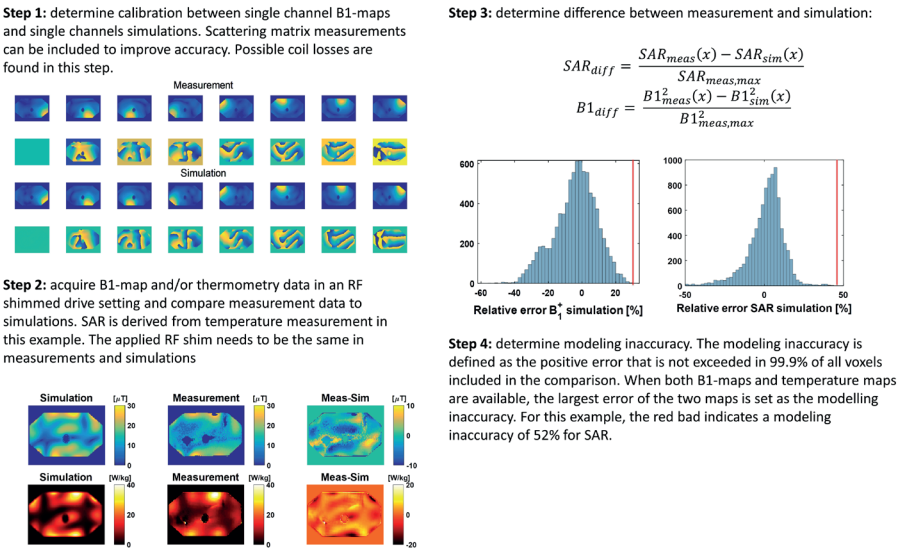

Figure 1: procedure to achieve validation tier 3 for the fractionated dipole array.

Imaging target	SAR limit [W/kg]	SAR level [W/kg]	Inter-subject variability	Model	Power	Safety Factor	Power Limit [W/
Prostate	20	2.4	0.8	0.52	0.10	$1+\sqrt{(0.80^2+0.52^2+0.21^2)}=1.98$	4.2

Table 2: Results of a tier 3 validation procedure for the fractionated dipole array, resulting in an allowed average power limit of 4.2 W/channel.

References

[1] IEC, "Medical electrical equipment. Part 2-33: particular requirements for the safety of magnetic resonance equipment for medical diagnosis.," *IEC 60601-2-33*, 2015.

[2] N. Boulant, V. Gras, A. Amadon, M. Luong, G. Ferrand, and A. Vignaud, "Workflow proposal for defining SAR safety margins in parallel transmission," in *Proceedings of the 26th Annual Meeting of ISMRM, Paris, France*, 2018, p. 0295.

[3] G. Ferrand, M. Luong, A. Amadon, and N. Boulant, "Mathematical Tools to Define SAR Margins for Phased Array Coil In-Vivo Aplications Given E-field Uncertainties," in *Proc. Intl. Soc. Mag. Reson. Med. 23 Toronto*, 2015, p. 1862.

[4] M. De Greef, O. Ipek, A. J. E. Raaijmakers, J. Crezee, and C. A. T. Van Den Berg, "Specific absorption rate intersubject variability in 7T parallel transmit MRI of the head," *Magn. Reson. Med.*, vol. 69, no. 5, pp. 1476–1485, 2013.

[5] Ö. Ipek, A. J. Raaijmakers, J. J. Lagendijk, P. R. Luijten, and C. A. T. Van Den Berg,

538843-L-bw-Steensma
Processed on: 17-12-2019
PDF page: 195

"Intersubject local SAR variation for 7T prostate MR imaging with an eight-channel single-side adapted dipole antenna array," *Magn. Reson. Med.*, vol. 71, no. 4, pp. 1559–1567, 2014.

[6] E. F. Meliadò, C. A. T. van den Berg, P. R. Luijten, and A. J. E. Raaijmakers, "Intersubject specific absorption rate variability analysis through construction of 23 realistic body models for prostate imaging at 7T," *Magn. Reson. Med.*, no. April 2018, pp. 2106–2119, 2018.

[7] M. Le Garrec, V. Gras, M. F. Hang, G. Ferrand, M. Luong, and N. Boulant, "Probabilistic analysis of the specific absorption rate intersubject variability safety factor in parallel transmission MRI," *Magn. Reson. Med.*, 2017.

[8] J. Hoffmann *et al.*, "Safety testing and operational procedures for self-developed radiofrequency coils," *NMR Biomed.*, 2016.

[9] I. 10974:2012(en), "Assessment of the safety of magnetic resonance imaging for patients with an active implantable medical device.," 2012. [Online]. Available: https://www.iso.org/standard/46462.html.

[10] A. Vignaud *et al.*, "Fast and unconditionally safe in vivo MR head protocol for home-made coil prototype assessment at 7T," in *Proc. 36th ESMRMB, Rotterdam*, 2019, p. 1289.

[11] A. J. E. Raaijmakers *et al.*, "The fractionated dipole antenna: A new antenna for body imaging at 7 Tesla," *Magn. Reson. Med.*, vol. 75, no. 3, pp. 1366–1374, 2016.

[12] C. Ianniello *et al.*, "Synthesized tissue-equivalent dielectric phantoms using salt and polyvinylpyrrolidone solutions," *Magn. Reson. Med.*, vol. 80, no. 1, pp. 413–419, 2018.

538843-L-bw-Steensma
Processed on: 17-12-2019
PDF page: 196

&

538843-L-bw-Steensma
Processed on: 17-12-2019

List of publications

Published manuscripts

De Feyter HM, Herzog RI, **Steensma BR**, Klomp DWJ, Brown, PB, Mason, GF, de Graaf, RA (2018). Selective proton-observed, carbon-edited (selPOCE) MRS method for measurement of glutamate and glutamine^{13}C-labeling in the human frontal cortex. *Magnetic Resonance in Medicine*, *80*(1), pp11-20.

Kurk, SA, **Steensma, BR,** May AM, Koopman M, Hoogduin HM, Velden TA Van Der, Kemp, W JM Van Der. (2018). Feasibility of 7-T fluorine magnetic resonance spectroscopic imaging (19 F MRSI) for TAS-102 metabolite detection in the liver of patients with metastatic colorectal cancer. *European Radiology Experimental Vols,* 2(16)

Steensma BR, Voogt IJ, Leiner T, Luijten PR, Habets J, Klomp DWJ, Raaijmakers AJE (2017). An 8 - channel Tx / Rx dipole array combined with 16 Rx loops for high - resolution functional cardiac imaging at 7 T. *Magnetic Resonance Materials in Physics, Biology and Medicine*, 31(1)

Steensma BR, Voogt IJ, van der Werf AJ, van den Berg CAT, Luijten PR, Klomp DWJ, & Raaijmakers AJE (2018). Design of a forward view antenna for prostate imaging at 7T. *NMR in Biomedicine*, (January), 1–10. 31(9), e3993, pp7-18

&

Steensma BR, Luttje MP, Voogt IJ, Klomp DWJ, Luijten PR, van den Berg CAT, & Raaijmakers, AJE (2018). Comparing signal-to-noise ratio for prostate imaging at 7T and 3T. *Journal of Magnetic Resonance*, 49(5), pp1446-1455

Krikken E, **Steensma BR**, Voogt IJ, Luijten PR, Klomp DWJ, Raaijmakers AJE, & Wijnen JP (2019). Homogeneous B1+ for bilateral breast imaging at 7 T using a five dipole transmit array merged with a high density receive loop array. *NMR in Biomedicine*, *32*(2), 10–17.

Raaijmakers AJE & Steensma BR (2019). Local SAR Assessment for Multitransmit Systems : A Study on the Peak Local SAR Value as a Function of Magnetic Field Strength, *8(1)*, https://doi.org/10.1002/9780470034590.emrstm1577

Meliadò EF, Raaijmakers AJE, Sbrizzi A, **Steensma BR**, Luijten PR, & van den Berg CAT (2020). Deep learning method for image-based subject specific local SAR assessment. *Magnetic Resonance in Medicine*, 83(2), pp695-711.

538843-L-bw-Steensma
Processed on: 17-12-2019
PDF page: 198

Conference proceedings (ISMRM and first author only)

Steensma BR, Obando AV., Klomp DWJ, van den Berg CAT, & Raaijmakers AJE (2016). Body imaging at 7 tesla with much lower SAR levels: an introduction of the Snake Antenna Array. In *Proceedings of the 24th Annual Meeting of ISMRM, Singapore*, 0395. (Oral presentation)

Steensma BR, Raaijmakers AJE, Voogt IJ, Haghnejad SA, Klomp DWJ, van den Berg CAT, Luijten, PR (2016). Design of a forward view antenna for prostate imaging at 7 tesla. In *Proceedings of the 24th Annual Meeting of ISMRM, Singapore*, 2126. (Traditional poster)

Steensma BR, Teixeira J, Voogt IJ, Luijten PR, Klomp DWJ, van den Berg, CAT, & Raaijmakers AJE (2017). Towards massively parallel multi-transmit for body imaging at 7T. *Proceedings of the 25th Annual Meeting of ISMRM, Honolulu, Hawaii*, 1218. (Oral presentation)

Steensma BR, Voogt IJ, Leiner T, Luijten PR, Klomp DWJ, van den Berg CAT, & Raaijmakers AJE (2017). DREAM-based B1-shimming for cardiac imaging at 7 T. *Proceedings of the 25th Annual Meeting of ISMRM, Honolulu, Hawaii*, 3916. (Electronic poster)

Steensma, BR, Ertürk, MA, Ugurbil, K, Luijten, PR, Klomp, DWJ, van den Berg, CAT, … Raaijmakers AJE (2017). Combining loops and dipoles at 7 T and 10.5 T: a simulation study. *Proceedings of the 25th Annual Meeting of ISMRM, Honolulu, Hawaii*, 4137. (Electronic poster)

Steensma BR, van de Moortele P-F., Erturk MA, Grant A, Adriany G, Metzger GJ, & Raaijmakers, AJ E (2018). Optimization and validation of dipole antenna geometry for body imaging at 10.5T. In *Proceedings of the 26th Annual Meeting of ISMRM, Paris, France*, 0138. (Oral presentation)

Steensma BR, Voogt IJ, Kraaij T, Cloos MA, Sodickson DK, Klomp DW J, Raaijmakers A J E (2019). Approaching the ultimate intrinsic coil performance for 7T body imaging with high-density parallel transmit/receive arrays. In *Proceedings of the 27th Annual Meeting of ISMRM, Montreal, Canada*, 0564. (Power pitch)

Steensma BR, Meliadò EF, Huijng ER, Luijten PR, Klomp DWJ, van den Berg CAT & Raaijmakers, AJE (2019). SAR and temperature distributions in a database of realistic human models for 7T cardiac imaging. In *Proceedings of the 27th Annual Meeting of ISMRM, Montreal, Canada*, 4153. (Electronic poster)

538843-L-bw-Steensma
Processed on: 17-12-2019
PDF page: 199

Manuscripts in preparation (first author only)

Steensma BR, Meliado EF, Luijten PR, Klomp DWJ, van den Berg CAT, Raaijmakers AJE, SAR and temperature distributions in a database of realistic human models for cardiac imaging at 7T (Submitted to Magnetic Resonance in Medicine)

Steensma BR, van de Moortele PF, Ertürk MA, Grant A, Adriany G, Klomp DWJ, van den Berg CAT, Metzger G, Raaijmakers AJE, Optimization and validation of dipole antenna geometry for body imaging at 10.5T (In preparation)

Steensma BR, Voogt IJ, Luijten PR, Klomp DWJ, van den Berg CAT, Raaijmakers AJE, Design of a 32 channel local transmit array for body imaging at 7T (In preparation)

Steensma BR, Voogt IJ, Luijten PR, Klomp DWJ, van den Berg CAT, Raaijmakers AJE, Tier based formalism for safety assessment of custom-built RF coils (In preparation)

538843-L-bw-Steensma
Processed on: 17-12-2019
PDF page: 200

Dankwoord

Al het werk dat ik in de afgelopen 4 à 5 jaar heb gedaan om mijn promotie te volbrengen had ik niet kunnen doen zonder de steun en bijdrage van een grote groep mensen. Ik wil graag dit hoofdstuk gebruiken om al deze mensen hiervoor te bedanken.

Allereerst wil ik mijn copromotor en directe begeleider **Alexander** bedanken. Ik kan me nog goed herinneren dat ik kwam kijken voor een stageplek in Utrecht en dat je mij hierbij een rondleiding gaf bij de 7T. Al het soldeerwerk en de hobby-achtige projecten die ik daar zag staan spraken me heel erg aan en ik denk dat deze specifieke actie eigenlijk de aanleiding is voor het ontstaan van dit boekje. Ik wil je met name bedanken voor je begeleiding die inhoudelijk altijd van een uitzonderlijk hoog niveau is geweest en voor het geduld dat je opbrengt bij het uitleggen van complexe onderwerpen. Een aantal kansen die ik tijdens mijn PhD heb gehad, zoals het onderzoek in Minneapolis en nu de postdoc op NIH heb ik direct te danken aan jouw contacten in de onderzoekswereld. Ik wil je veel succes wensen in de komende periode op het UMC Utrecht en als docent in Eindhoven.

Nico, als tweede copromotor wil ik jou bedanken voor je inhoudelijke bijdrage aan het project, met name voor de nieuwe ideeën en alternatieve inzichten die je heb ingebracht. Wat mij vooral zal bijblijven zijn lange maar goede discussies in de RF meeting en je presentatie over het reciprociteitsprincipe op de ISMRM in Honolulu, waarvoor jij en Alexander van te voren nog een nacht hadden doorgehaald om de wiskunde te verifiëren. Ik wens je veel succes met het continueren van je nieuwe Computational Imaging Group, hopelijk mag ik je snel professor noemen.

Professor **Dennis**, als promotor wil jou bedanken voor alle positieve energie die je continu overdraagt op mij en eigenlijk iedereen om je heen. Dankzij jou heb ik in een aantal andere interessante projecten kunnen meedoen, zoals het PETMR project en meer recentelijk WaveTronica. Ook zal ik niet vergeten dat ik dankzij jou een plaatje van een simulatie in een boek van Robin de Graaf heb mogen plaatsen. Veel succes met je nieuwe functie als professor, en hopelijk komt die 14 Tesla MRI er zo snel mogelijk!

For their careful review of my PhD thesis and for enabling me to obtain my PhD degree I want to thank the jury of my PhD defense: **Prof. Dr.**

538843-L-bw-Steensma
Processed on: 17-12-2019
PDF page: 201

Hugo de Jong, Prof. Dr. Ir. Jan Lagendijk, Dr.Ir. Mariëlle Philippens, Prof. Dr. Sc. Techn. Mark Ladd, Prof. Richard Bowtell, Dr. Alexandre Vignaud and Prof. Dr. Saskia van Mil. I want to especially thank Mark Ladd, Richard Bowtell and Alexandre Vignaud for travelling all the way to Utrecht and for their contribution to the symposium "From 7T to 14T: possibilities and development of MRI beyond 7T".

Goed onderzoek kan natuurlijk alleen tot stand komen onder goede werkomstandigheden en daarvoor wil ik de **7 Tesla** groep bedanken. De vele bezoekjes aan de basket, promotiefeesten, kerstfeesten en nieuwjaarsdiners zal ik in de Verenigde Staten gaan missen. Met name mijn kamergenoten, bedankt dat jullie het al die tijd op Q02.4309 met mij hebben uitgehouden. Bedankt voor alle pepernoten (**Erwin**), bedankt voor het laten crashen van Sim4Life (**Carel**), veel plezier met je nieuwe racefiets (**Tijl**) en sterkte met de ethische commissie van het PMC (**Evita**).

Mijn sportieve hobby's heb ik met veel mensen van de 7 Tesla altijd goed kunnen delen. **Alex, Casper, Fredy, Jannie, Peter, Cyril, Alexandre Arjen,**en de rest van de Cycling for Science bedankt voor de vele mooie en snelle fietsrondjes en voor het verslaan van Leiden in de Utrecht-Leiden race van twee jaar terug (in het speciaal **Anita** voor dat laatste). **Sander**, hopelijk lukt het voor maart nog om een paar keer stuk(je) te gaan rennen en veel succes bij de marathon van Rotterdam. **Janot, Lisa en Erwin**, die blauwe maandag dat ik naar cross-challenge en GRIT ben geweest vergeet ik niet meer, en dan vooral niet de spierpijn die eraan achteraf ging. Ook wil ik de koffie-crew: **Janot, Erwin, Tim en Peter** bedanken voor alle brew die er in de afgelopen jaren is gemaakt en mij verontschuldigen voor het maken van double-brew. Misschien wordt het tijd om nieuwe leden te gaan recruteren gezien de slinkende grootte van de groep.

Anneloes, Stefano, Arrie, Ellis en Oscar bedankt voor een hele mooie vakantie in Hawaï en **Anneloes** ook bedankt voor het organiseren een aantal mooie schaatsactiviteiten. De smash-bros en andere Nintendo switch-spelers: **Oscar, Peter, Seb, Lieke, Carel, Tijl en Quincy:** ik zal niet meer vergeten dat jullie mij elke keer hebben ingemaakt met Smash en Mario kart. Volgens mij staat er een nieuwe switch avond ingepland op het moment van schrijven, ik ben alvast aan het oefenen. **Flavio**, thanks for the opportunity to give even more presentations than I was already doing and thanks for working with me on some interesting projects. Just to let you know: I have sent in an abstract to ISMRM but won't be there, so it might be time that I get my revenge.

538843-L-bw-Steensma
Processed on: 17-12-2019
PDF page: 202

Voor alle hulp bij het bouwen en ontwikkelen van nieuwe spoelen wil ik het **Coillab** bedanken. **Luka, Dimitri, Mark, Cezar, Erik,** bedankt! Met name **Aidin en Ingmar**, jullie waren er al bij ver voordat ik startte als student en hebben mij betrokken bij WaveTronica. Veel succes met jullie (ons) nieuwe bedrijf in de komende jaren.

Als laatste van de 7 Tesla **Sylvia;** bedankt voor alle steun bij de laatste lotjes van mijn project. Zonder jou was de planning van mijn verdediging niet gelukt. Ook het goedkeuren van uitgaven of het doen van declaraties in de mysterieuze informatiesystemen van het ziekenhuis werd een stuk makkelijker met jouw steun. Ik zou ook graag mijn excuses willen aanbieden voor alle onleesbare dingen die ik in de vrijwilligersmap heb geschreven, gelukkig kunnen papers tegenwoordig op de computer worden geschreven.

Ook de rest van de groep en alle mensen met wie ik heb samengewerkt;- bedankt voor de leuke tijd die we hebben gehad in Utrecht: **Hans, Jeroen, Martijn, Wouter, Jannie, Catalina, Jeanine, Jacob-Jan, Kees, Deji, Mariska, Mariska, Alessandro, Natalia, Mike, Vitaliy, Carlo, Tine, Mario, Jolanda, Ria, Edwin, Anna, Niek, Jaco, Lennart, Matthew, Nikki, Anja, Aihan, Zahra, Kyung-min, Mimount, Woutjan, Robin, Stefan.** Bedankt allemaal!

Chapter 8 of this PhD thesis was completed as part of a research project I did at the Center for Magnetic Resonance Research in Minneapolis. I'm very thankful to have spent a short period at one of the most if not the most important research center in ultra-high field MRI. **Greg**, thank you for the supervision during this period, thanks for the nice bike ride we had and I probably shouldn't have left my bike at your place... **Arcan**, thanks for initiating the project and thanks for working me on multiple abstracts and hopefully soon a publication. **Gregor, Jessica and Ivan**, thank a lot for being so open to new people and for the good times we had at CMRR.

Naast mijn onderzoek is er gelukkig altijd genoeg tijd overgebleven om leuke dingen te doen. Daarvoor wil ik al mijn vrienden bedanken. Als eerste natuurlijk **D&J. Lydia (Good appliances), Lisa, Robin (Mario), Fabian (Fabbie), Robin, Remco (Ietjse Meer), Vincent (Finsj), Pieter-Bas (Pebai), Marty (Denk aan je toekomst), Remy (Sultans of Swing), Michael, Sander, Wessel (Dit Gaat te Fur), Jesper (De Kale Boer).** Ik weet niet iedereens bijnaam meer, hebben sommige mensen wel bijnamen? Bedankt voor alle 90's parties, Leeman, kalkoen met Leeman, voor elk

538843-L-bw-Steensma
Processed on: 17-12-2019
PDF page: 203

nieuwjaarsfeest en voor elk hardstyle/hardcore-feest. Hopelijk kunnen we hier nog jaren mee door gaan en ik hoop jullie allemaal in Washington te zien. De Utrecht/**Enschede** crew: **Ruth, Fitski, Xander, Robin, Renée, Jorik, Mark en Christina** bedankt voor het vele bier en goede eten. Ik hoop dat de groep nog groter is geworden als ik weer terug ben. **Jasmien**, bedankt voor alle series-marathons en voor de mooie (of minder mooie) feestjes in Tivoli. De heren van **Isis** en **Licht 2012**, bedankt voor de mooie borrels, alle stukken roeien en voor de mooie fietsvakanties die we samen hebben gedaan.

Als allerlaatste wil ik natuurlijk mijn familie, **Romke, Margreet en Nienke**, bedanken voor alle steun die ik altijd van jullie heb gehad. Alhoewel Utrecht een ontzettend fijne plek is geweest om te wonen ben ik pas echt thuis als ik bij jullie in Almere ben. De komende anderhalf jaar ben ik verder weg, maar ik kijk er naar uit om mijn nieuwe woonplaats aan jullie te laten zien.

&

538843-L-bw-Steensma
Processed on: 17-12-2019
PDF page: 204

Curriculum vitae

Bart Steensma (10-02-1991) grew up in Almere and completed his high school in 2008 at the Oostvaarderscollege in Almere Buiten. After a sabbatical of 1 year he started his study of Biomedical Engineering at the University Twente. He completed his bachelor's degree in 2012 at the neuroimaging group of the University of Twente with research on the calibration of a magnetometer for axillary lymph node staging with superparamagnetic iron particles. After one year of courses for his Master's degree in Biomedical Engineering with a focus on biomedical physics, he was a fulltime member of the board for the University Rowing club D.R.V. Euros. Upon completing all his courses and after finishing as a board member, he left for a research internship at the Bionics Institute in Melbourne to do a research internship on new materials for use in retinal prostheses.

Finally, when starting his Master's project, Bart decided to move into the field of MRI to do a masters project about 7T MRI at the University Medical Center Utrecht. This research project continued into a PhD which lead to this thesis. During his PhD, Bart moved to the city of Minneapolis in the United States for 4 months to translate his research to a new 10.5T MRI system. In addition to being a researcher, Bart competes in running and triathlon races. After receiving his PhD degree, Bart will move to the United States for a period of 15 months to work as an on-site scientist for Siemens at the National Institute of Health in Bethesda.

538843-L-bw-Steensma
Processed on: 17-12-2019
PDF page: 205